SECOND EDITION

Phase Transitions in Materials:

Advanced Topics (Online Chapters)

BRENT FULTZ

Phase Transitions in Materials: Advanced Topics (Online Chapters)

Second Edition

BRENT FULTZ
California Institute of Technology

Information about the *Phase Transitions in Materials: Advanced Topics (Online Chapters)*

Please cite this open source reference as:

B. Fultz, *Phase Transitions in Materials: Advanced Topics* (California Institute of Technology, 2020).
DOI: 10.7907/05BY-QX43.

ISBN 978-1-60049-101-1

It is available at no cost from www.library.caltech.edu
https://resolver.caltech.edu/CaltechAUTHORS:20190207-125601247

Reasonable efforts have been made to publish reliable data and information, but the author and publisher cannot assume responsibility for the validity of all information and its use. The author and publisher have attempted to find the copyright holders of all images reproduced in this book, and apologize to copyright holders if permission was not obtained. If copyrighted materials were not acknowledged properly, please write to us so we can do so in future reprints.

Except as permitted under U.S. Copyright Law, no part of this book may be reproduced by any means, electronic, magnetic, chemical, mechanical, or other methods not yet invented, without written permission from the publisher.

The use of general descriptive names, registered names, trademarks, etc., in this publication does not imply that such names are exempt from the relevant protective laws and regulations and therefore free for general use.

© Brent Fultz 2020

This publication is in copyright. Subject to statutory exception and to the provisions of relevant collective licensing agreements, no reproduction of any part may take place without the written permission of the author.

Information about *Phase Transitions in Materials*, Second Edition

Chapters 1 through 21 are available from Cambridge University Press.

www.cambridge.org
Information on this title: www.cambridge.org/9781108485784
DOI: 10.1017/9781108641449

© Brent Fultz 2014
© Cambridge University Press 2020

This publication is in copyright. Subject to statutory exception and to the provisions of relevant collective licensing agreements, no reproduction of any part may take place without the written permission of Cambridge University Press.

First published 2014
Second edition 2020

ISBN 978-1-108-48578-4 Hardback

Additional resources for this publication at www.cambridge.org/fultz2

Contents

Preface

Content

This book explains the thermodynamics and kinetics of most of the important phase transitions in materials science. It is a textbook, so the emphasis is on explanations of phenomena rather than a scholarly assessment of their origins. The goal is explanations that are concise, clear, and reasonably complete. The level and detail are appropriate for upper division undergraduate students and graduate students in materials science and materials physics. The book should also be useful for researchers who are not specialists in these fields. The book is organized for approximately sequential coverage in a graduate-level course. The four parts of the book serve different purposes, however, and should be approached differently.

Part I presents topics that all graduate students in materials science must know.[1] After a general overview of phase transitions, temperature–composition phase diagrams are explained from classical thermodynamics and from the statistical mechanics of Ising lattices. Diffusion, equilibration, and nucleation are then covered, and general aspects of diffusion and nucleation are used with T–c phase diagrams to explain the rates of some phase transformations.

Part II addresses the origins of materials thermodynamics and kinetics at the level of atoms and electrons. Electronic and elastic energy are covered at the level needed in some of the later chapters. The physical origins of entropy (a topic that receives scant coverage in other texts) are presented in the context of phase transitions on Ising lattices. Effects of pressure, combined with temperature, are explained with a few concepts of chemical bonding and antibonding. The thermodynamics of real materials typically involves minimizing a free energy with multiple degrees of freedom, and Chapter 9 shows directions beyond one variable. Chapter 10 on kinetics emphasizes atom movements for diffusion in solids, especially features of atom–vacancy interchanges.

Part III is the longest. It describes important phase transformations in materials, with their underlying concepts. Topics include surface phenomena, melting, solidification, nucleation and growth in solids, spinodal decomposition, phase field theory, continuous ordering, martensitic transformations, phenomena in nanomaterials, and phase transitions involving electrons or spins. Many topics from metallurgy and ceramic engineering are

[1] The author asks graduate students to explain some of the key concepts at a blackboard during their Ph.D. candidacy examinations.

covered, although the connection between processing and properties is less emphasized, allowing for a more concise presentation than in traditional texts.

The online Advanced Topics present modern topics that have proved their importance. These chapters are available online at doi:10.7907/05BY-QX43 and can be downloaded at no cost from https://www.library.caltech.edu. The chapters cover low- and high-temperature treatments of the partition function, nonequilibrium states in crystalline alloys, a *k*-space formulation of elastic energy, fluctuations and how they are measured, high-temperature thermodynamics, the renormalization group, scaling theory, and an introduction to quantum phase transitions. The topics are explained at a fundamental level, but unlike Parts I through III, for conciseness there are more omissions of methods and steps.

Many topics in phase transitions and related phenomena are not covered in this text. These include: polymer flow and dynamics including reptation, phase transitions in fluid systems including phenomena near the critical temperature, crystallographic symmetry in displacive transformations, and massive transformations. Also beyond the scope of the book are computational methods that are increasingly important for studies of phase transformations in materials, including: Monte Carlo methods, molecular dynamics methods (classical and quantum), and density functional theory with time or ensemble averages for materials at finite temperatures.

The field of phase transitions is huge, and continues to grow. This text is a snapshot of the field taken from the viewpoint of the author near the year 2020. Impressively, this field continues to offer a rich source of new ideas and results for both fundamental and applied research, and parts of it will look different in a decade or so. I expect, however, that the core will remain the same – the free energy of materials will be at the center, surrounded by issues of kinetics.

Teaching

I use this text in a course for Ph.D. students in both materials science and in applied physics at the California Institute of Technology. The 10-week course is offered in the third academic quarter as part of a one-year sequence. The first two quarters in this sequence cover thermodynamics and statistical mechanics, so the students are already familiar with using a partition function to obtain thermodynamic quantities. Familiarity with some concepts from solid-state physics and chemistry is certainly helpful, but the text develops many of the important concepts as needed.

In the one-quarter course at Caltech, I cover most topics in Parts I and II, moving in sequence through the chapters. Time limitations force a selection of topics from Part III and Advanced Topics. For example, I tend to cover Chapters 12, 16, 18, and parts of 14, 19, 20 (although sometimes these later parts are replaced by an advanced chapter, such as 25). It is unrealistic to cover the entire content of the book in one course, even with a 15-week semester. An instructor will use discretion in selecting topics for the second half of his or her course.

The problems at the end of each chapter were used for weekly student assignments, and this helped to refine their wording and content. The majority of these problems are based on concepts explained in the text, sometimes filling in explanations or extending the analyses. Other problems, less popular with students, develop new concepts not described in the chapter. These problems usually include longer explanations and hints that may be worth reading even without working the problem. None of the problems are intended to be particularly difficult, and some can be answered quickly with one main idea. For homework, I assign five or six of these problems every week during the term. In their reviews of the course, most students reportedly spend 6–8 hours per week outside the classroom completing these problem sets and reading the text. An online solutions manual is available to course instructors whose identity can be verified. Please ask me for further information.

Acknowledgments

I thank J.J. Hoyt for collaborating with me on a book chapter about phase equilibria and phase transformations that prompted me to get started on the first edition of this book. The development of the topic of vibrational entropy would not have been possible without the contributions of my junior collaborators at Caltech, especially L. Anthony, L.J. Nagel, H.N. Frase, M.E. Manley, J.Y.Y. Lin, T.L. Swan-Wood, A.B. Papandrew, O. Delaire, M.S. Lucas, M.G. Kresch, M.L. Winterrose, J. Purewal, C.W. Li, T. Lan, H.L. Smith, L. Mauger, S.J. Tracy, D.S. Kim, and N. Weadock. Several of them are taking this field into new directions.

Important ideas have come from stimulating conversations over the years with O. Hellman, A. van de Walle, V. Ozolins, G. Ceder, M. Asta, L.-Q. Chen, D.D. Johnson, E.E. Alp, R. Hemley, J. Neugebauer, B. Grabowski, M. Sluiter, F. Körmann, D. de Fontaine, A.G. Khachaturyan, I. Abrikosov, A. Zunger, P. Rez, K. Samwer, and W.L. Johnson.

This work benefited from the support of NSF Award 1904714.

Brent Fultz

Notation

a	lattice parameter
A	area
$\vec{A}$	vector potential of magnetic field
A-atom	generic chemical element
APDB	antiphase domain boundary
α	coefficient of linear thermal expansion
α	critical exponent for heat capacity
α-phase	generic phase
α-sublattice	a lattice of like atoms within an ordered structure
α_i	root of Bessel function
α^2	electron–phonon coupling factor
$\vec{b}$	Burgers vector of dislocation
b_{A}	coherent neutron scattering length of isotope A
$b(\vec{k})$	Fourier transform of pairwise energy for two concentration waves
B	bulk modulus
$\vec{B}$	magnetic field
B-atom	generic chemical element
$B(\vec{R})$	pairwise energy between atoms
β	coefficient of volume thermal expansion
β	critical exponent for density
β-phase	generic phase
β-sublattice	a lattice of like atoms within an ordered structure
c	chemical composition (atomic fraction)
c_{l}^*	chemical composition of liquid at liquid–solid interface
c_{s}^*	chemical composition of solid at liquid–solid interface
c	speed of sound or light
c_{A}	concentration of A-atoms
c_{A}	weight of atomic wavefunction on atom A in a molecular wavefunction
C_{el}	electronic heat capacity
$C_P(T)$	heat capacity at constant pressure
$C_V(T)$	heat capacity at constant volume
C_{ij}, C_{ijlm}	elastic constant

D	diffusion coefficient
D	deformation potential
D_{h}	thermal (heat) diffusion coefficient
$\vec{D}$	electric polarization
D_0	prefactor for exponential form of diffusion coefficient
$\tilde{D}(c)$	interdiffusion coefficient
$\underline{D}(\vec{k})$, $D_{ij}(\vec{k})$	dynamical matrix, element of
δ	fractional change in volume (of misfitting sphere)
ΔG_{V}	change in Gibbs free energy per unit volume
ΔG^*	activation barrier for nucleation
$\Delta(\vec{r})$	static wave of chemical concentration
e	charge of electron
e_{A}	energy of an A-atom on a crystal site
e_{AB}	energy of a pair (bond) between an A- and a B-atom
e_{R}, e_{W}	energy of two atoms, A and B, on their right or wrong sublattices
$\vec{e}_{\kappa j}(\vec{k})$	polarization for atom of basis index κ in phonon of $\vec{k}$ in branch j
$\mathrm{erf}(z)$	error function
E	energy, thermodynamic energy
$\vec{E}$	electric field
E_{el}	elastic energy
E_{elec}	electrostatic energy
ε	energy, energy of phonon
ϵ	energy, energy of electron
ϵ	fractional difference in T from T_{c}
ϵ_{F}	Fermi energy
ϵ_j, ϵ_{ij}	strain
η	fractional change of lattice parameter with composition
η	order parameter
f	correlation factor
f_α	(atomic) fraction of α-phase
f_j	interaction free energy
$f(c)$	free energy per unit volume
F	Helmholtz free energy
$\mathcal{F}$	force
$F_\xi(c,T)$	free energy for phase ξ with composition c at temperature T
$g(\varepsilon)$	phonon density of states
$\vec{g}$	reciprocal lattice vector
grad(c) or $\overrightarrow{\nabla c}$	gradient (of concentration)
G	Gibbs free energy
$G(\vec{r},t)$	Van Hove space-time correlation function

$\mathcal{G}$	temperature gradient $\mathrm{d}T/\mathrm{d}x$
γ	coefficient for linear electronic heat capacity vs. T
γ	Grüneisen parameter
γ_j	Grüneisen parameter for phonon mode j
γ_{xy}	shear strain
Γ	atomic jump frequency
Γ	point at origin of reciprocal lattice
h	bond integral
$\hbar$	Planck constant divided by 2π
H	Hamiltonian
$\vec{H}$	magnetic field
$\vec{j}$	flux
$J_0(x)$, $J_1(x)$	Bessel functions of zero and first order
J_n	number of clusters per unit time that change from n to $n + 1$
J_{ss}	steady-state flux in number space of cluster sizes
J_{hs}, J_{hl}	heat flux in solid and liquid (1D)
$\vec{J}_{\mathrm{A}}$	flux of A-atoms
$J(\vec{r}_1 - \vec{r}_j)$	magnetic exchange energy
k	partitioning ratio $k = c_{\mathrm{s}}/c_{\mathrm{l}}$
$\vec{k}$	wavevector
k_{B}	Boltzmann constant
κ	coefficient for square gradient energy
κ	Ginzburg–Landau parameter
L	latent heat
L	long-range order parameter
$L(\tau E_0/k_{\mathrm{B}}T)$	Langevin function
LHS	left-hand side
λ	wavelength
λ	electron–phonon coupling parameter
m	mass
m	slope of liquidus curve on phase diagram $\mathrm{d}T_{\mathrm{l}}/\mathrm{d}c$
M	mobility
$\vec{M}$	magnetization
$\mathcal{M}$	Mendeleev number
μ	chemical potential
μ	shear modulus
$\vec{\mu}$	magnetic moment

$n(\varepsilon_i, T)$	Planck distribution
N	number (of atoms)
N_{A}^{α}	number of A-atoms on α-sublattice (point variable)
$N_{\mathrm{AB}}^{\alpha\beta}$	number of A–B pairs with A on α and B on β (pair variable)
$N(k)$	number of quantum states with wavevector less than k
$\underset{\sim}{N}(t)$	vector of number occupancies of states at time t
ν	frequency
ν	Poisson ratio
ν	critical exponent for correlation length
ω	angular frequency
Ω	number of states accessible to the system
Ω	atomic volume
Ω_j	configurations of a system with energy j
p_i	probability of a state
$\vec{p}$	momentum
p_{A}	partial pressure of vapor of element A
p_{A}^{α}	probability of A-atom on α-sublattice (point variable)
$p_{\mathrm{AB}}^{\alpha\beta}$	probability of A–B pair with A on α and B on β (pair variable)
P	pressure
P_{th}	thermal pressure (from expansion against a bulk modulus)
$\mathcal{P}$	Péclet number
$\Phi(r)$	interatomic, central-force potential
$\Phi_{\mathrm{M}}(r)$, $\Phi_{\mathrm{L\text{-}J}}(r)$	Morse potential, Lennard-Jones potential
Φ_0	quantum of magnetic flux $hc/2e$
Q	compositional wavevector $2\pi/\lambda$
Q	total electrostatic charge
$\vec{Q}$	momentum transfer in scattering
Q	quality factor of damped harmonic oscillator
r_{B}	Bohr radius $r_{\mathrm{B}} = \hbar^2/(m_e e^2)$
r_{WS}	Wigner–Seitz radius
$\vec{r}_l$	position of unit cell
$\vec{r}_k$	basis vector within unit cell
R	number of right atoms on a sublattice of an ordered structure
$R(Q)$	growth rate for compositional wavevector Q
R^*	critical radius for nucleation
$\vec{R}$	position of atom center
$\vec{R}_n$	displacement after n jumps
$\mathcal{R}$	number of atoms in unit cell
RHS	right-hand side

ρ	density, e.g., [atoms cm^{-3}]
$\rho(\epsilon)$	electronic density of states
$\rho(\epsilon_{\mathrm{F}})$	electronic density of states at the Fermi energy
$\vec{s}_i$	electronic spin at site i
S	entropy
S	overlap integral
S_{conf}	configurational entropy
S_{vib}	vibrational entropy
S_{h}	harmonic entropy
S_{qh}	entropy contribution from quasiharmonicity
S_{anh}	entropy contribution from anharmonicity
S_{el}	electronic entropy
S_{epi}	entropy contribution from electron–phonon interaction
S_{mag}	magnetic entropy
$S(\vec{Q}, \omega)$	scattering function
σ	surface energy per unit area
σ	electrical conductivity
σ	spin number (± 1)
σ_{gb}	energy per unit area of grain boundary
σ_{ij}	stress
t	time
T	temperature
T_{c}	critical temperature
T_{C}	Curie temperature
T_{m}	melting temperature
T_{N}	Néel temperature
$T_1, T_2, \ldots$	sequence of temperatures such that $T_2 > T_1$
$\vec{T}$	translation vector of real space lattice
τ	characteristic time (e.g., for diffusion)
$\vec{\tau}$	electrostatic dipole moment
$\theta(\vec{r})$	Heaviside function, 1 in the region, 0 outside
$\theta(\vec{r}, t)$	phase of wavefunction in space and time
Θ_{D}	Debye temperature
$\vec{u}(x, y, z)$	displacement vector
U	difference in chemical preferences of A- and B-atoms $U = (e_{\mathrm{AA}} - e_{\mathrm{BB}})/4V$
U	Coulomb energy penalty for placing a second electron on a site in Hubbard model
Υ_j	Grüneisen parameter for energy of electronic state j

$\vec{v}$	velocity
V	interchange energy $V = (e_{AA} + e_{BB} - 2e_{AB})/4$
V	volume
$V(\vec{r})$	potential energy
V_Q	quantum volume, related to cube of de Broglie wavelength
v_0	volume per atom
W	number of wrong atoms on a sublattice of an ordered structure
W_{ij}	transition rate from state j to state i
$W^{\uparrow}_{\beta A \alpha}$	rate of increase of LRO parameter by jump of A from β- to α-sublattice
$\underset{\approx}{W}(\Delta t)$	transition matrix for time interval Δt
ξ	correlation function
ξ	length
$\{\chi_i\}$	reaction coordinates
χ	susceptibility
Y	Young's modulus
$\psi(\vec{r})$	wavefunction
z	coordination number of lattice
z	partition function of subsystem
Z	partition function
$\mathcal{Z}$	Zeldovich factor

PART IV

ADVANCED TOPICS

Chapters 22–28 are integrated into the main text with cross-references, citations, and index, but are not included in the printed edition of the book. These chapters are available online as a free download from www.library.caltech.edu.

The chapters present advanced techniques and methods that are useful for understanding phase transitions in materials. The emphasis is on aspects of free energy, energy, entropy, and kinetic processes, and less on specific phase transformations. The chapters are far from a complete set of advanced topics, however, and other topics can be argued to be just as important. The topics have proved their value, though, and appear in the literature with some frequency. The reader is warned that some of the presentations assume a higher level of mathematics or physics than the other sections in the book, and some important results are stated without proof.

The chapters that cover energy (Chapter 24), entropy (Chapter 26), and atom movements (Chapters 23, 25) are continuations of content in Chapters 6, 7, and 10 of Part II. Chapter 22 presents analyses of phase boundaries at low and high temperatures, and Chapter 27 presents techniques for analyzing thermodynamics and physical properties very close to a critical temperature. Chapter 28 addresses quantum phase transitions, ending by touching upon quantum criticality.

22 Low-Temperature Analysis of Phase Boundaries

Since Chapter 2, we have based analyses of phase diagrams at finite temperatures on free energy functions, $F_\zeta(c, \eta, T)$, of different phases $\{\zeta\}$ with states of order η. It is conceptually straightforward to construct phase diagrams by minimizing the total free energy at different T, subject to constraints such as constant chemical composition. This chapter develops a different approach of finding the effect of temperature on phase boundaries by working directly with the partition function (Eq. 1.7). A partition function is usually less convenient than a free energy because it contains many nonlinear Boltzmann factors that are difficult to sum. Consider, however, an ordered alloy near $T = 0$. It has only a few misplaced atoms, and they occur only in small groups. At low temperatures, any defect structure containing many misplaced atoms has an energy that is large compared with $k_B T$, so its Boltzmann factors are small and can be neglected. Not many terms in the partition function need to be considered near $T = 0$.

We begin with $T = 0$ ground-state phase diagrams for an Ising lattice with first- and second-nearest-neighbor (1nn, 2nn) interactions. Because $T = 0$, entropy plays no role. The stable phase has the lowest bond energy, obtained by counting the energies of all 1nn and 2nn pairs in a structure with perfect chemical order. This "ground-state analysis" is performed in Section 22.1 for the two structures of Fig. 22.1a on a square lattice. Results for ordered structures on bcc and fcc lattices are presented in Section 22.2.

On a phase boundary at $T = 0$, the bond energies for the two phases are equal. Conveniently, and essential to the method, when the interatomic interactions place the material on a phase boundary at $T = 0$, at small T the partition functions of the two phases are dominated by a large common factor from the perfect structures of the two phases. The cancellation of these common factors leaves a simple comparison of partition functions from the defect structures in the two phases. Usually the defect structures in one phase are less costly to the free energy than the defects in the other phase, so we can find how the phase boundary shifts with temperature.

As an example, in Sections 22.3.1 and 22.3.2 low-temperature expansions of the partition functions are performed for the chessboard and striped phases. By considering the partition functions for structures with only a few defects, it is possible to assess how the phase boundary at $T = 0$ shifts with temperature. Some results for the low-temperature expansion for equiatomic bcc alloys with 1nn and 2nn interactions are explained, including the effects of temperature on the boundaries between the unmixed, B2, and B32 structures.

Finally we consider the different problem of a high-temperature expansion of the partition function. Although different mathematical forms arise, the high-temperature expansion has conceptual similarities to the low-temperature one. Instead of considering

small departures from a perfectly ordered structure as is done at low temperatures, at high temperatures we consider small departures from a random alloy.

22.1 Ground-State Analysis for $T = 0$

"Ground-state" structures are the stable phases in the low-temperature limit of the free energy. As $T \rightarrow 0$, the entropic term in the free energy $F = E - TS$ is negligible, and only the energy E needs consideration. Here we compare the bond energies of different ordered structures on an Ising lattice by bond counting as in Chapter 2, but now second-nearest-neighbor (2nn) pairs are included. Since different ordered structures have different types of 1nn and 2nn pairs, by changing the strengths or signs of the 1nn and 2nn interatomic potentials, one structure can be favored over another. The procedure is quite straightforward, and is illustrated with the striped and chessboard ordered structures in Fig. 22.1a.

Our first question is what combination of 1nn and 2nn pair interactions are required to stabilize the chessboard versus striped ordered phases of Fig. 22.1a. The energy of both is the sum of bonds over the four 1nn and four 2nn pairs, and for an equiatomic alloy the bonds to one A-atom and one B-atom must be counted. For the chessboard structure, each A-atom and B-atom has opposite species as 1nn, and like species as 2nn

$$E_{\text{ch}} = \frac{N}{4}\left[4e_{\text{AB1}} + 4e_{\text{AB1}} + 4e_{\text{AA2}} + 4e_{\text{BB2}}\right], \tag{22.1}$$

$$E_{\text{ch}} = \frac{N}{2}\left[4e_{\text{AB1}} + 2e_{\text{AA2}} + 2e_{\text{BB2}}\right]. \tag{22.2}$$

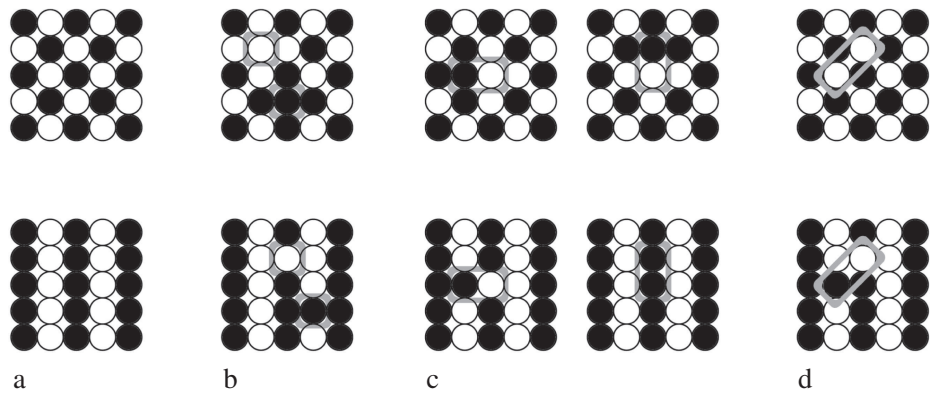

Figure 22.1 (**a**) Chessboard and striped ordered phases on a 2D Ising lattice. (**b**) Point defects in the structures of part a. (**c**) Two-atom defects in the structures of part a. (**d**) Defect with 2nn separation in striped phase. A 2nn swap does not generate a defect in the chessboard structure. Gray rectangle highlights the two atoms with swapped positions in the defect structures.

Likewise, counting bond energies for one A-atom and one B-atom in the striped structure gives

$$E_{st} = \frac{N}{4}\Big[2e_{AB1} + 2e_{AA1} + 2e_{AB1} + 2e_{BB1} + 4e_{AB2} + 4e_{AB2}\Big], \tag{22.3}$$

$$E_{st} = \frac{N}{2}\Big[2e_{AB1} + e_{AA1} + e_{BB1} + 4e_{AB2}\Big]. \tag{22.4}$$

To compare the stability of the chessboard and striped structures, take the difference

$$\Delta E = E_{ch} - E_{st}, \tag{22.5}$$

$$\Delta E = \frac{N}{2}\Big[2e_{AB1} - e_{AA1} - e_{BB1} - 4e_{AB2} + 2e_{AA2} + 2e_{BB2}\Big], \tag{22.6}$$

$$\Delta E = \frac{N}{2}\Big[-4V_1 + 8V_2\Big], \tag{22.7}$$

using definitions like that of Eq. 2.32

$$4V_1 \equiv e_{AA1} + e_{BB1} - 2e_{AB1}, \tag{22.8}$$

$$4V_2 \equiv e_{AA2} + e_{BB2} - 2e_{AB2}. \tag{22.9}$$

Notice that ΔE is expressed in terms of integer multiples of the 1nn and 2nn exchange energies V_1 and V_2. For different combinations of V_1 and V_2, the ΔE of Eq. 22.7 can be positive or negative, favoring the striped or chessboard structures, respectively. The critical condition $\Delta E = 0$ gives the phase boundary between the chessboard and striped structures. Equation 22.7 shows that this boundary is at $V_2 = V_1/2$. The phase boundary at $T = 0$ is shown in Fig. 22.2a, sometimes called a "ground-state diagram." This reflects the fact that the two ordered structures have the same chemical compositions, but differ in the exchanges of atoms between different sites. Figure 22.2a is an incomplete ground-state diagram, however. A more complete diagram with the unmixed structure is shown in Fig. 22.2b.

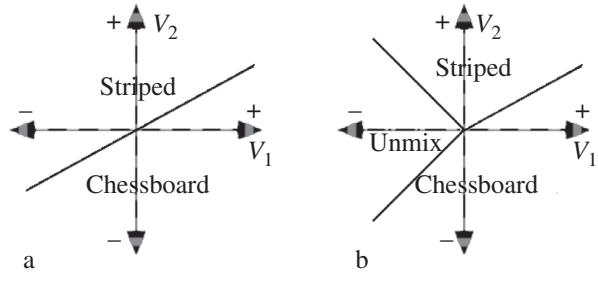

Figure 22.2 (**a**) Ground-state diagram of the chessboard and striped structures of Fig. 22.1a. (**b**) Ground-state diagram that includes the unmixed phase.

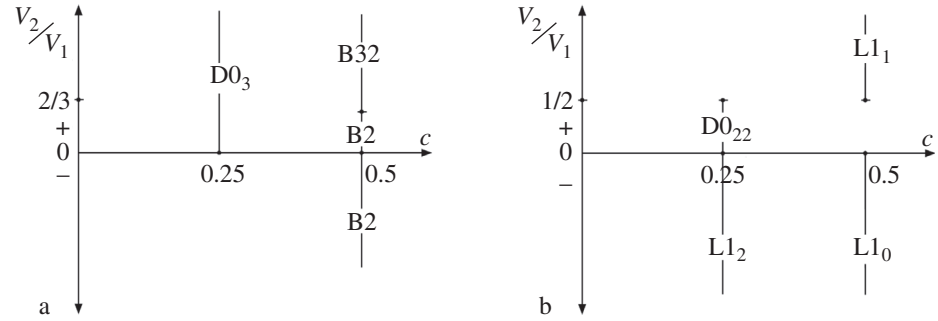

Figure 22.3 (**a**) Ground-state diagram for some ordered phases on bcc lattice for different chemical compositions, c. (**b**) Ground-state diagram for some ordered phases on fcc lattice for different chemical compositions, c.

22.2 Richards, Allen, and Cahn Ground-State Maps

Three-dimensional ordered structures can be analyzed in the same way. The challenge is to be sure that all ordered structures are included in the analysis, specifically those structures consistent with the range of the interatomic interactions. Determining all allowed ground-state structures is a topic beyond the scope of this text. Especially for stoichiometries away from integer compositions such as 1/4 and 1/2, it can be tricky to find all structures, and search algorithms are probably necessary. Ground-state maps were developed by Richards, Allen, and Cahn [372, 373] for bcc and fcc alloys,[1] and some of the more common phases are shown in Fig. 22.3. Because the diagrams are for $T = 0$, the ordered phases appear at exact compositions. Some points of note:

- The diagram repeats for $0.5 < c < 1.0$ because the roles of solute and solvent are reversed.
- For compositions between the vertical lines, two-phase mixtures are predicted, with fractions obtained from the lever rule of Section 2.2.
- There are other phases on the diagrams at compositions such as 1/8, 1/4, 1/6. With pair interactions beyond the 2nn, many more phases are possible.
- Ternary alloys allow new structures, and require their own maps [376].

22.3 Low but Finite Temperatures

Entropy has no importance at $T = 0$, and ground-state analyses of the previous sections give the state of equilibrium and the phase diagram. At finite temperature we expect some defects that cost energy, but contribute considerably to the configurational entropy as $-k_B c \ln c$ when their concentration c is small. Near $T = 0$, Boltzmann factors are very

[1] Kanamori performed thorough ground-state analyses for spin systems on Ising lattices [374, 375].

sensitive to energy. Structural defects of higher energy are much less probable, so only the low-energy defects need be considered when evaluating the partition function. Writing the energy as the ground-state energy of the perfect crystal, plus a correction for the alloy with a defect, $E_0 + \delta E_i$, the free energy is

$$F(T) = -k_\mathrm{B}T \ln\left(\sum_i \mathrm{e}^{-\frac{E_0+\delta E_i}{k_\mathrm{B}T}}\right), \tag{22.10}$$

$$F(T) = E_0 - k_\mathrm{B}T \ln\left(\sum_i \mathrm{e}^{-\frac{\delta E_i}{k_\mathrm{B}T}}\right). \tag{22.11}$$

Box 22.1 Point Defects

Vacancy concentrations in a crystal are perhaps a more familiar way to illustrate some key ideas. At finite temperature, the energy penalty of a vacancy is offset by the large gain in configurational entropy from placing a vacancy at an arbitrary crystal site, and the number of vacancies n_V on N sites of the crystal is

$$\frac{n_\mathrm{V}}{N} = \mathrm{e}^{-E_\mathrm{f}/k_\mathrm{B}T}, \tag{22.12}$$

where the energy of formation of a vacancy, E_f, is much greater than $k_\mathrm{B}T$ and n_V/N is small. On the other hand, a divacancy, which is more costly energetically, does not increase the entropy by much over a single vacancy, since there are only z positions to place the second vacancy around the first (where z is the coordination number of the lattice). At modest temperatures, divacancy populations are far lower than monovacancy populations.

The trick is to include only a few terms in the partition function, but these must be chosen appropriately for the structure. For illustration we pick three, which are for

- the perfect crystal with $\delta E = 0$ and a degeneracy of 1,
- a defect that has the extra energy δE_1 and a number of ways of placing it on a lattice of N sites as Nm_1, and
- a second defect with δE_2 and Nm_2.

These give three terms in the sum of Eq. 22.11

$$F(T) = E_0 - k_\mathrm{B}T \ln\left(1 + Nm_1\mathrm{e}^{-\frac{\delta E_1}{k_\mathrm{B}T}} + Nm_2\mathrm{e}^{-\frac{\delta E_2}{k_\mathrm{B}T}}\right). \tag{22.13}$$

If the temperature is very low so the Boltzmann factors are less than Nm,[2] the approximation $\ln(1+\delta) \simeq \delta$ can be used for small δ, giving

$$F(T) = E_0 - k_\mathrm{B}T\left(Nm_1\mathrm{e}^{-\frac{\delta E_1}{k_\mathrm{B}T}} + Nm_2\mathrm{e}^{-\frac{\delta E_2}{k_\mathrm{B}T}}\right). \tag{22.14}$$

Our goal is to identify how a phase boundary changes with temperature – does one phase become more stable at the expense of the other? We select a composition and interatomic

[2] In what follows, the factor N cancels, so this requirement need not be so restrictive.

interactions for which the two phases (α and β) have equal energies E_0 (consistent with the phase boundary at $T = 0$). The next step is to perform an analysis of the difference in free energy at infinitesimal T

$$\Delta F^{\beta-\alpha}(T) = F^{\beta}(T) - F^{\alpha}(T), \tag{22.15}$$

$$\Delta F^{\beta-\alpha}(T) = -k_{\mathrm{B}}T\Big(Nm_{1\beta}\mathrm{e}^{-\frac{\delta E_{1\beta}}{k_{\mathrm{B}}T}} + Nm_{2\beta}\mathrm{e}^{-\frac{\delta E_{2\beta}}{k_{\mathrm{B}}T}} - Nm_{1\alpha}\mathrm{e}^{-\frac{\delta E_{1\alpha}}{k_{\mathrm{B}}T}} - Nm_{2\alpha}\mathrm{e}^{-\frac{\delta E_{2\alpha}}{k_{\mathrm{B}}T}}\Big). \tag{22.16}$$

At the phase boundary for finite T, $\Delta F^{\beta-\alpha}(T) = 0$, so

$$m_{1\beta}\mathrm{e}^{-\frac{\delta E_{1\beta}}{k_{\mathrm{B}}T}} + m_{2\beta}\mathrm{e}^{-\frac{\delta E_{2\beta}}{k_{\mathrm{B}}T}} = m_{1\alpha}\mathrm{e}^{-\frac{\delta E_{1\alpha}}{k_{\mathrm{B}}T}} + m_{2\alpha}\mathrm{e}^{-\frac{\delta E_{2\alpha}}{k_{\mathrm{B}}T}}. \tag{22.17}$$

For the next steps it may be possible to ignore some of the exponentials with the largest δE_i. Even if not, for points on the phase boundary for $T = 0$, equality in Eq. 22.17 is not expected for finite T. For equilibrium, as discussed below, Eq. 22.16 is considered at finite temperature to evaluate if the α-phase or β-phase has the lower free energy at the original $T = 0$ phase boundary. This gives the direction of shift of the phase boundary with temperature.

22.3.1 Chessboard Phase

At very low temperatures, the partition function is dominated by defects with the lowest energies. We will compare the defects in the chessboard and striped phases in Fig. 22.1. Two antisite defects are shown in Fig. 22.1b, and the two-atom defects in Fig. 22.1c. As usual, both A-atom and B-atom defects must be considered, since the defects are created in pairs to conserve the chemical composition of the equiatomic alloy.

The partition function for all states shown for the chessboard structure at the top of Fig. 22.1 is

$$\begin{aligned} Z_{\mathrm{ch}}(T) \simeq\ & 2\exp\left(-\frac{E_{\mathrm{ch0}}}{k_{\mathrm{B}}T}\right) \\ & + \left(\frac{N}{2}\right)^2 \exp\left(\frac{-z_1(e_{\mathrm{AA1}} + e_{\mathrm{BB1}} - 2e_{\mathrm{AB1}}) - z_2(2e_{\mathrm{AB2}} - e_{\mathrm{AA2}} - e_{\mathrm{BB2}})}{k_{\mathrm{B}}T}\right) \\ & \quad \times \exp\left(-\frac{E_{\mathrm{ch0}}}{k_{\mathrm{B}}T}\right) \\ & + z_1 N \exp\left(\frac{-(z_1-1)(e_{\mathrm{AA1}} - e_{\mathrm{AB1}}) - (z_1-1)(e_{\mathrm{BB1}} - e_{\mathrm{AB1}})}{k_{\mathrm{B}}T}\right) \\ & \quad \times \exp\left(\frac{-z_2(e_{\mathrm{AB2}} - e_{\mathrm{AA2}}) - z_2(e_{\mathrm{AB2}} - e_{\mathrm{BB2}})}{k_{\mathrm{B}}T}\right)\exp\left(-\frac{E_{\mathrm{ch0}}}{k_{\mathrm{B}}T}\right), \end{aligned} \tag{22.18}$$

where the Boltzmann factor for the perfect structure has the energy

$$E_{\text{ch0}} \equiv \frac{z_1 N}{2} e_{\text{AB1}} + \frac{z_2 N}{4} e_{\text{AA2}} + \frac{z_2 N}{4} e_{\text{BB2}}. \tag{22.19}$$

Simplifying with Eqs. 22.8 and 22.9

$$\begin{aligned} Z_{\text{ch}}(T) \simeq\ & 2 \exp\left(\frac{-E_{\text{ch0}}}{k_{\text{B}}T}\right) \\ & + \left(\frac{N}{2}\right)^2 \exp\left(\frac{-z_1 4V_1 + z_2 4V_2 - E_{\text{ch0}}}{k_{\text{B}}T}\right) \\ & + \frac{z_1 N}{2} \exp\left(\frac{-(z_1 - 1)4V_1 + z_2 4V_2 - E_{\text{ch0}}}{k_{\text{B}}T}\right). \end{aligned} \tag{22.20}$$

The three terms in Eq. 22.20 (and Eq. 22.18) correspond to the four diagrams at the top of Fig. 22.1.

- The first term is the Boltzmann factor for the perfect chessboard structure in Fig. 22.1a. It has a degeneracy of 2 because an equivalent structure can be made by swapping all A- and B-atoms.[3]
- The second term is the Boltzmann factor for a structure with two separated antisite atoms as in Fig. 22.1b. Each sublattice contains $N/2$ sites that are available for an antisite atom.[4] The first exponential factor in Eq. 22.18 shows that $2z_1$ 1nn AB pairs were replaced with z_1 AA and z_1 BB pairs, for example, so the second exponential factor has the full energy of the perfect structure.
- The third term is the Boltzmann factor for a structure with a two-atom defect as shown in two orientations in Fig. 22.1c. All N sites of the crystal are available for the first atom of the defect. The second atom has z_1 possible locations around the first, but this must be divided by 2 to avoid double counting. Alternatively stated, all possible defect pairs can be obtained from swaps of neighboring pairs starting on the white sublattice only. The energy of the two-atom defect is a bit lower than that of two isolated antisite atoms because the two atoms share an A–B bond, and have unfavorable bonds to only $z_1 - 1$ first-nearest neighbors.

Equation 1.19, $F = -k_{\text{B}}T \ln Z$, gives the free energy of the chessboard structure at low temperature

$$\begin{aligned} F_{\text{ch}}(T) = -k_{\text{B}}T \ln \Bigg\{ 2 \exp\left(\frac{-E_{\text{ch0}}}{k_{\text{B}}T}\right) \Bigg[1 + \frac{1}{2}\left(\frac{N}{2}\right)^2 \exp\left(\frac{-z_1 4V_1 + z_2 4V_2}{k_{\text{B}}T}\right) \\ + \frac{z_1 N}{4} \exp\left(\frac{-(z_1 - 1)4V_1 + z_2 4V_2}{k_{\text{B}}T}\right) \Bigg] \Bigg\}. \end{aligned} \tag{22.21}$$

To this point we have only made the modest approximation that the temperature is low enough that only one pair of misplaced atoms is likely in the chessboard structure. We now make an even more severe restriction that the exponentials in Eq. 22.21 are very

[3] This causes an infinitesimal violation of the third law of thermodynamics for large N.
[4] We ignore a small correction that the second antisite atom cannot be in the 1nn shell of the first atom.

small – even smaller than N^{-2}. This is a very low temperature, at least for a system with large N. This assumption is motivated by the approximation $\ln(1+\delta) \simeq \delta$ for small δ, allowing us to write

$$\begin{aligned} F_{\mathrm{ch}}(T) = &-k_{\mathrm{B}}T\ln 2 + E_{\mathrm{ch0}} \\ &- k_{\mathrm{B}}T\frac{1}{2}\left(\frac{N}{2}\right)^2 \exp\!\left(\frac{-z_1 4V_1 + z_2 4V_2}{k_{\mathrm{B}}T}\right) \\ &- k_{\mathrm{B}}T\frac{z_1 N}{4}\exp\!\left(\frac{-(z_1-1)4V_1 + z_2 4V_2}{k_{\mathrm{B}}T}\right). \end{aligned} \tag{22.22}$$

22.3.2 Striped Phase

To find how the phase boundaries of Fig. 22.2 change with temperature, a comparable $F_{\mathrm{st}}(T)$ for the striped phase is needed for comparison with $F_{\mathrm{ch}}(T)$ of Eq. 22.22. The procedure is essentially the same as we performed for the chessboard phase. For example, the reference energy is

$$E_{\mathrm{st0}} = \frac{z_1 N}{4}e_{\mathrm{AB1}} + \frac{z_1 N}{8}e_{\mathrm{AA1}} + \frac{z_1 N}{8}e_{\mathrm{BB1}} + \frac{z_2 N}{2}e_{\mathrm{AB2}}. \tag{22.23}$$

Using the defect structures of Figs. 22.1b and 22.1c, the partition function at very low temperature, the equivalent of Eq. 22.20 for $Z_{\mathrm{ch}}(T)$, is

$$\begin{aligned} Z_{\mathrm{st}}(T) \simeq\ & 2\exp\!\left(\frac{-E_{\mathrm{st0}}}{k_{\mathrm{B}}T}\right) \\ &+ \left(\frac{N}{2}\right)^2 \exp\!\left(\frac{-z_2 4V_2}{k_{\mathrm{B}}T}\right)\exp\!\left(\frac{-E_{\mathrm{st0}}}{k_{\mathrm{B}}T}\right) \\ &+ \frac{z_1 N}{4}\exp\!\left(\frac{+4V_1 - z_2 4V_2}{k_{\mathrm{B}}T}\right)\exp\!\left(\frac{-E_{\mathrm{st0}}}{k_{\mathrm{B}}T}\right) \\ &+ \frac{z_2 N}{2}\exp\!\left(\frac{-(z_2-1)4V_2}{k_{\mathrm{B}}T}\right)\exp\!\left(\frac{-E_{\mathrm{st0}}}{k_{\mathrm{B}}T}\right), \end{aligned} \tag{22.24}$$

and we follow the same procedure to obtain a free energy as for $F_{\mathrm{ch}}(T)$ in Eq. 22.22

$$\begin{aligned} F_{\mathrm{st}}(T) = &-k_{\mathrm{B}}T\ln 2 + E_{\mathrm{st0}} \\ &- k_{\mathrm{B}}T\frac{1}{2}\left(\frac{N}{2}\right)^2 \exp\!\left(\frac{-z_2 4V_2}{k_{\mathrm{B}}T}\right) - k_{\mathrm{B}}T\frac{z_1 N}{4}\exp\!\left(\frac{+4V_1 - z_2 4V_2}{k_{\mathrm{B}}T}\right) \\ &- k_{\mathrm{B}}T\frac{z_2 N}{2}\exp\!\left(\frac{-(z_2-1)4V_2}{k_{\mathrm{B}}T}\right). \end{aligned} \tag{22.25}$$

Note that the prefactor of the third term in Eq. 22.24 from the paired defects is half the prefactor of the corresponding third term in Eq. 22.20 because only half of the orientations in Fig. 22.1c give two-atom defects in the striped phase.

22.3.3 Difference in *F* and Thermal Shift of Phase Boundary

To determine the effect of temperature on the phase boundaries in Fig. 22.2a, we take the difference

$$\Delta F^{c-s}(T) = F_{ch}(T) - F_{st}(T). \tag{22.26}$$

At the $T = 0$ phase boundary with $V_2 = V_1/2$, the first two terms cancel in Eqs. 22.22 and 22.25 because $E_{ch0} = E_{st0}$ at the phase boundary of the perfect structures at $T = 0$. This was our criterion for finding the phase boundaries in Fig. 22.2a, and this is the basis of the approach to finite T. It is interesting that the third terms cancel at the phase boundary. The isolated antisite defects sample the 1nn and 2nn sites of the perfect structures, so at the phase boundary their energies are the same. There is a fortuitous cancellation of the fourth terms from 1nn pair swaps. There is, however, a difference in the last term of Eq. 22.25, giving the result (again, when $V_2 = V_1/2$ and $z_1 = z_2 = 4$)

$$\Delta F^{c-s}(T) = -k_B T\, 2N\, \exp\left(\frac{-12V_2}{k_B T}\right). \tag{22.27}$$

For V_1, $V_2 > 0$ and finite T, $\Delta F(T)$ is small and negative. Compared with Fig. 22.2, the phase boundaries are shifted to favor the chessboard phase as shown with the arrow in Fig. 22.4.

A physical explanation is possible. Figure 22.1d shows how defects cause a bigger change in 2nn bonds for the striped than the chessboard structure. When $V_2 > 0$ there is a smaller energy penalty for two-atom 2nn defects in the chessboard structure, and its stable region expands at the expense of the striped structure. In the analysis so far, we did not normalize the probabilities of defect states, so their temperature dependence is not expected to be reliable. This deficiency can be addressed, but another problem is that we evaluated the free energy difference at the phase boundary for $T = 0$. As the phase boundary moves away from the condition $V_2 = V_1/2$, the calculation of $\Delta F(T)$ will be less reliable. Although the analysis of the partition function is valid only at very low temperatures, the directions of change of the phase boundaries should be reliable so long as the dominant types of

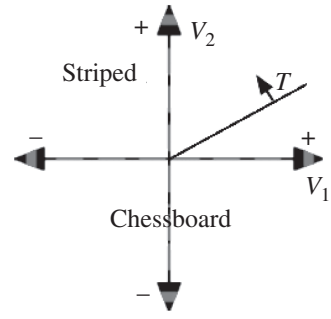

Figure 22.4 Displacement with temperature of the phase boundary between the chessboard and striped structures. Line is the boundary of Fig. 22.2 for $V_2 = V_1/2$.

defects are antisite defects in the structure. The magnitude of the effects requires a more complete analysis, however.

22.4 Analysis of Equiatomic bcc Alloys

Results from a ground-state analysis of equiatomic bcc alloys are shown in Fig. 22.5a. It is essentially equivalent to $c = 0.5$ in Fig. 22.3a, but with the inclusion of the unmixed state along with the B2 and B32 structures. The boundaries of the B32 phase have slopes of $\pm 2/3$, and the boundary between the unmixed and B2 phase is at $V_1 = 0$.

We seek the effect of temperature on the phase boundaries by analysis of the partition function at low temperature

$$Z \exp\left(\frac{N\varepsilon_0}{k_B T}\right) = 1 + \exp\left(\frac{V_1}{k_B T}\right) + N \exp\left(\frac{-\delta\varepsilon_1}{k_B T}\right) + 4N \exp\left(\frac{-\delta\varepsilon_{2a}}{k_B T}\right) + 3N \exp\left(\frac{-\delta\varepsilon_{2b}}{k_B T}\right), \tag{22.28}$$

where the energies are listed for the three structures in Table 22.1.

Table 22.1 Terms of Eq. 22.5

B2	B32	Unmixed
$\delta\varepsilon_0 = -4V_1 + 3V_2$	$\delta\varepsilon_0 = -3V_2$	$\delta\varepsilon_0 = 4V_1 + 3V_2$
$\delta\varepsilon_1 = 16V_1 - 12V_2$	$\delta\varepsilon_1 = 12V_2$	$\delta\varepsilon_1 = -16V_1 - 12V_2$
$\delta\varepsilon_{2a} = 28V_1 - 24V_2$	$\delta\varepsilon_{2ai} = 4V_1 + 24V_2$	$\delta\varepsilon_{2a} = -28V_1 - 24V_2$
	$\delta\varepsilon_{2aii} = -4V_1 + 24V_2$	
$\delta\varepsilon_{2b} = 32V_1 - 20V_2$	$\delta\varepsilon_{2b} = 20V_2$	$\delta\varepsilon_{2b} = -32V_1 - 20V_2$

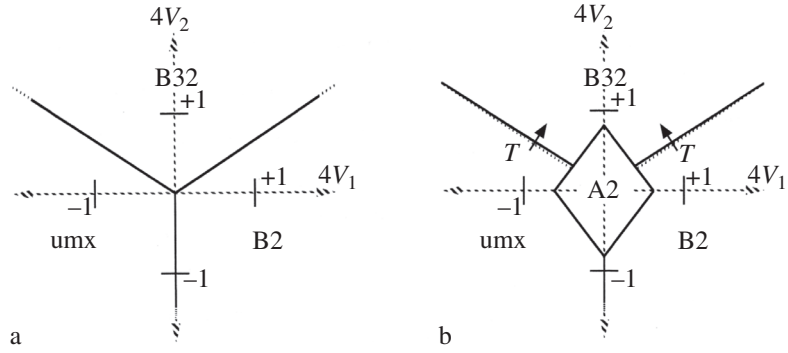

Figure 22.5 Phase diagram for equiatomic bcc alloys. (**a**) Ground-state diagram. (**b**) Finite-temperature diagram ($T \simeq 1$), with axis units in $k_B T$. Dotted lines have slope $\pm 2/3$.

The first term on the right of Eq. 22.28, the 1, is for the perfect crystal (here the inverse of its Boltzmann factor, common to the other terms, is moved to the left side of the equation). The second term is for a crystal with an isolated antisite atom, an average for an A-atom and a B-atom.[5] The third term accounts for a pair of antisite atoms that are separated by a 1nn distance. On the bcc lattice these dimer defects have a degeneracy of $4N$. The fourth term is for a pair of antisite atoms separated by a 2nn distance, with degeneracy $3N$. Table 22.1 shows that the B32 structure requires a slightly different analysis of 1nn pairs. The two atoms can be on two sublattices populated with either like or unlike species. The analysis of Eq. 22.28 at the phase boundaries of Fig. 22.5a has been done [377, 378]. To this order of approximation, the boundary between the B2 and unmixed phases is unchanged with temperature. On the other hand, both the unmixed and B2 phases encroach into the region of B32 phase by the same amount with increasing temperature, as shown in Fig. 22.5b.

Also shown in Fig. 22.5 is a region for the disordered solid solution, the A2 phase, which is expected at elevated temperature (or small V_1 and V_2). Its phase boundaries are not found from the present analysis of the partition function, but from consideration of the critical temperatures for ordering and unmixing. Its boundaries are shown approximately in Fig. 22.5.

22.5 High-Temperature Expansion of the Partition Function

For comparison, consider the opposite extreme of a high-temperature expansion of the partition function for an Ising lattice. We expect, of course, that at infinite temperature the alloy is random. The high-temperature expansion works with small departures from randomness, in analogy to the way that the low-temperature expansion works by accounting for the simplest defects in perfectly ordered alloys. The total bond energy of a random alloy is from an equal mix of A–B, B–A, A–A, and B–B pairs, here assumed first-nearest neighbors

$$E_{\text{rndT}} = \frac{Nz}{2}\left[\frac{1}{2}e_{\text{AB}} + \frac{1}{4}e_{\text{AA}} + \frac{1}{4}e_{\text{BB}}\right], \tag{22.29}$$

and for a single atom on the lattice

$$E_{\text{rnd1}} = \frac{z}{2}\left[\frac{1}{2}e_{\text{AB}} + \frac{1}{4}e_{\text{AA}} + \frac{1}{4}e_{\text{BB}}\right]. \tag{22.30}$$

Likewise, for a single ordered atom

$$E_{\text{ord1}} = \frac{z}{2}e_{\text{AB}}. \tag{22.31}$$

At the highest temperatures, the partition function is a sum over all random atoms, except that one atom is replaced with an ordered one

[5] As for our analysis of 2D problems, the isolated antisite atoms have no effect on thermal shifts of phase boundaries.

$$Z = \sum_{i=1}^{N} \exp\left(-\frac{E_{\mathrm{rndT}} + E_{\mathrm{ord1}} - E_{\mathrm{rnd1}}}{k_{\mathrm{B}}T}\right), \tag{22.32}$$

$$Z = \exp\left(-\frac{E_{\mathrm{rndT}}}{k_{\mathrm{B}}T}\right)\sum_{i=1}^{N} \exp\left(\frac{-E_{\mathrm{ord1}} + E_{\mathrm{rnd1}}}{k_{\mathrm{B}}T}\right), \tag{22.33}$$

$$Z = \exp\left(-\frac{E_{\mathrm{rndT}}}{k_{\mathrm{B}}T}\right)\sum_{i=1}^{N} \exp\left(\frac{+Vz}{2k_{\mathrm{B}}T}\right), \tag{22.34}$$

where V is again defined for 1nn pairs

$$4V = e_{\mathrm{AA}} + e_{\mathrm{BB}} - 2e_{\mathrm{AB}}. \tag{22.35}$$

At high temperatures, $Vz \ll 2k_{\mathrm{B}}T$, so the exponential in Eq. 22.34 can be linearized

$$Z = \exp\left(-\frac{E_{\mathrm{rndT}}}{k_{\mathrm{B}}T}\right)\sum_{i=1}^{N}\left(1 + \frac{Vz}{2k_{\mathrm{B}}T}\right), \tag{22.36}$$

$$Z = \exp\left(-\frac{E_{\mathrm{rndT}}}{k_{\mathrm{B}}T}\right)N\left(1 + \frac{Vz}{2k_{\mathrm{B}}T}\right), \tag{22.37}$$

and the free energy, $F = -k_{\mathrm{B}}T\ln Z$, is

$$F(T) = E_{\mathrm{rndT}} - \frac{zV}{2} - k_{\mathrm{B}}T\ln(N). \tag{22.38}$$

Equation 22.38 is for a single site that differs from the random average. Of course we expect that at reasonable temperatures there will be many such sites, pairs, squares, and other ordered objects, so we should seek many more terms in the expansion. Our purpose here is only to illustrate the key step, which is the factoring of the partition function in Eq. 22.33, allowing linearization of the much smaller factor on the right.

The high-temperature expansion of the partition function is usually presented in terms of the hyperbolic functions, shown in Fig. 22.6

$$\sinh(x) = \frac{\mathrm{e}^{x} - \mathrm{e}^{-x}}{2}, \qquad \cosh(x) = \frac{\mathrm{e}^{x} + \mathrm{e}^{-x}}{2}, \tag{22.39}$$

$$\tanh(x) = \frac{\sinh(x)}{\cosh(x)} = \frac{\mathrm{e}^{x} - \mathrm{e}^{-x}}{\mathrm{e}^{x} + \mathrm{e}^{-x}}. \tag{22.40}$$

It can be seen from Fig. 22.6, or shown by expanding the exponentials, that in the limits

$$\lim_{x\to 0}\tanh(x) = \lim_{x\to 0}\sinh(x) = x, \qquad \lim_{x\to 0}\cosh(x) = 1 + \frac{x^2}{2}\ . \tag{22.41}$$

With this hyperbolic mathematics, Eq. 22.34 can be rewritten as

$$Z = \cosh^{N}\left(-\frac{E_{\mathrm{rnd1}}}{k_{\mathrm{B}}T}\right)N\left[1 + \tanh\left(+\frac{Vz}{2k_{\mathrm{B}}T}\right)\right], \tag{22.42}$$

which is a more typical expression for such work.

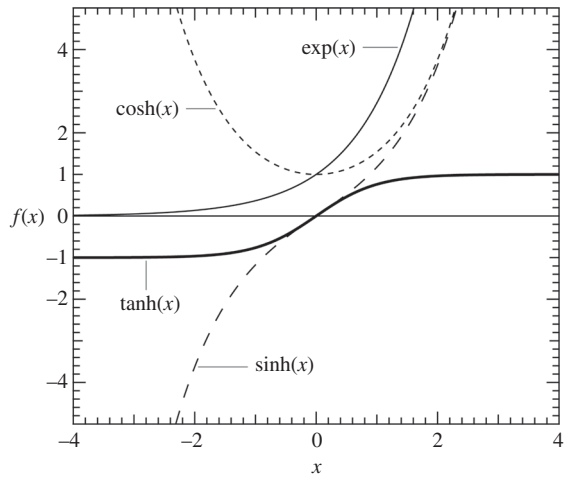

Figure 22.6 Graphs of exponential function exp(x) and the hyperbolic functions sinh(x), cosh(x), and tanh(x).

Problems

22.1 Consider the phase boundary between a B2 ordered structure and an unmixed alloy at low temperatures.

(**a**) In the case where $4V_2 = 0$, for what values of $4V_1$ is the ordered B2 structure (Fig. 18.3) stable over the unmixed state? Explain your answer.

(**b**) Which structure, B2 or unmixed (i.e., random solid solution), is favored for different values of $4V_2$ when $4V_1 = 0$? Explain your answer.

(**c**) A third dimension is needed to make an analogous ground-state diagram for an alloy with first-, second-, and third-nearest-neighbor interations. Without trying to draw such a plot, what is the direction of change in the boundaries of part c when $4V_3 > 0$?

22.2 (**a**) Calculate the ground-state phase boundary between the chessboard structure and an unmixed equiatomic alloy in terms of V_1 and V_2.

(**b**) At finite temperature, will there be a shift in phase boundary when isolated point defects are considered in the low-temperature expansion of the partition function? If so, in what direction?

(**c**) At finite temperature, will there be a shift in phase boundary when defect pairs from 1nn swaps on the chessboard structure, and 1nn defect pairs on the unmixed structure, are considered in the low-temperature expansion of the partition function? If so, in what direction?

22.3 (**a**) Use relations among the hyperbolic functions to obtain Eq. 22.42 from Eq. 22.34.

(**b**) Higher-order terms in the high-temperature expansion of the partition function are often obtained in powers of $\tanh(Vz/k_BT)$. What is the advantage of this approach over powers of Vz/k_BT as T is reduced?

23 Statistical Kinetics of Ordering Transformations

This chapter describes the kinetics of chemical ordering at temperatures below T_c when an initially disordered alloy evolves towards its state of thermodynamic equilibrium. The mechanism of atom–vacancy interchange plays no role in the thermodynamics of phase transitions, but vacancies are essential for the kinetics of a phase transformation. New effects emerge from the kinetics, not associated with thermodynamics. Obviously the rates of change scale with the number of vacancies and their exchange probabilities, but the intermediate states of the alloy structure can also depend on features of the kinetic mechanism.

We define the trajectory through a space of independent order parameters as a "kinetic path" that links the initial state to the final state. The kinetic path is expected to terminate at the state of thermodynamic equilibrium.[1] Nevertheless, most of a kinetic path is through nonequilibrium states, and the path itself may vary with temperature or composition in ways that cannot be obtained by thermodynamic considerations. For example, kinetics can lead to transient ordered structures that are inconsistent with the chemical interactions between atoms (i.e., inconsistent with the ground-state diagrams of Section 22.1). Figure 23.1a suggests why such transient ordered states may form. Here the free energy F depends on two independent order parameters, η_1 and η_2. The kinetic paths through both transient states Tr1 and Tr2 are downhill in free energy, but there are more ways to access the less favorable state Tr2. The kinetic path tends to run through this state Tr2, even though it may not be down the steepest gradient in free energy. The tendency to form the structure of Tr2 may depend on temperature, as suggested in Fig. 23.1b.

Short-range order between A–B pairs occurs quickly, but in the early times of an ordering transformation the A atoms do not make a consistent α-sublattice over long distances.[2] For intermediate length scales, the alloy needs time to decide whether the A-atoms segregate predominantly to the α- or β-sublattice. By symmetry, both segregations are acceptable, and the same free energy is obtained when the pair variable $p_{AB}^{\alpha\beta}$ is dominant or $p_{BA}^{\alpha\beta}$ is dominant.[3] With long-range order (LRO) and sublattice formation as in Fig. 2.19, it is necessary to define sublattice preferences, so $p_{AB}^{\alpha\beta} \neq p_{BA}^{\alpha\beta}$. Conditional pair probabilities, such as the probability of having an A on α, given a B on β, $p(A\alpha|B\beta)$, are also useful for describing short-range order (SRO), and these $p(A\alpha|B\beta)$ are related

[1] Assuming no additional driving mechanisms as in Section 10.6.
[2] For example, the process of domain growth described in Section 17.4 occurs over much longer timescales than short-range ordering.
[3] The pair variable p_{ij} is, for example, the probability p_{AB} that the two sites on an arbitrary nearest-neighbor pair are occupied by an A-atom and a B-atom.

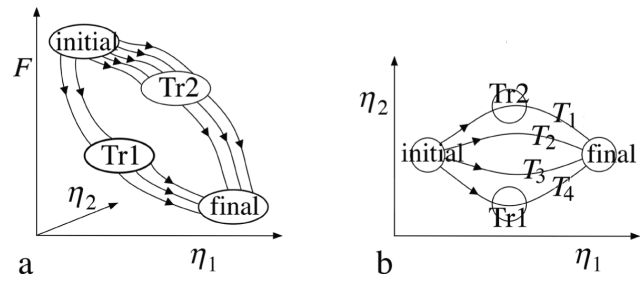

Figure 23.1 (**a**) Connections between states in two order parameters. The transient state Tr2 has higher free energy, but is accessible by more connections. (**b**) Average kinetic paths between initial states and final states at different temperatures, where $T_1 < T_2 < T_3 < T_4$.

to $p_{\mathrm{AB}}^{\alpha\beta}$ by the Bayes theorem of statistics. In short-range ordering, these will be equal, i.e., $p_{\mathrm{AB}}^{\alpha\beta} = p_{\mathrm{BA}}^{\alpha\beta}$. However, the free energy can be lowered further by selecting one of the sublattices for longer-range ordering. Until this sublattice symmetry is broken, at intermediate length scales the kinetic path may experience an arrest, and the phase transformation pauses at this "pseudostable" state. By symmetry of the sublattices, this pseudostable state is at a saddle point of the free energy as a function of short- and intermediate-range order parameters.

23.1 Kinetic Master Equation and Diffusion

23.1.1 Kinetic Master Equation for Atom Jumps between Planes

In this preliminary section, the diffusion equation is derived from the kinetic master equation. Many of the details are repeated in the same sequence as in Section 3.2.2, so the present section should seem less abstract if compared to Section 3.2.2. The kinetic master equation is more versatile than the diffusion equation, however. For example, it can accommodate changes in atom jump rates (e.g., changes in D) when atom jump probabilities depend on their local chemical environment, and this environment changes with time. Section 23.3.2 gives a straightforward example for the kinetics of chemical ordering. Using the kinetic master equation for diffusion is more straightforward, however, so we develop this first.

The kinetic master equation (Eq. 1.25) is, in matrix form

$$\underset{\approx}{W}(\Delta t)\,\underset{\sim}{N}(t) = \underset{\sim}{N}(t + \Delta t). \tag{23.1}$$

The $\underset{\sim}{N}(t)$ is a column vector[4] whose elements are the contents of the bins of Fig. 1.9a (or Fig. 3.3)

$$\underset{\sim}{N}(t) = \left[\ldots N_{n-1}(t),\, N_n(t),\, N_{n+1}(t)\ldots\right]. \tag{23.2}$$

[4] Written here sideways, as its transpose.

The $\underset{\approx}{W}(\Delta t)$ in Eq. 23.1 is a two-dimensional matrix that operates on $\underset{\sim}{N}(t)$ and changes its contents in the time interval Δt. Two such matrix elements are shown in Fig. 1.9b. This approach is natural for numerical computations. If Δt is small, after m intervals of Δt the new contents of the bins are

$$\left[\underset{\approx}{W}(\Delta t)\right]^m \underset{\sim}{N}(t) = \underset{\sim}{N}(t + m\Delta t). \tag{23.3}$$

The following assumptions are fundamental to the derivation of the diffusion equation, and are important to remember whenever using the diffusion equation for a problem in materials science (see assumptions at the start of Section 3.2.1):

- All atoms have the same jump probability (unaffected by the presence of other atoms).
- If an atom has probability δ of jumping out of a bin in Fig. 1.9, it has an equal probability $\delta/2$ of going left or right (in three dimensions the probability is shared as $\delta/6$ between left, right, up, down, in, out).
- An atom can jump only into an adjacent bin (but this is not an essential assumption for obtaining the diffusion equation, as shown by Problem 10.2).

To understand the structure of $\underset{\approx}{W}(\Delta t)$, first assume zero atom jumps in the time Δt. In this case $\underset{\approx}{W}(\Delta t)$ must be the identity matrix, $\underset{\approx}{I}$, with all 1s on its diagonal, and 0s elsewhere. The operation of this identity matrix on the vector $\underset{\sim}{N}(t)$ preserves the contents of all bins at time $t + \Delta t$, so in this case $\underset{\approx}{I}\,\underset{\sim}{N}(t) = \underset{\sim}{N}(t + \Delta t) = \underset{\sim}{N}(t)$.

Next, assume each atom has only a small probability δ of leaving its bin in the short time interval Δt. The probability of it remaining in the bin is therefore $1 - \delta$, and from the second assumption above, its probability of entering an adjacent bin is $\delta/2$. Likewise, the probability of an atom entering a bin from an adjacent bin is also $\delta/2$. The W-matrix is close to diagonal, but the elements positioned one off the diagonal are now $\delta/2$. Equation 23.1 is

$$\begin{bmatrix}
1-\delta & \delta/2 & & & & & & \dots & 0 \\
\delta/2 & \dots & & & & & & \dots & 0 \\
\vdots & \dots & & & & & & \dots & \vdots \\
0 & \dots & \delta/2 & 1-\delta & \delta/2 & 0 & 0 & \dots & 0 \\
0 & \dots & 0 & \delta/2 & 1-\delta & \delta/2 & 0 & \dots & 0 \\
0 & \dots & 0 & 0 & \delta/2 & 1-\delta & \delta/2 & \dots & 0 \\
\vdots & \dots & & & & & & \dots & \vdots \\
0 & \dots & & & & & & \dots & \delta/2 \\
0 & \dots & & & & & & \delta/2 & 1-\delta
\end{bmatrix}
\begin{bmatrix} \dots \\ \dots \\ \dots \\ N_{n-1}(t) \\ N_n(t) \\ N_{n+1}(t) \\ \dots \\ \dots \\ \dots \end{bmatrix}
=
\begin{bmatrix} \dots \\ \dots \\ \dots \\ \delta/2N_{n-2}(t) + (1-\delta)N_{n-1}(t) + \delta/2N_n(t) \\ \delta/2N_{n-1}(t) + (1-\delta)N_n(t) + \delta/2N_{n+1}(t) \\ \delta/2N_n(t) + (1-\delta)N_{n+1}(t) + \delta/2N_{n+2}(t) \\ \dots \\ \dots \\ \dots \end{bmatrix}. \tag{23.4}$$

The column vector on the right-hand side (RHS) of Eq. 23.4 is actually quite simple. Its largest terms are the middle ones with the factor $(1 - \delta)$, which is nearly 1. If δ were zero, meaning no atom movement, $\underset{\approx}{W}$ would be the identity matrix, the nth bin would have no change in the time Δt, and $N_n(t + \Delta t) = N_n(t)$.

With atom movements, the nth bin receives contributions from the two surrounding bins, proportional to $\delta/2$. Because δ is the dimensionless probability that an atom will jump from its bin in time Δt, the probability δ can be rewritten as the jump rate of one atom Γ (per second), times Δt

$$\delta = \Gamma \, \Delta t. \tag{23.5}$$

Consider the middle line on the RHS of Eq. 23.4, which is the value of N_n at time $t + \Delta t$, and use Eq. 23.5 for δ

$$N_n(t + \Delta t) = \Gamma \, \Delta t/2 \, N_{n-1}(t) + (1 - \Gamma \, \Delta t) N_n(t) + \Gamma \, \Delta t/2 \, N_{n+1}(t), \tag{23.6}$$

$$\frac{N_n(t + \Delta t) - N_n(t)}{\Delta t} = \frac{\Gamma}{2} \Big[N_{n-1}(t) + N_{n+1}(t) - 2 \, N_n(t) \Big]. \tag{23.7}$$

23.1.2 Diffusion in a Continuum

As Δt becomes small, the difference ratio on the left-hand side (LHS) of Eq. 23.7 becomes a partial derivative of N_n

$$\frac{\partial N_n}{\partial t} = \frac{N_n(t + \Delta t) - N_n(t)}{\Delta t}. \tag{23.8}$$

The RHS of Eq. 23.7 has differences between the contents of adjacent bins at fixed t. To convert to a spatial coordinate, we need the physical distance between bins. For the problem of atom diffusion in one dimension, we use a stack of crystal planes as concentration bins. The elementary kinetic process is an atom jump between adjacent planes, which are separated by the distance a. The indices n and $n + 1$ now correspond to adjacent planes. The second derivative of the spatial coordinate is the difference ratio

$$\frac{\partial^2 N_n}{\partial x^2} = \frac{N_{n-1}(t) + N_{n+1}(t) - 2 \, N_n(t)}{a^2}, \tag{23.9}$$

which we identify in the RHS of Eq. 23.7, giving

$$\frac{\partial N_n}{\partial t} = \frac{\Gamma \, a^2}{2} \frac{\partial^2 N_n}{\partial x^2}. \tag{23.10}$$

To extend this result to diffusion in a bulk material, define a concentration $c(x, t)$ [atoms cm^{-3}] at the position x of the nth bin by giving the bin an area A and width a

$$c(x, t) \equiv \frac{N_n(t)}{aA}, \tag{23.11}$$

Equation 23.11 is rearranged to obtain $N_n(t)$ for substitution into Eq. 23.10. The constant $a\,A$ appears on both sides and cancels, giving the one-dimensional diffusion equation

$$\frac{\partial c(x, t)}{\partial t} = \frac{\Gamma \, a^2}{2} \frac{\partial^2 c(x, t)}{\partial x^2}, \tag{23.12}$$

$$\frac{\partial c}{\partial t} = D \frac{\partial^2 c}{\partial x^2}, \tag{23.13}$$

where the diffusion coefficient was defined as $D = \Gamma \, a^2/2$ (which has units [cm^2/s]). The three-dimensional diffusion equation is obtained by recognizing that only 1/6 of the

atom jumps go to the right, with the other 5/6 going left, up, down, in, out. In three dimensions

$$\frac{\partial c(x,y,z,t)}{\partial t} = \frac{\Gamma a^2}{6}\left[\frac{\partial^2}{\partial x^2} + \frac{\partial^2}{\partial y^2} + \frac{\partial^2}{\partial z^2}\right] c(x,y,z,t), \tag{23.14}$$

$$\frac{\partial c}{\partial t} = D\nabla^2 c, \tag{23.15}$$

where

$$D = \frac{\Gamma a^2}{6}. \tag{23.16}$$

Equation 23.15 is "the diffusion equation," sometimes called "Fick's second law." It was obtained previously as Eq. 3.28.

23.2 Ordering Transformations with Vacancies

The elementary atom movement in most crystalline solids is an atom–vacancy interchange. The interchange frequency is determined in part by the species that undergoes the atom–vacancy interchange; each species is assigned a characteristic attempt frequency for the interchange ν_A, and a characteristic energy for its activated state e^*_A during its jump into the vacancy. More interesting is how the jump rate depends on the local chemical environment of each atom. It is this chemical dependence of the activation energy that causes the atoms to settle into environments consistent with thermodynamic equilibrium.[5] This is illustrated with Fig. 23.2, which depicts the effect of the local chemical environment on the activation barrier for an atom–vacancy interchange. The more favorable the initial chemical environment, i.e., the deeper the bonding in the initial state at x_i, the larger the activation energy, and the less likely the jump. Although the local chemical environment in the final state does not affect the activation, thermodynamic equilibrium still occurs as discussed in Section 5.6.1.

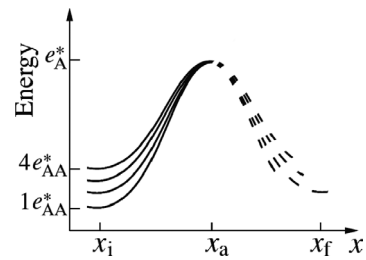

Figure 23.2 Schematic potential energy barrier for A-atom interchange with a vacancy. The A-atom is initially at position x_i, crosses the barrier at x_a, and is finally at the position x_f. Only the initial energy is affected by A–A interactions, in this case unfavorably, so more A-neighbors make it more likely for the A-atom to attain the activation barrier.

[5] If the atom movement depended only on ν and e^*_A, the alloy would undergo diffusion, but not unmixing or ordering.

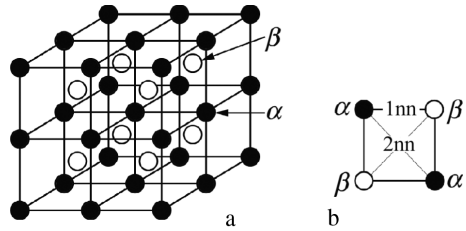

Figure 23.3 (**a**) Eight standard unit cells of the B2 structure, showing the α- and β-sublattices. (**b**) Unit depicting a two-dimensional analog (chessboard ordering), showing sublattices and distance relationships.

For example, if an A-atom has n A-neighbors, v vacancy neighbors, and $z - v - n$ B-neighbors (z is again coordination number), its jump rate, Γ_A, is

$$\Gamma_A(n) = \nu_A\, v\, \exp\left[-\frac{e_A^* - [ne_{AA} + (z-n-v)e_{AB}]}{k_B T}\right], \tag{23.17}$$

where e_A^* is an activation energy barrier for the A-atom, ν_A its attempt frequency, and e_{AA} and e_{AB} are the usual pair energies of Section 2.7. (When vacancies have low concentrations and do not interact, only $v = 1$ is important.)

Owing to chemical interactions, the rate $\Gamma_A(n)$ will be different for A-atoms with different numbers, n, of A-neighbors. How this distribution of neighborhoods is handled is set by the order of the kinetic approximation. The issues with the level of the approximation are much like those for the thermodynamic cluster expansion methods discussed after Eq. 2.58 in Section 2.9.2, and in Section 7.2. The simplest approximation is the point approximation, which we formulate for the problem of B2 ordering (Fig. 23.3). Here, for an atom on the α-sublattice with its neighbors on the β-sublattice, the probability that a site on the β-sublattice is occupied by an A-atom is p_A^β, and this can be used to obtain an average n. The parameter p_A^β is a long-range order (LRO) parameter because it pertains to the entire β-sublattice. The next higher-order approximation is the pair approximation, which uses short-range order (SRO) parameters such as $p_{AB}^{\alpha\beta}$, the probability of a neighboring pair being an A–B pair with A on α and B on β. This gives a more realistic accounting of the first-neighbor shell of the A-atom when determining n in Eq. 23.17. Higher-order approximations have more order parameters, although conservation of atoms and sublattice sites reduces the number of independent order parameters.[6]

23.3 B2 Ordering with Vacancies in the Point Approximation

23.3.1 Variables

For a binary alloy with vacancies there are three composition variables $\{c_A, c_B, c_V\}$. To describe the segregation of atoms to the sublattices α and β, there are six point

[6] Figure 7.4, for example, illustrates an issue of consistency between the point and pair variables.

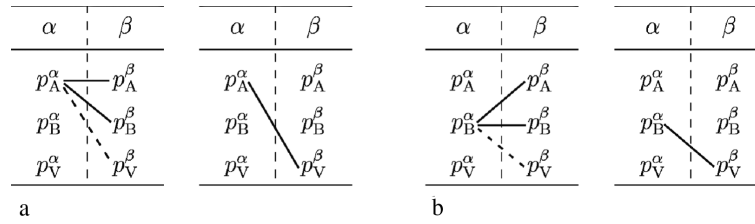

Figure 23.4 Interactions of first-nearest-neighbor variables in the point approximation for B2 ordering of a binary alloy. Left connection diagram is for the Boltzmann factors. Right connection diagram is for the atom–vacancy interchange. (**a**) For motion of an A-atom off the α-sublattice. (**b**) For motion of a B-atom off the α-sublattice.

variables $\{p_A^\alpha, p_B^\alpha, p_V^\alpha, p_A^\beta, p_B^\beta, p_V^\beta\}$. Figure 23.4 organizes these variables, and points out the connections between them that must be considered when changing the variables p_A^α and p_B^α in parts a and b of the figure. For these variables we seek the activation barrier for moving an A or B atom off the α-sublattice, but we also need to know how many vacancies are present on the β-sublattice for the interchange to occur.

Of these nine variables in the point approximation, $\{p_A^\alpha, p_B^\alpha, p_V^\alpha, p_A^\beta, p_B^\beta, p_V^\beta, c_A, c_B, c_V\}$, only four prove independent, however. Because

$$c_A + c_B + c_V = 1, \tag{23.18}$$

only two composition variables are independent. Likewise, the probabilities that a site on a sublattice is occupied by a specific species are constrained as

$$p_A^\alpha + p_B^\alpha + p_V^\alpha = 1\ , \quad p_A^\beta + p_B^\beta + p_V^\beta = 1 \tag{23.19}$$

and, finally, atom conservation gives

$$p_A^\alpha + p_A^\beta = 2c_A, \quad p_B^\alpha + p_B^\beta = 2c_B, \quad p_V^\alpha + p_V^\beta = 2c_V, \tag{23.20}$$

although one of these three is enforced already by Eqs. 23.18 and 23.19. With the two independent composition variables and the net four constraints on the point variables, four variables are independent. A convenient choice is $\{c_A, c_V, p_A^\alpha, p_V^\alpha\}$. After specifying the composition variables c_A and c_V, there are two independent order parameters.

23.3.2 *W*-matrix for the Kinetic Master Equation

The point variable p_A^α is a sublattice concentration that ranges from 0 to 1. We follow its evolution with the kinetic master equation, which was presented as Eq. 1.25, and arranged for diffusion problems as Eq. 23.1. Recall that for diffusion we could use planes of atoms as bins, and the master equation gave atom transfers along a row of planes. For the ordering problem the atom transfers occur one at a time between sublattices. The adjacent bins are states of order, differing by one atom after each vacancy jump. Instead of mapping the bins into planes of atoms, we map them onto sublattice occupancies. For example, three states of order in an equiatomic alloy are

$$\underset{\sim}{p}^{\alpha}_{\mathrm{A}}(t) = \begin{bmatrix} 1 \\ 0 \\ 0 \\ \dots \\ 0 \\ 0 \\ 0 \end{bmatrix}, \text{or} \begin{bmatrix} 0 \\ 0 \\ \dots \\ 1 \\ \dots \\ 0 \\ 0 \end{bmatrix}, \text{or} \begin{bmatrix} 0 \\ 0 \\ 0 \\ \dots \\ 0 \\ 0 \\ 1 \end{bmatrix}. \tag{23.21}$$

The column vector at left describes a certainty of perfect order with all A-atoms on the α-sublattice, the middle column vector describes a certain situation with half the A-atoms on the α-sublattice, and the column vector at right describes a certainty of perfect order with all A-atoms on the β-sublattice, and none on the α.

The W-matrix [379] moves probability between the different states of order. It is constructed so that each operation of $\underset{\approx}{W}$ on $\underset{\sim}{p}^{\alpha}_{\mathrm{A}}$ corresponds to one interchange of an A-atom and a vacancy. This causes probability to move up or down the column vector $\underset{\sim}{p}^{\alpha}_{\mathrm{A}}$, depending on whether an A-atom moves on or off the α-sublattice

$$\underset{\approx}{W}\,\underset{\sim}{p}^{\alpha}_{\mathrm{A}} = \underset{\sim}{p}^{\alpha\prime}_{\mathrm{A}}, \tag{23.22}$$

and in more detail [380, 381]

$$\begin{bmatrix} 1-\Delta_{11} & W^{\uparrow}_{12} & 0 & \dots & 0 & 0 & 0 \\ W^{\downarrow}_{21} & 1-\Delta_{22} & W^{\uparrow}_{23} & \dots & 0 & 0 & 0 \\ 0 & W^{\downarrow}_{32} & 1-\Delta_{33} & W^{\uparrow}_{34} & \dots & 0 & 0 \\ 0 & 0 & W^{\downarrow}_{43} & 1-\Delta_{44} & W^{\uparrow}_{45} & \dots & 0 \\ \dots & & & \dots & & & \dots \\ 0 & 0 & 0 & \dots & 0 & 1-\Delta_{N/2-1,N/2-1} & W^{\uparrow}_{N/2-1,N/2} \\ 0 & 0 & 0 & \dots & 0 & W^{\downarrow}_{N/2,N/2-1} & 1-\Delta_{N/2,N/2} \end{bmatrix} \times \begin{bmatrix} 0 \\ 0 \\ 1 \\ 0 \\ \dots \\ 0 \\ 0 \end{bmatrix} = \begin{bmatrix} 0 \\ W^{\uparrow}_{23} \\ 1-W^{\uparrow}_{23}-W^{\downarrow}_{43} \\ W^{\downarrow}_{43} \\ \dots \\ 0 \\ 0 \end{bmatrix}, \tag{23.23}$$

using the more compact notation $\Delta_{ii} \equiv W^{\uparrow}_{i-1,i} + W^{\downarrow}_{i+1,i}$. The appearance of Eq. 23.23 is much like Eq. 23.4 for diffusion. Beware, however, that unlike the random jumps for diffusion, the elements $W^{\downarrow}_{ij}$, $W^{\uparrow}_{ij}$, and Δ_{ii} are not constants. They depend on the state of order in the alloy (i.e., they vary with i and j). The difference between $W^{\downarrow}$ and $W^{\uparrow}$ directs the tendency for A-atoms to move on or off the α-sublattice for each A–vacancy interchange (and the arrows are redundant, but reminders of the direction of the flow). For n such atom–vacancy interchanges

$$\underset{\approx}{W}^{n}\ \underset{\sim}{p}^{\alpha}_{\mathrm{A}} = \underset{\sim}{p}^{\alpha\prime}_{\mathrm{A}}, \tag{23.24}$$

For calculating the movements of A-atoms on and off the α-sublattice, there are three factors in the W_{ij}:

- the probability that a site on the sublattice is occupied by an A-atom;
- the probability of a vacancy in its 1nn shell;
- a Boltzmann factor that accounts for the jump probability of the A-atom. This depends on the chemical environment of the A-atom (Fig. 23.2).

Consider a typical case of $W^{\uparrow}$, where an A-atom moves from the β- to the α-sublattice. The A starts on the β, and the V (vacancy) is on the α. The moving A has initially $z-1$ neighboring atoms and 1 V neighbor, all on the α-sublattice.

$$W^{\uparrow}_{i,i+1} = \left[p^{\beta}_{A}\right]\left[z\,p^{\alpha}_{V}\right]\exp\Big[-\frac{1}{k_{\mathrm{B}}T}\Big(e^{*}_{A} - (z-1)e_{\mathrm{AA}}p^{\alpha}_{A} - (z-1)e_{\mathrm{AB}}p^{\alpha}_{B}\Big)\Big], \tag{23.25}$$

and for A-atom movements off the α-sublattice in the reverse process

$$W^{\downarrow}_{i+1,i} = \left[p^{\alpha}_{A}\right]\left[z\,p^{\beta}_{V}\right]\exp\Big[-\frac{1}{k_{\mathrm{B}}T}\Big(e^{*}_{A} - (z-1)e_{\mathrm{AA}}p^{\beta}_{A} - (z-1)e_{\mathrm{AB}}p^{\beta}_{B}\Big)\Big]. \tag{23.26}$$

We have two independent order parameters. In addition to the rate of accumulation of A-atoms on the α-sublattice, $\mathrm{d}p^{\alpha}_{\mathrm{A}}/\mathrm{d}t$, the rate of accumulation of vacancies on the α-sublattice, $\mathrm{d}p^{\alpha}_{\mathrm{V}}/\mathrm{d}t$, must also be considered. Using the kinetic master equation (Eq. 1.25)

$$\frac{\mathrm{d}p^{\alpha}_{\mathrm{A}}}{\mathrm{d}t} = \underset{\beta\mathrm{A}\alpha}{W}{}^{\uparrow}_{j,j+1} - \underset{\alpha\mathrm{A}\beta}{W}{}^{\downarrow}_{j+1,j}, \tag{23.27}$$

$$\frac{\mathrm{d}p^{\alpha}_{\mathrm{V}}}{\mathrm{d}t} = \underset{\alpha\mathrm{A}\beta}{W}{}^{\downarrow}_{j+1,j} - \underset{\beta\mathrm{A}\alpha}{W}{}^{\uparrow}_{j,j+1} + \underset{\alpha\mathrm{B}\beta}{W}{}^{\uparrow}_{k,k+1} - \underset{\beta\mathrm{B}\alpha}{W}{}^{\downarrow}_{k+1,k}, \tag{23.28}$$

where $\underset{\beta\mathrm{B}\alpha}{W}{}^{\downarrow}$, for example, is the rate of jumps of B-atoms from the β-sublattice to the α-sublattice.[7] The changes in concentrations of A-atoms and vacancies depend oppositely on jump rates of A-atoms, giving two terms with opposite signs in Eqs. 23.27 and 23.28. The vacancy concentration has an additional dependence on the jumps of B-atoms, and two extra terms in Eq. 23.28 [380].

23.3.3 Equilibrium State

In equilibrium, the overall rates of atom and vacancy transfer between sublattices are zero. Steady sublattice populations of A-atoms require equality of the $W^{\uparrow}$ and $W^{\downarrow}$ of Eqs. 23.25 and 23.26 (i.e., set $\mathrm{d}p^{\alpha}_{\mathrm{A}}/\mathrm{d}t = 0$ in Eq. 23.27). There is an analogous relationship for the B-atoms which can be obtained by rewriting Eqs. 23.25 and 23.26 – simply replace all instances of "A" with "B" and simultaneously replace all instances of "α" with "β." The vacancy equilibrium, $\mathrm{d}p^{\alpha}_{\mathrm{V}}/\mathrm{d}t = 0$ in Eq. 23.28, is automatically satisfied when the A-atoms and B-atoms have no net transfers between the sublattices.

[7] The underset, for example $\alpha\mathrm{B}\beta$, denotes the jump of a B-atom from the α- to β-sublattice. It is added for clarity, but it is redundant.

Setting $\mathrm{d}p_{\mathrm{A}}^{\alpha}/\mathrm{d}t = 0$ in Eq. 23.27 gives a transcendental equation with no simple solution. We can, however, use the standard trick of linearizing this equation near the critical temperature. For example, consider the problem of an equiatomic alloy with a very small amount of order

$$p_{\mathrm{A}}^{\alpha} = \frac{1}{2} + \delta,\ p_{\mathrm{A}}^{\beta} = \frac{1}{2} - \delta,\ p_{\mathrm{B}}^{\alpha} = \frac{1}{2} - \delta,\ p_{\mathrm{B}}^{\beta} = \frac{1}{2} + \delta, \text{ and} \tag{23.29}$$

$$p_{\mathrm{V}}^{\alpha} = p_{\mathrm{V}}^{\beta} \equiv p_{\mathrm{V}}. \tag{23.30}$$

Because the order is small, $\delta \ll 1/2$. We have also assumed that there is no vacancy segregation between the two sublattices, an assumption to discuss later. There are large common factors in Eqs. 23.25 and 23.26. These common factors, defined as C, are

$$C \equiv p_{\mathrm{V}}\, z\, \exp\Big[-\frac{1}{k_{\mathrm{B}}T}e_{\mathrm{A}}^{*}\Big]\, \exp\Big[\frac{1}{k_{\mathrm{B}}T}(z-1)e_{\mathrm{AA}}\frac{1}{2}\Big]\, \exp\Big[\frac{1}{k_{\mathrm{B}}T}(z-1)e_{\mathrm{AB}}\frac{1}{2}\Big]. \tag{23.31}$$

With this definition of C, we continue with the process of setting $\mathrm{d}p_{\mathrm{A}}^{\alpha}/\mathrm{d}t = 0$ by equating Eqs. 23.25 and 23.26

$$C\Big(\frac{1}{2} - \delta\Big)\exp\Big[\frac{1}{k_{\mathrm{B}}T}(z-1)e_{\mathrm{AA}}(+\delta)\Big]\, \exp\Big[\frac{1}{k_{\mathrm{B}}T}(z-1)e_{\mathrm{AB}}(-\delta)\Big] \tag{23.32}$$

$$= C\Big(\frac{1}{2} + \delta\Big)\exp\Big[\frac{1}{k_{\mathrm{B}}T}(z-1)e_{\mathrm{AA}}(-\delta)\Big]\, \exp\Big[\frac{1}{k_{\mathrm{B}}T}(z-1)e_{\mathrm{AB}}(+\delta)\Big], \tag{23.33}$$

which is rearranged as

$$\frac{\frac{1}{2} + \delta}{\frac{1}{2} - \delta} = 2\exp\Big[\frac{1}{k_{\mathrm{B}}T}(z-1)2\delta[e_{\mathrm{AA}} - e_{\mathrm{AB}}]\Big]. \tag{23.34}$$

Just below the critical temperature for ordering, T_{c}, the sublattice segregation δ is infinitesimal, so we linearize the exponential (and simplify the fraction on the LHS for small δ), much as we did for a simpler case with Eqs. 2.56– 2.58,[8]

$$1 + 4\delta = 1 + \frac{1}{k_{\mathrm{B}}T_{\mathrm{c}}^{\mathrm{A}}}(z-1)(e_{\mathrm{AA}} - e_{\mathrm{AB}})\,2\delta, \tag{23.35}$$

$$T_{\mathrm{c}}^{\mathrm{A}} = \frac{1}{2k_{\mathrm{B}}}(z-1)(e_{\mathrm{AA}} - e_{\mathrm{AB}}). \tag{23.36}$$

Because we did not consider the motion of B-atoms, the energy e_{BB} is not included in Eq. 23.36. There is, of course, an analogous expression for the B-atoms, obtained by swapping all instances of "A" for "B," and changing all cases of $+\delta \rightarrow -\delta$, giving

$$T_{\mathrm{c}}^{\mathrm{B}} = \frac{1}{2k_{\mathrm{B}}}(z-1)(e_{\mathrm{BB}} - e_{\mathrm{AB}}). \tag{23.37}$$

When $e_{\mathrm{AA}} = e_{\mathrm{BB}}$, Eqs. 23.36 and 23.37 are the same, and

$$T_{\mathrm{c}} = \frac{1}{4k_{\mathrm{B}}}(z-1)(e_{\mathrm{AA}} + e_{\mathrm{BB}} - 2e_{\mathrm{AB}}), \tag{23.38}$$

$$T_{\mathrm{c}} = \frac{(z-1)V}{k_{\mathrm{B}}}. \tag{23.39}$$

[8] Unlike Eq. 2.56, Eq. 23.34 may become unreliable when the chemical sublattice segregation exceeds the vacancy concentration, but it should be appropriate when δ is very small.

Comparing this result to Eq. 2.58, we see that Eq. 23.39 has a different factor of $z-1$ instead of z. This is a characteristic of ordering with vacancies because the chemical interaction from one of the neighboring atoms is missing (it is replaced with a vacancy). The physical details from this simple model need not be taken too literally. Nevertheless, the atom arrangement near the vacancy, the agent of change, is different from atom arrangements around most of the atoms in the alloy. There will be some differences in chemical bonding for atoms next to a vacancy, compared to their bonding in a perfect crystal. This will have an effect on the steady state of the alloy at a given temperature. This kinetic effect for vacancies does not pertain to a dynamics that interchanges A and B atoms, which can produce the state of thermodynamic equilibrium.[9]

Finally, we address the difference between Eqs. 23.36 and 23.37. The sublattice segregation tendencies of A-atoms and B-atoms will be equal if $e_{\mathrm{AA}} = e_{\mathrm{BB}}$. In this case, there will be no vacancy imbalance between the sublattices, and Eq. 23.30 is appropriate. When $e_{\mathrm{AA}} \neq e_{\mathrm{BB}}$ the analysis is a bit more complicated, but for small vacancy concentrations the same critical temperature, Eq. 23.39, is obtained. Vacancy equilibration is discussed next.

23.4 Vacancy Ordering

To obtain a general feature of vacancy kinetics, we ignore chemical interactions and set the Boltzmann factor equal to 1 in Eqs. 23.25 and 23.26, allowing for a simple analytical result. The rate $\underset{\beta \mathrm{A}\alpha}{W}{}^{\uparrow}$ is the product of (1) the concentration of vacancies on the α sublattice, p_{V}^{α}, and (2) the probability of finding an A-atom on the β-sublattice in one of the z nearest-neighbor sites of such a vacancy, $z(1-p_{\mathrm{A}}^{\alpha})$

$$\underset{\beta \mathrm{A}\alpha}{W}{}^{\uparrow} = p_{\mathrm{V}}^{\alpha}\, z(1-p_{\mathrm{A}}^{\alpha})\, 1, \tag{23.40}$$

assuming an equiatomic alloy with $c_{\mathrm{V}} \ll c_{\mathrm{A}}$. By similar reasoning, expressions equivalent to Eqs. 23.27 and 23.28 are

$$\frac{\mathrm{d}p_{\mathrm{A}}^{\alpha}}{\mathrm{d}t} = \left(1-p_{\mathrm{A}}^{\alpha}\right) z\, p_{\mathrm{V}}^{\alpha} - p_{\mathrm{A}}^{\alpha} z\left(c_{\mathrm{V}} - p_{\mathrm{V}}^{\alpha}\right), \tag{23.41}$$

$$\frac{\mathrm{d}p_{\mathrm{V}}^{\alpha}}{\mathrm{d}t} = p_{\mathrm{A}}^{\alpha} z\left(c_{\mathrm{V}} - p_{\mathrm{V}}^{\alpha}\right) - \left(1-p_{\mathrm{A}}^{\alpha}\right) z\, p_{\mathrm{V}}^{\alpha} + \left(1-p_{\mathrm{A}}^{\alpha}\right) z\left(c_{\mathrm{V}} - p_{\mathrm{V}}^{\alpha}\right) - p_{\mathrm{A}}^{\alpha} z\, p_{\mathrm{V}}^{\alpha}. \tag{23.42}$$

Equations 23.41 and 23.42 are two coupled first-order differential equations that can be rearranged as

$$\begin{bmatrix} \frac{\mathrm{d}}{\mathrm{d}t} + z c_{\mathrm{V}} & -z \\ 0 & \frac{\mathrm{d}}{\mathrm{d}t} + 2z \end{bmatrix} \begin{bmatrix} p_{\mathrm{A}}^{\alpha} \\ p_{\mathrm{V}}^{\alpha} \end{bmatrix} = \begin{bmatrix} 0 \\ z c_{\mathrm{V}} \end{bmatrix}. \tag{23.43}$$

Solutions to Eqs. 23.43 have exponential relaxations with two time constants (which are dimensionless because prefactors were set to 1)

[9] For thermodynamic equilibrium, the interchange mechanism must interchange an A–B pair that are not in the range of the e_{AB}, however.

$$\tau_1 = \frac{1}{zc_V}, \tag{23.44}$$

$$\tau_2 = \frac{1}{2z}. \tag{23.45}$$

The time constant τ_1 is much longer than the time constant τ_2 because c_V is small. This τ_1 is the time constant for relaxation of A- and B-atoms onto their proper sublattice, and τ_1 depends inversely on the vacancy concentration. The other time constant, τ_2, is less familiar [126, 382–384]. It is the fast time constant for the relaxation of vacancies onto their preferred sublattice. It is a factor of c_V times shorter than the relaxation time for the observable order parameters of the atoms. Such vacancy relaxations may not be possible to observe experimentally, but they should affect the rates of ordering transformations, especially at low temperatures.

23.5 Kinetic Paths

In part because of new methods of synthesis (e.g., Table 5.1, Section 5.1), materials far-removed from thermodynamic equilibrium have attracted much recent attention. An understanding of how nonequilibrium materials move towards equilibrium can be used for obtaining different states in materials. Kinetic aspects of atom–vacancy interchanges can dominate over thermodynamic forces in controlling the large relaxations of chemical enthalpy. In such cases we cannot rely on our intuition that all order parameters will relax monotonically to equilibrium as described in Section 5.6.2. Especially for systems far from equilibrium, the mobility parameter M must be considered a function of the state variables, and the kinetic path may not go directly downhill in free energy (as described with Fig. 23.1a).

An alloy described by one order parameter can move at different rates through a series of states of order. Nevertheless, this behavior is one-dimensional, with the same states occurring in the same sequence. When the state of the material is characterized by two or more independent order parameters, however, the sequence of nonequilibrium states itself may be altered; given a particular value of one order parameter, we may be able to control the kinetics so the second order parameter assumes a range of different values. In theory and in practice, the "kinetic path" of an alloy through the space spanned by multiple state variables can be varied to encompass a wide range of states of order.[10]

Some examples of independent order parameter variables used for different levels of approximation are listed in Table 23.1. As can be deduced from Table 23.1, more degrees of freedom are available with

- additional chemical species in the alloy;
- additional sublattices (and larger unit cells for the ordered structure);
- a higher order of approximation (which adds new state variables).

[10] The vacancy concentration, assumed small, does not control the paths through these order parameters, although it does control the rate. Variations in kinetic paths may therefore offer some advantages for experimental determinations of the roles of activation energies and interatomic interactions in ordering transformations.

Table 23.1 Independent order parameters (compositions must also be specified)

Species	Sublattice	Approximation	Parameters	Examples
2	2	point	1	p_{A}^{α}
2	2	pair	2	$p_{\mathrm{A}}^{\alpha}\, p_{\mathrm{AA}}^{\alpha\beta}$
3	2	point	2	$p_{\mathrm{A}}^{\alpha}\, p_{\mathrm{C}}^{\alpha}$
2	4	point	3	$p_{\mathrm{A}}^{\alpha}\, p_{\mathrm{A}}^{\beta}\, p_{\mathrm{A}}^{\gamma}$
3	2	pair	4	$p_{\mathrm{A}}^{\alpha}\, p_{\mathrm{AA}}^{\alpha\beta}\, p_{\mathrm{C}}^{\alpha}\, p_{\mathrm{CC}}^{\alpha\beta}$
3	4	pair	16	...

23.5.1 Multicomponent Alloys

Consider again B2 ordering in the point approximation with vacancies, but now consider a ternary alloy [380, 385]. Ternary alloys (elements A, B, C) with two sublattices (α and β) have two independent order parameters in the point approximation, and different kinetic paths are possible through the state space spanned by p_{A}^{α} and p_{C}^{α}, for example. As a preliminary, consider a binary alloy. Assuming an infinitesimal vacancy concentration, the flow of A-atoms off a sublattice is compensated by a reverse flow of B-atoms. A higher activation energy e_{B}^{*} for the motion of B-atoms cannot retard the B-atoms without also affecting the motions of A-atoms. All kinetic paths through the variables p_{A}^{α} and p_{B}^{α} must be the same. For a ternary alloy, however, differences in activation barriers $\{e_{\mathrm{A}}^{*}, e_{\mathrm{B}}^{*}, e_{\mathrm{C}}^{*}\}$ can alter the kinetic path through p_{A}^{α} and p_{C}^{α}, even though these activation barriers have no effect on the end state of thermodynamic equilibrium.

Combinations of the 1nn pair energies $\{e_{\mathrm{AA}}, e_{\mathrm{BB}}, e_{\mathrm{CC}}, e_{\mathrm{AB}}, e_{\mathrm{AC}}, e_{\mathrm{BC}}\}$ determine the state of thermodynamic equilibrium. Individual pair energies set the chemical bias of a diffusive jump, so differences in $\{e_{ij}\}$ can cause variations in kinetic paths. Consider a case where the A-atoms are chemically active, and the B- and C-atoms have weaker energies e_{ij}. A kinetic path for such an alloy is presented in Fig. 23.5. The kinetic path starts with p_{C}^{α} changing in the wrong direction owing to a vacancy imbalance that occurs when the strongly segregating A-atoms push the vacancies onto the β-sublattice. This vacancy imbalance makes it more likely for the C-atoms to jump onto the β-sublattice, even though they have no chemical preference to do so. Eventually the path turns around, reaching an equilibrium state in the upper right corner at this low temperature.

23.5.2 Multiple Sublattices and Transient Ordered Structures

The B2, B32, and $\mathrm{D0_3}$ structures for A–B alloys can be understood with the supercell shown in Fig. 23.6. The B2 structure for an equiatomic alloy is obtained when the A-atoms occupy both black and white sites (γ and δ at corners), and the B-atoms occupy both gray sites (α and β at centers). A B2 structure has all 1nn atoms of the opposite species, whereas 2nn atoms are the same species, as depicted in Fig. 23.6c. A B32 structure for

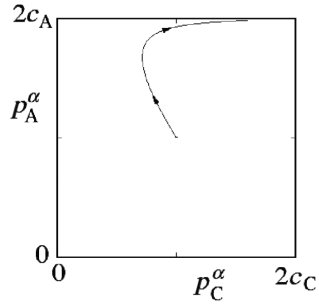

Figure 23.5 A kinetic path that initially goes backwards in the variable p_C^α for a ternary bcc alloy with B2 order in the point approximation. The initial state is a disordered solid solution; the final state has a strong segregation of both A- and C-atoms on the α-sublattice. Energy parameters in units of k_BT were $e_A^* = e_B^* = e_C^* = 0$, $e_{AA}^* = 1.3$, $e_{BB}^* = 0$, $e_{CC}^* = 0.8$, all other interatomic potentials were zero. Concentrations were $c_A = 0.48$, $c_B = 0.5$, $c_C = 0.02$, $c_V = 0.003$ [380].

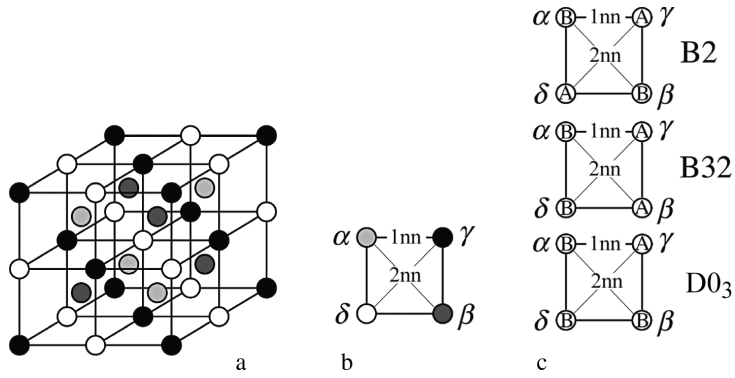

Figure 23.6 (**a**) Standard cubic supercell showing four fcc sublattices with different shadings. (**b**) Two-dimensional representation of sublattices, showing 1nn and 2nn relations (e.g., $\alpha-\gamma$ are 1nn, but $\alpha-\beta$ are 2nn). (**c**) Sublattice occupancies for B2, B32, and $D0_3$ ordered structures.

an equiatomic alloy is constructed by placing A-atoms on the black and dark gray sites (γ and β) and B-atoms at white and light gray sites (α and δ). The B32 structure has 1nn atoms with equal numbers of like and unlike species (i.e. no chemical preference), whereas all 2nn atoms are the opposite species. The $D0_3$ structure for an AB_3 composition is constructed by placing A-atoms on one of the three sublattices, γ for example, and the B-atoms on the other three. The minority A-atoms in the $D0_3$ structure have all 1nn and 2nn atoms of opposite species, but the majority B-atoms have a mixed 1nn environment, and B-atoms on 2nn sites. (Incidentally, the four sublattices in Fig. 23.6 are equivalent, and examination of the black γ-sublattice shows them to be fcc unit cells.)

Alloys that form the B2 structure often form the $D0_3$ structure at other compositions and temperatures, since both structures are compatible with 1nn interactions that favor opposite species, and 2nn interactions that favor like species. The B32 structure requires the opposite type of interatomic interactions, so the B32 structure does not appear on phase diagrams

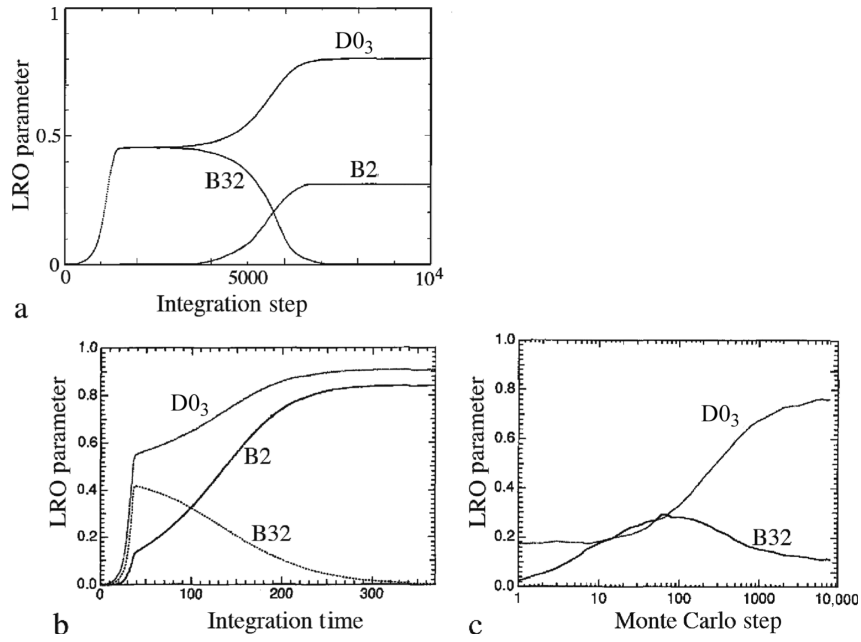

Figure 23.7 Time dependence of the B2, $D0_3$, and B32 order parameters for ordering on four sublattices of a binary AB_3 bcc lattice that develops $D0_3$ order in equilibrium. (**a**) Results from the point approximation. The 1nn and 2nn interatomic interactions were $e_{AA1} = e_{AA2} = 1.60\, k_B T$, corresponding to approximately 2/3 of the critical temperature for $D0_3$ ordering. (**b**) Results from the pair approximation, using the same interaction parameters as for panel a. (**c**) Results from Monte Carlo simulation, using $e_{AA1} = e_{BB1} = 1.00\, k_B T$, $e_{AA2} = 2.00\, k_B T$. All other pair and interaction energies were zero [388].

with the B2 and $D0_3$ structures.[11] Nevertheless, it is sometimes possible for the B32 phase to appear as a transient state on the way towards equilibrium [386, 387], as shown in Fig. 23.7. The 1nn interactions favor bonds between unlike atoms, so the kinetic path must eventually lead away from the transient B32 structure, and towards an equilibrium state with B2 and $D0_3$ order. The free energy decreases continuously during the evolution of the alloy of Fig. 23.7, and in doing so the degree of B32 order rises and then falls. As discussed in Section 23.5.3, the B32 structure is not a metastable state as usually defined because it does not provide a local minimum in free energy.

The formation of transient B32 order occurs because there are more variants of this structure than B2. Figure 23.6b aids the identification of four possible configurations for A-atoms in a B32 structure ($\alpha + \gamma, \gamma + \beta, \beta + \delta, \delta + \alpha$), but only two for B2 ($\alpha + \beta, \gamma + \delta$). The greater number of local atom configurations consistent with B32 order allow for more possibilities of forming B32 order than B2. Assuming the B32 state of order is more favorable than the initial solid solution, kinetic expediency provides a more rapid decrease in free energy by initially forming B32 instead of B2 order (as suggested by Fig. 23.1).

[11] An exception could occur if the chemical interactions changed dramatically with temperature, pressure, or composition.

The duration and robustness of transient states are not easy to estimate because they depend on several factors. Figures 23.7a and 23.7b show that the B32 state is more robust in the point approximation than the pair. This is in part related to the additional degrees of freedom for structural relaxation in the pair approximation, but also to initial conditions. If the initial conditions for LRO have no bias of A-atom occupancy on one of the sublattices, the kinetic master equation will have a detailed balance of rates of A-atom flux on and off both the α- and β-sublattices, so the LRO cannot evolve. With some initial bias, an incubation time for the evolution of LRO is observed. Larger cluster variables do not solve this problem, however, because the formation of LRO still requires a breaking of symmetry as sublattice formation occurs. Such incubation periods are also found in kinetic Monte Carlo simulations, as shown in Fig. 23.7c. The tendency to form a transient B32 structure also depends, of course, on the relative stability of the B32 and B2 structures – the transient state is more robust if the alloy is not too far from the B2/B32 phase boundary.

23.5.3 Timescales and Symmetry Breaking

An advantage of statistical kinetic theories is that they allow mapping of the kinetic path onto a corresponding free energy surface. For the case of Fig. 23.8a, this makes it possible to see why the difference in activation energy, $e^*_{\mathrm{A}} \neq e^*_{\mathrm{B}}$, can alter the kinetic path so easily when LRO is evolving because this part of the kinetic path lies in a broad minimum of the free energy surface in Fig. 23.8b. It is also clear that there is rapid variation of the free energy with SRO, whereas large changes in LRO have weaker effects on reducing the free energy.

The formation of a sublattice, which involves longer-range atom repositionings, is a relatively slow process. Although the vacancy mechanism still provides the kinetic steps, the later stages of an ordering transformation involve a different phenomenon of the growth of antiphase domains (Section 17.4). The statistical kinetics approach as developed here predicts three timescales [382]. The first is the equilibration of vacancies, which respond quickly to any change in atom configurations. The second longest timescale is

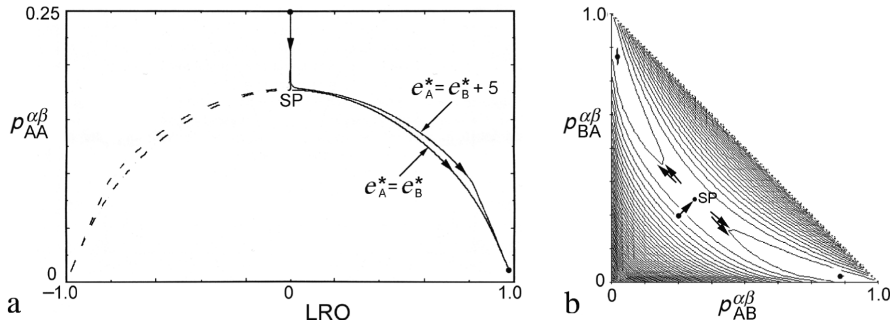

Figure 23.8 (**a**) Kinetic paths for $V = 0.3$, $U = 1$, $e_{AA} = 0.3$ for the two cases $e^*_A = e^*_B + 5$ and $e^*_A = e^*_B$. (**b**) Free energy surface showing initial and final states of panel a. Here LRO $= (p^{\alpha\beta}_{AB} - p^{\alpha\beta}_{BA})/4$.

for SRO evolution, and the slowest timescale is that for LRO. The rates of SRO and LRO scale with the number of vacancies.

In theories of kinetic evolution with multiple state variables, a free energy surface may show considerable structure beyond a simple thermodynamic minimum. The existence of local minima is widely known, and these are termed "metastable states." Less appreciated are saddle points, which become increasingly common in functions with more independent variables.[12] A saddle point in a free energy surface is marked "SP" in both Figs. 23.8a and 23.8b. The breaking of symmetry caused by atom preferences for α- or β-sublattices is a slow process because it occurs near a saddle point of the free energy surface where there are no gradients. A kinetic arrest often occurs at such points, and this is confirmed with Monte Carlo simulations [388]. Monte Carlo simulations show reconfigurations of the domain structure until one sublattice dominates across the crystal. Such states at saddle points can be termed "pseudostable" [389]. They are an example of kinetic processes where the initial breaking of symmetry is driven only weakly by the free energy.

Finally, consider the case when many state variables describe an alloy, such as may occur with multiple species, sublattices, or ranges of order parameters. If the free energy surface in these multiple dimensions has many local minima, we expect even more saddle points in the free energy function (cf. Section 12.6). Especially when a saddle point breaks symmetry, such as required to define sublattices, it may be responsible for an anomalous kinetic arrest.

Problems

23.1 The Metropolis algorithm is often used as the basis for Monte Carlo simulations of kinetic processes. In this algorithm, a transition from state 1 to state 2 will depend on the energy difference between the two states, $\Delta E = E_2 - E_1$, as:

when $\Delta E < 0$ the transition certainly occurs;
when $\Delta E > 0$ the transition occurs with a probability $p = \exp\left(-\frac{\Delta E}{k_B T}\right)$.

(**a**) Using the kinetic master equation, prove this algorithm leads to thermodynamic equilibrium between states 1 and 2.

(**b**) Suppose state 2 is an intermediate state between states 1 and 3. Show that the Metropolis algorithm involving states 2 and 3 (plus that for states 1 and 2 above) leads to thermodynamic equilibrium between states 1 and 3.

(**c**) Now consider the case of equilibrium between two states 1 and 2 when there is a fraction, f, of ballistic jumps, where $0 < f < 1$. These ballistic jumps do not depend on ΔE or direction. What is the equilibrium (not thermodynamic equilibrium) ratio of states 1 and 2 in the presence of these ballistic jumps at temperature T? Explain why your result makes sense in the limits when $f = 0$ and $f = 1$.

[12] At points on the free energy surface where the slope is zero, nonzero curvatures for all state variables are expected. A minimum or a maximum exists only if the curvatures are all positive or all negative. All other points of zero slope have curvatures of mixed sign, and are saddle points.

23.2 The matrix elements in Eq. 23.4 that are off the diagonal by one, $W_{n,n+1}$ and $W_{n+1,n}$, are labeled in Fig. 1.9b. For diffusion, they were shown to be $\delta/2$ or $\Gamma\,\Delta t/2$. The total flux, j, to the right across the boundary is the difference: (right flux) − (left flux).

(**a**) In the time Δt, give an expression for the net number of atoms moving across the boundary.

(**b**) A more practical flux has units of atoms/(cm^2 s), requiring c in units of atoms/cm^3 as in Eq. 23.11. From the result of part a, derive Fick's first law with these units of c.

23.3 Suppose that vacancies and interstitials are both created at a rate Γ_c during electron irradiation. The vacancies and interstitials recombine at a rate $\Gamma_r = \beta\, c_i\, c_v$, where c_i and c_v are the fractional concentrations of interstitials and vacancies, respectively, and β is a constant.

(**a**) What is the steady-state vacancy concentration in the material?

(**b**) How is this steady-state solution changed if vacancies diffuse out of the surface of the specimen at the rate $\Gamma_d = D\,l^{-2}$ (where l is a fixed distance and D is a diffusivity)?

23.4 Consider the kinetics of B2 ordering of a ternary alloy, where the atoms A and C have identical chemical preferences to segregate to the α-sublattice when this sublattice is enriched in A or C. For simplicity, assume the B-atoms have no chemical preferences, so are pushed onto the β-sublattice by default. Suppose the A-atoms are more mobile than the B- and C-atoms, with a lower activation barrier $e^*_A < e^*_C = e^*_B$.

Discuss the relative sublattice segregation rates of the C-atoms and the B-atoms with increasing difference between e^*_A and $e^*_C = e^*_B$. Do so by identifying the magnitudes of the terms in these rate equations, and discuss the evolution of p^α_V.

$$\frac{dp^\alpha_A}{dt} = +\Gamma p^\beta_A p^\alpha_V e^{+\Delta/k_BT} e^{+\Delta^*/k_BT} - \Gamma p^\alpha_A p^\beta_V e^{-\Delta/k_BT} e^{+\Delta^*/k_BT}, \tag{23.46}$$

$$\frac{dp^\alpha_B}{dt} = +\Gamma p^\beta_B p^\alpha_V - \Gamma p^\alpha_B p^\beta_V, \tag{23.47}$$

$$\frac{dp^\alpha_C}{dt} = +\Gamma p^\beta_C p^\alpha_V e^{+\Delta/k_BT} - \Gamma p^\alpha_C p^\beta_V e^{-\Delta/k_BT}, \tag{23.48}$$

$$\frac{dp^\alpha_V}{dt} = -\frac{dp^\alpha_A}{dt} - \frac{dp^\alpha_B}{dt} - \frac{dp^\alpha_C}{dt}, \tag{23.49}$$

where Δ is the chemical preference for the A- and C-atoms, including the sublattice segregation, Δ^* is the effect of the lower activation barrier for the A–V interchange, and Γ is a constant factor. You do not need to actually solve these coupled equations to explain the physical effects.

23.5 Suppose an ordered domain structure evolves into the shape of the Schwarz P-surface, the periodic minimal surface of Fig. 17.6. Is this state metastable or pseudostable? Why or why not?

24 Elastic Energy of Solid Precipitates

Section 6.8 gave an introduction to the elastic energy that is generated in a solid material when an internal region transforms into a new phase of different size or shape. Both the new particle and the surrounding matrix are distorted, and the positive elastic energy tends to suppress the phase change. Elastic energy can be large, and usually influences the thermodynamics, nucleation, growth, and morphology of solid–solid phase transformations, especially at low temperatures. Section 19.2.3 explained how the selection of a habit plane for a martensite plate is so dominated by the elastic energy that the problem is reduced to a set of geometrical conditions to accommodate the transformation strain. Detailed calculations of the elastic energy are difficult, however, and analytical results are not practical in most cases when the elastic constants of the new precipitate differ from those of the matrix. Even with the assumption that the elastic constants are equal for both phases, the solid mechanics of optimizing the shape of the precipitate for minimum elastic energy is an advanced topic. Crystallographic anisotropy is essential for understanding the orientation relationship between precipitate and matrix, and proper tensorial analysis is required for calculating the elastic energy.

Chapter 24 describes some of the methods for calculating the elastic energy of solid–solid phase transformations. A first approach finds a condition on the elastic field in real space that can guide the search for the minimum elastic energy. A distortion within a local volume at $\vec{r}$ generates strain at $\vec{r}'$. The response can be described by the convolution of a Green's function of elasticity with the structure of the distortion at the precipitate.[1] A convolution in real space becomes a multiplication in k-space. There is an advantage to transforming the problem to k-space, where a shape factor for the precipitate is multiplied by a response function $B(\hat{k})$. This k-space formulation by Khachaturyan [267] has proved valuable for computer simulations of solid–solid phase transformations, and with linear kinetic coefficients it has also been used to predict the kinetics of phase transformations [390–392]. The present chapter presents the basic tools used for these calculations, and comments on the tendency for precipitates to form as flat plates of specific orientations.

24.1 Transformation Strains and Elastic Energy

An important reference state for a solid-state phase transformation is the "stress-free strain." This strain ϵ_{ij}^{0} is defined in the same way as strains in Section 6.7.1 in terms of

[1] The elastic Green's function $G_{ij}(\vec{r} - \vec{r}')$ is a tensorial quantity that gives the displacement at the point $\vec{r}'$ in the direction j caused by a unit force at $\vec{r}$ in the direction i.

the Cartesian spatial derivatives of the displacement vector field $\vec{u}(\vec{r})$. The stress-free strain ϵ_{ij}^0 describes the shape change for the new phase in free space, where the transformation occurs free of any elastic stresses caused by its misfit in the surrounding parent phase. For a cubic-to-cubic transformation, which is an isotropic, homogeneous expansion, the stress-free strains would be tensile strains, and would be the fractional change of the lattice parameter after the transformation. There is no elastic energy within a precipitate if it undergoes a stress-free strain of ϵ_{ij}^0. The problem is more complicated when a particle transforms within a surrounding matrix.

In the very special case where the precipitate phase is infinitely stiff, we can use the ϵ_{ij}^0 to calculate an elastic energy because all of the elastic energy is in the surrounding parent material, and none in the inflexible precipitate. (Shear strains in the matrix around a misfitting sphere were discussed in Section 6.8.) In general, however, we expect the precipitate and the matrix to have similar elastic constants C_{ijlm}. In fact, for all of what follows, we will assume that the C_{ijlm} are the same everywhere.

The transformed particle cannot achieve its stress-free strain because it is compressed by the matrix. There is now elastic energy in the new precipitate, but less in the surrounding matrix. The system of precipitate and matrix develops strain fields to minimize the total elastic energy, and with an extra degree of freedom to apportion the elastic energy between precipitate and matrix, the total elastic energy is less than that for a precipitate expanding with its full stress-free strain. The elastic energy is quadratic in the strains, so spreading the displacement field $\vec{u}(\vec{r})$ allows a lower energy. (This argument was given previously in Section 6.8.)

The total elastic energy in the material, consistent with Hooke's law, has the quadratic form of Eq. 6.123

$$E_{\text{el}} = \frac{1}{2} \int \sum_{i,j} \sum_{l,m} \left[C_{ijlm}\, \epsilon_{ij}(\vec{r})\, \epsilon_{lm}(\vec{r}) \right] \mathrm{d}V, \tag{24.1}$$

$$E_{\text{el}} = \frac{1}{2} \int \left[C_{ijlm}\, \epsilon_{ij}(\vec{r})\, \epsilon_{lm}(\vec{r}) \right] \mathrm{d}V. \tag{24.2}$$

where Eq. 24.2 (and all of what follows) switched to the Einstein convention, meaning that there is a sum over any index that appears twice in any product.

The challenge is to find the strains $\epsilon_{ij}(\vec{r})$ that minimize E_{el}. It proves convenient to rewrite the strains in the entire material as

$$\epsilon_{ij}(\vec{r}) = \overline{\epsilon}_{ij} + \delta\epsilon_{ij}(\vec{r}) - \theta(\vec{r})\epsilon_{ij}^0. \tag{24.3}$$

In the first two terms, the strain was separated into a homogeneous average part $\overline{\epsilon}_{ij}$, and a part with spatial variation $\delta\epsilon_{ij}(\vec{r})$. It turns out that the homogeneous part is determined primarily by boundary conditions and forces applied to the outside of the entire material. We show below that with stress-free surfaces, when the elastic energy of the transformation is minimized it is possible to have phase transformations in a material for which $\overline{\epsilon}_{ij}$ is unchanged after the transformation, so $\overline{\epsilon}_{ij}$ may be neglected.[2]

[2] Calculating the effects of applied stress on the phase transformation requires the consideration of $\overline{\epsilon}_{ij}$, of course.

The third term in Eq. 24.3 contains the function $\theta(\vec{r})$, which is much like a Heaviside function. This $\theta(\vec{r})$ defines the shape of the transformed particle – it is 1 inside the transformed particle, and 0 in the untransformed matrix. Suppose $\theta(\vec{r}) = 1$, so $\vec{r}$ is inside the transformed particle. If the strain at this $\vec{r}$ inside the particle is the stress-free strain, i.e., $\overline{\epsilon}_{ij} + \delta\epsilon_{ij}(\vec{r}) = \epsilon^0_{ij}$, the elastic strain is zero in Eq. 24.3, giving zero elastic energy density. For local regions inside and outside the particle, the $\theta(\vec{r})$ allows different reference strains for zero elastic energy.

Substituting Eq. 24.3 in 24.2, and neglecting the homogeneous strain, the change in elastic energy after forming the precipitate particle is

$$\Delta E_{\text{el}} = \frac{1}{2}\int C_{ijlm}\left[\delta\epsilon_{ij}(\vec{r}) - \theta(\vec{r})\epsilon^0_{ij}\right]\left[\delta\epsilon_{lm}(\vec{r}) - \theta(\vec{r})\epsilon^0_{lm}\right]\mathrm{d}V, \tag{24.4}$$

$$\begin{aligned}\Delta E_{\text{el}} = {} & \frac{V_{\text{p}}}{2}C_{ijlm}\epsilon^0_{ij}\epsilon^0_{lm} \\ & + \frac{1}{2}\int C_{ijlm}\Big[-\delta\epsilon_{ij}(\vec{r})\theta(\vec{r})\epsilon^0_{lm} - \delta\epsilon_{lm}(\vec{r})\theta(\vec{r})\epsilon^0_{ij} + \delta\epsilon_{ij}(\vec{r})\delta\epsilon_{lm}(\vec{r})\Big]\mathrm{d}V,\end{aligned} \tag{24.5}$$

$$\begin{aligned}\Delta E_{\text{el}} = {} & \frac{V_{\text{p}}}{2}C_{ijlm}\epsilon^0_{ij}\epsilon^0_{lm} \\ & + \int C_{ijlm}\Big[-\delta\epsilon_{ij}(\vec{r})\theta(\vec{r})\epsilon^0_{lm} + \frac{1}{2}\delta\epsilon_{ij}(\vec{r})\delta\epsilon_{lm}(\vec{r})\Big]\mathrm{d}V\,,\end{aligned} \tag{24.6}$$

$$\begin{aligned}\Delta E_{\text{el}} = {} & \frac{V_{\text{p}}}{2}\,C_{ijlm}\,\epsilon^0_{ij}\,\epsilon^0_{lm} \\ & + \int\Big[-\sigma^0_{ij}\,\delta\epsilon_{ij}(\vec{r})\,\theta(\vec{r}) + \frac{1}{2}C_{ijlm}\,\delta\epsilon_{ij}(\vec{r})\,\delta\epsilon_{lm}(\vec{r})\Big]\mathrm{d}V\,,\end{aligned} \tag{24.7}$$

where V_{p} was defined as the volume of the precipitate,[3] the relationship $C_{ijlm} = C_{lmij}$ was used, and the definition was made

$$\sigma^0_{ij} \equiv C_{ijlm}\,\epsilon^0_{lm}. \tag{24.8}$$

While Eq. 24.7 is a central result for the elastic energy of precipitation, minimizing this ΔE_{el} remains a challenge. Two approaches for finding the minimum elastic energy are sketched below. The first continues in real space, and uses arguments of mechanical equilibrium to minimize the elastic energy. The second approach transforms the problem to k-space. One advantage of k-space is that the elastic fields are long range, and Fourier analysis naturally spans the full dimension of the material.

24.2 Real Space Approach

The elastic energy ΔE_{el} of precipitation, Eq. 24.7, is a functional of the strain fields, so it may be reasonable to apply the machinery of calculus of variations as in Section 16.3.1,

[3] $V_{\text{p}} = \int \theta(\vec{r})\,\mathrm{d}V$.

with the Euler equation 16.31 to find the stationary value of δE_{el}. However, Eq. 24.7 is not yet in the proper form for this direct approach. It needs to be expressed in terms of a displacement field, so we could solve for the displacement field that gives a stationary δE_{el}. Nevertheless, we take a similar approach, and seek the conditions for which ΔE_{el} is stationary with respect to small changes in the inhomogeneous strain field. This condition is

$$\delta E_{\text{el}} = 0. \tag{24.9}$$

In brief, we substitute the variations in the displacement fields for the variations in the strains as

$$\delta\epsilon_{ij} = \frac{1}{2}\left(\frac{\partial \delta u_i}{\partial x_j} + \frac{\partial \delta u_j}{\partial x_i}\right), \tag{24.10}$$

to rewrite Eq. 24.7, noting how the sum of two terms in Eq. 24.10 fits into the sum of indices in Eq. 24.7

$$\delta E_{\text{el}} = \int \Big[-\sigma^0_{ij}\,\theta(\vec{r})\frac{\partial \delta u_i}{\partial x_j} + \frac{1}{2}C_{ijlm}\frac{\partial \delta u_i}{\partial x_j}\frac{\partial \delta u_l}{\partial x_m}\Big]\mathrm{d}V. \tag{24.11}$$

The contribution from the stress-free strains (first term in Eq. 24.7) was neglected because it does not depend on variations in the inhomogeneous strain field.

Each different δu_i is a field in x, y, and z. Multiplying these scalar fields with the Cartesian unit vectors, Eq. 24.11 contains sums with the form of a divergence

$$\vec{\nabla}\cdot\vec{\delta u_i} = \frac{\partial \delta u_i}{\partial x_1} + \frac{\partial \delta u_i}{\partial x_2} + \frac{\partial \delta u_i}{\partial x_3}, \tag{24.12}$$

allowing us to rewrite Eq. 24.11 as

$$\delta E_{\text{el}} = \int \left[-\sigma^0_{ij}\,\theta(\vec{r}) + C_{ijlm}\frac{\partial \delta u_l}{\partial x_m}\right]\vec{\nabla}\cdot\vec{\delta u_i}\,\mathrm{d}V. \tag{24.13}$$

Two more steps are needed to obtain a key relationship between local strains and the shape of the precipitate. The first step uses the product rule, i.e.

$$\frac{\mathrm{d}}{\mathrm{d}x}(UV) = V\frac{\mathrm{d}U}{\mathrm{d}x} + U\frac{\mathrm{d}V}{\mathrm{d}x}, \tag{24.14}$$

$$U\frac{\mathrm{d}V}{\mathrm{d}x} = \frac{\mathrm{d}}{\mathrm{d}x}(UV) - V\frac{\mathrm{d}U}{\mathrm{d}x}, \tag{24.15}$$

but in a comparable form for a product of a scalar field U and a vector field $\vec{V}$. This involves divergences and gradients[4] as

$$U\,\vec{\nabla}\cdot\vec{V} = \vec{\nabla}\cdot(U\vec{V}) - \vec{V}\cdot\overrightarrow{\nabla U}. \tag{24.16}$$

[4] Notation for the gradient of $f(\vec{r})$ is either $\mathbf{grad}\big(f(\vec{r})\big)$ or $\overrightarrow{\nabla f}(\vec{r})$, which are equal.

Using the form of Eq. 24.16 with the integrand of Eq. 24.13,

$$\Big[-\sigma^0_{ij}\,\theta(\vec{r}) + C_{ijlm}\frac{\partial \delta u_l}{\partial x_m}\Big]\vec{\nabla}\cdot\vec{\delta u}_i$$
$$= \vec{\nabla}\cdot\Big(\Big[-\sigma^0_{ij}\,\theta(\vec{r}) + C_{ijlm}\frac{\partial \delta u_l}{\partial x_m}\Big]\vec{\delta u}_i\Big)$$
$$- \vec{\delta u}_i\cdot\mathbf{grad}\Big(\sigma^0_{ij}\,\theta(\vec{r}) + C_{ijlm}\frac{\partial \delta u_l}{\partial x_m}\Big). \tag{24.17}$$

The second step will show that the integral of the first term on the RHS of Eq. 24.17 is zero. Recall that Gauss's theorem states the divergence of $\vec{\delta u}_i$ in a volume equals the flux of $\vec{\delta u}_i$ through the bounding surface $\vec{S}$, allowing us to transform the volume integral of this term in Eq. 24.17 to a surface integral

$$\int \vec{\nabla}\cdot\Big(\Big[-\sigma^0_{ij}\,\theta(\vec{r}) + C_{ijlm}\frac{\partial \delta u_l}{\partial x_m}\Big]\vec{\delta u}_i\Big)\mathrm{d}V$$
$$= \oint_{\mathrm{surf}}\Big(-\sigma^0_{ij}\,\theta(\vec{r}) + C_{ijlm}\frac{\partial \delta u_l}{\partial x_m}\Big)\vec{\delta u}_i\cdot\mathrm{d}\vec{S}\,, \tag{24.18}$$
$$= 0\,. \tag{24.19}$$

This integral is zero because the displacement variation $\vec{\delta u}_i(\vec{r}_{\mathrm{surf}})$ is negligible on the surface of the bulk material for a small precipitate in a large matrix, and the surface-to-volume ratio becomes small for a large matrix. Rearranging slightly the remaining second term on the right of Eq. 24.17 (**grad** is distributive, and scalar products commute), and using it in Eq. 24.13

$$\delta E_{\mathrm{el}} = \int \Big(\sigma^0_{ij}\overrightarrow{\nabla\theta}(\vec{r}) - C_{ijlm}\overrightarrow{\nabla\epsilon}_{lm}\Big)\cdot\vec{\delta u}_i\,\mathrm{d}V. \tag{24.20}$$

Our goal is to find the minimum of ΔE_{el}. This elastic energy is assumed a smooth function of the displacement field caused by the precipitate, so at its minimum, ΔE_{el} will be stationary against small variations in the displacement field. That is, variations in the displacement field $\vec{\delta u}_i$ of inhomogeneous strains, $\delta\epsilon_{ij}(\vec{r})$, will not alter ΔE_{el}. Therefore $\delta E_{\mathrm{el}} = 0$ as in Eq. 24.9, and Eq 24.20 can be set equal to zero for this condition of stationarity. The variation of $\vec{\delta u}_i$ is arbitrary, so it can change its value with location to favor different values of the factor in parentheses.[5] To ensure that the integral is zero, the integrand must be zero. We obtain the equation for real space elasticity theory, equivalent to Cauchy's first law (obtained from the condition of mechanical equilibrium)

$$\sigma^0_{ij}\overrightarrow{\nabla\theta}(\vec{r}) - C_{ijlm}\overrightarrow{\nabla\epsilon}_{lm} = 0. \tag{24.21}$$

Using the definition of Eq. 24.8

$$\epsilon^0_{lm}\overrightarrow{\nabla\theta}(\vec{r}) = \overrightarrow{\nabla\epsilon}_{lm}. \tag{24.22}$$

It is rarely easy to use Eq. 24.21 for the strain gradient to find the strain field around a precipitate. We can, however, understand a general aspect of how the strain field is related

[5] This is essentially the same condition as from Eq. 16.30 for a scalar product.

to the shape of the precipitate $\theta(\vec{r})$. From Eq. 24.22, discontinuities in the precipitate shape cause gradients in strain. The way to minimize the resulting energy is to maximize the volume where $\overrightarrow{\nabla\theta}$ is oriented along directions for which the stress-free strain ϵ^0_{lm} is small.

A precipitate will seek maximum surface with minimum stress-free strain.

As mentioned earlier in Sections 6.8.5 and 15.4, a plate-shaped precipitate often minimizes the energy from transformation strains. For example, if ϵ^0_{lm} specifies a tetragonal distortion of one crystallographic dimension, the axis of tetragonality tends to be perpendicular to the plate of the precipitate. Other dimensions of the precipitate are of course required to give it a finite volume, and a proper shape optimization requires further analysis. A thin edge of the plate gives a smaller contribution to the LHS of Eq. 24.22, so making a precipitate into the shape of a lens (lenticular shape) may be an effective design to minimize ΔE_{el}.

It is often necessary to also consider the energy of the surface between a precipitate and matrix. Especially when the surface energy is anisotropic, it is not easy to calculate the shape of a precipitate that minimizes the sum of elastic energy plus surface energy. Computational approaches are appropriate for these complex optimizations.

24.3 *k*-Space Approach

This section recasts the problem of elastic energy of precipitation into *k*-space, following the classic approach of Khachaturyan [267].

24.3.1 Transformation to *k*-Space

As a preliminary, we first derive a convenient form for the Fourier transform of a derivative quantity (Eq. 24.29 below). We use the equivalent of Eq. 24.14 for a 3D scalar field

$$\mathbf{grad}\Big(UV\Big) = V\,\mathbf{grad}\Big(U\Big) + U\,\mathbf{grad}\Big(V\Big). \tag{24.23}$$

For the gradient of the product of the two scalar fields $f(\vec{r})$ and $\mathrm{e}^{-\mathrm{i}\vec{k}\cdot\vec{r}}$

$$\mathbf{grad}\Big(f(\vec{r})\,\mathrm{e}^{-\mathrm{i}\vec{k}\cdot\vec{r}}\Big) = \mathrm{e}^{-\mathrm{i}\vec{k}\cdot\vec{r}}\mathbf{grad}\Big(f(\vec{r})\Big) + f(\vec{r})\,\mathbf{grad}\Big(\mathrm{e}^{-\mathrm{i}\vec{k}\cdot\vec{r}}\Big). \tag{24.24}$$

This allows us to rearrange a Fourier transform as

$$\int \mathrm{e}^{-\mathrm{i}\vec{k}\cdot\vec{r}}\mathbf{grad}\Big(f(\vec{r})\Big)\,\mathrm{d}V = \int \mathbf{grad}\Big(f(\vec{r})\,\mathrm{e}^{-\mathrm{i}\vec{k}\cdot\vec{r}}\Big)\,\mathrm{d}V - \int f(\vec{r})\,\mathbf{grad}\Big(\mathrm{e}^{-\mathrm{i}\vec{k}\cdot\vec{r}}\Big)\,\mathrm{d}V. \tag{24.25}$$

Another relationship, essentially Gauss's theorem,[6] allows the simplification

$$\int \mathbf{grad}\left(f(\vec{r})\,\mathrm{e}^{-\mathrm{i}\vec{k}\cdot\vec{r}}\right)\mathrm{d}V = \oint \left(f(\vec{r})\,\mathrm{e}^{-\mathrm{i}\vec{k}\cdot\vec{r}}\right)\mathrm{d}S, \tag{24.26}$$

$$\int \mathbf{grad}\left(f(\vec{r})\,\mathrm{e}^{-\mathrm{i}\vec{k}\cdot\vec{r}}\right)\mathrm{d}V = 0, \tag{24.27}$$

assuming the integrand vanishes appropriately on the surface of a very large volume of material. Finally, note that

$$\mathbf{grad}\left(\mathrm{e}^{-\mathrm{i}\vec{k}\cdot\vec{r}}\right) = -\mathrm{i}\vec{k}\,\mathrm{e}^{-\mathrm{i}\vec{k}\cdot\vec{r}}. \tag{24.28}$$

Equations 24.27 and 24.28 allow us to rewrite Eq. 24.25 as

$$\int \mathrm{e}^{-\mathrm{i}\vec{k}\cdot\vec{r}}\mathbf{grad}\left(f(\vec{r})\right)\mathrm{d}V = +\mathrm{i}\vec{k}\,\tilde{f}(\vec{k}), \tag{24.29}$$

where $\tilde{f}(\vec{k})$ is the Fourier transform of $f(\vec{r})$

$$\tilde{f}(\vec{k}) \equiv \int \mathrm{e}^{-\mathrm{i}\vec{k}\cdot\vec{r}} f(\vec{r})\,\mathrm{d}V. \tag{24.30}$$

Equation 24.29 states that the Fourier transform of a field gradient is simply $+\mathrm{i}\vec{k}$ times the Fourier transform of the field.

Using this transformation of Eq. 24.29, the real space result Eq. 24.21 is brought into a simpler form in k-space (bringing a factor $-\vec{k}_j\vec{k}_l$ from $\mathbf{grad}(\epsilon_{ij})$)

$$\left(C_{ijlm}\vec{k}_j\vec{k}_l\right)\tilde{u}_m(\vec{k}) = -\mathrm{i}\sigma^0_{ij}\vec{k}_j\,\tilde{\theta}(\vec{k}), \tag{24.31}$$

$$D_{im}(\vec{k})\,\tilde{u}_m(\vec{k}) = -\mathrm{i}\sigma^0_{ij}\vec{k}_j\,\tilde{\theta}(\vec{k}), \tag{24.32}$$

where the tilde designates Fourier transformation as in Eq. 24.30, and the dynamical matrix is defined as

$$D_{im}(\vec{k}) \equiv C_{ijlm}\vec{k}_j\vec{k}_l. \tag{24.33}$$

Equation 24.32 works with products of Fourier-transformed quantities, whereas the real space formulation of Eq. 24.21 works with their gradients. For computational work, products are often more convenient.

Box 24.1 Sound Waves

As an aside, we point out that this dynamical matrix of Eq. 24.33 is the same as that of Eq. 26.14, which is derived from the interatomic forces. The interatomic forces are, of course, the origin of the elastic constants of the crystal, but it is beyond the present scope to show the detailed relationship between the interatomic forces and the elastic constants.[7] Nevertheless, if the form of Eq. 26.12 is used for $u(\vec{k})$, i.e., a traveling wave of wavevector $\vec{k}_j$ and angular frequency ω_j,

[6] Obtained, for example, by assuming a small $f(\vec{r})$ at the center of a large bounding sphere.
[7] These relationships depend on the crystal structure, for example.

$$\vec{u}_j(\vec{k},t) = \vec{u}_{0j}\, e^{i(\vec{k}_j\cdot\vec{r}_l-\omega_j t)}\,, \tag{24.34}$$

and using Newton's law to relate the restoring force to the acceleration, we can obtain

$$D_{im}(\vec{k})\,\vec{u}_j(\vec{k},t) = \rho\,\omega_j^2\,\vec{u}_j(\vec{k},t), \tag{24.35}$$

where ρ is density. Solving this eigenvalue equation gives dispersion relationships between ω_j and $\vec{k}_j$, i.e., $\omega_j(\vec{k}_j)$. The slopes $d\omega_j/dk_j$ are the sound velocities of longitudinal and transverse acoustic waves along the direction $\hat{k}_j$.

24.3.2 Precipitate Shapes in k-Space

At a higher level of abstraction, we can define a function of the precipitate shape to calculate the elastic energy. This function, $B(\hat{k})$, depends only on direction. It depends on the dynamical matrix and elastic constants through a number of relationships that are not proved here (see [267]), but are collected here:

$$D_{im}(\vec{k}) = C_{ijlm}\vec{k}_j\vec{k}_l, \tag{24.36}$$

$$G_{im}(\vec{k})\,D_{im}(\vec{k}) = \mathbf{I}, \tag{24.37}$$

$$\Omega_{ij}(\hat{k}) = k^2\,G_{ij}(\vec{k}), \tag{24.38}$$

where $\mathbf{I}$ is the identity matrix. This function, $B(\hat{k})$, is

$$B(\hat{k}) \equiv C_{ijlm}\,\epsilon^0_{ij}\epsilon^0_{lm} - \hat{k}_i\sigma^0_{ij}\Omega_{jl}(\hat{k})\sigma^0_{lm}\hat{k}_m. \tag{24.39}$$

The elastic energy can be shown to be

$$E_{\rm el} = \frac{1}{(2\pi)^3}\int B(\hat{k})\,|\tilde{\theta}(\vec{k})|^2\,d^3k, \tag{24.40}$$

where $||^2$ denotes the function times its complex conjugate. The interested reader should consult [267] for the derivations of these relationships, but some of their features are noteworthy. First, the shape of the particle is separated from the elastic response. This is the big advantage of the k-space formulation. The function $G_{im}(\vec{k})$ is the Fourier transform of a real-space Green's function (which gave the elastic response at a distance from a point in the precipitate). In real space the Green's function would be convoluted with the precipitate shape, but in k-space these functions appear as a product.[8] The $\sigma^0_{ij} = C_{ijlm}\epsilon^0_{lm}$ of Eq. 24.8 is the stress-free strain that contains a crystallographic relationship between the precipitate and the matrix. The elastic properties of the material are in σ^0_{ij} and $\Omega_{jl}(\hat{k})$ in Eq. 24.39, and note again that $B(\hat{k})$ is a function only of direction.

The function $|\tilde{\theta}(\vec{k})|^2$ is the same as a shape factor intensity of a small crystal, used in diffraction studies of materials. For example, for a rectangular parallelopipedon of a crystal

[8] The "convolution theorem" states that the convolution of two functions in real space is equivalent to the product of their Fourier transforms in k-space. That is, the convolution $h(x) = \int f(x-x')\,g(x')\,dx'$ has a Fourier transform $\tilde{h}(k) = \int h(x)\,e^{-ikx}\,dk/(2\pi)$ equal to the product of the Fourier transforms: $\tilde{h}(k) = \tilde{f}(k)\,\tilde{g}(k)$.

with lattice parameters $\{a_x, a_y, a_z\}$ and $\{N_x, N_y, N_z\}$ unit cells along the Cartesian directions, the result is [85]

$$|\tilde{\theta}(\vec{k})|^2 = \frac{\sin^2(\pi N_x k_x a_x)}{\sin^2(\pi k_x a_x)} \frac{\sin^2(\pi N_y k_y a_y)}{\sin^2(\pi k_y a_y)} \frac{\sin^2(\pi N_z k_z a_z)}{\sin^2(\pi k_z a_z)}, \tag{24.41}$$

where $\vec{k} = k_x\hat{x} + k_y\hat{y} + k_z\hat{z}$.

Suppose a precipitate particle were a flat plate, and for simplicity choose the thin direction to be along $\hat{z}$ so N_z is much smaller than N_x and N_y. The factor $\sin^2(\pi N_z k_z a_z)$ in Eq. 24.41 is wider in k-space than the other two numerators because a larger value of k_z is required to obtain the same argument of $\sin^2$. The shape factor, $|\tilde{\theta}(\vec{k})|^2$, is a thin rod in k-space that points along the z-direction.[9]

What is important about the elastic energy is that the function $B(\hat{k})$ has a minimum along some direction of $\hat{k}$. Call this minimum value $B(\hat{k}_{\min})$. If the precipitate is shaped as a plate, all of its shape factor intensity can be aligned along the one direction $\hat{k}_{\min}$. This allows only $B(\hat{k}_{\min})$ to appear in the integral of Eq. 24.40. A thin plate, suitably oriented, is the shape with minimum elastic energy. On the other hand, a precipitate of general shape, a sphere for example, will have shape factor intensity along all directions in k-space. The shape factor intensity that is not aligned along $\hat{k}_{\min}$ contributes more elastic energy to the integral of Eq. 24.40.

Problems

24.1 Consider a plate-shaped precipitate of width L and thickness D. If D were infinitesimal, Section 24.3.2 discussed how the elastic energy would be

$$E_{\text{el, min}} = \frac{1}{(2\pi)^3} \int B(\hat{k}_{\min})\, |\tilde{\theta}(\vec{k})|^2 \, \mathrm{d}^3k. \tag{24.42}$$

For finite D, show that the first-order correction to this energy scales with D/L.

(*Hint*: Consider the form of $B(\hat{k})$ around a smooth minimum, and consider the integration of Eq. 24.40 in three dimensions.)

24.2 (**a**) Derive Eq. 24.23.
(**b**) Derive Eq. 24.28.
(**c**) Derive Eq. 24.16.

[9] The selection of the z-direction was one of convenience – any wide, thin plate has a shape factor that is a long rod in the direction normal to the plate.

25 Diffusion, Dissipation, and Inelastic Scattering

We return to the random walk problem of Section 10.1, and recast it in terms of velocities over short intervals of time. The result is that the diffusion coefficient is a "velocity–velocity autocorrelation function." The velocity of a moving atom or nanoparticle occurs in spurts, which we treat as fluctuations in its energy. The total energy is conserved, however, and by considering the energy of the surrounding material, the velocity fluctuations are related to the underlying thermodynamics. The fluctuation–dissipation theorem relates fluctuations in the velocity of a moving atom or nanoparticle to the time correlations of atomic processes such as the vibrations of surrounding atoms.

Fluctuation spectra in real space and time, $\vec{r}$ and t, can be determined from inelastic scattering experiments. Inelastic scattering experiments detect the momentum and frequency distribution of the intensity, $I(\vec{Q}, \omega) \sim \psi^* \psi$, from a wave or wavefunction ψ scattered by the sample. The double Fourier transformation of this I from $\{\vec{Q}, \omega\}$ to $\{\vec{r}, t\}$, turns the product $\psi^* \psi$ into a convolution in $\vec{r}$ and t, known as the Van Hove space-time correlation function, $G(\vec{r}, t)$. It is possible to calculate $G(\vec{r}, t)$ from the fluctuation spectra in the material, and we do so for atomic diffusion and calculate the quasielastic scattering. The chapter ends with an overview of scattering processes that excite different numbers of quantized vibrations in a material, phonons, and discusses how phonons can be measured.

25.1 Atomic Processes and Diffusion

25.1.1 Velocity Correlations

Consider again the random walk problem, in particular the square of $\vec{R}_n$ of Eq. 10.1

$$R_n^2 = \vec{R}_n \cdot \vec{R}_n = \sum_{i=1}^{n} \vec{r}_i \cdot \sum_{j=1}^{n} \vec{r}_j. \tag{25.1}$$

Also, from Eq. 10.8

$$\frac{1}{6} R_n^2 = Dt, \tag{25.2}$$

so

$$\frac{\mathrm{d}}{\mathrm{d}t} R_n^2 = 6D, \tag{25.3}$$

where D is the diffusion coefficient.

We now recast the random walk problem from one based on structure (using distances, $\{\vec{r}_i\}$) to one based on dynamics (using velocities, $\{\vec{v}_i\}$). This allows us to address more directly the dynamical processes at the atomic level, and relate atomic-level dynamics to dissipative processes at the macroscopic scale. For appropriate time intervals, each displacement vector $\vec{r}_i$ is $\vec{r}_i = \vec{v}_i \delta t_i$.

$$R_n^2 = \sum_{i=1}^{n} \vec{v}_i \delta t_i \cdot \sum_{j=1}^{n} \vec{v}_j \delta t_j, \tag{25.4}$$

$$R_n^2 = \sum_{i=1}^{n} \sum_{j=1}^{n} \vec{v}_i \cdot \vec{v}_j \, \delta t_i \delta t_j, \tag{25.5}$$

$$R^2(\tau) = \int_{t_i=0}^{\tau} \int_{t_j=0}^{\tau} \vec{v}(t_i) \cdot \vec{v}(t_j) \, \mathrm{d}t_i \mathrm{d}t_j. \tag{25.6}$$

Anticipating causal relationships below, we pick a direction for time, and set $t_i \geq t_j$. Half of the combinations of t_i, t_j are now inaccessible, and hence a factor of two in the revised expression

$$R^2(\tau) = 2 \int_{t_i=t_j}^{\tau} \int_{t_j=0}^{\tau} \vec{v}(t_i) \cdot \vec{v}(t_j) \, \mathrm{d}t_i \mathrm{d}t_j. \tag{25.7}$$

The integrand does not depend on the absolute value of t_j, but only on the difference in time between the two velocities, $\tau' = t_i - t_j$. The zero in time is arbitrary, so we set $t_j = 0$. The complicated relationship between $\vec{v}(t_i)$ and $\vec{v}(t_j)$ does not change with any time offset, so the integration over the starting time t_i gives τ

$$R^2(\tau) = 2\tau \int_0^{\tau} \vec{v}(t) \cdot \vec{v}(0) \, \mathrm{d}t. \tag{25.8}$$

Following Eq. 25.3, take the time derivative of Eq. 25.6 to obtain the diffusion coefficient. For a good macroscopic average we perform an ensemble average over many identical systems to obtain the different values of $\vec{v}(t) \cdot \vec{v}(0)$

$$\frac{\mathrm{d}}{\mathrm{d}\tau} R^2 = 6D = 2 \int_0^{\tau} \left\langle \vec{v}(t) \cdot \vec{v}(0) \right\rangle \mathrm{d}t \; + \; 2\tau \left\langle \vec{v}(\tau) \cdot \vec{v}(0) \right\rangle. \tag{25.9}$$

At moderate τ we expect $\left\langle \vec{v}(\tau) \cdot \vec{v}(0) \right\rangle = 0$ as the particle motion becomes uncorrelated, so

$$D = \frac{1}{3} \int_0^{\tau} \left\langle \vec{v}(t) \cdot \vec{v}(0) \right\rangle \mathrm{d}t. \tag{25.10}$$

This diffusion coefficient, D, has the correct units, such as [cm^2/s]. Another interesting relationship can be obtained by differentiating again Eq. 25.9

$$\frac{\mathrm{d}^2}{\mathrm{d}\tau^2} R^2 \Big|_t = 2 \left\langle \vec{v}(t) \cdot \vec{v}(0) \right\rangle. \tag{25.11}$$

In practice, for defining a diffusion constant we seek a very large number of jumps where Eq. 25.11 is zero. This occurs after a long time between the first and last jump, so the upper limit is extended to infinity

$$D = \frac{1}{3} \int_0^\infty \left\langle \vec{v}(t) \cdot \vec{v}(0) \right\rangle \mathrm{d}t. \tag{25.12}$$

25.1.2 A Model Autocorrelation Function

The integral in Eq. 25.10 is an ensemble-averaged autocorrelation function.[1] It depends on the time sequence of velocities, $\vec{v}(t)$, specifically how well, after a time t, the atom velocity aligns with its initial velocity.

A discrete model of a velocity–velocity autocorrelation function is constructed in Fig. 25.1, using a time sequence of velocities on the upper left. The steps to construct the velocity–velocity autocorrelation function are:

- Shift the time sequence by various times t_j, as in Fig. 25.1a.
- Overlap the shifted time sequences with the original function.
- Multiply the functions at all time intervals as in Fig. 25.1b.
- Sum the products from all time intervals (or integrate over time if the variable is continuous). For the illustrated shift of 3 in Fig. 25.1b, this sum was +3. Analogous results were obtained for all other shifts.
- Graph the sum of all products for each time shift as in Fig. 25.1c. This is the velocity–velocity autocorrelation function.
- If materials can be prepared with similar velocity fluctuations as in Fig. 25.1a, it is appropriate to evaluate the ensemble average.

There are several points to note about the velocity–velocity autocorrelation function of Fig. 25.1c.

- The time sequence overlaps perfectly with itself when there is no shift, so the velocity–velocity autocorrelation function has a maximum value at $t = 0$.
- It is symmetrical about $t = 0$. This is understandable because it can be constructed for $-t$ by relabeling the bottom time sequence of Fig. 25.1a as the t_0, and recognizing that the sequences above it are for negative (earlier) times.
- The peak in the autocorrelation function is wider in time, up to twice as wide, as the main peak in the velocity sequence of Fig. 25.1a.

[1] Averaging over ensembles allows a good sampling of the different atomic-level processes. It is expected to be the same as the time average for the motion of one atom, but this is challenging to prove (discussion after Eq. 10.9).

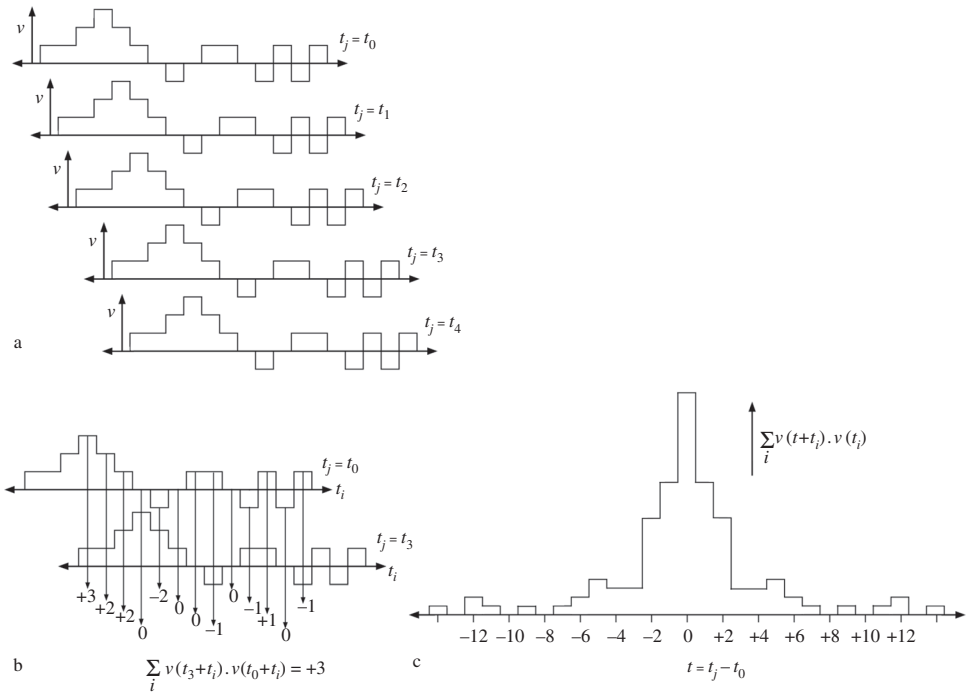

Figure 25.1 (**a**) A time sequence of discrete velocities, shown for different time shifts t_j. (**b**) Evaluation of the velocity–velocity autocorrelation function for the particular time shift of $t_3 - t_0$. The numbers at the bottom sum to +3, and this is plotted at +3 in part c. (**c**) The velocity–velocity autocorrelation function, evaluated for all shifts, t. Its maximum is 25.

- This peak in the autocorrelation function is also more prominent, since it is the square of the velocity.
- An ensemble average should be performed with velocity sequences having similar initial fluctuations. One way to prepare such fluctuations is to suddenly apply an external force to a system, or suddenly turn off such a force. This leads into the theory of linear response, with "susceptibility functions" that are much like our velocity–velocity autocorrelation function.

25.1.3 Relaxation Time

For short times the atom carries much of its initial velocity, so $\vec{v}(t) \cdot \vec{v}(0)$ is large, and there is a maximum at $t = 0$. At long times, however, we expect the atom to have lost all memory of its velocity at $t = 0$, and the average of $\vec{v}(t) \cdot \vec{v}(0)$ is zero. The atom loses memory of its initial velocity after a time τ_r, a "relaxation time," defined as

$$\tau_r = \frac{\int_0^\tau \left\langle \vec{v}(t) \cdot \vec{v}(0) \right\rangle \mathrm{d}t}{\frac{1}{\tau} \int_0^\tau \vec{v}^2(t)\, \mathrm{d}t}, \tag{25.13}$$

where $\tau \gg \tau_r$. The denominator, used for normalization, is just the average squared velocity, so

$$\tau_r = \frac{\int_0^\tau \left\langle \vec{v}(t) \cdot \vec{v}(0) \right\rangle \mathrm{d}t}{\overline{v}^2}. \tag{25.14}$$

The denominator is related to the thermal kinetic energy

$$E_{\mathrm{kin}} = \frac{1}{2} m \overline{v}^2 = \frac{1}{2} k_B T, \tag{25.15}$$

where m is the mass of the atom. Using also Eq. 25.10 for the diffusion coefficient, Eq. 25.14 gives an interesting expression for the relaxation time of the moving atom or nanoparticle[2]

$$\tau_r = \frac{m D}{k_B T}. \tag{25.16}$$

Equation 25.16 could be transformed to a definition of D in terms of the thermal energy and the relaxation time. We probe this connection more deeply in Section 25.2.

25.1.4 Green–Kubo Relationships

Equation 25.10 for the diffusion coefficient is an example of a Green–Kubo relationship. Green–Kubo relationships connect a transport coefficient to an autocorrelation function of the underlying atomic-scale motions. Other transport coefficients are a thermal conductivity and an electrical conductivity. For example, the current density from an electron can be expressed as a series of microscopic trajectories

$$\vec{J} = \sum_i e \, \vec{v}_i \, , \tag{25.17}$$

where $\vec{v}_i$ is the velocity of the electron during trajectory i. In analogy with Eq. 25.10 for atom transport, for electrical transport we have another Green–Kubo relationship

$$\sigma = \frac{N}{k_B T} \int_0^\infty \langle \vec{J}(t) \cdot \vec{J}(0) \rangle \, \mathrm{d}t \, , \tag{25.18}$$

where σ is electrical conductivity and $\vec{J}(t)$ is assumed to be isotropic. Such transport coefficients arise from numerous individual processes, e.g., atom jumps, phonon scattering, or electron scattering.[3] This viewpoint based on autocorrelation functions has some powerful features:

- Simulations of transport processes such as thermal conductivity are difficult to perform at the atomic scale by imposing temperature gradients across a simulated material. The length scale quickly becomes too large for realistic computations. On the other hand, Green–Kubo relationships can be used with many fewer atoms.

[2] We can draw a connection to the simplified process described in Section 10.4 with Fig. 10.12 by equating the collision time and the relaxation time, i.e., $t_c = \tau_r$. We obtain the mobility, $M \equiv \overline{v}/F = D/k_B T$, and $\tau_r = mM$ (within a factor of 2).

[3] Ballistic transport, such as the acceleration of an electron in a vacuum, is not normally treated by a Green–Kubo relationship.

- These autocorrelation functions can be used to obtain timescales for dissipative processes, such as damping of disturbances in the atom motion, or thermal pulses, for example. This is covered in Section 25.2.1.
- The Fourier transform of the autocorrelation function gives a frequency-dependent susceptibility function $\chi(\omega)$, which is central to inelastic scattering experiments. (Section 25.3.)

25.2 Dissipation and Fluctuations

25.2.1 Dissipation and the Langevin Equation

The Langevin equation of motion is an adaptation of Newton's law

$$m\frac{\mathrm{d}\vec{v}(t)}{\mathrm{d}t} = -\gamma m\vec{v}(t) + \delta\vec{F}(t), \tag{25.19}$$

where the first term on the RHS is a dissipative frictional force that is proportional to the velocity. The second term on the right is a force from atomic collisions or vibrations, and this force varies rapidly. Here we use the Langevin equation (25.19) to study the velocity of a nanoparticle or an atom, but we have to be careful about timescales.

We need a timescale that is long compared with that of atom vibrations (which are of order 10^{-13} s). It is then possible to neglect the second term on the RHS of Eq. 25.19 because it averages to zero, and obtain the solution

$$\vec{v}(t) = \vec{v}(0)\,\mathrm{e}^{-\gamma t}. \tag{25.20}$$

Consider how the velocity $\vec{v}(t)$ of our atom or nanoparticle compares with its velocity at time 0. To do so, take an ensemble average of the projection of $\vec{v}(0)$ onto the terms of Eq. 25.20

$$\left\langle \vec{v}(t)\cdot\vec{v}(0)\right\rangle = \left\langle \vec{v}(0)\cdot\vec{v}(0)\right\rangle \mathrm{e}^{-\gamma t}, \tag{25.21}$$

$$\left\langle \vec{v}(t)\cdot\vec{v}(0)\right\rangle = \left\langle v^2(0)\right\rangle \mathrm{e}^{-\gamma t}, \tag{25.22}$$

$$\left\langle \vec{v}(t)\cdot\vec{v}(0)\right\rangle = \overline{v}^2\,\mathrm{e}^{-\gamma t}. \tag{25.23}$$

This result for the velocity–velocity autocorrelation function does not include any structure at short time intervals because we simply ignored the rapid atom vibrations, but it is handy as an approximate result. Substituting Eq. 25.23 into Eq. 25.14

$$\tau_\mathrm{r} = \frac{\int_0^\tau \overline{v}^2\,\mathrm{e}^{-\gamma t}\,\mathrm{d}t}{\overline{v}^2}, \tag{25.24}$$

$$\tau_\mathrm{r} = -\frac{(\mathrm{e}^{-\gamma\tau}-1)}{\gamma}, \tag{25.25}$$

$$\tau_\mathrm{r} = \frac{1}{\gamma}, \tag{25.26}$$

where Eq. 25.26 was obtained by assuming that the averaging time τ is long.

Equation 25.26, although approximate, is still useful. It states that the dissipative damping of the velocity of an atom or nanoparticle (through γ) has the same timescale as the fluctuations in the velocity–velocity autocorrelation function that defines the diffusion coefficient (Eq. 25.10). Relating the dissipation to the fluctuations is understandable because both originate with atom collisions or vibrations. These atomic processes are essential to the thermodynamics of the material, however, and the next section gives a deeper insight into the thermodynamic characteristics of these fast forces. Nevertheless, we now have the essential idea that the fast atomic-level vibrational processes are the ones that dissipate the kinetic energy during the diffusional transport of atoms. In more modern parlance we can say that phonon excitations remove energy from diffusing atoms, but we do not need such detailed mechanisms to understand the thermodynamics.

25.2.2 Fluctuation–Dissipation Theorem

We have just seen how the velocity trajectory of an atom is influenced by fast atomic-level forces, $\delta F(t)$, such as from atom vibrations in the material. The velocity of an atom is also influenced by applied macroscopic forces, $F_{\text{ap}}(t)$.[4] The equation of motion, $ma = F_{\text{tot}}$, for the time increment Δt is

$$m\Big[v(t+\Delta t) - v(t)\Big] = \Delta t\, F_{\text{ap}}(t) + \int_{t}^{t+\Delta t} \delta F(t')\, \mathrm{d}t', \tag{25.27}$$

where Δt is short compared with the timescale of the applied force F_{ap}, but the δF from the atomic processes varies rapidly and requires integration over the time Δt.

Suppose an atom of interest moves a bit over the time Δt as a fluctuation occurs in its velocity. Since energy is conserved, the material has a reduction in energy by the amount ΔE as its atomic forces do work on the moving atom in the time from t to t'

$$\Delta E = \int_{t}^{t'} v(t'')\, \delta F(t'')\, \mathrm{d}t'', \tag{25.28}$$

$$\Delta E = v(t) \int_{t}^{t'} \delta F(t'')\, \mathrm{d}t'', \tag{25.29}$$

assuming the atom itself changes velocity slowly as it moves in response to phonons, for example.[5]

We now invoke a deep point. *The rapidly varying forces originate from the same atomic degrees of freedom that are responsible for the thermodynamics of the material*. This is worth a pause for thought. The ΔE of Eq. 25.29 is therefore directly associated with a change in entropy, $S = k_{\text{B}} \ln \Omega$, or the number of states accessible to the system, Ω. The entropy is dominated by the states of the material, which serves as a large heat reservoir.

[4] We will not emphasize $F_{\text{ap}}(t)$ in this section, but it was useful for the Langevin equation (25.19), and it is easy to include for completeness.

[5] The shortest timescale is for the atomic-level vibrations. A somewhat longer time is associated with the translational motion of the atom, and we will usually pick an applied force with a yet longer timescale.

The probabilities of the states of the material before and after the transfer of ΔE to the atom are in the ratio

$$\frac{\Omega(E-\Delta E)}{\Omega(E)} = \exp\left(\frac{-\Delta E}{k_{\mathrm{B}}T}\right). \tag{25.30}$$

For $\Delta E < k_{\mathrm{B}}T$, it is appropriate to linearize

$$\Omega(E-\Delta E) = \Omega(E)\left(1-\frac{\Delta E}{k_{\mathrm{B}}T}\right). \tag{25.31}$$

Consider an ensemble of N systems, in which Ω_i systems have δF_i, and calculate the ensemble average of δF. This average is computed in the time when the material has transferred the energy ΔE to the moving atom

$$\langle \delta F\rangle = \frac{1}{N}\sum_i \Omega_i(E-\Delta E)\,\delta F_i, \tag{25.32}$$

$$\langle \delta F\rangle = \frac{1}{N}\sum_i \Omega_i(E)\left(1-\frac{\Delta E}{k_{\mathrm{B}}T}\right)\delta F_i, \tag{25.33}$$

$$\langle \delta F\rangle = \left\langle\left(1-\frac{\Delta E}{k_{\mathrm{B}}T}\right)\delta F\right\rangle_0, \tag{25.34}$$

$$\langle \delta F\rangle = \langle \delta F\rangle_0 - \frac{1}{k_{\mathrm{B}}T}\left\langle \Delta E\,\delta F\right\rangle_0, \tag{25.35}$$

where the angle brackets and the subscript "0" denote an ensemble average over the equilibrium state of the material at temperature T (without transfer of energy to the atom). In this case of equilibrium, the average $\langle \delta F\rangle_0 = 0$, so

$$\langle \delta F\rangle = -\frac{1}{k_{\mathrm{B}}T}\left\langle \Delta E\,\delta F\right\rangle_0. \tag{25.36}$$

Here $\langle \delta F\rangle \neq 0$, since an energy transfer to the atom brings the surrounding material slightly out of equilibrium.

Substitute the result from Eq. 25.29 into Eq. 25.36

$$\langle \delta F\rangle = -\frac{\overline{v}(t)}{k_{\mathrm{B}}T}\left\langle \int_{t''=t}^{t'} \delta F(t'')\,\delta F(t)\,\mathrm{d}t''\right\rangle_0. \tag{25.37}$$

Finally, substitute Eq. 25.37 into the equation of motion, Eq. 25.27

$$m\Big[v(t+\Delta t)-v(t)\Big] = \Delta t\,F_{\mathrm{ap}}(t) - \frac{\overline{v}(t)}{k_{\mathrm{B}}T}\int_{t''=t}^{t'}\int_{t'=t}^{t+\Delta t}\left\langle \delta F(t')\,\delta F(t'')\right\rangle_0 \mathrm{d}t'\,\mathrm{d}t''. \tag{25.38}$$

The two $\delta F(t)$ are evaluated at different times, and $t'' \geq t'$. We emphasize this difference in time with the definition of $\tau \equiv t''-t'$. Using the same arguments given between Eqs. 25.7 and 25.8

$$m\Big[v(t+\Delta t)-v(t)\Big] = \Delta t\, F_{\rm ap}(t) - \Delta t\, \frac{\overline{v}(t)}{k_{\rm B}T} \int_0^{\tau} \Big\langle \delta F(0)\, \delta F(t) \Big\rangle_0 \, {\rm d}t, \tag{25.39}$$

$$m\Big[v(t+\Delta t)-v(t)\Big] = \Delta t\, F_{\rm ap}(t) - \Delta t\, \frac{\overline{v}(t)}{k_{\rm B}T} \int_0^{\infty} \Big\langle \delta F(0)\, \delta F(t) \Big\rangle_0 \, {\rm d}t. \tag{25.40}$$

In practice we expect the integral to reach its full value when τ is small, but it is convenient to extend it to all time correlations between forces.

Equation 25.40 is the "fluctuation–dissipation theorem." Equation 25.40 relates the fluctuations in velocity on the LHS to the time correlations of atomic processes on the right. If there is a time interval when the atomic processes are correlated, they provide a more persistent force in a given direction, and the moving atom will undergo a larger fluctuation in its velocity. On the other hand, when the atomic-scale forces become uncorrelated quickly, the integral on the right will have positive and negative δF and a small integrated value. Fluctuations in the velocity are caused by statistical variations in the atomic-level dynamics, whose probability was obtained from the Boltzmann factor of thermodynamics. These atomic level dynamics also serve as a heat reservoir that dissipates the kinetic energy when the moving atom loses its velocity.

25.3 Inelastic Scattering

25.3.1 Scattering by Vibrations of Individual Atoms

For simplicity, consider a thermally averaged velocity–velocity autocorrelation function, $\langle \vec{v}_i(0) \cdot \vec{v}_i(t) \rangle$, that involves only the ith atom and itself at a later time. Here we confine the atom to its lattice site in a crystal, but allow it to vibrate. First suppose that this ith atom can move only as a pure sine wave of frequency $2\pi\omega'$. In other words, suppose $\vec{v}_i(t) = \vec{v}_{i,0}\, {\rm e}^{+{\rm i}\omega' t}$, where the notation emphasizes that $\vec{v}_{i,0}$ is a constant. If we take the Fourier transform of the thermally averaged velocity–velocity autocorrelation function, appropriately normalized

$$g_i(\omega) = \frac{\int_{-\infty}^{+\infty} \langle \vec{v}_i(0) \cdot \vec{v}_i(t) \rangle\, {\rm e}^{-{\rm i}\omega t}\, {\rm d}t}{\langle \vec{v}_i(0) \cdot \vec{v}_i(0) \rangle}, \tag{25.41}$$

$$g_i(\omega) = \frac{\int_{-\infty}^{+\infty} v_{i,0}^2\, {\rm e}^{+{\rm i}\omega' t} {\rm e}^{-{\rm i}\omega t}\, {\rm d}t}{v_{i,0}^2}, \tag{25.42}$$

$$g_i(\omega) = \delta(\omega - \omega')\,, \tag{25.43}$$

for this special case when $\vec{v}_i(t) = \vec{v}_{i,0}\, {\rm e}^{{\rm i}\omega' t}$. Atoms do not generally vibrate as a single sine wave, but in general Eq. 25.41 does serve to extract the frequency spectrum of vibrations of the ith atom. When all atoms in the crystal are equivalent to the ith atom, this $g_i(\omega)$

(normalized to 1) is a "vibrational density of states" of the entire material. We used $g(\omega)$ (or $g(\varepsilon)$, where $\varepsilon = \hbar\omega$) in Section 7.5.1 to calculate the vibrational entropy of a material.

In what follows, the focus is on measuring $g(\omega)$ by inelastic scattering. Many details will be omitted, but a key idea is to send a monochromatic wave (or wavefunction) into a material to drive the atomic dynamics at a frequency ω_0, and test if the outgoing wave has changed frequency by the amount ω'. When there are more vibrational modes at ω', more incident waves will undergo inelastic scattering by transferring the energy $\hbar\omega'$ to the material. Likewise, if the material is at an elevated temperature with many vibrational modes excited, the incident wave is more likely to gain the energy $\hbar\omega'$, and leave the material with frequency $\omega_0+\omega'$. Although the spectrum of vibrations is all that is necessary to obtain the vibrational partition function of a material, more information is obtained from correlations of velocities for atoms at different sites in a material. Wavelengths of the different vibrations in a material can be obtained if these correlations are known in space, as well as in time.

25.3.2 The Van Hove Function and the Scattering Law

In general, by "inelastic scattering" we mean wave scattering where both the frequency and direction of the outgoing wave differ from those of the plane wave incident into the material. The change in frequency is directly interpretable as a transfer of energy from the wave to the material, $\hbar\omega$. Combining the energy transfer with the change in angle, the momentum transfer, $\hbar\vec{Q}$, can be determined. The total energy is conserved, so a loss of energy by the wave corresponds to a gain of energy in the material. Likewise, the change in momentum of the scattered wave corresponds to a change in crystal momentum in the material. When the experiment is designed properly, these energy transfers can reveal the energy and wavevectors of single-quantum excitations in the material.

We define the essential form of the scattered intensity (sometimes called the "scattering law") as $S(\vec{Q},\omega)$. A large amount of scattering physics is needed to explain the methods and formalism of inelastic scattering, but here we start with a key result. We first define the Van Hove function $G(\vec{r},t)$ as a correlation function of the atom positions at different times

$$G(\vec{r},t) \equiv \frac{1}{\tau}\int_{t'=0}^{+\tau}\int_{\vec{r}=-\infty}^{+\infty} f^*(\vec{r}',t')\,f(\vec{r}+\vec{r}',t+t')\,\mathrm{d}^3\vec{r}'\mathrm{d}t'. \tag{25.44}$$

For neutron scattering, the scattering factor $f(\vec{r},t)$ is the efficiency that a nucleus, located at position $\vec{r}$ and time t, scatters a neutron wavefunction. Equation 25.44 is a "space-time correlation function," meaning that it shows how events at different positions are correlated in time. For example, two atoms in different locations may undergo the same vibrational pattern at different times when a phonon wavepacket goes through one and then the other. Using different starting times, the time average can be written as an ensemble average

$$G(\vec{r},t) \equiv \int_{-\infty}^{+\infty} \Big\langle f^*(\vec{r}',0)\,f(\vec{r}+\vec{r}',t)\Big\rangle\,\mathrm{d}^3\vec{r}'. \tag{25.45}$$

The key result from scattering theory is that the double Fourier transform of the Van Hove function,[6] Eq. 25.45, is the inelastic intensity, corrected for some experimental factors

$$S(\vec{Q},\omega) = \frac{1}{2\pi\hbar}\iint_{-\infty}^{+\infty} G(\vec{r},t)\,\mathrm{e}^{-\mathrm{i}(\vec{Q}\cdot\vec{r}-\omega t)}\,\mathrm{d}^3\vec{r}\,\mathrm{d}t, \tag{25.46}$$

$$S(\vec{Q},\omega) = \frac{1}{2\pi\hbar}F_{\vec{r}}F_t G(\vec{r},t). \tag{25.47}$$

To understand a particular process of inelastic scattering, we need to understand the underlying Van Hove function, $G(\vec{r},t)$, of the material. There are many different $G(\vec{r},t)$, such as from spin–spin correlations in magnetic neutron inelastic scattering, charge–charge correlations in electron inelastic scattering, or displacement–displacement correlations in neutron inelastic scattering from phonons. Mathematically, a correlation function such as $G(\vec{r},t)$ of Eq. 25.45 is a convolution, as illustrated for the time variable in Fig. 25.1. Convolutions are usually troublesome to evaluate analytically, unless they are Gaussians or Lorentzians.

25.3.3 Inelastic Scattering from Diffusion

Here we pick a simple case for uncorrelated atom movements in diffusion, using the 1D Gaussian solution for $c(x,t)$ of Eq. 3.29, which is

$$c(x,t) = \frac{c'}{\sqrt{4\pi Dt}}\,\mathrm{e}^{-\frac{x^2}{4Dt}}. \tag{25.48}$$

The Van Hove function of Eq. 25.45 is

$$G_{\mathrm{diff}}(x,t) = \int_{-\infty}^{+\infty}\Big\langle c(x',0)\,c(x'+x,t)\Big\rangle\,\mathrm{d}x'. \tag{25.49}$$

An important point about diffusion is that there are no space or time correlations between different atoms – two different atoms do not know about each other's jumps, and all atoms follow the same concentration profile. Ensemble averaging is therefore unnecessary.

$$G_{\mathrm{diff}}(x,t) = \int_{-\infty}^{+\infty} c(x',0)\,c(x'+x,t)\,\mathrm{d}x'. \tag{25.50}$$

As $t \to 0$, the function $c(x', t \to 0)$ of Eq. 25.48 becomes a Dirac delta function of unit area

$$G_{\mathrm{diff}}(x,t) = \int_{-\infty}^{+\infty} \delta(x')\,c(x',t)\,\mathrm{d}x', \tag{25.51}$$

[6] Note that the $G(\vec{r},t)$ involves two positions, separated by $\vec{r}$, and two times separated by $\vec{t}$. The exponential has the form of a traveling wave, but it uses these separations as arguments. The exponential is not a real wave, but it is a phase relationship between the incident and scattered waves.

so the spatial integral simply returns the function $c(x,t)$ of Eq. 3.29 or 25.48

$$G_{\text{diff}}(x,t) = \frac{c'}{\sqrt{4\pi Dt}}\, \mathrm{e}^{-\frac{x^2}{4Dt}}. \tag{25.52}$$

We calculate the $S(Q,\omega)$ by using Eq. 25.52 in the Fourier transform relationship of Eq. 25.46

$$S(Q,\omega) = \frac{c'}{2\pi\hbar} \int_{t=0}^{+\infty} \int_{x=-\infty}^{+\infty} \frac{\mathrm{e}^{-\frac{x^2}{4Dt}}}{\sqrt{4\pi Dt}}\, \mathrm{e}^{-\mathrm{i}(Qx-\omega t)}\, \mathrm{d}x\, \mathrm{d}t\ , \tag{25.53}$$

$$S(Q,\omega) = \frac{c'}{2\pi\hbar} \int_{t=0}^{+\infty} \mathrm{e}^{-Q^2 Dt}\, \mathrm{e}^{\mathrm{i}\omega t}\, \mathrm{d}t, \tag{25.54}$$

$$S(Q,\omega) = \frac{c'}{2\pi\hbar}\, \frac{DQ^2}{(DQ^2)^2 + \omega^2}, \tag{25.55}$$

where we used a standard result, that the Fourier transform of a Gaussian in x^2 is a Gaussian in Q^2, to obtain Eq. 25.54, and another standard result that the Fourier transform of a decaying exponential is a Lorentzian function to obtain Eq. 25.55. The Lorentzian function is a symmetrical, peaked function with a maximum at $\omega = 0$, or $\Delta E = 0$. Its half-width at half-maximum is at $\omega = DQ^2$, or

$$\Delta E = \hbar\, D\, Q^2. \tag{25.56}$$

25.3.4 Physical Interpretation: Quasielastic Scattering

We can interpret Eq. 25.55 in terms of how inelastic scattering is sensitive to the atom jumps in diffusion. The energy width of the inelastic intensity of Eq. 25.56 corresponds to a time $\Delta\tau$ by the uncertainty relationship

$$\Delta\tau = \frac{\hbar}{\Delta E} = \frac{1}{D\, Q^2}. \tag{25.57}$$

Recall the result of Eq. 3.18

$$D = \frac{\Gamma\, a^2}{6}, \tag{25.58}$$

where Γ is the atom jump frequency and a is its jump length. For a representative Q of $2\pi/a$, the time uncertainty becomes

$$\Delta\tau = \frac{1}{\left(\frac{\Gamma a^2}{6}\right)\left(\frac{2\pi}{a}\right)^2}, \tag{25.59}$$

$$\Delta\tau = \frac{0.30}{\Gamma}. \tag{25.60}$$

In other words, without diffusion ($D = 0$) the inelastic spectrum would be a sharp peak at $E = 0$, corresponding to elastic scattering only. When the atoms jump frequently, there is

time-broadening of the energy $\Delta E = \hbar\Gamma$ at a characteristic Q. This is caused when wave scattering is interrupted by a jump of the scattering center. The jump that occurs during scattering shortens the coherence time for the emitted wave, broadening it in energy. This process of scattering by moving atoms is often called "quasielastic scattering" because it can be considered as elastic scattering (no overall energy shift), but with an energy broadening because the atoms have residence times shorter than the lifetime of the incident wavepacket.

25.4 Atom Jump Directions and Quasielastic Scattering

An innovative quasielastic scattering experiment has measured both the directions and the rates of atomic jumps during diffusion [393]. For reference, a simple scattering process is illustrated in Fig. 25.2a. A wave, a γ-ray, is incident on a nucleus, which oscillates resonantly with the same frequency. The nucleus absorbs the energy of the γ-ray and then re-emits a γ-ray of the same frequency. The incident wavevector, $\vec{Q}_\mathrm{i}$, is $2\pi/\lambda$, where λ is the wavelength, and the direction of $\vec{Q}_\mathrm{i}$ is shown in Fig. 25.2a. The outgoing wave in Fig. 25.2a is depicted as a circular wave in all directions, but an experimenter can select the direction of the scattered (final) wave by the position of a γ-ray detector. Figure 25.2b shows a $\vec{Q}_\mathrm{f}$ that points towards a remote detector to the upper right. The detector is far away, so any curvature of the wavefront is negligible, and we treat the detected wave as a plane wave. What is important for the scattering is the difference $\vec{Q}$ between the incident and final wavevector, defined here as $\vec{Q} \equiv \vec{Q}_\mathrm{i} - \vec{Q}_\mathrm{f}$, and drawn as a vector sum in Fig. 25.2b. The wave undergoes no change in energy after the scattering, so the scattering event is fully defined by $\vec{Q}$, which represents a change in direction of the wave.

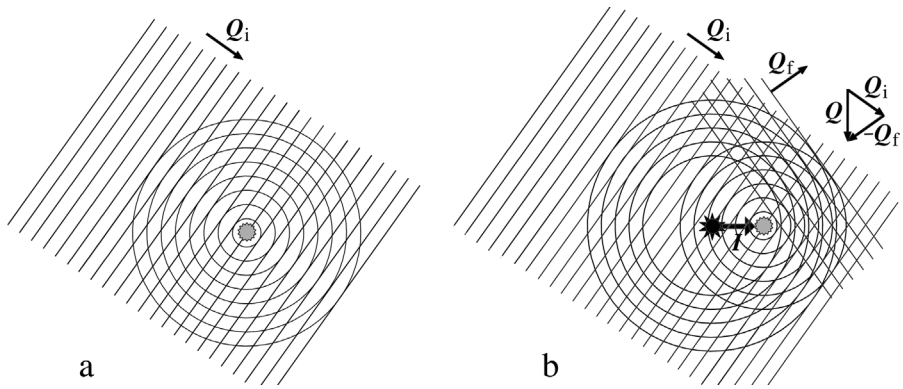

Figure 25.2 (**a**) A γ-ray of wavevector $\vec{Q}_\mathrm{i}$ incident on a resonant nucleus, which radiates a long wavepacket after it is excited. (**b**) A resonant nucleus that moves by the distance $\vec{l}$ while it is scattering the incident γ-ray. A remote detector along the direction of $\vec{Q}_\mathrm{f}$ sees plane wave emissions from the two outgoing wavepackets that are in phase, as indicated by lines through their wave crests.

An assumption of Section 25.3.3 was that the diffusive jumps were not correlated to the direction of the scattering vector $\vec{Q}$. If the sample is a single crystal, however, the quasielastic scattering can vary with the orientation of $\vec{Q}$ with respect to the jump vector of the resonant nucleus, $\vec{I}$. Figure 25.2b depicts a nuclear de-excitation where the nucleus jumps the distance $\vec{I}$ during the time of its nuclear decay. The emitted wavepacket is divided into two parts with fractions **f** and $1 - \mathbf{f}$. The two wavepackets, ψ_{f1} and ψ_{f2}, may undergo constructive or destructive interference depending on the phase relationship between them. A complex exponential of modulus unity, $e^{i\vec{Q}\cdot\vec{I}}$, is a convenient way to express the difference in phase of the second wavepacket with respect to the first. The two wavepackets add to make the total wave at the position of the detector, $\vec{R}$

$$\psi_{\mathrm{f}}(\vec{R}) = \mathbf{f}\,\psi_{\mathrm{f1}}(\vec{R}) + (1-\mathbf{f})\,\psi_{\mathrm{f2}}\,, \tag{25.61}$$

$$\psi_{\mathrm{f}}(\vec{R}) = \mathbf{f}\,\psi_{\mathrm{f1}}(\vec{R}) + (1-\mathbf{f})\,\psi_{\mathrm{f1}}(\vec{R})e^{i\vec{Q}\cdot\vec{I}}\,. \tag{25.62}$$

Consider first the special case where this phase factor is $e^{i\vec{Q}\cdot\vec{I}} = e^{i0} = 1$. In this special case, there is no effect of the jump on the length of the detected wavepacket

$$\mathbf{f}\,\psi_{\mathrm{f1}}(\vec{R}) + (1-\mathbf{f})\,\psi_{\mathrm{f1}}(\vec{R})e^{i0} = \psi_{\mathrm{f1}}(\vec{R})\,, \tag{25.63}$$

so the measured energy breadth of the detected wave is the same as the reference case with no jump during the nuclear decay, Fig. 25.2a. An example of this special case is depicted in Fig. 25.2b, for which $\vec{Q}\cdot\vec{I} = 0$ because $\vec{Q}$ and $\vec{I}$ are perpendicular for the $\vec{Q}_{\mathrm{f}}$ selected in the figure.[7] Most orientations of $\vec{Q}$ are not perpendicular to the jump directions $\vec{I}$, of course. Furthermore, with diffusive jumps along different symmetry-related directions in a crystal there are usually several values of $\vec{Q}\cdot\vec{I}$. Nevertheless, models of diffusion mechanisms can be tested by calculating their effect on the intensity and broadening of the quasielastic scattering, and comparing to experimental measurements of energy spectra along different crystallographic directions.

Sepiol and Vogl studied a single crystal of Fe_3Si with $D0_3$ chemical order (Fig. 18.3) by ^{57}Fe Mössbauer spectrometry. Measurements were made at elevated temperature so the hopping time of ^{57}Fe atoms was comparable to the 100 ns lifetime of the nuclear excited state. The spectral energy broadening was observed to vary with crystallographic alignment of the scattering vector $\vec{Q}$, as shown in Fig. 25.3. Numerous spectra were acquired, and the authors were able to fit the broadened components and their intensities to models of diffusion jumps and directions in the crystal. Their results were consistent with a vacancy mechanism, where Fe atoms jumped primarily with nearest-neighbor jumps between the different Fe-sublattices, which have neighboring sites in the $D0_3$ structure. For an off-stoichiometric crystal, however, the Fe atoms on the Si sites (antisite Fe atoms) were found to jump rapidly, again with dynamics consistent with a first-nearest-neighbor vacancy mechanism. These experiments on hot single crystals are technically challenging, but further work has been done with this method and related techniques [394–397].

[7] The condition $e^{\vec{Q}\cdot\vec{I}} = 1$ is also possible when $\vec{Q}\cdot\vec{I} = n2\pi$, somewhat analogous to the Laue condition for diffraction in a crystal.

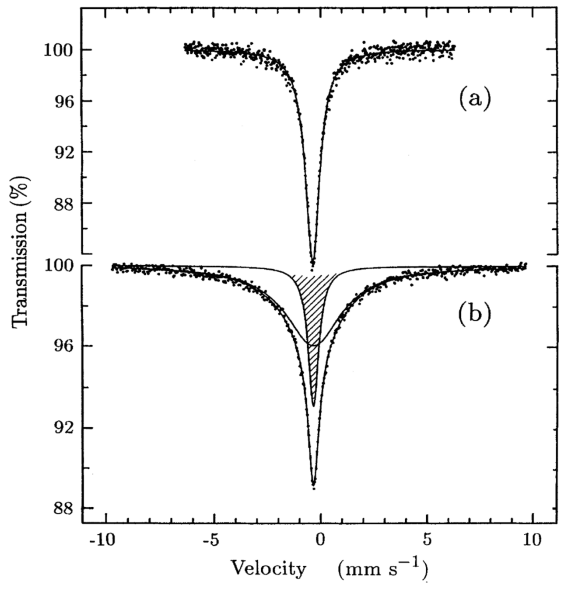

Figure 25.3 Mössbauer spectra from a single crystal of Fe_3Si at 993 K. The orientations of $\vec{Q}$ were along [111] in spectrum (a) and along [113] in spectrum (b). Spectrum (b) has a spectral component that is much broader than in spectrum (a). From [393].

25.5 Phonons and Quantum Mechanics

25.5.1 Quantum Mechanics of Neutron Scattering

To calculate the inelastic scattering of neutrons by phonons, it might seem that we should find an expression analogous to the Van Hove function of Eq. 25.45, and then take its Fourier transform as in Eq. 25.47. The situation is a bit different with quantum mechanics, however. The algebraic expressions of classical mechanics are transformed into expressions involving position and momentum operators, which do not commute. A detailed derivation of the scattering probability is not possible in a small section, and books on this are available [398, 399], along with a superb original paper [400]. A sketch of the derivation is given here.

The approach starts with Fermi's Golden Rule, with an instantaneous transition rate

$$W = \frac{2\pi}{\hbar}|\langle \mathrm{f}|V|\mathrm{i}\rangle|^2. \tag{25.64}$$

The initial and final states are products of states for both neutron and nucleus

$$|\mathrm{i}(\vec{r},t)\rangle = |\lambda_\mathrm{i}(\vec{r}_\mathrm{nu},t)\rangle|\vec{k}_\mathrm{i}(\vec{r}_\mathrm{ne},t)\rangle\,, \tag{25.65}$$

$$|\mathrm{f}(\vec{r},t)\rangle = |\lambda_\mathrm{f}(\vec{r}_\mathrm{nu},t)\rangle|\vec{k}_\mathrm{f}(\vec{r}_\mathrm{ne},t)\rangle\,, \tag{25.66}$$

where the independent coordinates $\vec{r}_{\rm nu}$ and $\vec{r}_{\rm ne}$ refer to the positions of the nucleus and the neutron, respectively. The neutron wavefunctions are assumed to be plane wave states, but the initial wavevector is altered by inelastic scattering, so $k_{\rm i} \neq k_{\rm f}$.

Neutron scattering from different atoms j and k involves neutron wavefunctions containing factors such as $\exp(\mathrm{i}\vec{k}_{\rm i} \cdot \vec{R}_j)$, and the change in neutron momentum after a scattered neutron transfers the momentum $\hbar\vec{Q}$ to the material is

$$\vec{Q} = \vec{k}_{\rm i} - \vec{k}_{\rm f}. \tag{25.67}$$

The nuclei change position with time as they vibrate in phonons. The time projection operator $\exp(\mathrm{i}\underline{H}t)$ is a general way to account for time evolution, but with well-defined energies for the neutron, the factors $\exp(\mathrm{i}\omega_{\rm i}t)$ and $\exp(\mathrm{i}\omega_{\rm f}t)$ can be used instead. Important definitions of differences are

$$\omega = \omega_{\rm i} - \omega_{\rm f}, \tag{25.68}$$

$$t = t_j - t_k. \tag{25.69}$$

Likewise, the position projection operator $\exp(\mathrm{i}\vec{k}_{\rm i} \cdot \underline{\vec{r}})$ is used to account for the neutron at different atom locations.

The total probability P for scattering is an integration of the transition rate W over the time when the neutron is near the nucleus. Writing out Eq. 25.64 as a function times its complex conjugate, and considering the interference of neutron wavefunctions scattered from atoms j and k

$$P = \frac{2\pi}{\hbar} \int \mathrm{e}^{\mathrm{i}\omega t} \sum_j b_j^* \ \langle \lambda_{\rm i}(0) | \mathrm{e}^{\mathrm{i}\vec{Q}\cdot\underline{\vec{R}}_j(t)} | \lambda_{\rm f}(0) \rangle$$
$$\times \sum_k b_k \ \langle \lambda_{\rm f}(0) | \mathrm{e}^{-\mathrm{i}\vec{Q}\cdot\underline{\vec{R}}_k(0)} | \lambda_{\rm i}(0) \rangle \ \mathrm{d}t. \tag{25.70}$$

The initial state of the crystal is best described by a thermal average, denoted as $\langle\ \rangle_T$. The final states of the crystal are not controlled, however. All possible final states are expected in an average over many scatterings. Since these final states make a complete set, and $\sum |\lambda_{\rm f}(0)\rangle\langle\lambda_{\rm f}(0)| = 1$

$$P = \frac{2\pi}{\hbar} \int \mathrm{e}^{\mathrm{i}\omega t} \sum_j \sum_k b_j^* b_k \left\langle \mathrm{e}^{\mathrm{i}\vec{Q}\cdot\underline{\vec{R}}_j(t)} \mathrm{e}^{-\mathrm{i}\vec{Q}\cdot\underline{\vec{R}}_k(0)} \right\rangle_T \mathrm{d}t. \tag{25.71}$$

The next part is subtle. The position operators $\underline{\vec{R}}_j(t)$ and $\underline{\vec{R}}_k(0)$ are related by the time evolution operator $\exp(\mathrm{i}\underline{H}t)$, which contains the momentum. As a result, these position operators do not commute. It is traditional to define, for simplicity, the operators $\underline{U} = \mathrm{i}\vec{Q} \cdot \underline{\vec{R}}_j(t)$ and $\underline{V} = -\mathrm{i}\vec{Q} \cdot \underline{\vec{R}}_k(0)$, rewriting Eq. 25.71 for a monoatomic crystal as

$$P = \frac{2\pi}{\hbar} \int \mathrm{e}^{\mathrm{i}\omega t} \sum_l |b|^2 \mathrm{e}^{\mathrm{i}\vec{Q}\cdot\vec{x}_l} \left\langle \mathrm{e}^{\underline{V}} \, \mathrm{e}^{\underline{U}} \right\rangle_T \mathrm{d}t, \tag{25.72}$$

where $\{\vec{x}_l\}$ are the interatomic separations in a crystal. From an advanced calculation that considers the commutation properties of $\underline{U}$ and $\underline{V}$, plus the fact that they have the same thermal average, it is possible to show that

$$P = \frac{2\pi}{\hbar}|b|^2 \sum_l \mathrm{e}^{\mathrm{i}\vec{Q}\cdot\vec{x}_l} \int \mathrm{e}^{\mathrm{i}\omega t} \left\langle \mathrm{e}^{\underline{U}^2} \mathrm{e}^{\underline{U}\ \underline{V}} \right\rangle_T \mathrm{d}t\ , \tag{25.73}$$

$$P = \frac{2\pi}{\hbar}|b|^2 \mathrm{e}^{\langle \underline{U}^2 \rangle_T} \sum_l \mathrm{e}^{\mathrm{i}\vec{Q}\cdot\vec{x}_l} \int \mathrm{e}^{\mathrm{i}\omega t} \mathrm{e}^{\langle \underline{U}\ \underline{V} \rangle_T} \mathrm{d}t, \tag{25.74}$$

where it was recognized that $\exp(\langle \underline{U}^2 \rangle_T)$ does not depend on time. This factor is the Debye–Waller factor, equal to $\exp(-\langle [\vec{Q}\cdot u_l(0)]^2 \rangle_T)$, which reduces the coherence of scattering with increasing vibrational amplitude.

25.5.2 Elastic and Phonon Scattering

Equation 25.74 is a general result for neutron scattering, and can be used in a variety of ways. Here it is used to show some general principles of phonon scattering, with the convenience of the "incoherent approximation." This approximation assumes no phase relationship between the vibrations of different atoms, allowing the separation

$$\mathrm{e}^{\langle \underline{U}\ \underline{V} \rangle_T} \rightarrow \mathrm{e}^{\langle \underline{U} \rangle_T \langle \underline{V} \rangle_T} = \mathrm{e}^{\langle \underline{U} \rangle_T \langle \underline{U}^* \rangle_T}. \tag{25.75}$$

Equation 25.74 becomes

$$P = \frac{2\pi}{\hbar}|b|^2 \mathrm{e}^{-\langle [\vec{Q}\cdot\vec{u}_l(0)]^2 \rangle_T} \sum_l \mathrm{e}^{\mathrm{i}\vec{Q}\cdot\vec{x}_l} \int \mathrm{e}^{\mathrm{i}\omega t} \mathrm{e}^{\langle \underline{U} \rangle_T \langle \underline{U}^* \rangle_T} \mathrm{d}t. \tag{25.76}$$

It is appropriate to note that the P (proportional to the cross-section for neutron scattering) is a conserved quantity, dependent on $|b|^2$. The Debye–Waller factor, $\mathrm{e}^{-\langle [\vec{Q}\cdot u_l(0)]^2 \rangle_T}$, decreases with Q, so it must be compensated by an increase with Q from the factors at the right.

The thermal average displacement of a harmonic oscillator is related to its energy as $\hbar\omega = 2M\omega^2 \langle x \rangle_T^2$, so $\langle x \rangle_T = \sqrt{\hbar/(2M\omega)}$. Replace $\langle \underline{U} \rangle_T \rightarrow \mathrm{i}Q\sqrt{\hbar/(2M\omega)}$ and $\langle \underline{U} \rangle_T \langle \underline{U}^* \rangle_T \rightarrow \hbar^2 Q^2/(2M\hbar\omega)$. Next, expand the exponential as

$$P = \frac{2\pi}{\hbar}|b|^2 \mathrm{e}^{-\langle [\vec{Q}\cdot\vec{u}_l(0)]^2 \rangle_T} \sum_l \mathrm{e}^{\mathrm{i}\vec{Q}\cdot\vec{x}_l} \int \mathrm{e}^{\mathrm{i}\omega t} \left(1 + \frac{\hbar^2 Q^2}{2M\hbar\omega} + \frac{\hbar^4 Q^4}{2(2M\hbar\omega)^2} + \cdots \right) \mathrm{d}t. \tag{25.77}$$

The recoil of a nucleus of mass M after a momentum transfer p is $E_\mathrm{R} = p^2/(2M)$. Recognizing $E_\mathrm{R} = \hbar^2 Q^2/(2M)$ in Eq. 25.77, we see that the terms are in powers of E_R/ε, where the phonon energy is $\varepsilon = \hbar\omega$. Analyzing the expansion in Eq. 25.77 term-by-term:[8]

- The first term, the 1, is the elastic scattering. Its time spectrum is a constant, and the Fourier transform of a constant is a delta function, $\delta(\omega)$. The sum of phase factors $\mathrm{e}^{\mathrm{i}\vec{Q}\cdot\vec{x}_l}$ over interatomic separations and the Debye–Waller factor $\mathrm{e}^{\langle \vec{\underline{U}}^2 \rangle_T}$ are as expected for neutron diffraction, which is valuable for measuring crystal structures, for example.

[8] This analysis ignores possible phase relationships in multiphonon scattering. Multiphonon scattering is usually analyzed in the incoherent approximation, so the transition from quantum mechanics to classical thermodynamics is approximate. Perhaps, however, there are cases where coherent multiphonon scattering can produce interesting features in the scattering $S(\vec{Q}, \omega)$.

- The second term, involving $\frac{\hbar^2 Q^2}{2M} \Big/ (\hbar\omega) = E_R/\varepsilon$, is the inelastic scattering that occurs by exciting one phonon. While the expansion of Eq. 25.77 gives its total intensity, its time spectrum is not included. Its Fourier transform must give a delta function $\delta(\omega - \omega(\vec{q}))$ from the conservation of energy, however. Conservation of momentum gives a similar delta function, $\delta\left((\vec{q} - \vec{Q}) - \vec{g}\right)$. Single-phonon scattering increases as Q^2.
- The third term, involving $\left(\frac{\hbar^2 Q^2}{2M} \Big/ (\hbar\omega)\right)^2 = (E_R/\varepsilon)^2$, is from a scattering process that creates two phonons. This "two-phonon scattering" occurs in one scattering event, not through the creation of two phonons by two different deflections of the neutron. (The latter is "multiple scattering.") When the time spectrum is squared, such as $\cos^2(\omega t) = 1/2\left(1 + \cos(2\omega t)\right)$, the frequency is doubled, and energy conservation provides the delta function $\delta(\omega - 2\omega(\vec{q}))$. Two-phonon scattering can involve twice the energy transfer as a one-phonon process, but two-phonon scattering can also have annihilation processes along with creation processes, giving lower energy transfers, too. Note how the fraction of two-phonon scattering increases rapidly as Q^4.
- Higher-order terms, denoted by $+\cdots$, involve the creation or annihilation of many phonons in one scattering of the neutron. These higher-order terms approach classical behavior. Typically the scattering of a particle with a large momentum transfer causes the excitation of many phonons, features of the energy spectrum are lost, and the spectrum becomes Gaussian shaped. Large momentum transfers are of course possible with particles heavier than neutrons, such as bullets. In this case, the phonon creation is better

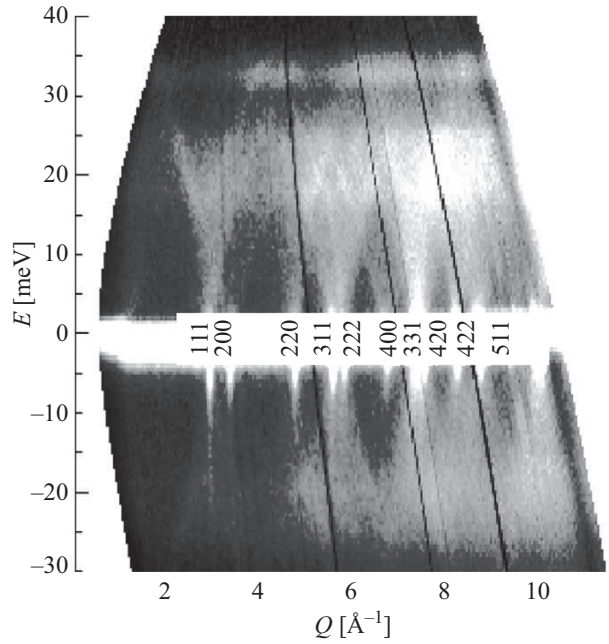

Figure 25.4 Reduced data from an fcc Fe–Ni alloy, obtained with the Fermi chopper spectrometer "Pharos" at Los Alamos National Laboratory. The detector coverage of the instrument does not permit measurements at some combinations of $\{E, Q\}$, which are empty at the left and right of this dataset.

described as the creation of heat. Nevertheless, the transition from quantum behavior to classical behavior is described systematically by higher-order terms in Eq. 25.77.

Data from a Fermi chopper neutron spectrometer are shown in Fig. 25.4. The intensity along the elastic line $E = 0$ is seriously overexposed because the elastic scattering is dominant under the experimental conditions used. (Typically 90% of the scattering is elastic, and the 10% inelastic scattering is spread widely over energy.) The fcc Bragg diffractions are indexed with *hkl* that are all even or all odd integers. Up and down from the Bragg diffractions emerge phonon dispersions, averaged over different crystallographic directions for this polycrystalline sample. These bright streaks are from coherent inelastic neutron scattering, for which the phonon dispersions contribute intensity at particular values of E and Q. Incidentally, a very dim magnon dispersion, concave upwards at low Q, emerges from the point $E = 0$, $Q = 0$.

Problems

25.1 (**a**) Express the diffusion coefficient D in terms of the variables of the Langevin equation.
(**b**) Using Eq. 25.23, explain why the diffusion coefficient is not appropriate for describing atom motions at very short times.

25.2 Consider Eq. 25.6 for the mean-square displacement, using a velocity profile such as that of Fig. 25.1a.
(**a**) Discuss how the behavior of $R^2(\tau)$ at small τ differs from that at large τ.
(**b**) How do the features in Fig. 25.1c affect $R^2(\tau)$?

25.3 Assume the velocity $\vec{v}_i(t)$ in Eq. 25.41 is a Fourier series with different frequencies having different weights. Obtain an expression for $g(\omega)$ in terms of these weights and frequencies.

25.4 The Debye–Waller factor of Section 25.5 is usually written as $D(Q) = \exp(-Q^2\langle x^2\rangle)$. Assume the thermal displacements of an atom of mass m are those of a simple harmonic oscillator, so $\langle x^2\rangle = 2k_BT/(m\omega^2)$.
(**a**) Explain why $E_{rec} = (\hbar Q)^2/2m$ is defined as the recoil energy of scattering.
(**b**) Show that $D(Q) = \exp[-(E_{rec}/\hbar\omega)(k_BT/\hbar\omega)]$.
(**c**) Show how the two fractions in the exponential of part b are related to the probability of exciting a phonon of frequency ω, and the number of phonons in this mode.

25.5 Figure 25.4 is from data acquired at room temperature. Why is the intensity weaker on the phonon annihilation side of the spectrum ($E < 0$) than on the phonon creation side? What sort of intensity imbalance would you expect to observe at a low temperature, such as 4 K? What does this say about extracting energy from the zero-point energy of a harmonic oscillator?

26 Vibrational Thermodynamics of Materials at High Temperatures

This chapter begins with the theory of lattice dynamics for a harmonic crystal. The harmonic model predicts normal modes of vibrations, where each normal mode is specified by wavevector $\vec{k}_i = \hat{k}\, 2\pi/\lambda_i$, and frequency $2\pi\omega_i$. Starting with an interatomic potential, a first goal is to calculate the set $\{\omega_i\}$ for all normal modes of vibration in a periodic crystal. A "phonon" is a quantum of energy ε_i in the normal mode i, with $\varepsilon_i = \hbar\omega_i$. The energy spectrum of all phonon modes, or density of states $g(\varepsilon)$, is the quantity of importance for calculating the heat capacity and vibrational entropy (extending the results of Section 7.5.1). Along the way, dispersion relations $\omega(\vec{k})$ are obtained.

In a harmonic model the vibrations are not damped. In classical mechanics, vibrational damping usually occurs by creating heat, but in quantum theory the phonons are the heat. An absence of damping means that phonons in different normal modes do not interact with each other. The energy of a harmonic phonon remains forever in its normal mode, oblivious to the other phonons in the crystal. Harmonic models are the cornerstone of vibrational thermodynamics because so many mathematical results are available for harmonic oscillators [72–74]. Harmonic models can account for most of the vibrational entropy in a crystal at all temperatures, but at high temperatures the vibrational entropy is so large that an error of 10% would exceed the magnitude of entire configurational entropy, for example. Such inaccuracies of the harmonic model are fairly typical at high temperatures, however. The harmonic model and its convenient features are usually inadequate for understanding the thermodynamics of real materials at moderate temperatures.

Most crystals expand with temperature, so vibrating atoms usually experience a reduced curvature of their potential energy (see Fig. 12.3), and have lower vibrational frequencies. An effect of thermal expansion on entropy can be calculated by assuming that harmonic phonons change their frequencies with temperature, but the phonons remain noninteracting and long lived. This "quasiharmonic approximation" is developed below. It is fairly easy to make predictions about high-temperature thermodynamics with the quasiharmonic approximation, but it is based on harmonic frequencies that depend only on volume. It accounts for only part of the nonharmonic thermodynamics.

Another thermodynamic contribution is from "anharmonic" effects, where phonons interact with each other owing to the cubic and quartic components of the interatomic potential. Anharmonic contributions cause phonon frequencies and lifetimes to change with temperature, even without thermal expansion. These anharmonic effects are challenging to calculate, and are described qualitatively in this chapter.

For metals, another nonharmonic contribution is from the adiabatic electron–phonon interaction (EPI), which depends on the electronic structure near the Fermi level. Quasiharmonicity, anharmonicity, and the temperature dependence of the adiabatic EPI typically

make comparable contributions to the high-temperature thermodynamics of materials, and it takes real effort to sort them out today.

26.1 Lattice Dynamics

26.1.1 Hamiltonian of a Crystal

Essentially all the mass of an atom is in its tiny nucleus, so for lattice dynamics we consider the vibrations of nuclei connected by massless electronic springs. The Hamiltonian for these nuclear motions is

$$H_{\mathrm{n}} = \sum_{l,\kappa} \frac{\vec{p}_{l\kappa}^{\,2}}{2m_\kappa} + \Phi, \tag{26.1}$$

and the characteristics of the atom vibrations depend on the potential energy, Φ. Each atom κ in the unit cell l, of mass m_κ, vibrates about equilibrium with the displacement $\vec{u}_{l\kappa}(t)$. In the notation of Maradudin *et al.* [72], the basis vectors of the unit cell are $\{\vec{r}_\kappa, \kappa = 1, 2, \ldots, \mathcal{R}\}$. The instantaneous position $\vec{R}_{l\kappa}(t)$ of atom $l\kappa$ at time t is

$$\vec{R}_{l\kappa}(t) = \vec{r}_l + \vec{r}_\kappa + \vec{u}_{l\kappa}(t). \tag{26.2}$$

Here $\vec{r}_l$ is the position of the unit cell, $\vec{r}_\kappa$ is the basis vector for an atom in this cell, and $\vec{u}_{l\kappa}(t)$ is the instantaneous displacement of the specific atom $l\kappa$ from its official position in the crystal. The displacement vector is given by Cartesian components $u_{\alpha l\kappa}$, where $\alpha = \{x, y, z\}$

$$\vec{u}_{l\kappa}(t) = u_{xl\kappa}(t)\,\hat{x} + u_{yl\kappa}(t)\,\hat{y} + u_{zl\kappa}(t)\,\hat{z}. \tag{26.3}$$

The total potential energy of the crystal, Φ, is expanded in a Taylor series of the small, instantaneous displacements $\vec{u}_{l\kappa}$, i.e., expanded about the equilibrium positions of the atoms $\vec{R}_{l\kappa} = \vec{r}_l + \vec{r}_\kappa$

$$\begin{aligned}\Phi = \Phi_0 &+ \sum_{\alpha l\kappa} \Phi_{\alpha l\kappa}\, u_{\alpha l\kappa} \\ &+ \frac{1}{2} \sum_{\alpha l\kappa} \sum_{\alpha' l'\kappa'} \Phi_{\alpha\alpha' l\kappa l'\kappa'}\, u_{\alpha l\kappa}\, u_{\alpha' l'\kappa'} + \cdots,\end{aligned} \tag{26.4}$$

where the coefficients of the Taylor series are the derivatives of the potential with respect to the displacements

$$\Phi_{\alpha l\kappa} = \left(\frac{\partial \Phi}{\partial u_{\alpha l\kappa}}\right)_0, \tag{26.5}$$

$$\Phi_{\alpha\alpha' l\kappa l'\kappa'} = \left(\frac{\partial^2 \Phi}{\partial u_{\alpha l\kappa}\, \partial u_{\alpha' l'\kappa'}}\right)_0. \tag{26.6}$$

The subscript zero means that derivatives are evaluated in the equilibrium configuration of a static lattice at equilibrium (all displacements, including zero point, are zero). The Φ_0 is the static potential energy of the crystal, which could be set as its cohesive energy. Because the force on any atom must vanish in the equilibrium configuration

$$\Phi_{\alpha l\kappa} = 0 \qquad \forall\ \alpha, l, \kappa. \tag{26.7}$$

The harmonic approximation of lattice dynamics uses only the terms of the series written explicitly in Eq. 26.4. Terms with cubic, quartic, and higher combinations of the atom displacements are neglected, but we return to them in Section 26.4. In matrix form, the harmonic nuclear Hamiltonian is

$$H_{\mathrm{n}} = \sum_{l\kappa} \frac{\vec{p}_{l\kappa}^{\,2}}{2m_\kappa} + \Phi_0 + \frac{1}{2} \sum_{l\kappa} \sum_{l'\kappa'} \vec{u}_{l\kappa}^{\,T}\, \underline{\Phi}_{l\kappa l'\kappa'}\, \vec{u}_{l'\kappa'}, \tag{26.8}$$

where a force-constant submatrix is defined for each atom pair $(l\kappa; l'\kappa')$

$$\underline{\Phi}_{l\kappa l'\kappa'} = \left[\Phi_{\alpha\alpha' l\kappa l'\kappa'}\right], \tag{26.9}$$

which is a 3×3 matrix with the three Cartesian directions. Equation 26.6 is used directly when $(l, \kappa) \neq (l', \kappa')$. If $(l, \kappa) = (l', \kappa')$, $\Phi_{\alpha\alpha' l\kappa l\kappa}$ is a "self-force constant," derived from the requirement of no overall translation of the crystal

$$\underline{\Phi}_{l\kappa l\kappa} = - \sum_{(l',\kappa') \neq (l,\kappa)} \underline{\Phi}_{l\kappa l'\kappa'}. \tag{26.10}$$

26.1.2 Equations of Motion with Phonon Solutions

In the harmonic approximation, Newton's law gives the equations of motion for each nucleus at $l\kappa$

$$m_\kappa \frac{\partial^2 u_{l\kappa}(t)}{\partial t^2}\, \hat{u} = - \sum_{l',\kappa'} \underline{\Phi}_{l\kappa l'\kappa'}\, \vec{u}_{l'\kappa'}(t) \qquad \forall\ l, \kappa. \tag{26.11}$$

In three dimensions Eq. 26.11 represents $3 \times \mathcal{R} \times N^{\mathrm{cell}}$ coupled equations, where the finite crystal contains N^{cell} unit cells.

We now assume that the crystal has periodic boundary conditions. These require the set of possible wavevectors $\{\vec{k}\}$ to have N^{cell} values, a large number that gives a very fine mesh of points in k-space. With $\mathcal{R}$ atoms in the basis of the unit cell, the crystal has $3 \times \mathcal{R} \times N^{\mathrm{cell}}$ vibrational modes, satisfying the requirement that the number of mechanical degrees of freedom always equals $3\times$ the number of atoms. The solutions for the vibrational displacements are now simplified and organized by Bloch's theorem (Section 6.3).

We seek a phonon solution having the form of a plane wave of wavevector $\vec{k}$, angular frequency $\omega_{\vec{k}j}$, and "polarization" $\vec{e}_{\kappa j}(\vec{k})$ (where j is a "branch index" discussed below)

$$\vec{u}_{l\kappa\vec{k}j}(t) = \sqrt{\frac{2\hbar}{N m_\kappa\, \omega_{\vec{k}j}}}\, \vec{e}_{\kappa j}(\vec{k})\, \mathrm{e}^{\mathrm{i}(\vec{k}\cdot\vec{r}_l - \omega_{\vec{k}j} t)}, \tag{26.12}$$

or with the Planck occupancy to include the contributions from all $n(\varepsilon_{\vec{k}j}, T) + 1/2$ phonons at temperature T

$$\vec{u}_{l\kappa\vec{k}j}(t) = \hbar \sqrt{\frac{2n(\varepsilon_{\vec{k}j}, T) + 1}{N\, m_\kappa\, \varepsilon_{\vec{k}j}}}\; \vec{e}_{\kappa j}(\vec{k})\, \mathrm{e}^{\mathrm{i}(\vec{k}\cdot\vec{r}_l - \omega_{\vec{k}j} t)}. \tag{26.13}$$

We take the real part to obtain physical displacements, or we use the convention of adding the complex conjugate of the exponential, and halving the prefactor.[1] In general, the motion of an atom $\vec{u}_{l\kappa}(t)$ will be a sum over all modes $\vec{u}_{l\kappa\vec{k}j}(t)$ (cf. Eq. 26.57), but it is the individual normal mode that is quantized.

26.1.3 The Polarization Vector $\vec{e}_{\kappa j}(\vec{k})$

Atom Displacement and Phase

The phase factor $\mathrm{e}^{\mathrm{i}\vec{k}\cdot\vec{r}_l}$ in Eqs. 26.12 or 26.13 provides all the long-range spatial modulation of $\vec{u}_{l\kappa\vec{k}j}(t)$. A phonon mode is specified in part by the long-range behavior associated with $\vec{k}$, but also by κ, the index denoting a short-range basis vector of the unit cell of the crystal. This dependence on κ was taken out of the phase factor and placed in the constant $\vec{e}_{\kappa j}(\vec{k})$, called the "polarization vector" for the atom at κ. The polarization vector describes

- the displacement direction of the atom, and
- its phase lag or phase advance with respect to the other atoms in its unit cell.

The phase $\phi_{\kappa\vec{k}j}$ of each atom in the unit cell is dimensionless and spans a range of 2π. The phase appears in the polarization vector $\vec{e}_{\kappa j}(\vec{k})$ in a phase factor $\exp(\mathrm{i}\phi_{\kappa\vec{k}j})$, which is generally a complex number. In the phonon of wavevector $\vec{k}$ and branch j, the different atoms of the unit cell $\{\kappa\}$ vibrate at the same frequency. These atoms of the basis have different amplitudes, but also have different phases with respect to each other. This is in addition to the phase $\vec{k}\cdot\vec{r}_l$ in the exponential of Eq. 26.12, which gives a difference of phase for the different unit cells, l.

One Atom per Unit Cell: Acoustic Modes

The polarization vector is easiest to understand when there is one atom per unit cell. In this case we could dispense with κ, but for consistency we set $\kappa = 1$. The phase information for all atoms is included by the long-range factor for unit cell l, $\mathrm{e}^{\mathrm{i}\vec{k}\cdot\vec{r}_l}$ in Eqs. 26.12 or 26.13. In three dimensions with $\mathcal{R} = 1$, there are three phonon branches – low transverse, high transverse, and longitudinal. Each branch has a different $\vec{e}_{1j}(\vec{k})$ with its own orientation with respect to $\vec{k}$ and its own type of atom displacements. A simple longitudinal branch,

[1] It is convenient for the $\vec{e}_{\kappa j}(\vec{k})$ of Eq. 26.12 to have modulus unity, as does the exponential. The prefactors are consistent with the quantization of energy for one phonon, $\hbar\omega = m\,\omega^2\langle u^2\rangle = \frac{1}{2}\, m\,\omega^2\, u^2_{\max}$, or for the thermal population of phonons in mode $\varepsilon_{\vec{k}j}$, having energy $\varepsilon_{\vec{k}j}\left[n(\varepsilon_{\vec{k}j}, T) + \frac{1}{2}\right]$. (For root-mean-squared displacements, delete the $\sqrt{2}$ in Eqs. 26.12 and 26.13.)

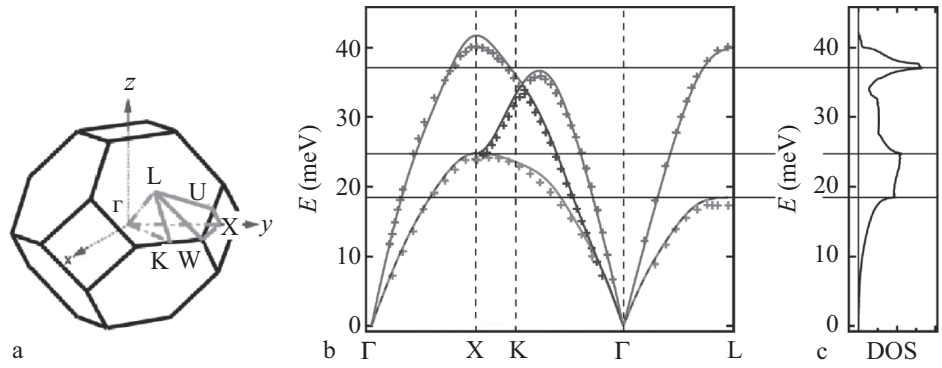

Figure 26.1 (**a**) Notation for directions in the fcc Brillouin zone. (**b**) Dispersion curves for fcc Al, showing experimental points as crosses, and computations with density functional theory. (**c**) Phonon density of states of Al, shown with the same energy scale as dispersions in part b. From [182].

denoted j', has $\vec{e}_{1j'}(\vec{k})$ parallel to $\vec{k}$. The two transverse branches can be degenerate owing to symmetry, but for most directions they have different frequencies because they displace atoms in different directions towards their neighbors.

For a large crystal the wavevectors are essentially continuous, so the frequencies are essentially continuous. The frequencies can be plotted on a set of curves called "dispersions," $\omega_j(\vec{k})$, as shown in Fig. 26.1b. The dispersions have different shapes as $\vec{k}$ points along different crystallographic directions such as [100], [110], [111] (the notation of Fig. 26.1a is used at the bottom of Fig. 26.1b).[2]

At long wavelengths (small k near the origin, called the "Γ-point" in Fig. 26.1b) the phonons are sound waves. Phonon branches that approach zero frequency at the Γ-point are called "acoustic" branches. (All branches in Fig. 26.1b are acoustic branches, since fcc Al has one atom per unit cell.) A feature of long-wavelength acoustic phonons is that neighboring atoms move nearly in unison. The speed of a sound wave is $v = (1/\hbar)\partial\varepsilon/\partial k$, which is the linear slope of a dispersion near the Γ-point. The dispersion curves show that the transverse waves are slower than the longitudinal, and agreement with measurements of elastic wave velocities is good at low temperatures.

At the highest frequencies, i.e., the edges of the Brillouin zone discussed in Section 18.1.1, the dispersions are flat, and the wave speeds are zero. Because the phonon energy does not vary much with $\vec{k}$ near the edges of the Brillouin zone, there is a large volume of k-space with similar values of energies. This causes peaks in the phonon density of state (DOS) as shown in Fig. 26.1c.[3] These peaks in the DOS are called Van Hove singularities, and the horizontal lines between Figs. 26.1b and c show their correspondence to parts of the phonon dispersions near the edges of the Brillouin zone.

[2] Most phonons have wavevectors off the directions of high symmetry, however, where the classification of branches is not simple. Twists or librations of groups of atoms can mix the character of transverse and longitudinal displacements, for example.

[3] Figure 6.3 and its discussion in terms of electronic bands also explain why shallow slopes in dispersions give peaks in a DOS.

Two or More Atoms per Unit Cell: Optical Modes

The polarization vector $\vec{e}_{\kappa j}(\vec{k})$ is more interesting when there are $\mathcal{R} > 1$ atoms in the unit cell. In three dimensions, there are $3 \times \mathcal{R}$ branches of different vibrational modes for each wavevector $\vec{k}$, and each type of mode is identified by a branch index j and a polarization vector $\vec{e}_{\kappa j}(\vec{k})$. The simplest case is two atoms per unit cell, so $\{\kappa\} = \{1, 2\}$. There are now six phonon branches, the three acoustic branches as before, plus three "optical" branches with transverse and longitudinal polarization. The optical branches are distinguished by the relative phases of the two atoms in the unit cell. For modes with long wavelengths near the Γ-point, the two atoms move towards and away from each other in optical modes, instead of in unison for acoustic modes. The frequencies of optical modes do not go to zero at the Γ point. For each additional atom in the unit cell, there are three more optical branches for phonons.

In ionic crystals, where neighboring ions in the unit cell have opposite charge, at the Γ-point an oscillating electric field across the crystal can excite optical phonons (hence the name). Methods of light scattering, such as Raman spectrometry and infrared spectrometry, are sensitive to optical phonons. These methods can measure phonon energies and linewidths to high accuracy. In practice, however, optical methods usually measure only phonon modes very close to the Γ-point, owing to the small momentum of a photon of light.

26.1.4 The Eigenvalue Problem

The vectors $\vec{e}_{\kappa j}(\vec{k})$ for all the atoms in the basis ($1 \le \kappa \le \mathcal{R}$) and their associated angular frequencies $\omega_{\vec{k}j}$ can be calculated by diagonalizing the "dynamical matrix," $\underline{D}(\vec{k})$. The dynamical matrix is obtained after substituting Eq. 26.12 into 26.11. This substitution and sum over unit cells gives Fourier transforms of the real-space atomic forces. The dynamical matrix has the dimensions $3\mathcal{R} \times 3\mathcal{R}$ and is constructed from 3×3 submatrices $\underline{D}_{\kappa\kappa'}(\vec{k})$

$$\underline{D}(\vec{k}) = \begin{pmatrix} \underline{D}_{11}(\vec{k}) & \cdots & \underline{D}_{1\mathcal{R}}(\vec{k}) \\ \vdots & \ddots & \vdots \\ \underline{D}_{\mathcal{R}1}(\vec{k}) & \cdots & \underline{D}_{\mathcal{R}\mathcal{R}}(\vec{k}) \end{pmatrix}. \tag{26.14}$$

Each submatrix $\underline{D}_{\kappa\kappa'}(\vec{k})$ is the Fourier transform of the force-constant matrix $\underline{\Phi}_{l\kappa l'\kappa'}$, considered as a function of $(l' - l)$

$$\underline{D}_{\kappa\kappa'}(\vec{k}) = \frac{1}{\sqrt{m_\kappa m_{\kappa'}}} \sum_{l'} \underline{\Phi}_{0\kappa l'\kappa'} \, e^{i\vec{k}\cdot(\vec{r}_{l'} - \vec{r}_0)}, \tag{26.15}$$

where l was chosen to be 0 because the summation is over all l' and the origin is arbitrary.

Substituting the plane-wave solutions of Eq. 26.12 into the system of differential equations of Eq. 26.11, after organizing the polarization vectors into a vector of size $3\mathcal{R}$, the result can be written as an eigenvalue problem

$$\underline{D}(\vec{k})\, \vec{e}_j(\vec{k}) = \omega^2_{\vec{k}j}\, \vec{e}_j(\vec{k}) \,, \tag{26.16}$$

where the full polarization vector includes all the atoms in the unit cell (all κ from 1, 2 $\ldots \mathcal{R}$)

$$\vec{e}_j(\vec{k}) = \begin{pmatrix} e_{x1j}(\vec{k}) \\ e_{y1j}(\vec{k}) \\ e_{z1j}(\vec{k}) \\ e_{x2j}(\vec{k}) \\ \vdots \\ e_{z\mathcal{R}j}(\vec{k}) \end{pmatrix}. \tag{26.17}$$

In the usual case where the crystal is stable against small vibrations, it can be shown that the $3\mathcal{R} \times 3\mathcal{R}$ dynamical matrix $\underline{D}(\vec{k})$ is Hermitian (for any value of $\vec{k}$), and the $\omega^2_{\vec{k}j}$ are real. After diagonalizing a dynamical matrix constructed with a particular wavevector $\vec{k}$, the $3\mathcal{R}$ eigenvectors and eigenvalues are the $3\mathcal{R}$ polarization vectors $\vec{e}_j(\vec{k})$ and their (squared) frequencies $\omega^2_{\vec{k}j}$.

To calculate the phonon density of states (DOS) of the crystal, $g(\varepsilon)$, the dynamical matrix is diagonalized at a large number of points in reciprocal space, typically covering the first Brillouin zone. These $\vec{k}$ points are chosen to be representative of all the phonon modes in the crystal. The diagonalization of $\underline{D}(\vec{k})$ at each $\vec{k}$ point returns an eigenvalue of angular frequency $\omega_{\vec{k}j}$ for each phonon branch j (where $1 \le j \le 3\mathcal{R}$). These frequencies are added to a histogram of phonon energies. This histogram is the phonon DOS, $g(\varepsilon)$, or the energy spectrum of all phonon modes in the crystal (e.g., Fig. 26.1c). From this energy spectrum, the thermodynamic partition function can be calculated with Eq. 7.47.

26.2 Harmonic Thermodynamics

General Results of a Harmonic Model

First consider a harmonic model where the heat capacity C_V is obtained with a fixed set of oscillator frequencies, i.e., a phonon DOS that is unchanged with temperature. The temperature derivative of the Planck occupancy distribution (Eq. 7.44), weighted by the energy of the mode, ε_i, shows that the ith mode of energy ε_i contributes to the heat capacity at T

$$C_{V,i}(T) = k_\mathrm{B} \left(\frac{\varepsilon_i}{k_\mathrm{B}T}\right)^2 \frac{\exp(\varepsilon_i/k_\mathrm{B}T)}{(\exp(\varepsilon_i/k_\mathrm{B}T) - 1)^2}. \tag{26.18}$$

In the high-temperature (classical) limit where $k_\mathrm{B}T \gg \varepsilon_i$, the heat capacity becomes $1\,k_\mathrm{B}$ per mode.[4] Equation 26.18 is consistent with Eq. 7.43 after integrating over T for all modes

$$S_{V,\mathrm{vib}}(T) = \int_0^T \sum_i^{3N} \frac{C_{V,i}(T')}{T'}\,\mathrm{d}T'. \tag{26.19}$$

[4] This could remain true even if phonon frequencies are reduced with temperature (phonon softening). In the high-temperature limit, with phonon occupancies of $k_\mathrm{B}T/\varepsilon_i$ per mode, the softening of the modes gives an increase in occupancy proportional to $1/\varepsilon_i$, but a decrease in energy proportional to ε_i. The product of these two factors produces a heat capacity C_V at high temperatures that is unaffected by mode softening, so C_V can remain as $3k_\mathrm{B}$/atom at high temperatures. If this softening occurs with thermal expansion, however, there is an additional contribution from elastic energy, as in Eq. 26.39.

Strengths of the Debye Model

A "Debye model" [43] is useful for some predictions about heat capacity. The Debye model assumes a proportionality between phonon energy and wavevector, $\omega = c\,k$, and assumes equal speeds of sound, c, for all phonons. All phonon DOS curves, $g_D(\varepsilon)$, of Debye models in three dimensions have the same shape, being proportional to ε^2 up to a cutoff energy ε_D. At higher energies, $\varepsilon > \varepsilon_D$, the $g_D(\varepsilon)$ is zero. The cutoff energy is found by integrating all phonon modes, and selecting ε_D to give $3N$ modes for a three-dimensional material with N atoms. Figure 26.2a shows heat capacity curves for two materials with slightly different Debye temperatures. Their most pronounced difference is at approximately one-quarter of the Debye temperature. The difference between these two curves, shown in Fig. 26.2b, is typical of the shape of a differential heat capacity curve obtained from real phonon DOSs (e.g., curve "DOS 11 K" in Fig. 9.5). The integral over temperature of this $\Delta C_V/T$ gives the difference in vibrational entropy of the two materials (see Problem 26.2).

Because a Debye model includes a mostly realistic distribution of long-wavelength, low-energy phonons, it predicts a heat capacity at low temperatures that is much more accurate than the heat capacity of a simple harmonic oscillator of fixed frequency (the "Einstein model"). The Debye model can also be useful for interpreting measurements of phonon frequencies at long wavelengths to deduce sound velocities and elastic constants. Problems

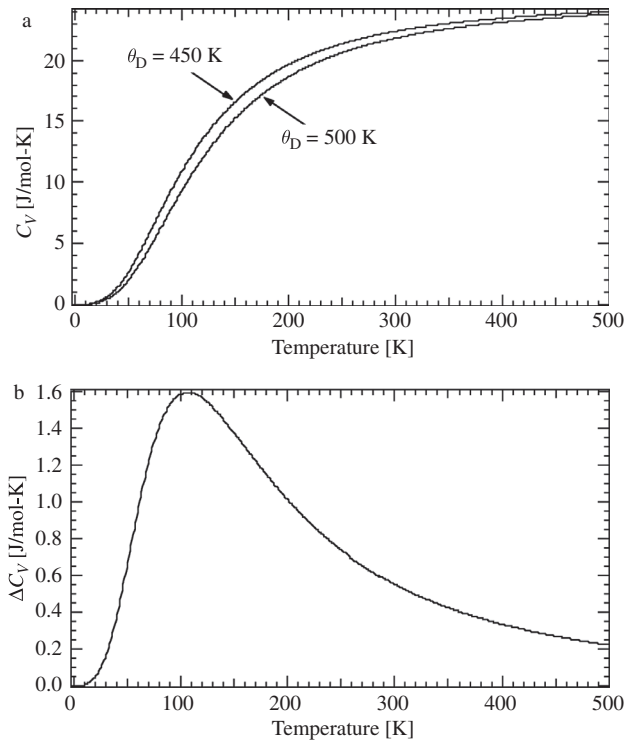

Figure 26.2 (**a**) Heat capacity versus temperature for two Debye solids with Debye temperatures of 450 and 500 K. (**b**) Difference of the two curves in part a.

arise when the Debye model is used for predictions involving short-wavelength phonons, however. Since a phonon DOS is dominated by short-wavelength phonons, a phonon DOS from the Debye model is generally inadequate for thermodynamic predictions.

Weaknesses of the Debye Model

A Debye model does not account for the differences in speeds of transverse and longitudinal sound waves. As an improvement, the phonon DOS of a simple crystal could be approximated with a separate Debye model for each branch, as shown in Fig. 26.3a. The sum of the three Debye functions begins to look like a phonon DOS of a real crystal, as shown in Fig. 26.3b, but there are obvious differences.

One important difference seen in Fig. 26.3 occurs because the velocity of sound is not constant for all wavevectors, as assumed in the Debye model. At the highest values of k, i.e., at the edge of a Brillouin zone, the phonons have zero velocity, $d\omega/dk = 0$. This gives a much greater weight to phonons at the top of the longitudinal branch, giving a sharper peak near the top of the subspectrum from the longitudinal modes.

Another important feature of a real phonon DOS is more subtle than can be shown in simple dispersion plots of Fig. 26.1b. Notice that the $g(\varepsilon)$ in Fig. 26.1c does not show a sharp drop at energies slightly higher than the energies at the X- and L-points (marked with horizontal lines between Figs. 26.1b and 26.1c). This is a feature of phonon dispersions in three dimensions, because a peak in a dispersion curve along one direction may actually be at a saddle point in three dimensions. Some dispersions along directions slightly out of the plane of the paper (slightly off [100] and [111] in these two cases) have maxima at somewhat higher energies than the peaks at X- and L-points. The $g(\varepsilon)$ therefore does not decrease above the energy of the X-point, and does not decrease as abruptly above the energy of the L-point as would be expected from a Debye DOS with one parameter. The volumes in k-space where $d\omega/dk \simeq 0$ cause discernable discontinuities in the slope of $g(\varepsilon)$, however, known as "Van Hove singularities."

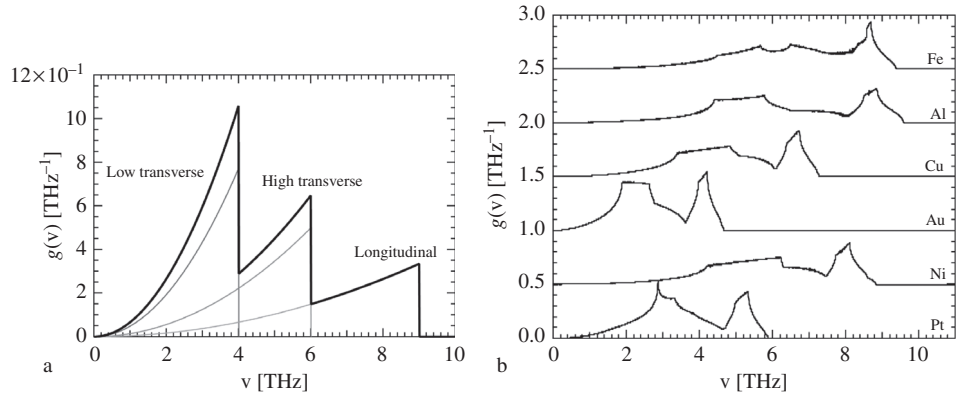

Figure 26.3 (**a**) The sum of three Debye functions of equal areas, with nominal cutoffs appropriate for low transverse, high transverse, and longitudinal branches. (**b**) Phonon DOS curves for five fcc metals and for bcc Fe, showing several kinks that are Van Hove singularities.

26.3 Quasiharmonic Thermodynamics

26.3.1 General Features of the QHA

In the quasiharmonic approximation (QHA), phonons are still quanta of energy of harmonic vibrational modes, but their energies depend on the volume of the material. The QHA assumes a linear relationship between ω_i and V

$$\omega_i(V) = \omega_{i,0}\,(1 - \gamma_i \delta) \ , \quad \text{or with} \quad \varepsilon_i = \hbar\omega_i \tag{26.20}$$

$$\varepsilon_i(V) = \varepsilon_{i,0}\,(1 - \gamma_i \delta)\,, \tag{26.21}$$

where $\omega_{i,0}$ and $\varepsilon_{i,0}$ are the phonon frequency and phonon energy of a stress-free crystal at $T = 0$. The fractional change in volume is

$$\delta \equiv \frac{\delta V}{V}, \tag{26.22}$$

and γ_i is a "mode Grüneisen parameter," defined previously in Eqs. 7.77 and 8.21

$$\gamma_i \equiv -\frac{V}{\omega_i}\frac{\partial \omega_i}{\partial V} = -\frac{1}{\omega_i}\frac{\partial \omega_i}{\partial \delta}. \tag{26.23}$$

The quasiharmonic approximation predicts

- thermal expansion,
- phonon pressure (Section 8.2),
- some nonharmonic entropy at high temperatures,
- the relationship between heat capacity at constant pressure and at constant volume: $C_P - C_V = BV\beta^2 T$,
- the bond stiffness versus bond length theory (Section 7.7).

The QHA ignores any pure temperature dependence of phonon frequencies, however. It considers effects of temperature only through thermal expansion. If the volume is fixed, the QHA predicts no change in phonon frequencies with temperature. Also in the QHA, phonons have infinite lifetimes, so thermal conductivity is infinite.

26.3.2 Thermal Expansion in the QHA

Part of the appeal of the QHA for phonons is that it combines naturally with the elastic energy in the crystal. With reference to a stress-free crystal at $T = 0$, the elastic energy per atom is always positive (energy penalty) for a positive or negative fractional change in volume $\pm\delta$ of Eq. 26.22. At finite temperatures, the thermal expansion depends on how the phonon entropy changes with δ. To calculate an equilibrium $\delta(T)$, we begin with the free energy of the ith phonon in a crystal, and later add E_{elas} that accompanies δ, giving a total free energy in Eq. 26.30 below. To predict thermal expansion, the free energy of the crystal is minimized with respect to δ, giving the result of Eq. 26.36 for all temperatures.

Recall the partition function for a quantum harmonic oscillator and its free energy ($F_{\text{ph}} = -k_{\text{B}}T \ln Z_i$)

$$Z_i = \sum_n \mathrm{e}^{-\frac{(n+\frac{1}{2})\,\varepsilon_i}{k_{\text{B}}T}}, \tag{26.24}$$

$$Z_i = \mathrm{e}^{-\frac{\frac{1}{2}\varepsilon_i}{k_{\text{B}}T}} \sum_n \mathrm{e}^{-\frac{n\,\varepsilon_i}{k_{\text{B}}T}}, \tag{26.25}$$

$$Z_i = \mathrm{e}^{-\frac{\frac{1}{2}\varepsilon_i}{k_{\text{B}}T}} \; \frac{1}{1-\mathrm{e}^{-\frac{\varepsilon_i}{k_{\text{B}}T}}}, \tag{26.26}$$

$$F_{\text{ph},i} = \frac{\varepsilon_i}{2} + k_{\text{B}}T \ln\left(1-\mathrm{e}^{-\frac{\varepsilon_i}{k_{\text{B}}T}}\right). \tag{26.27}$$

For the entire crystal of volume V, the elastic energy is

$$E_{\text{elas}} = \frac{1}{2} B V\, \delta^2, \tag{26.28}$$

where B is the bulk modulus. Adding this elastic energy to the free energy of all vibrational modes

$$F_{\text{tot}} = E_{\text{elas}}(\delta) + \sum_i F_{\text{ph},i}(T,\delta)\,, \tag{26.29}$$

$$F_{\text{tot}} = \frac{1}{2} B V\, \delta^2 + \sum_i^{3N} \left[\frac{\varepsilon_i}{2} + k_{\text{B}}T \ln\left(1-\mathrm{e}^{-\frac{\varepsilon_i}{k_{\text{B}}T}}\right)\right], \tag{26.30}$$

where we have used three normal modes per atom for a three-dimensional crystal of N atoms.

To find the equilibrium expansion that minimizes F_{tot} at finite temperature, take the first derivative with respect to δ

$$\frac{\mathrm{d}}{\mathrm{d}\delta} F_{\text{tot}} = B\,V\,\delta + \sum_i^{3N} \left[\frac{1}{2}\frac{\mathrm{d}\varepsilon_i}{\mathrm{d}\delta} + k_{\text{B}}T \frac{1}{1-\mathrm{e}^{-\frac{\varepsilon_i}{k_{\text{B}}T}}} (-1)\,\mathrm{e}^{-\frac{\varepsilon_i}{k_{\text{B}}T}} \left(\frac{-1}{k_{\text{B}}T}\right) \frac{\mathrm{d}\varepsilon_i}{\mathrm{d}\delta}\right], \tag{26.31}$$

$$\frac{\mathrm{d}}{\mathrm{d}\delta} F_{\text{tot}} = B\,V\,\delta + \sum_i^{3N} \left(\frac{1}{2} + \frac{1}{\mathrm{e}^{\frac{\varepsilon_i}{k_{\text{B}}T}} - 1}\right) \frac{\mathrm{d}\varepsilon_i}{\mathrm{d}\delta}, \tag{26.32}$$

$$\frac{\mathrm{d}}{\mathrm{d}\delta} F_{\text{tot}} = B\,V\,\delta + \sum_i^{3N} \left(n_{\varepsilon_i,T} + \frac{1}{2}\right) \frac{\mathrm{d}\varepsilon_i}{\mathrm{d}\delta}\,, \tag{26.33}$$

where $n_{\varepsilon_i,T}$ is the Planck occupancy factor, and the zero point adds 1/2 to the occupation number of the ith mode. Equation 26.21, $\varepsilon_i(V) = \varepsilon_{i,0}\,(1-\gamma_i\delta)$, is a linear relationship between phonon energy and dilation, so $\mathrm{d}\varepsilon_i/\mathrm{d}\delta = -\varepsilon_{i,0}\,\gamma_i$ and

$$\frac{\mathrm{d}}{\mathrm{d}\delta} F_{\text{tot}} = B\,V\,\delta - \sum_i^{3N} \left(n_{\varepsilon_i,T} + \frac{1}{2}\right) \varepsilon_{i,0}\,\gamma_i. \tag{26.34}$$

For the minimum free energy, setting $dF_{tot}/d\delta = 0$ gives

$$\delta(T) = \frac{1}{BV} \sum_i^{3N} \gamma_i \left(n_{\varepsilon_i,T} + \frac{1}{2} \right) \varepsilon_{i,0}. \tag{26.35}$$

This is the fractional volume expansion at temperature T in the quasiharmonic approximation.[5] The fractional change in volume is positive if γ is positive (since all other quantities are always positive). The volume thermal expansivity,[6] β, is the temperature derivative of $\delta(T)$

$$\beta(T) \equiv \frac{d\delta}{dT} = \frac{1}{BV} \sum_i^{3N} \gamma_i \frac{d}{dT} \left(n_{\varepsilon_i,T} + \frac{1}{2} \right) \varepsilon_{i,0}. \tag{26.36}$$

Here only the Planck occupancy depends on temperature. Its derivative with respect to temperature gives the change in thermal energy in each vibrational mode, or the heat capacity $C_{V,i}(T)$

$$\beta(T) = \frac{1}{BV} \sum_i^{3N} \gamma_i C_{V,i}(T). \tag{26.37}$$

In the QHA, Eq. 26.37 is expected to be valid at all temperatures. It is common practice to construct an average Grüneisen parameter $\overline{\gamma}$, so the thermal expansivity is

$$\beta(T) = \frac{\overline{\gamma} C_V(T)}{BV}. \tag{26.38}$$

Equation 26.38 is risky for many reasons including its neglect of anharmonicity, and the care required to average over a distribution of Grüneisen parameters as broad as shown below in Fig. 26.7. As is the practice with a Debye temperature, a Grüneisen parameter should be presented with information about how it was determined, and especially at low temperatures, $\overline{\gamma}$ is expected to be a function of T. Finally, a Grüneisen parameter obtained from the change of phonon frequencies under pressure (e.g., Eq. 26.23) is probably unreliable for calculating thermal expansion with Eq. 26.38, as discussed in Section 26.4.1.

26.3.3 Heat Capacity and Entropy in the QHA

Much thermodynamic information has been learned from calorimetry, which measures the amount of heat going into the solid for a small change in temperature, $C_P(T)$ (and using a constant pressure on the sample). The difference between C_P and C_V is a classical thermodynamic relationship

$$C_P - C_V = BV\beta^2 T. \tag{26.39}$$

Equation 26.39 can be derived from formal thermodynamic manipulations, aided for example by techniques of Jacobian transformations.

[5] Even when $T = 0$, there is some expansion from the zero-point contribution of 1/2 to each phonon occupancy.
[6] The more common coefficient of linear thermal expansivity, α, is equal to $\beta/3$ for small expansions in three dimensions.

A physical derivation of Eq. 26.39 can be performed by considering the free energy of a crystal with N atoms, but with only phonons and thermal expansion. There are energy terms from the phonons and from the elastic energy, and an entropy from the phonons. The free energy is

$$F(T) = E_{\text{elas}}(T) + E_{\text{ph}}(T) - TS_{\text{ph}}. \tag{26.40}$$

Assume a crystal with N atoms and volume V. The elastic energy of thermal expansion is found by using $\delta = \beta T$ in Eq. 26.28. The phonon energy and the phonon entropy, both in the high-T limit (cf. Eq. 7.51), are used in Eq. 26.40 to give

$$F(T) = \frac{1}{2}BV\beta^2T^2 + 3Nk_{\text{B}}T - Tk_{\text{B}}\sum_i^{3N}\ln\left(\frac{k_{\text{B}}T}{\hbar\omega_i}\right). \tag{26.41}$$

In the QHA we assume that the phonon frequency ω_i is dependent only on volume, so its temperature dependence comes entirely from thermal expansion. Using the same approach as Eq. 7.80 with $\omega_i = \omega_i^0(1 - \gamma\delta)$, and again $\delta = \beta T$ from the thermal expansion

$$S_{\text{ph}}(T) = k_{\text{B}}\sum_i^{3N}\ln\left(\frac{k_{\text{B}}T}{\hbar\omega_i^0(1-\gamma_i\beta T)}\right), \tag{26.42}$$

$$S_{\text{ph}}(T) = k_{\text{B}}\sum_i^{3N}\ln\left(\frac{k_{\text{B}}T}{\hbar\omega_i^0}\right) + k_{\text{B}}\sum_i^{3N}\gamma_i\beta k_{\text{B}}T\,, \tag{26.43}$$

$$S_{\text{ph}}(T) = S_{\text{ph}}^0(T) + \Delta S_{\text{q}}(T), \tag{26.44}$$

where the term $S_{\text{ph}}^0(T)$ is recognized as the harmonic phonon entropy with phonon frequencies ω_i^0 characteristic of $T = 0$, and the quasiharmonic correction to it is

$$\Delta S_{\text{q}} = 3N\overline{\gamma}\beta k_{\text{B}}T, \tag{26.45}$$

where $\overline{\gamma}$ is an average of the mode Grüneisen parameters, and high temperatures were assumed.

Most experimental measurements of heat capacity allow the sample to expand thermally during the measurement, so the heat capacity is measured at constant pressure (not volume). This C_P is defined as

$$C_P(T) = T\left(\frac{\partial S}{\partial T}\right)_P. \tag{26.46}$$

To allow for volume changes from thermal expansion, substitute Eq. 26.38 into 26.45, and use Eq. 26.46 to get the correction to the heat capacity from the QHA, ΔC_{q}. (This is straightforward in the classical limit because ΔS_{q} is linear in T, and $C_V = 3Nk_{\text{B}}$.)

$$\Delta C_{\text{q}} = C_P - C_V = BV\beta^2T, \tag{26.47}$$

where C_V is from harmonic phonons at constant volume, and C_P includes correction for thermal expansion. Typical effects on the heat capacity are shown in Fig. 26.4. This ΔS_{q} of

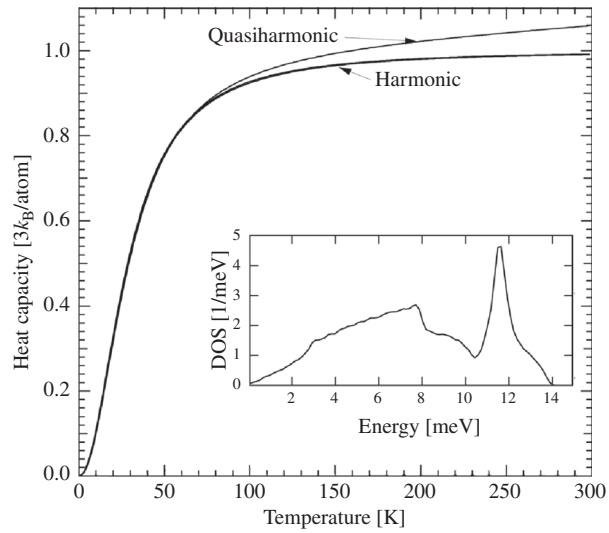

Figure 26.4 Heat capacity versus temperature for models of cerium metal. Inset is the phonon DOS at 0 K, and the harmonic heat capacity curve was obtained from this DOS ($3k_B$/atom is the classical limit). The elastic energy from thermal expansion was added to the harmonic curve to obtain the quasiharmonic curve. Using experimental β and B, a γ was obtained from Eq. 26.38 which predicted the phonon DOS would soften by 6.5% from 0 to 300 K. (The real heat capacity of cerium also includes electronic and anharmonic contributions.)

Eq. 26.45 should always be considered when comparing the vibrational thermodynamics of different materials at elevated temperatures.

The QHA offers a fully consistent picture of the thermodynamics of thermal expansion, including a derivation of the general relationship Eq. 26.47. However, this does not prove that the QHA is complete. As discussed in Section 26.4.1, anharmonicity can invalidate Eq. 26.38 if δ is obtained from the volume dependence of phonon frequencies.

26.3.4 A General Thermodynamic Relationship

This last analysis of the difference $C_P - C_V$ assumed the high-temperature limit. A classical but convenient way to evaluate the difference $C_P - C_V$ at any temperature is by considering a cyclic process that converts thermal expansion into mechanical work. Suppose we have a system that constrains a material to allow heating and cooling at constant volume. By constraining the solid to suppress thermal expansion or contraction, elastic energy will accumulate upon heating and cooling. At both the high and low temperatures we assume the constraints are released quasistatically, and mechanical work is done by the system. The four-step process is shown and described in Fig. 26.5. It is a Carnot cycle.

The essential analysis is bookkeeping of the changes in heat and work during the four steps shown in Table 26.1. With all four steps, which return to the initial state (so $dE = 0$), and defining $\Delta T \equiv T_2 - T_1$

Table 26.1 Steps of thermal expansion engine

Step	$đQ$	$đW$
1	$C_V\,\Delta T$	0
2	$(C_P - C_V)T_2$	$-\frac{1}{2}BV(\beta\,\Delta T)^2$
3	$-C_V\,\Delta T$	0
4	$-(C_P - C_V)T_1$	$-\frac{1}{2}BV(\beta\,\Delta T)^2$

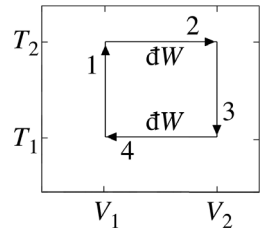

Figure 26.5 A cyclic quasistatic process that returns to the initial state at low temperature and low volume after four steps. Step 1 is heating at constant volume, Step 2 is expansion at constant temperature, Step 3 is cooling constant volume, Step 4 is contraction at constant temperature. Work on an external system is done in steps 2 and 4.

$$\mathrm{d}E = 0 = \sum_{i=1}^{4} đQ_i + đW_i, \tag{26.48}$$

$$0 = C_V\,\Delta T + 0 + (C_P - C_V)T_2 - \frac{1}{2}BV(\beta\,\Delta T)^2 - C_V\,\Delta T + 0 - (C_P - C_V)T_1 - \frac{1}{2}BV(\beta\,\Delta T)^2, \tag{26.49}$$

$$(C_P - C_V)(T_2 - T_1) = BV(\beta\,\Delta T)^2, \tag{26.50}$$

$$C_P - C_V = BV\beta^2\,\Delta T. \tag{26.51}$$

This is the same as Eq. 26.47, but obtained in a more general way. Equation 26.51 is valid at all temperatures. It did not require the quasiharmonic approximation, but the QHA is consistent with Eq. 26.51.

26.3.5 Concepts beyond the QHA

Here is a short overview of concepts that are generally important for materials thermodynamics at finite temperature, with illustrations in Fig. 26.6. Three of them are beyond the volume-dependent effects of the quasiharmonic approximation, QHA. Diagrams are shown for low temperatures at the bottom and high temperatures at the top. Phonon concepts for a fixed interatomic potential $\Phi(r)$ are on the left; electron concepts with a simple free electron band structure are on the right.

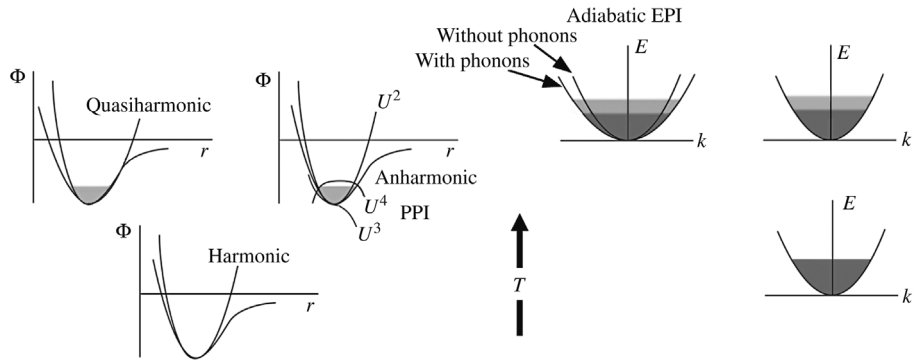

Figure 26.6 Effects of temperature, increasing from bottom to top, on phonons (left, affecting H_n), electrons (right, affecting H_e), and the existence of the adiabatic EPI when phonons alter the electronic bandstructure in the presence of electron excitations (top, affecting H_{ep}). Increasing width of light shading indicates increasing thermal energy spreads.

At low temperatures, the vibrating atoms usually explore a small part of their interatomic potential wells. As in the lower left of Fig. 26.6, a parabolic fit to the interatomic potential is appropriate, and the harmonic model follows. In the QHA, the parabola is altered in position and curvature to accommodate small shifts in the effective potential as the atoms vibrate with greater amplitudes. (The thermal spread in energy, of order $k_B T$, is shown by light shading.)

The QHA assumes that phonons are eigenstates of a harmonic Hamiltonian for a crystal that has undergone some thermal expansion. As a harmonic model, the QHA predicts that phonons have no interactions and have infinite lifetimes. In reality, the shortening of phonon lifetimes causes an energy broadening of the phonon spectrum of fcc Al metal, for example, as in Fig. 12.5b. This broadening is dominated by effects of cubic anharmonicity in the interatomic potential. The cubic and quartic contributions to the potential energy both cause additional shifts of phonon frequencies with temperature, and these shifts do not originate with thermal expansion. The energy cost to add a phonon depends on the number of phonons already present. This "phonon–phonon interaction" (PPI) is a "many-body effect," and it occurs even when there is no thermal expansion.

In analyses where the cubic and quartic anharmonicities are "small," the anharmonic shifts of phonon frequencies are found to be linear with temperature. Equation 26.45 shows that the quasiharmonic correction is also expected to be linear with temperature. To a good approximation, therefore, the relative importances of quasiharmonicity and anharmonicity are unchanged with temperature. If anharmonicity is more important than quasiharmonicity at high temperatures, it will be more important at intermediate temperatures, too.

The electron states at the lower right in Fig. 26.6 are filled to the Fermi level at $T = 0$, but at higher temperatures the shading illustrates a thermal spread of energies from the Fermi–Dirac distribution. At higher temperatures, as more phonons cause the nuclei to have larger excursions about their equilibrium positions, the electron band structure is altered. If this occurs without thermal excitations of electrons, the change in energy is that for anharmonic phonons, which is already counted.

On the other hand, when there are thermal excitations of both phonons and electrons, there is usually a change in energy that depends on both types of excitations. The conditions for obtaining this extra energy are illustrated at the top of Fig. 26.6. This is an adiabatic electron–phonon interaction, and gives $H_{\rm ep}$ of Eq. 28.43. Although differing in its thermal factor, the adiabatic EPI has similarities to the nonadiabatic EPI responsible for Cooper pairing in conventional superconductors (and the EPI was sometimes mistakenly assumed to be only a low-temperature phenomenon). The next sections give more details about the PPI and the EPI at high temperatures.

26.4 Anharmonicity and Phonon–Phonon Interactions

26.4.1 Anharmonicity or Quasiharmonicity?

The mode Grüneisen parameter, γ_i of Eq. 26.23, is properly defined for each phonon mode i, but the temptation is to assign the same γ for all phonon modes, or to assume that an average $\overline{\gamma}$ can account for thermodynamic trends. Obtaining an average of $\{\gamma_i\}$ misses much of the rich detail shown in Fig. 26.7a for monoclinic ZrO_2, of course, so it may be risky to interpret thermophysical trends with such a simplified approach.

Nevertheless, Eq. 26.38 is useful for separating anharmonic from quasiharmonic behavior.[7] Suppose we know the thermal shifts of the phonon frequencies, from which we calculate an average Grüneisen parameter $\overline{\gamma}$. With the phonon DOS we can also calculate C_V, and conventional measurements can provide B, V, and β, accounting for all unknowns in Eq. 26.38. If Eq. 26.38 is found to be true when $\overline{\gamma}$ is determined from the phonon shifts with thermal expansion, the solid may be "quasiharmonic." The validity of Eq. 26.38 with a $\overline{\gamma}$ derived from phonons is a necessary condition for identifying quasiharmonicity without anharmonicity, but it is not a sufficient condition. Detailed phonon behavior may be different than the average, for example.

Quasiharmonic behavior can be better separated from anharmonic behavior by comparing the temperature dependence of a phonon frequency to its pressure dependence [403]. These are given by isothermal and isobaric Grüneisen parameters, γ_{iT} and γ_{iP}, respectively

$$\gamma_{iT} \equiv -\frac{V}{\omega_i}\left(\frac{\partial \omega_i}{\partial V}\right)_T, \tag{26.52}$$

$$\gamma_{iP} \equiv -\frac{V}{\omega_i}\left(\frac{\partial \omega_i}{\partial V}\right)_P, \tag{26.53}$$

$$\gamma_{iP}^{\rm QHA} = -\frac{V}{\omega_i}\left(\frac{\partial \omega_i}{\partial T}\right)_P \frac{{\rm d}T}{{\rm d}V} = -\frac{1}{\beta\,\omega_i}\left(\frac{\partial \omega_i}{\partial T}\right)_P, \tag{26.54}$$

where γ_{iT} has been used previously, and is general. In Eq. 26.54 $\gamma_{iP}^{\rm QHA}$ was assumed to originate with volume alone (and, therefore, thermal expansivity, β). The QHA therefore

[7] In the past, the effect of volume expansion on phonons was considered part of the anharmonicity, as in [401].

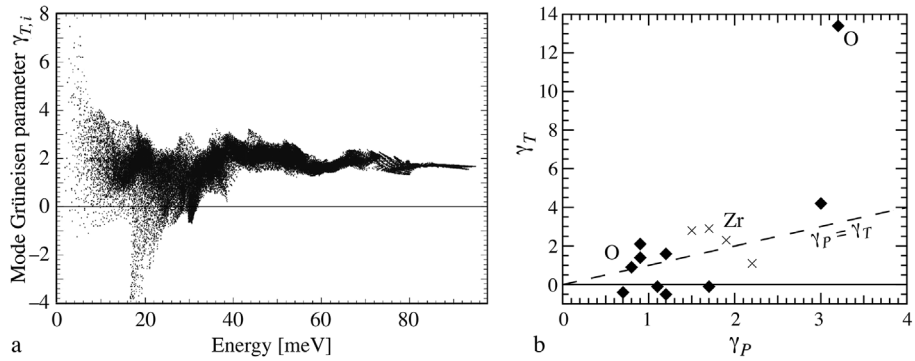

Figure 26.7 (**a**) Mode Grüneisen parameters for many phonon modes in monoclinic ZrO_2, calculated by first-principles methods at low temperatures (these are γ_{iT}). From C.W. Li and B. Fultz, unpublished results. (**b**) Mode Grüneisen parameters for 14 phonon modes in monoclinic ZrO_2, measured by Raman spectrometry. The γ_{iT} were obtained from phonon energy shifts at increasing pressure at a constant temperature of 300 K, and the γ_{iP} were measured from phonon energy shifts at increasing temperature at ambient pressure, with volume changes obtained from thermal expansion. Phonon modes dominated by motions of Zr atoms are shown as crosses, and modes dominated by motions of O atoms are shown as diamonds. The dashed line has a slope of 1. See also [402].

predicts $\gamma_{iT} = \gamma_{iP}$. Differences between γ_{iT} and γ_{iP} indicate pure anharmonicity (although metals can have additional contributions from electron–phonon interactions). For example, Fig. 26.7b shows Grüneisen parameters for 14 Raman modes that were obtained by measuring frequency shifts caused by volume changes induced by pressure or by thermal expansion. These should lie along the dashed line if the material is quasiharmonic and $\gamma_{iT} = \gamma_{iP}$. Evidently monoclinic ZrO_2 is rather anharmonic. Substantial deviations from quasiharmonic behavior are known for Cr [317], V [404], Ce [405], Mo, W, Si, Ge [192, 406, 407], A15 compounds [408], B2 FeV [409], the oxides HfO_2, ZrO_2, TiO_2, SnO_2, Ag_2O [402, 410–413], and the alkali halides NaI and KBr [414]. Hints of anharmonic behavior can often be found from anomalies in thermal expansion, especially if no phase transition occurs [415].

In the case of metals, electron–phonon interactions may also cause deviations from quasiharmonic behavior. The next sections treat separately the effects of phonon–phonon interactions and electron–phonon interactions, but these are difficult to separate by experimental measurements alone.

26.4.2 Anharmonicity in *k*-Space

To understand anharmonicity, we consider in detail the Hamiltonian for nuclear motions H_n of Eq. 28.43, extending the Taylor series beyond the harmonic term (e.g., Eq. 26.4)

$$H_{\mathrm{n}} = \Phi_0 + \sum_{l} \frac{\vec{p}_l^{\,2}}{2m} + \frac{1}{2!} \sum_{l\alpha} \sum_{l'\alpha'} \Phi_{\alpha\alpha' ll'}\, u_{\alpha l}\, u_{\alpha' l'} + \frac{1}{3!} \sum_{l\alpha} \sum_{l'\alpha'} \sum_{l''\alpha''} \Phi_{\alpha\alpha'\alpha'' ll'l''}\, u_{\alpha l}\, u_{\alpha' l'}\, u_{\alpha'' l''} + \frac{1}{4!} \sum_{l\alpha} \sum_{l'\alpha'} \sum_{l''\alpha''} \sum_{l'''\alpha'''} \Phi_{\alpha\alpha'\alpha''\alpha''' ll'l''l'''}\, u_{\alpha l}\, u_{\alpha' l'}\, u_{\alpha'' l''}\, u_{\alpha''' l'''} + \cdots, \qquad (26.55)$$

where the development was simplified to one atom per unit cell, so $u_{\alpha l}$ is the displacement of atom l along Cartesian direction α.

The transformation to normal coordinates for an infinite periodic crystal is

$$\vec{U}_{\vec{k}_i} = \frac{1}{\sqrt{N\,m}} \sum_{\vec{r}_l} \vec{u}_{\vec{r}_l} \mathrm{e}^{-\mathrm{i}\vec{k}_i \cdot \vec{r}_l}, \qquad (26.56)$$

and by Fourier inversion

$$\vec{u}_{\vec{r}_l} = \frac{1}{\sqrt{N\,m}} \sum_{\vec{k}_i} \vec{U}_{\vec{k}_i} \mathrm{e}^{+\mathrm{i}\vec{k}_i \cdot \vec{r}_l}. \qquad (26.57)$$

Substituting Eq. 26.57 into Eq. 26.55, the Fourier transform of $\Phi_{\alpha\alpha' ll'}$ is identified, and used to define the dynamical matrix of Eqs. 26.14 and 26.15.

Our interest is how the higher-order terms of Eq. 26.55, the cubic and quartic terms with the 1/3! and 1/4! prefactors, cause anharmonic behavior when the atoms are vibrating with substantial amplitude. After substituting Eq. 26.57 for instances of displacement such as $u_{\alpha'' l''}$ in Eq. 26.55, the cubic and quartic terms become Fourier transforms of the anharmonicity tensors. For example, the cubic term becomes

$$V(\vec{k}_i, \vec{k}_j, \vec{k}_k) = \frac{1}{3!} \sqrt{\frac{1}{N\,m^3} \left(\frac{\hbar}{2}\right)^3 \frac{1}{\omega_{\vec{k}_i}\, \omega_{\vec{k}_j}\, \omega_{\vec{k}_k}}}\; \delta(\vec{k}_i + \vec{k}_j + \vec{k}_k - \vec{g}) \times \sum_{\vec{r}_\kappa} \vec{e}(\vec{k}_i)\, \vec{e}(\vec{k}_j)\, \vec{e}(\vec{k}_k)\, \mathrm{e}^{+\mathrm{i}(\vec{k}_i + \vec{k}_j + \vec{k}_k) \cdot \vec{r}_\kappa}\; \Phi_{\alpha,\alpha',\alpha'' \kappa,\kappa',\kappa''}, \qquad (26.58)$$

where the factor δ signifies that the sum $\vec{k}_i + \vec{k}_j + \vec{k}_k$ equals a reciprocal lattice vector, $\vec{g}$. Energy conservation is also required for each individual three-phonon process. The term $V(\vec{k}_i, \vec{k}_j, \vec{k}_k)$ from the cubic part of the potential, and a separate $V(\vec{k}_i, \vec{k}_j, \vec{k}_k, \vec{k}_l)$ from the quartic part, give energies of "phonon–phonon interactions." These alter the energy of a phonon when more phonons are present in the crystal (i.e., when the vibrational amplitudes of all atoms are larger).

These alterations of the "self-energy" of a phonon can have both real and imaginary parts. The real part, an energy shift, is directly relevant to the vibrational entropy. The imaginary part shortens the lifetime of a phonon, giving an energy broadening that can be large.

26.4.3 Many-Body Theory

In perturbation theory, the cubic and quartic anharmonicities are assumed small, so harmonic phonons are a good basis set for describing vibrational dynamics. In a harmonic potential these phonon states are orthogonal and non-interacting, but cubic and quartic perturbations bring interactions that change the phonon states and their energies. The energy of a phonon is increasingly altered when more phonons are present. This is a many-body effect, and an interacting phonon is sometimes called a "quasiparticle." This interacting phonon has shortened lifetime as it decays into two phonons, or combines with another to make a third. Further discussion of methods of many-body perturbation theory [416–418] becomes too heavy to carry in the present text. Some important results are well known, however [419]:

- To first order in perturbation theory, the cubic term of Eq. 26.58 is not important for crystals in which all atoms have inversion symmetry because the potential must be an even function of phonon amplitude.
- The lifetime broadening of phonons originates primarily from the cubic anharmonicity to second order in perturbation theory. This cubic term (but not the quartic) contributes an imaginary part to the phonon self-energy that shortens the phonon lifetime, giving a broadening to its energy spectrum.
- Both the cubic anharmonicity to second order and the quartic anharmonicity to first order make comparable contributions to the phonon frequency shifts. These contributions are often comparable to, or larger than, the quasiharmonic frequency shifts. To varying degrees, these different contributions may add or cancel.

The signs of the contributions to frequency shifts may be positive or negative. For fcc aluminum metal, the effects of cubic and quartic anharmonicities are of opposite sign and nearly cancel, so the phonon frequency shifts actually appear consistent with quasiharmonic predictions. The anharmonicities are large, however, and cause substantial lifetime broadening of the phonon energies in aluminum. Other fcc metals have significant lifetime broadenings, but moderate phonon frequency shifts, perhaps for the same reasons as aluminum.

26.4.4 Kinematics of Phonon–Phonon Interactions

Energy and Momentum Conservation

In quantum mechanics, the cubic and quartic perturbations serve to "scatter" harmonic phonons, such as having one phonon separate into two, for example. This phonon scattering must satisfy momentum and energy conservation, and these conditions depend on the wavevectors and energies of the specific three (or four) phonons that interact. Details of the phonon dispersions are immediately relevant when attempting to calculate anharmonic behavior, and several concepts have been developed. For example, if the phonon dispersion relation $\varepsilon(\vec{k})$ were linear, it would be easy to add two wavevectors $\vec{k}+\vec{k}' = \vec{k}''$, and simultaneously conserve energy $\varepsilon + \varepsilon' = \varepsilon''$. The number of three-phonon

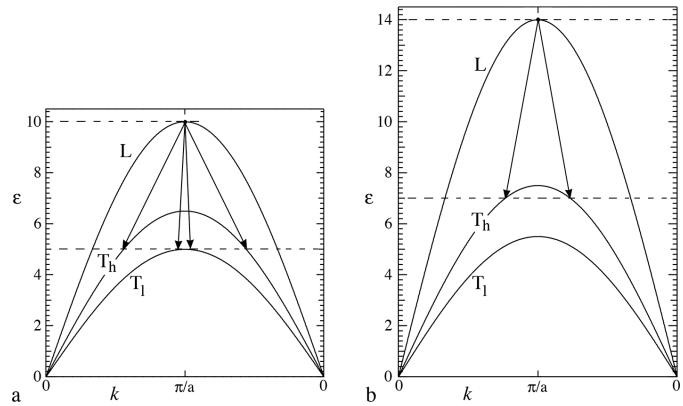

Figure 26.8 (**a**) Downscattering of a longitudinal phonon to both transverse branches. (**b**) Altered phonon dispersions where downscattering of the longitudinal phonon is possible to only one transverse branch.

processes increases as k^2 at small k where the dispersions are approximately linear. Many phonon dispersions, $\varepsilon(\vec{k})$, are concave downwards, however, so simultaneous energy and momentum conservation is impossible for larger k unless at least one phonon lies on a different branch.

An example is shown in Fig. 26.8a, where a phonon in the longitudinal branch is downscattered into one of two possible pairs of transverse phonons in the T_h and T_l branches. In both cases, the energies of the two new phonons sum to the energy of the longitudinal phonon, and the momenta also satisfy their conservation condition. (For the $k = 0$ point on the right of the x-axis, it is possible to add a reciprocal lattice vector of $2\pi/a$ to make a linear increase of k from left to right.)

For larger phonon wavevectors $\vec{k}$, momentum conservation is possible by adding a reciprocal lattice vector. The idea is that the momentum transferred to the entire crystal occurs with zero energy because of the large mass of the crystal. Such "umklapp" processes allow many more three-phonon interactions, but the phonon wavevectors must be of length comparable to the reciprocal lattice vector if the vector additions are possible.

Kinematics Alone

In general when summing contributions of Eq. 26.58, it is not strictly possible to separate the problem into a kinematic factor from momentum and energy conservation, and a factor from the anharmonicity for different atom displacements. Nevertheless, it does appear that the kinematic factor has a much stronger variation with wavevector than does the anharmonicity factor, so approximate methods have been based on this separation. In an older model by Klemens [420], the sum in Eq. 26.58 (which is a Fourier transform) was approximated as

$$\Phi(\vec{k}_i, \vec{k}_j, \vec{k}_k) = \frac{2\mathrm{i}\,\gamma}{v\sqrt{3m}}\,\omega(\vec{k}_i)\,\omega(\vec{k}_j)\,\omega(\vec{k}_k)\,, \tag{26.59}$$

where v is a velocity of sound and γ is an averaged Grüneisen parameter. To calculate the lifetime broadening in this approximation, it is necessary to separate the thermal factors for "downscattering," where a phonon decays into two others of lower energy, from "upscattering," where a phonon combines with another to create a phonon of higher energy. These kinematic factors conserve momentum and energy as

$$D_{\downarrow}(\vec{k},\omega) = \frac{1}{N}\sum_{\vec{k_1},\vec{k_2}} \delta(\vec{k}-\vec{k}_1-\vec{k}_2)\,\delta(\omega-\omega_1-\omega_2), \tag{26.60}$$

$$D_{\uparrow}(\vec{k},\omega) = \frac{1}{N}\sum_{\vec{k_1},\vec{k_2}} \delta(\vec{k}+\vec{k}_1-\vec{k}_2)\,\delta(\omega+\omega_1-\omega_2), \tag{26.61}$$

where the sums over $\vec{k}$ should include phonons in different branches. (Downscattering of a phonon from a longitudinal branch into two phonons in transverse branches, as illustrated in Fig. 26.8, is quite common, for example.) With the definition of these upscattering and downscattering factors, the half-width of the phonon energy broadening Γ in the Klemens model at high temperatures is

$$\Gamma(\vec{k}) = \frac{\pi k_B T}{12}\,\frac{\gamma^2\omega^2}{mv^2}\left(D_{\downarrow}(\vec{k},\omega) - 2D_{\uparrow}(\vec{k},\omega)\right). \tag{26.62}$$

This approximation can be successful [421], indicating that kinematic factors can dominate the $\vec{k}$-dependence of the phonon lifetime broadening. For quantitative work, the problem is the choice of γ, which differs from Grüneisen parameters obtained in other ways. Furthermore, its importance is magnified because it is squared in Eq. 26.62. In practice, this Grüneisen parameter is perhaps best considered a scaling parameter, but the $\vec{k}$-dependence of Eq. 26.62 may be useful.

26.4.5 Phonon–Phonon Interactions at Temperature and Pressure

In general, phonon frequencies depend on the average positions of nuclei and temperature, so $\omega = \omega(V,T)$. The Grüneisen parameter is proportional to the volume derivative, $\gamma \sim (\partial\omega/\partial V)_T$, and the anharmonicity is proportional to the temperature derivative, $A \sim (\partial\omega/\partial T)_V$. By taking derivatives of these quantities with respect to the other variable, and equating mixed derivatives as $(\partial^2\omega/\partial T\partial V)_{VT} = (\partial^2\omega/\partial V\partial T)_{TV}$, it can be shown that the temperature derivative of the Grüneisen parameter $(\partial\gamma/\partial T)_V$ equals the volume derivative of the anharmonicity $(\partial A/\partial V)_T$. The physical origins of these two effects must be the same.

Figure 26.8b illustrates phonon dispersions that differ from those of Fig. 26.8a. All three phonon dispersions are depicted as increasing with pressure, but not by the same fractional amounts. Such behavior is expected under pressures of tens of GPa if the different phonon branches have different Grüneisen parameters. This difference causes the anharmonicity from phonon–phonon interactions to be altered by pressure. The figure shows how the longitudinal mode can no longer decay into two phonons on the low transverse branch because energy would not be conserved. Furthermore, there are fewer decay channels to

the high transverse branch, which also extends out of the plane of the paper for a two-dimensional material (and the arrows touch a surface for three-dimensional materials). In this case, Fig. 26.8b illustrates how the cubic anharmonicity for phonons near the peak in the longitudinal branch would be reduced with pressure. In the context of Eq. 26.54, Fig. 26.8 illustrates why $(\partial\omega_i/\partial T)_P$ may vary with P.

Likewise, we expect that $(\partial\omega_i/\partial V)_T$ may vary with T, i.e., the Grüneisen parameter γ_{iT} may change with temperature. At both high temperature and high pressure, the thermodynamics of materials may require cross-terms, not just adding contributions from quasiharmonicity and anharmonicity.

Thermodynamics does give a few identities that are valid at all T and P. One of them is particularly useful for understanding equations of state, which are relationships between V, T, and P, such as the functional form of $V(T,P)$. Consider a free energy of the general form $F(V,T)$, and take its mixed second derivative

$$\frac{\partial^2 F}{\partial V\,\partial T} = \frac{\partial}{\partial V}\left(\frac{\partial F}{\partial T}\right)_V, \tag{26.63}$$

$$\frac{\partial^2 F}{\partial V\,\partial T} = -\frac{\partial}{\partial V}S = -\left(\frac{\partial S}{\partial V}\right)_T, \tag{26.64}$$

where we used the relationship $(\partial F/\partial T)_V = -S$. Taking the mixed derivative in opposite order

$$\frac{\partial^2 F}{\partial T\,\partial V} = \frac{\partial}{\partial T}\left(\frac{\partial F}{\partial V}\right)_T = \frac{\partial}{\partial T}(-P), \tag{26.65}$$

$$\frac{\partial^2 F}{\partial T\,\partial V} = -\left(\frac{\partial P}{\partial V}\right)_T \frac{\mathrm{d}V}{\mathrm{d}T} = -B_T\,\frac{1}{V}\,\frac{\mathrm{d}V}{\mathrm{d}T}, \tag{26.66}$$

$$\frac{\partial^2 F}{\partial T\,\partial V} = -B_T\,\beta, \tag{26.67}$$

where these three relationships were used in sequence

$$\left(\frac{\partial F}{\partial V}\right)_T = -P, \qquad \left(\frac{\partial P}{\partial V}\right)_T V = B_T, \qquad \frac{1}{V}\,\frac{\mathrm{d}V}{\mathrm{d}T} = \beta, \tag{26.68}$$

for the pressure, isothermal bulk modulus, and volume thermal expansion, respectively. Equating the mixed derivatives taken in opposite order, Eqs. 26.64 and 26.67 give

$$\left(\frac{\partial S}{\partial V}\right)_T = B_T\,\beta. \tag{26.69}$$

Any non-harmonic effects that change the vibrational entropy with T or V will also change the thermal expansion and the bulk modulus.

26.5 Electron–Phonon Interactions and Temperature

26.5.1 Screening and the EPI

The large difference in energy scales of phonons and electrons can motivate the separation of the Hamiltonian of the solid into a term with nuclear coordinates for the phonons H_n (Eq. 26.55), and a term with electron coordinates H_e (Eq. 28.43). The energy of a crystal deformation caused by a phonon originates with the electrons, of course, but although this potential energy of deformation is electronic in origin, it transfers back-and-forth to kinetic energy of the nuclei as they vibrate. If the electrons were always in their ground states, all this energy of deformation would be associated with H_n alone (i.e., the phonons). Treating the electrons and the phonons as two independent thermodynamic systems becomes inconsistent at finite temperature, however, because the presence of phonons alters the thermal excitations of electrons, and vice versa.

Section 28.4.1 shows that the electron–phonon interaction (EPI) involves the coordinates of the electrons and coordinates of the nuclei. First assume the nuclear motions are slow enough so the electron levels adapt continuously to the evolving structure. This "adiabatic approximation" does not allow the nuclear kinetic energy to alter the electron states; only the nuclear positions do so. The adiabatic EPI increases with the number of phonons (i.e., amplitudes of nuclear displacements), and also scales with the thermal excitations of electrons. (Effects from how the interatomic potential depends on phonon populations alone are already counted as phonon–phonon interactions.) More specifically, the adiabatic EPI is proportional to the number of phonons, $n(\varepsilon, T) + 1/2$, times the difference of electron occupancy with respect to the ground state, $f(T) - f(0)$, where $f(T)$ is the Fermi–Dirac distribution.

The strength of the adiabatic EPI depends on electronic screening of ion motions. During ion motions in metals, it can be advantageous energetically to excite some electrons above the Fermi level if these new electron states place negative electron charge in strategic locations that screen out the Coulombic interactions between the ions. This effect can reduce the energy cost of an ionic displacement, and therefore reduce the interatomic force constants. Note that it involves the excitations of phonons (the atom displacements) and the excitations of electrons (moving some above the Fermi surface to give more effective screening), and it is the origin of the adiabatic electron–phonon interaction.[8]

The adiabatic EPI reduces the energy of the ion displacements, which involves the energies of both electrons and phonons.[9] If this effect were constant with temperature, perhaps it would not be noticed. However, effects of temperature on the adiabatic EPI can alter the interatomic force constants and the phonon thermodynamics.

[8] Suppose there were no free electrons in the material, and the ion cores interacted by Coulomb forces, which are large. To reduce the potential energy as the atoms are displaced in a phonon, the ions may distort in shape. This is sometimes treated with a "shell model," where a massless shell of outer electrons around the ion core has its own degree of freedom, coupled to the ion core with a spring.

[9] If measured for either electrons or harmonic phonons, the EPI affects their energies equally, but the EPI should be counted only once in the thermodynamics.

26.5.2 Effects of Composition and Temperature on Screening and the Adiabatic EPI

Chemical composition affects the numbers of electrons at the Fermi level, and alters the phonon frequencies in a number of ways. For example, suppose a metal behaves as a free electron gas, and solute atoms are added that donate electrons to the gas. The density of the electron gas is increased, and a denser electron gas has a higher elastic modulus and stiffer interatomic forces, as described in Section 6.6.1 [422, 423]. A free electron model is generally too simple, however, and can predict the wrong sign for the energy shifts of short-wavelength phonons.

A more detailed structure of the Fermi surface is important for accurate predictions of how phonon frequencies are affected by the adiabatic EPI. Nevertheless, some trends can be predicted with less information than the full structure of the Fermi surface. The simpler electron DOS at the Fermi level seems semi-quantitatively useful for alloys of transition metals. When solute atoms increase the DOS of *d*-electrons at the Fermi level, the increased possibilities of low-energy excitations of electrons at the Fermi level allow better accommodation of the atomic distortions in a phonon, reducing the interatomic forces and lowering the phonon frequencies [409, 424] – see Fig. 26.9.

Temperature can alter the electron DOS at the Fermi level, causing some effects similar to composition [425]. Important effects arise from the thermal broadening of electronic energy levels. There is, of course, a thermal broadening from the Fermi–Dirac distribution at elevated temperature. Also with temperature, electrons near the Fermi energy scatter out of their states owing to interactions with phonons, giving a lifetime broadening to the electron energy levels. (The lifetime broadening occurs in addition to the energy

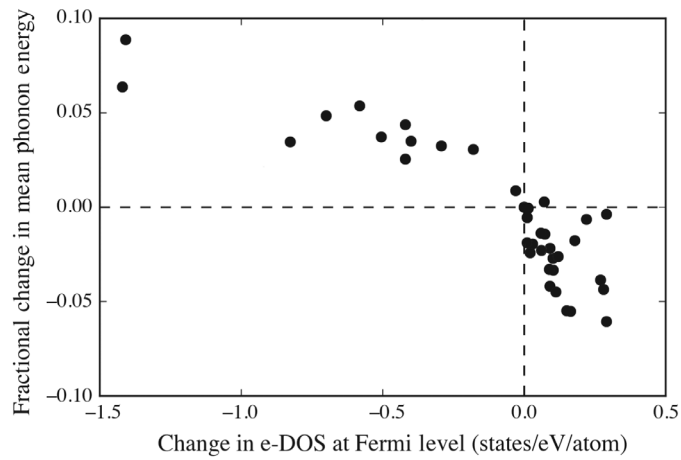

Figure 26.9 Change in the mean phonon energy from experiment versus calculated change in electronic DOS at the Fermi level of some 3*d* transition metal alloys. The mean phonon energy was measured by inelastic scattering on several Fe alloys and V alloys and compounds at different temperatures, and the change in phonon energy was corrected by the expected effects of quasiharmonicity. The electronic DOS at the Fermi level was calculated approximately by broadening a low-temperature electronic DOS with a function of electron lifetime.

broadening from the Fermi–Dirac distribution.) Metals with sharp features in their electron DOS at the Fermi level are especially susceptible to changes in the adiabatic EPI with temperature. The thermal broadening of the electron DOS can take sharp peaks near the Fermi level and level them, or fill states in a narrow valley. For example, for A15 V_3Si the Fermi level is at a peak in the electron DOS. Thermal smearing reduces markedly the numbers of electrons and holes available for screening, reducing the EPI and increasing the phonon frequencies over a range of temperature of approximately 500 K [408]. On the other hand, for FeSi at high temperatures, a valley in the electron DOS is filled [426], giving the opposite trend. Figure 26.9 shows a correlation between the changes with temperature of the average phonon energy and the change in the effective electron DOS at the Fermi level. As the electron DOS at the Fermi level increases, the average phonon energy decreases. The screening of ion displacements is more effective when there are more *d*-electrons at the Fermi level of these transition metal alloys and compounds.

With increasing temperature, in general the adiabatic EPI will be suppressed most strongly along directions in *k*-space where the EPI is strong (and likewise enhanced along directions where it is weak), and this should tend to equalize the strength of the EPI in all directions. The thermal smearing of the electron states and the increased isotropy of the adiabatic EPI is expected to wash out any intricate structures of the Fermi surface found at $T = 0$ (e.g., see Fig. 6.7). For a Fermi surface with one sheet, its low-temperature structure may evolve towards a fuzzy sphere at high temperatures.

A different type of thermal evolution of the Fermi surface is also possible. With increased thermal displacements of atoms, some electron levels are shifted more than others. Some electronic bands near the Fermi energy may shift with temperature so that they cross the Fermi level, and this crossing can be assisted by the thermal broadening of the electron energy levels (from effects of the Fermi–Dirac distribution and from lifetime broadening). This crossing can create new features on the Fermi surface, and their appearance (or disappearance) is called an electronic topological transition, or a Lifshitz transition [427]. The adiabatic EPI can be altered dramatically when temperature causes a Lifshitz transition, and is responsible for an anomalous phonon softening with temperature in FeTi, for example [428].

Problems

26.1 Derive Eq. 26.18.

26.2 For the Debye model in the high-temperature limit, show that the difference in vibrational entropy of two phases α and β with Debye temperatures θ_D^α and θ_D^β is

$$\Delta S_{vib}^{\alpha-\beta} = 3k_B \ln\left(\frac{\theta_D^\beta}{\theta_D^\alpha}\right). \tag{26.70}$$

26.3 Consider a damped harmonic oscillator with the equation of motion

$$m\frac{\mathrm{d}^2x}{\mathrm{d}t^2} + b\frac{\mathrm{d}x}{\mathrm{d}t} + kx = 0. \tag{26.71}$$

Define the dimensionless quality factor Q as

$$Q = \frac{\sqrt{km}}{b}. \tag{26.72}$$

(**a**) Show that an acceptable solution to the equation of motion, Eq. 26.71, is

$$x(t) = X_0\, \mathrm{e}^{-[\mathrm{i}+(2Q)^{-1}]\,\omega t}, \tag{26.73}$$

where the frequency ω differs from the undamped frequency $\omega_0 = \sqrt{k/m}$.

(**b**) When the quality factor Q is large, and the damping is small, find the frequency shift $\Delta = \omega - \omega_0$, if you have not already done so in part a.

(**c**) The spectral shape of a damped harmonic oscillator is

$$D_{\omega'}(\omega) = \frac{1}{\pi Q \omega'}\,\frac{1}{\left(\frac{\omega'}{\omega} - \frac{\omega}{\omega'}\right)^2 + \left(\frac{1}{Q}\right)^2}, \tag{26.74}$$

where ω is a range of frequencies around the central frequency ω'. For large Q, how does the breadth of the spectrum Γ change with Q?

(**d**) Using the results from parts b and c, find the ratio between the peak broadening and shift Γ/Δ in terms of Q.

(**e**) Assuming the displacement x increases as $\sqrt{T}$, how might you expect the ratio $Q/\sqrt{m}$ to scale with the ratio T/T_m, where T_m is the melting temperature, assuming that interatomic potentials are similar, as suggested by Fig. 12.3?

26.4 The energy levels of a quantum quartic oscillator $\{\epsilon_i\}$ are not spaced evenly, as they are for a quantum harmonic oscillator. Approximately, the levels are at relative energies

$$\epsilon_i = 0.69 + 3.14i + 0.188i^2. \tag{26.75}$$

For temperatures corresponding to $\epsilon_i = 0.3, 1.0, 3.0$, and 10, calculate numerically a partition function, and then evaluate the free energy and entropy of this approximate quantum quartic oscillator. Compare your results with those of a harmonic oscillator with the same spacing between ϵ_0 and ϵ_1.

27 Cooperative Behavior near a Critical Temperature

Section 1.1 put phase transitions in materials into a broader context of phase transitions in general. Most of this book has been on how atoms arrange themselves at different T and P, and how these arrangements change abruptly through a phase transition. Atoms in solids tend to be a bit sluggish in their movements, however, and their arrangements can be slow to attain states of thermodynamic equilibrium. Diffusion and nucleation, which retard, redirect, or even arrest the paths to equilibrium, are kinetic phenomena of interest and importance. Those nonthermodynamic phenomena are essential to the full life cycle of a phase transformation, but they obscure the singularities in the free energy function or its derivatives that underlie the thermodynamics of a phase transition.

The more general field of phase transitions often places rigorous emphasis on thermodynamic equilibrium, even at temperatures that are very low, or at temperatures very near a critical temperature where atomic structures may not attain equilibrium in reasonable times. Liquid–gas transitions and magnetic transitions are often better candidates for studies of phase transitions for their own sake. Nevertheless, concepts from the broader field of phase transitions do help our understanding of phase transformations in solid materials. Much of the interest in the basic physics of phase transitions is in how a system behaves very close to the critical temperature.

The cooperative interactions between elements of the system tend to preserve the state of low-temperature order, but temperature disrupts this order over rapidly increasing spatial scales near T_c. For example, as a spin becomes misaligned with temperature, the energy for the alignment of its neighbors is less favorable. As they lose alignment, the alignment of their neighbors (including the original spin) becomes less favorable. Equilibration near T_c requires different parts of the system to communicate across long distances. The catastrophic collapse of order over a large system is interesting in many contexts. Typical questions are:

- How does the spatial range of magnetic order diverge as a paramagnet is cooled to the Curie temperature?
- What is the change in density, compressibility, and specific heat very close to the critical temperature?

27.1 Critical Exponents

The equilibrium values of many properties such as magnetic susceptibility, or correlations between pairs of atoms, have divergences or singularities at the critical temperature of

a phase transition, T_c. They are parameterized by ϵ, the normalized departure from the critical temperature

$$\epsilon \equiv \frac{T - T_c}{T_c}, \tag{27.1}$$

so ϵ is positive above T_c and negative below. Many modern studies of phase transitions predict or conjecture that properties such as specific heat depend on ϵ through a power law relationship with a "critical exponent," in this case α

$$C_V \sim \epsilon^{-\alpha} \quad \text{for } \epsilon > 0, \tag{27.2}$$

$$C_V \sim (-\epsilon)^{-\alpha'} \quad \text{for } \epsilon < 0. \tag{27.3}$$

In general, we do not expect the same divergence of the specific heat as T_c is approached from above or from below (although the scaling theory of Section 27.4 predicts $\alpha = \alpha'$). A property of interest in liquid systems is the difference in density of the gas and liquid phases near the critical temperature[1]

$$\rho_L - \rho_g \sim (-\epsilon)^{\beta}. \tag{27.4}$$

For both heat capacity and density, we expect correction terms as $|\epsilon|$ becomes larger. It turns out that critical exponents often prove useful for interpreting experimental data, and this is a justification for giving them attention. Near a critical temperature, log–log graphs of physical properties versus ϵ are often straight lines.

A singularity is always interesting in science and mathematics, and critical exponents are a way to classify different critical behaviors. For the many properties that diverge near T_c, many of their critical exponents are different. Today there is a long list of critical exponents that spans the Greek alphabet. Thermodynamic relationships between intensive and extensive variables can sometimes impose relationships between critical exponents, as shown in Section 27.3, and thermodynamic relationships sometimes suggest that critical exponents are identical for phase transitions in different systems. On the other hand, critical exponents are sometimes found to be the same for no obvious thermodynamic reason, so critical exponents sometimes stimulate questions about the universal features of phase transitions.

27.2 Critical Slowing Down

Critical exponents are difficult to measure reliably for phase transitions in materials, and it is useful to consider why. As an example, consider a chemical order–disorder transition in an alloy. The long-range order parameter L was graphed in Fig. 2.21, although this was from a simple calculation in the point approximation. We already know that by including an additional short-range order parameter in the pair approximation, the critical temperature falls considerably, as shown in Table 7.2. Also, the shape of $L(T)$ has a more abrupt decline

[1] Like the exponents α and α', β is defined for zero pressure.

in the pair approximation than in the point, as can be seen with Figs. 7.5 and 2.21. It is therefore no surprise that the shape of $L(T)$ just below T_c is not predicted correctly by either of these approximations. The LRO follows a power law

$$L \sim (-\epsilon)^{\beta}. \tag{27.5}$$

Both the point and pair approximations give $\beta = 1/2$, whereas a Monte Carlo simulation gives $\beta = 0.313$ in three dimensions.

This abstruse observation has more relevance to order–disorder transitions once we understand the reason for the difference in critical exponents. Suppose we seek to find the equilibrium state of order near T_c.[2] We may plan to anneal a disordered material for a long time just below T_c to attain equilibrium. Using Eq. 5.33, a long equilibration time is expected because there is little difference in free energy between the disordered and ordered phases for small ϵ (e.g., $\mathrm{d}^2F/\mathrm{d}L^2$ is very small near T_c). Nevertheless, the equilibration rate of Eq. 5.33 depends strongly on the deviation in order parameter, ΔL, not directly on ϵ, so from Fig. 2.21 we might optimistically expect some help in equilibration from the rapid rise of $L(T)$ below T_c. Unfortunately, the issue not addressed by Eq. 5.33 (and the theories behind Figs. 2.21 and 7.5) is that the equilibration of L requires relaxations across longer correlation lengths, ξ, at temperatures closer to T_c.[3] The spatial range of response to a disturbance in the order parameter diverges near T_c as

$$\xi \sim (-\epsilon)^{-\nu'} \quad \text{for } \epsilon < 0. \tag{27.6}$$

Even without knowing the value of ν', we see that just below T_c a correlation length diverges to infinite distance. Equilibration cannot take place only in the first few neighbor shells of an atom, but larger and larger clusters must equilibrate as T_c is approached from below. This requires longer diffusion times $\tau = x^2/D$, giving an additional factor for the equilibration time that goes as

$$\mathcal{T} \sim \epsilon^{-2\nu'}/D, \quad \text{or simply} \tag{27.7}$$

$$\mathcal{T} \sim \epsilon^{-2\nu'}. \tag{27.8}$$

This factor $\mathcal{T}$ should multiply the RHS of Eq. 5.33. Arguably there are too many variables for this analysis to be useful quantitatively, but this issue of divergence of the correlation length in the ordered region shows why equilibrium is very difficult to achieve in solids near T_c.

We have just considered an example of "critical slowing down." Classical critical slowing down is described by Eq. 5.33 alone. It does predict, correctly, that the rate of change of an order parameter goes to zero at T_c. Modern, and more accurate, theories of critical slowing down include equilibration of the order parameter over a diverging correlation length. The couplings between state variables of different spatial scales are nonlinear, and reflect the cooperative nature of the phase transition. Experimental studies

[2] This might be helpful for determining if the transition occurs continuously or by nucleation and growth.

[3] For now, consider the correlation length to be the size of a patch of ordered region that occurs as a fluctuation in a material above T_c. Below T_c there is an analogous idea that equilibration must occur over longer distances as T_c is approached.

of critical slowing down have largely used magnetic systems [429], which achieve equilibrium more readily than chemical order–disorder transitions in solids. Nevertheless, these systems still require measurements over a wide range in the logarithm of time, and studies of critical slowing down are challenging for any experiment or simulation.

27.3 The Rushbrooke Inequality

A few dozen relationships between different critical exponents are known from thermodynamics, although some make additional assumptions about the forms of thermodynamic functions (as done in Section 27.4, for example). Perhaps the most famous is the Rushbrooke inequality for magnetic systems. It uses the thermodynamic relationship

$$C_H - C_M = \frac{\left[\left(\frac{\partial M}{\partial T}\right)_H\right]^2}{\chi_T}, \tag{27.9}$$

where C_H and C_M are heat capacities at constant applied field and at constant magnetization. Equation 27.9 is derived in the same way as the more familiar relationship between the heat capacities at constant pressure and volume

$$C_P - C_V = \frac{\left[\frac{1}{V}\left(\frac{\partial V}{\partial T}\right)_P\right]^2}{\kappa_T}, \tag{27.10}$$

where the numerator is the coefficient of thermal expansion (squared). In Eqs. 27.9 and 27.10, χ_T and κ_T are the isothermal susceptibility and isothermal compressibility.

The heat capacity C_M is positive, so Eq. 27.9 gives

$$C_H \geq \frac{\left[\left(\frac{\partial M}{\partial T}\right)_H\right]^2}{\chi_T}. \tag{27.11}$$

Critical exponents are defined for all three factors in Eq. 27.11 as

$$C_H \sim \epsilon^{-\alpha'}, \quad M \sim \epsilon^{\beta}, \quad \chi_T \sim \epsilon^{-\gamma'}. \tag{27.12}$$

Differentiating with respect to T gives a result proportional to differentiating with respect to ϵ, so the products in Eq. 27.11 give sums and differences of the critical exponents

$$-\alpha' \leq 2(\beta - 1) + \gamma', \tag{27.13}$$

$$\alpha' + 2\beta + \gamma' \geq 2. \tag{27.14}$$

This is the Rushbrooke inequality.[4] It is interesting that experimental measurements on magnetic systems show that the Rushbrooke inequality is often an equality, consistent with the scaling theory discussed below. Other relationships between critical exponents can be deduced from stability conditions of the free energy and temperature derivatives of the

[4] Unfortunately, there is no equivalent that can be obtained from Eq. 27.10. The thermal expansion is not a divergent quantity near T_c, and $\partial V/\partial T$ gives zero in comparison to the other quantities.

magnetization, for example. Many relations between critical exponents are also known for physical properties near liquid–gas transitions in fluids.

27.4 Scaling Theory

27.4.1 Divergences of Correlation Lengths

Correlation lengths, here called ξ, have been mentioned throughout this text, starting from our earliest discussions of phase transitions. For efficiency we did not develop the formalism for correlation lengths by Fourier analysis of atom distributions.[5] For our present purpose, the physical idea of a correlation length can be conveyed by a simple algorithm. Place an arbitrary atom at the origin, and record the atomic structure at distances away from the origin. If the atom is in a crystal, a regular pattern of other atoms will be found over long distances. The correlation length is long, sometimes approximately the size of the crystal itself. On the other hand, in a gas the correlation length is quite short, typically the size of a molecule – the molecules cannot overlap each other, but otherwise they are at random positions. The correlation length is the spatial range over which the atomic structure has memory of the atom at the origin (or is "influenced" by the atom at the origin).[6]

There are many different correlation lengths in a material. The long-range order parameter L was defined to account for chemical order, and the critical temperature was defined as the temperature where L changed from zero to a finite value. It is interesting that a reasonable estimate of T_c could be obtained from the simple Gorsky–Bragg–Williams model of Section 2.9.1, which was based only on the sublattice occupations R and W. While it is true that $L = 0$ above T_c, the structure of the material varies considerably at temperatures slightly above T_c. Short-range order parameters in the pair approximation could account for some of this, and the cluster expansion method is a way to generalize an order parameter to groups of atoms of intermediate size. (Sections 7.2– 7.3.3 discussed some of these issues.)

Unfortunately, the intermediate-range order parameters also become unreliable closer and closer to T_c, as the correlation length for order in the material grows ever larger. This is a natural consequence of the cooperative nature of phase transitions – as the temperature decreases to T_c, the interactions between atoms induce more order that in turn allows stronger interactions. There has been success in extending the cluster expansion method to work with short-range order parameters of growing length scale closer to T_c. While instructive, these methods are either fortuitous [62] or very difficult [430].

[5] This approach connects elegantly to scattering and diffraction measurements. In essence, a correlation length is determined from Eq. 25.45 at a snapshot in time for $t = 0$. The spatial Fourier transform of Eq. 25.46 is the corresponding quantity of measurement.

[6] Even more properly, the correlation length is obtained by the convolution of the atom distribution with itself, giving a large peak at zero distance and features that decay over a characteristic correlation length.

The correlation length ξ for the order parameter undergoing a phase transition gives important information about the configuration of atoms near T_c. We know that the energy and entropy of an assembly of atoms originates from the atomic structure, and these depend on ξ. We therefore elevate the correlation length ξ to a new level of importance for understanding phase transitions. In fact, we hypothesize that the free energy is *entirely* a function of the correlation length [431]. The correlation length is normalized to the size of the material $\mathcal{L}$, which is the upper limit of ξ, and the total free energy change ΔG is required to increase with the size of the material. Expanding the change in free energy with correlation length gives

$$\Delta G = \sum_j a_j \left(\frac{\mathcal{L}}{\xi}\right)^j . \tag{27.15}$$

A term with $j = 0$ should already be included as a constant factor in ΔG. There are problems with the terms $j = 1$ and $j = 2$ because they scale with the length of the material or its area. For a large volume of material, these terms $j = 1$ and $j = 2$ make no contribution.

The lowest-order term in Eq. 27.15 is therefore $j = 3$ for a three-dimensional material. It proves the dominant term near T_c, so all others are ignored

$$\Delta G = a_3 \left(\frac{\mathcal{L}}{\xi}\right)^3 . \tag{27.16}$$

As in our previous discussion of critical exponents, the correlation length is now transformed to be in terms of ϵ, the deviation from T_c. Using the exponent $-\nu$ (cf. Eq. 27.6)

$$\Delta G \sim \mathcal{L}^3 \, \epsilon^{3\nu}. \tag{27.17}$$

This hypothesized expression for ΔG can be used to obtain critical exponents of thermodynamic quantities. Start with the heat capacity, using its thermodynamic relationship to the free energy

$$C_V = -T \left(\frac{\partial^2 G}{\partial T^2}\right)_V , \tag{27.18}$$

$$C_V \sim \mathcal{L}^3 \, \epsilon^{3\nu-2}, \tag{27.19}$$

where we used $\epsilon \sim T$, and the prefactor of T in the thermodynamic relationship made no contribution because it is not singular near the critical temperature. Comparing Eq. 27.19 to Eq. 27.2

$$2 - \alpha = 3\nu, \tag{27.20}$$

which has proven correct in a number of cases. Many other relationships between critical exponents can be obtained from the assumed scaling relation of Eq. 27.16.

Scaling theory has had considerable success in magnetic and fluid systems, for which the state of equilibrium is more readily attained than in solids. What seems to be emerging is a view that the correlation length is a central quantity for describing phase transitions near the critical temperature. As used today, however, ξ is a simple quantity, without anisotropy or absolute magnitude. Nevertheless, it does a reasonable job of showing how increasingly

large numbers of atoms cooperate to develop ordered fluctuations near T_c. To some extent it has become a specialized topic of research – certainly it is quite different from the methods described in Chapter 22 for working at temperatures well below T_c or well above T_c.

27.4.2 Scaling and Decimation

Scaling methods have a wide range of applications in physical science, and we now develop a scaling method to obtain a critical temperature and some characteristics of a system near the critical temperature. Above the critical temperature we know that short-range order exists in a system of atoms, and the range of this order grows as the temperature is lowered to T_c. Likewise, a ferromagnet with spins aligned over short distances at high temperatures develops spin alignment over longer distances with decreasing temperature, approaching infinity at T_c. This behavior motivates an analysis of self-similarity near T_c, where the same behavior is seen over a wide range of spatial scales. The "renormalization group" method translates this aggregate behavior of the system into a mathematical method, notable for a Nobel prize to K. Wilson in 1982, and some excellent overviews [432, 433].

Central to the renormalization group is the concept of "decimation" of degrees of freedom, where microscopic atoms or spins are "coarse-grained" into entities of larger size. The concept is illustrated in Fig. 27.1. Suppose the smallest dots are atoms on a triangular lattice. The idea is that if a majority of the three atoms in a triangle are species B, for example, a B is assigned to all three atoms, and is placed at the position of the larger spot in the figure. The larger spots form a triangular lattice, too, although with one-quarter the density – we have decimated three-quarters of the degrees of freedom of the original system. The process repeats itself. At the very large spots we place the average of the three nearest intermediate spots – another three-quarters of the remaining degrees of freedom were decimated in this step.

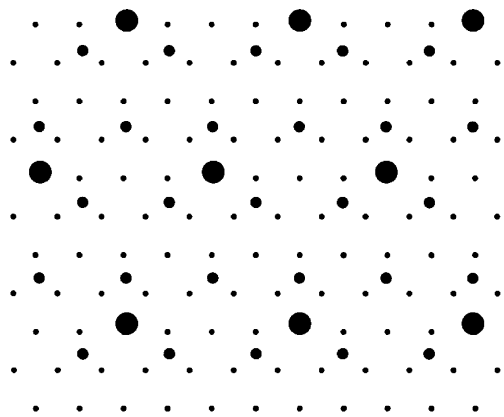

Figure 27.1 A triangle lattice (small dots), and two generations of coarse-graining (larger spots). Notice that the three sizes of spots are all on triangle lattices, with larger spots fitting into the center of three surrounding spots of smaller size.

It is obvious that this coarse-graining method will work well for an unmixing alloy. If the B-rich zones are large, covering many lattice sites, then the coarse-graining will continue to show B-rich regions. This process works even for infinite length scales, assuming the unmixing occurs over an infinite lattice, infinite distances, and infinite time.

27.5 Partition Function for One-Dimensional Chain

27.5.1 Form of Partition Function after Decimation of Spins

We now apply the visual algorithm illustrated in Fig. 27.1 to a mathematical partition function. We pick the simplest possible case – a one-dimensional chain of spins σ having values of +1 or –1, with first-nearest-neighbor (1nn) interactions only. For the total energy, sum the energies of all 1nn pairs, which depend on whether the two spins in a pair are parallel or antiparallel. The product of the two spins gives their mutual alignment and the energy of the pair

$$E = J \sum_j \sigma_j \, \sigma_{j+1}, \tag{27.21}$$

where J is the "spin exchange energy" so that neighboring spins of like sign contribute $+J$ to the energy, and neighboring spins of opposite sign contribute $-J$. (J would be negative for a ferromagnet.) The partition function is a sum of terms for all possible orientations of all N spins in the chain.

$$\mathcal{Z} = \sum_{\sigma_1=-1}^{+1} \sum_{\sigma_2=-1}^{+1} \cdots \sum_{\sigma_N=-1}^{+1} \mathrm{e}^{-\beta J[\sigma_1\sigma_2+\sigma_2\sigma_3+\sigma_3\sigma_4 \ldots +\sigma_{N-1}\sigma_N]}, \tag{27.22}$$

$$\mathcal{Z} = \sum_{\sigma_1=-1}^{+1} \sum_{\sigma_2=-1}^{+1} \cdots \sum_{\sigma_N=-1}^{+1} \mathrm{e}^{-\beta J[\sigma_1\sigma_2+\sigma_2\sigma_3]} \, \mathrm{e}^{-\beta J[\sigma_3\sigma_4+\sigma_4\sigma_5]} \ldots, \tag{27.23}$$

where $\beta = 1/k_{\mathrm{B}}T$.

Notice the grouping of two pairs of spins in each exponential of Eq. 27.23. Please inspect the subscripts because the next step is the decimation of half of them. This is done by summing over spins with even subscripts. The spins take on only two values, and, for example, when we sum over the two values of σ_2, each exponential of Eq. 27.23 takes the form

$$\sum_{\sigma_2=-1}^{+1} \mathrm{e}^{-\beta J[\sigma_1\sigma_2+\sigma_2\sigma_3]} = \mathrm{e}^{+\beta J[\sigma_1+\sigma_3]} + \mathrm{e}^{-\beta J[\sigma_1+\sigma_3]}. \tag{27.24}$$

We successfully eliminated half of the spin variables, but at the expense of changing a single exponential into the sum of two. Doing this with the even indices down the chain gives

$$\mathcal{Z} = \sum_{\sigma_1=-1}^{+1} \sum_{\sigma_3=-1}^{+1} \sum_{\sigma_5=-1}^{+1} \sum_{\sigma_7=-1}^{+1} \cdots \left[e^{+\beta J[\sigma_1+\sigma_3]} + e^{-\beta J[\sigma_1+\sigma_3]} \right] \times \left[e^{+\beta J[\sigma_3+\sigma_5]} + e^{-\beta J[\sigma_3+\sigma_5]} \right] \left[e^{+\beta J[\sigma_5+\sigma_7]} + e^{-\beta J[\sigma_5+\sigma_7]} \right] \ldots, \tag{27.25}$$

which, unfortunately, does not look like Eq. 27.22. It proves possible to achieve self-similarity by forcing the two terms in the [ ] brackets into one exponential, but for the result to equal the original two terms, it is necessary to multiply by a function of J

$$\left[e^{+\beta J[\sigma_1+\sigma_3]} + e^{-\beta J[\sigma_1+\sigma_3]} \right] = f(J)\, e^{+\beta J' \sigma_1 \sigma_3}, \tag{27.26}$$

allowing for the possibility that the exponent will have to be rescaled with a new J'. Importantly, the function $f(J)$ will be independent of the individual spins, and becomes a common factor for all the terms in the [ ] brackets. (Look ahead at Eq. 27.36 to see the consequence for rescaling the partition function by changing the number of spins $N \to N/2$.)

27.5.2 Rescaling of Exchange Energy

For what follows we need an expression for $f(J)$ and some relations between J and J'. It is again convenient that σ can be only +1 or –1, and only two cases need be considered for Eq. 27.26. The first case is when $\sigma_1 = \sigma_3$ (giving the same result when they are both +1 or −1)

$$\left[e^{+\beta 2J} + e^{-\beta 2J} \right] = f(J)\, e^{+\beta J'}, \tag{27.27}$$

$$2\, \cosh(\beta 2J) = f(J)\, e^{+\beta J'}, \tag{27.28}$$

and the second case is when $\sigma_1 = -\sigma_3$

$$\left[e^{+0} + e^{-0} \right] = f(J)\, e^{-\beta J'}, \tag{27.29}$$

$$f(J) = 2\, e^{+\beta J'}. \tag{27.30}$$

Substituting Eq. 27.30 into Eq. 27.28

$$\cosh(\beta 2J) = e^{\beta 2J'}, \tag{27.31}$$

RG-Jdec

$$\beta J' = \frac{1}{2} \ln\left(\cosh(\beta 2J)\right), \tag{27.32}$$

and substituting Eq. 27.32 into 27.30

$$f(J) = 2\cosh^{\frac{1}{2}}(\beta 2J). \tag{27.33}$$

The inverse of Eq. 27.32 is obtained easily

RG-Jgen

$$\beta J = \frac{1}{2} \cosh^{-1}\left(e^{\beta 2J'}\right). \tag{27.34}$$

This inverse process involves generating degrees of freedom, rather than decimating them (i.e., going backwards to finer detail in Fig. 27.1). We will soon return to the "renormalization group" (RG) equations 27.32 and 27.34.

27.5.3 Rescaling of Partition Function and Free Energy

We now recast the partition function and the free energy into forms that remain self-similar after spins are decimated. Using Eq. 27.26 for each factor in the partition function, Eq. 27.25 takes the form

$$\mathcal{Z}(J,N) = [f(J)]^{\frac{N}{2}} \sum_{\sigma_1=-1}^{+1} \sum_{\sigma_3=-1}^{+1} \sum_{\sigma_5=-1}^{+1} \sum_{\sigma_7=-1}^{+1} \cdots \left[\mathrm{e}^{+\beta J' \sigma_1 \sigma_3}\right] \times \left[\mathrm{e}^{+\beta J' \sigma_3 \sigma_5}\right] \left[\mathrm{e}^{+\beta J' [\sigma_5 \sigma_7]}\right] \ldots, \tag{27.35}$$

$$\mathcal{Z}(J,N) = [f(J)]^{\frac{N}{2}}\, \mathcal{Z}(J', N/2). \tag{27.36}$$

Equation 27.36 is a recursion relation for the partition function of the rescaled system. The free energy is obtained in the standard way

$$F(J) = -k_{\mathrm{B}} T \, \ln\Big(\mathcal{Z}(J,N)\Big). \tag{27.37}$$

With the recursion relation of Eq. 27.36

$$F(J) = -k_{\mathrm{B}} T \left[\frac{N}{2} \ln\left(f\left(J\right)\right) + \ln\left(\mathcal{Z}\left(J', \frac{N}{2}\right)\right)\right]. \tag{27.38}$$

Since we are rescaling the size of the system, it is more convenient to work with the free energy per atom, $\mathcal{F}$

$$\mathcal{F}(J) = \frac{F(J)}{N}, \tag{27.39}$$

$$\mathcal{F}(J) = -k_{\mathrm{B}} T \frac{1}{2} \ln\left(f\left(J\right)\right) + \frac{1}{N} F\left(J', \frac{N}{2}\right), \tag{27.40}$$

$$\mathcal{F}(J) = -k_{\mathrm{B}} T \frac{1}{2} \ln\left(2\cosh^{\frac{1}{2}}(\beta 2J)\right) + \frac{1}{2} \mathcal{F}\left(J'\right), \tag{27.41}$$

RG-Fdec
$$\mathcal{F}\left(J'\right) = k_{\mathrm{B}} T \ln\left(2\cosh^{\frac{1}{2}}(\beta 2J)\right) + 2\mathcal{F}\left(J\right), \tag{27.42}$$

where the transition from Eq. 27.40 to 27.41 was possible by using Eq. 27.33 and because the total free energy F for $N/2$ sites is $N/2$ times larger than the free energy per atom, $\mathcal{F}$. Finally, the inverse of Eq. 27.42 is obtained by substituting Eq. 27.30 into 27.40 and rearranging

RG-Fgen
$$\mathcal{F}\left(J\right) = \frac{1}{2}\left[\mathcal{F}\left(J'\right) - J' - k_{\mathrm{B}} T \ln 2\right]. \tag{27.43}$$

As for RG-Jgen of Eq. 27.34, this inverse transformation gives a next generation with more degrees of freedom.

27.5.4 Renormalization Group

Equations {27.32, 27.42} and {27.34, 27.43} are pairs of "renormalization group equations." They show how the interaction energy and the free energy evolve as the

system is rescaled and spin degrees of freedom are decimated (or generated when going in the other direction). A pair of examples illustrates their effect. Figure 27.2 shows the result of iterating Eq. RG-Jdec (Eq. 27.32) for different generations of J'. Ignoring some variable definitions, the Python code to do the iteration of Eq. RG-Jdec, and for calculating $\mathcal{F}(J')$ at each step, is

```
while j > 0.0001:
    jp = log(cosh(2.0*j))/2.0
    Fjp = log(2.0*sqrt( cosh(2.0*j))) + 2.0*Fj
    print jp, Fjp
    j = jp
```

Likewise for Eq. RG-Jgen the code for iteration is

```
while jp < 30:
    j = acosh(exp(2*jp))/2.0
    Fj = (Fjp - jp - log(2.0))/2.0
    print j, Fj
    jp = j
```

Iterating the renormalization group equation RG-Jdec leads to convergence of J/k_BT to 0, whereas iterating RG-Jgen leads to divergence of J/k_BT to ∞. These values of 0 and ∞ are fixed points of the system. At these values of J/k_BT, as we decimate or generate additional spins there is no change in the interaction energy or the free energy. The system looks the same at all spatial scales. The fixed point at $J = \infty$, or equivalently $T = 0$, corresponds to a perfectly ordered array of spins (and an ordering transition at $T = 0$). We

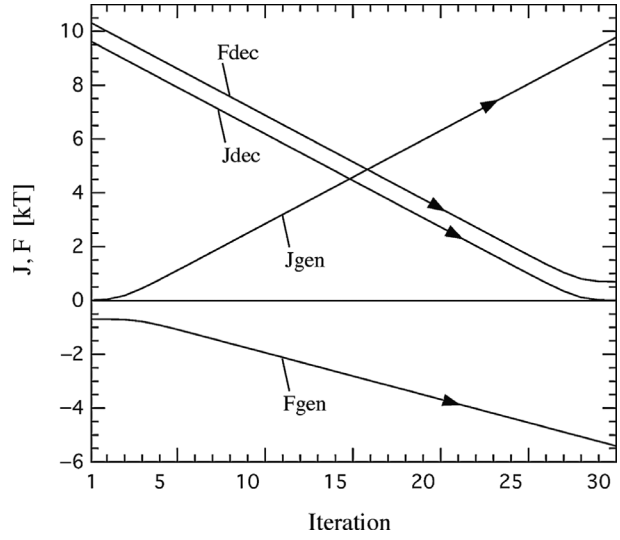

Figure 27.2 Repeated application of Eq. RG-Jdec (Eq. 27.32) with initial condition $J = 10$ gives convergence of J' and $\mathcal{F}(J')$ of RG-Fdec (Eq. 27.42), whereas repeat application of Eq. RG-Jgen (Eq. 27.34) gives divergence of J and $\mathcal{F}$ of RG-Fgen (Eq. 27.43).

see that the one-dimensional spin system does not have a phase transition, except at zero temperature. For two- or three-dimensional systems, however, there are fixed points at finite $J/k_{\mathrm{B}}T$, corresponding to ordering transitions at finite temperature.

Another physical insight is that for intermediate values of J, decimating degrees of freedom causes a weakening of J. This is expected because the length scale is larger, and an effectively weaker interaction energy is consistent with a lower quality of order over the larger length scale. Adding degrees of freedom does the opposite, and our iterations with RG-Jgen moved towards large J, or low temperature.

27.6 Partition Function for Two-Dimensional Lattice

We attempt the same approach with the two-dimensional square lattice with interactions between 1nn spins, but we need a more general expression than Eq. 27.21 because the sites are not connected sequentially

$$E = J \sum_{j}^{\text{sites}} \sum_{k}^{\text{nn}\,\prime} \sigma_j \, \sigma_k, \tag{27.44}$$

and the prime on the second sum over nearest neighbors reminds us not to double-count neighboring pairs (as in Fig. 2.14c). Figure 27.3 shows a set of labeled sites, of which two (numbers 8 and 12) will be decimated when the gray sublattice is removed. As in Eq. 27.22, the partition function is a sum of terms for all possible orientations of all N spins in the lattice, but each spin has four neighbors

$$\mathcal{Z} = \sum_{\sigma_1=-1}^{+1} \sum_{\sigma_2=-1}^{+1} \cdots \sum_{\sigma_N=-1}^{+1} \mathrm{e}^{-\beta J[\sigma_1\sigma_2+\sigma_1\sigma_6+\sigma_2\sigma_3 \ldots +\sigma_{N-1}\sigma_N]}. \tag{27.45}$$

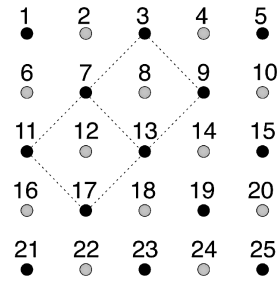

Figure 27.3 A square lattice with labeled sites. The gray sublattice will be decimated, eliminating half of the degrees of freedom. Our attention is focused on sites 8 and 12, and their neighbors.

Much as for Eq. 27.23, we regroup factors to isolate all spin–spin pairs around sites 8 and 12

$$\mathcal{Z} = \sum_{\sigma_1=-1}^{+1} \sum_{\sigma_2=-1}^{+1} \cdots \sum_{\sigma_5=-1}^{+1} \cdots \; \mathrm{e}^{-\beta J \sigma_8(\sigma_3+\sigma_7+\sigma_9+\sigma_{13})} \, \mathrm{e}^{-\beta J \sigma_{12}(\sigma_7+\sigma_{11}+\sigma_{13}+\sigma_{17})} \cdots \tag{27.46}$$

When we sum over the two values of the two spin variables σ_8 and σ_{12}

$$\mathcal{Z} = \sum_{\sigma_1=-1}^{+1} \sum_{\sigma_2=-1}^{+1} \cdots \left[\mathrm{e}^{+\beta J(\sigma_3+\sigma_7+\sigma_9+\sigma_{13})} + \mathrm{e}^{-\beta J(\sigma_3+\sigma_7+\sigma_9+\sigma_{13})}\right] \times \left[\mathrm{e}^{+\beta J(\sigma_7+\sigma_{11}+\sigma_{13}+\sigma_{17})} + \mathrm{e}^{-\beta J(\sigma_7+\sigma_{11}+\sigma_{13}+\sigma_{17})}\right] \cdots \tag{27.47}$$

We hope to recast this Eq. 27.47 into the form of Eq. 27.45, much as we did with Eq. 27.26 and then Eq. 27.35 for the one-dimensional spin chain. Unfortunately, the spin variable σ_7 (and σ_{13}) appears in both sets of square brackets in Eq. 27.47, and furthermore, the site 7 is also a first neighbor of the sites 2 and 6 in Fig. 27.3 which have not yet been considered (as is site 13). The interconnectivity of the square lattice, a feature not present in the 1D chain, causes a spin variable to appear in several exponentials of the partition function. Grouping them together, as we did to simplify the accounting for the central sites 8 and 12, only makes things worse for other spin variables that become scattered among other exponentials.

For the square lattice, it is not really possible to perform the elegant rescaling of the partition function that worked so well for the linear chain. Nevertheless it is useful to try by summing over the values of σ_7 in Eq. 27.47. We seek the analogous equation to Eq. 27.26 as

$$\left[\mathrm{e}^{+\beta J(\sigma_3+\sigma_7+\sigma_9+\sigma_{13})} + \mathrm{e}^{-\beta J(\sigma_3+\sigma_7+\sigma_9+\sigma_{13})}\right] = f(J) \, \mathrm{e}^{\beta J'/2(\sigma_3\sigma_7+\sigma_7\sigma_{13}+\sigma_{13}\sigma_9+\sigma_9\sigma_3)}. \tag{27.48}$$

The RHS of Eq. 27.48 is actually a product of the factors like $\mathrm{e}^{-\beta J' \sigma_i \sigma_{i+1}}$, as found for the 1D chain. In the present case, however, summing over the four spin variables of ± 1 can give {–4, –2, 0, +2, +4} (although results with opposite sign will give the same sum of exponentials in the square brackets in 27.47). Therefore there are several possibilities for $f(J)$ and J', and additional variables are required for a proper rescaling of terms in the partition function. Nevertheless, if we use cases where all spin variables are equal to +1 (or -1), and the case where the spins alternate, we obtain a J' of

$$\beta J' = \frac{1}{4} \ln\left[\cosh(4\beta J)\right], \tag{27.49}$$

which is analogous to the 1D result RG-Jdec for four spins. (We also obtain $f(J) = 2\sqrt{\cosh(2J)}$, the same as for the 1D result.) The problem with this result for $\beta J'$ is that it has a fixed point at infinity, and has the same behavior as the curve "Jgen" in Fig. 27.2. Equation 27.49 does not lead to a phase transition at a finite temperature. Of course we know that the present renormalization equation 27.49 is incorrect, since it does such a poor job in accounting for the connectivity of the spins on the square lattice, and for

the different spin possibilities on the four neighboring sites. In fact, the RHS of Eq. 27.48 is the partition function for a ring of four spins.

It turns out that Eq. 27.49 is on the very edge of having a finite fixed point, and we can make a physical argument why a finite fixed point is expected for the square lattice. Compared with the linear chain, the connectivity of the square lattice increases the effective range of the spin interactions, since, for example, an atom shares two common first neighbors with its second neighbor. (For the linear chain, there is only one intervening atom between second neighbors.) As a result, for the square lattice we do not expect the rescaled exchange interaction to be quite so weak as for the linear chain. We modify Eq. 27.49 as

$$\beta J' = \frac{1}{D} \ln\left[\cosh(4\beta J)\right], \tag{27.50}$$

where we expect D to be smaller than 4. It turns out that as soon as $D < 4$, there is a finite fixed point when $\beta J'$ is calculated iteratively by repeated application of Eq. 27.50. Numerical calculations give the results shown in Fig. 27.4. The denominator of $D = 4$ at the far right of the x-axis shows the fixed point at infinity. Only a small deviation of D below 4 gives a finite fixed point, however, corresponding to a phase transition at a finite temperature.

The exact value for the critical J (or critical temperature) on a square lattice with first-neighbor interactions was given in Table 7.2 as $\beta J = 1/(4 \times 0.5673) = 0.4407$. This is, of course, the only critical temperature for the lattice, so it gives one fixed point of physical significance on Fig. 27.4. The point is marked with a solid circle at $\ln(0.4407) = -0.819$,

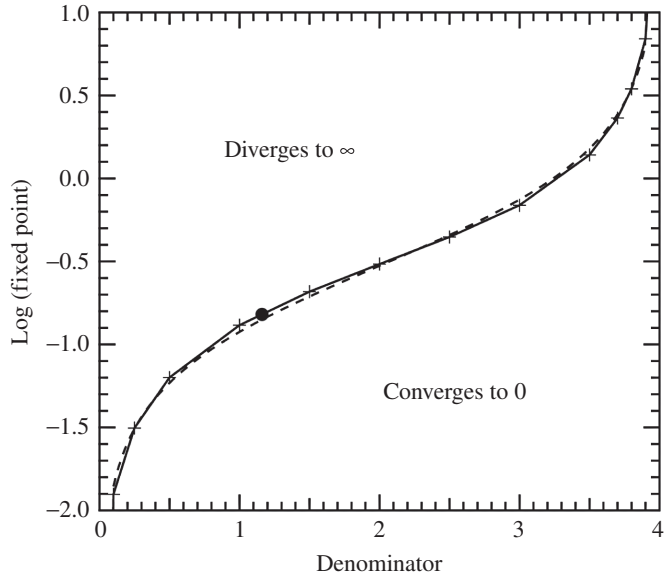

Figure 27.4 Log plot of unstable fixed points of J' versus the denominator, D, of the function $J' = \ln[\cosh(4J)]/D$ for multiple iterations of this equation. Crosses are numerical results, connected by solid lines. Dashed curve is the function $-0.83536\ln(4/J - 1) - 0.52623$, making an approximate fit to the calculated curve. The dot is the actual value for the 2D phase transition, as explained in the text.

corresponding to a denominator in Eq. 27.50 of approximately 1.16. This is significantly less than 4, showing that the interconnectivity of the square lattice makes the exchange energy much more robust upon renormalization under the decimation of spins.

Problems

27.1 For an order–disorder transition at a temperature at 1000 K, make an estimate of the range of temperature where the critical slowing down of Eq. 27.8 will dominate over the free energy effects that set Eq. 5.33.

27.2 Consider an experiment to measure the dependence of a quantity χ near a critical temperature near 100 K [431]. Temperature control was built to vary ϵ from 10^{-5} to 10^{-2}, but the thermal accuracy is 10^{-3} K. The data are fitted to an expression $\chi \sim \epsilon^{-x}$, where x is hoped to be a critical exponent. You need to test for the value of T_c itself, since it is not known exactly. Approximately, what accuracy can be expected for x from these measurements, assuming x is of order unity?

28 Phase Transitions in Quantum Materials

Groups of boson particles undergo quantum phase transitions at low temperatures. These are often prefaced with "super-", as in superfluidity and superconductivity. In essence, a large fraction of the boson particles go into the same ground state, a possibility forbidden for fermions. Their collective behavior in this condensed state shows quantum mechanical effects on a macroscopic scale. The collective state is described by a macroscopic wavefunction ψ and a probability density $|\psi|^2$.

This macroscopic quantum state accounts for many of the boson particles, such as ^{4}He atoms for superfluidity or Cooper pairs for superconductivity. Above 0 K, however, the integrated probability does not account for all the ^{4}He atoms, and we speak of a "two-phase" mixture of normal helium (He I) and superfluid helium (He II). These two phases need not exist in two distinct regions, however, as we have been considering for all phase transitions so far. It may be more appropriate to consider individual He atoms as having some amplitude in the He II state, and some in the He I state.

After a description of new "high T_c" superconductors, Chapter 28 describes electron correlations in position and time, with an introduction to the Hubbard model. This chapter, and the book itself, ends with a brief description of quantum phase transitions, a topic of intense recent interest in condensed matter physics. Because a quantum phase transition occurs at $T = 0$, it is not driven by temperature and does not involve a spatial divergence of thermal fluctuations. Instead, it is driven by a physical parameter such as a magnetic field, and involves a spatial divergence of quantum fluctuations. Effects of quantum phase transitions should be evident at finite temperatures, however, and more effects of quantum critical points may be identified in the near future.

28.1 Bose–Einstein Condensation

The process of "Bose–Einstein condensation" is a useful starting point for understanding the quantum and thermodynamic features of these phase transitions. Although the condensation temperatures are low, they are not so low as one might guess from the energy levels of the system. The peculiar behavior does not originate from the energy levels so much as from the Bose–Einstein occupancy factor

$$n(\epsilon, T) = \frac{1}{e^{(\epsilon-\mu)/k_B T} - 1}, \tag{28.1}$$

which was given for phonons as Eq. 7.44. Notice the chemical potential, μ. This was zero for phonons because there was no need to fix the number of phonons in a box. For atoms, specifically ^{4}He which are spinless bosons, we fix their number at N, and the chemical potential, $\mu(T)$, is our means to do so. There is no Bose–Einstein condensation for phonons, which are energy, not matter.

Box 28.1 Energy Level Spacings

We take a short detour and consider the energy levels for a helium atom in a cubic box of 1 cm on edge. Section 6.4.1 showed that fitting wavefunctions in a cubic box gives an energy

$$\epsilon = \frac{(\hbar k)^2}{2m}, \tag{28.2}$$

where

$$k = \frac{\pi}{L}(n_x^2 + n_y^2 + n_z^2). \tag{28.3}$$

The smallest separation between quantum levels for an atom of atomic number A is therefore

$$\Delta\epsilon = \frac{\hbar^2}{2M}\left(\frac{\pi}{L}\right)^2\left[\left(2^2+1^2+1^2\right) - \left(1^2+1^2+1^2\right)\right], \tag{28.4}$$

$$\Delta\epsilon = \frac{6.0 \times 10^{-18}\ \text{eV}}{A}, \tag{28.5}$$

which is 1.5×10^{-18} eV for ^{4}He (for which $A = 4$), corresponding to a temperature of 2×10^{-14} K. This is a very, very low temperature, not yet achieved in the laboratory. We would not observe superfluidity in ^{4}He at 2.17 K if it were necessary to reduce the temperature to the energy level separations of the material. Furthermore, this energy level separation is not unique to bosons. Fermions such as ^{3}He could have similar energy levels in a box, but ^{3}He does not undergo Bose–Einstein condensation by the mechanism described here.

Box 28.2 Condensate Fraction and Chemical Potential

A more detailed calculation of the Bose–Einstein condensation temperature predicts the fractional molar volume for BE condensation.

Set the ground state energy $\epsilon = 0$ for reference. Positive occupancies of the energy levels requires $\mu < \epsilon$, so μ is negative. (Otherwise the exponential function in Eq. 28.1 is less than 1, giving an unphysical situation where $n(\epsilon, T) < 0$.) The interesting behavior occurs as μ approaches zero. Nevertheless, μ cannot be exactly zero, or there would be a divergence of $n(\epsilon, T)$ as Eq. 28.1 approaches $1/(1-1) \to \infty$. This shows the tendency for Bose–Einstein condensation, where a large number of atoms enter the ground state. However, we want this large number to approach N, the total number of atoms in the system, not ∞. This criterion gives the appropriate μ. With the ground state having $\epsilon = 0$

$$N = \frac{1}{e^{-\mu/k_B T} - 1} \simeq \frac{1}{1 - \mu/k_B T - 1}, \tag{28.6}$$

$$\mu \simeq -\frac{k_B T}{N}. \tag{28.7}$$

We now seek the number of atoms in all energy levels above the ground state, N_{ex}, and how this number varies with temperature. We use the density of states for a gas from Eq. 6.71 (the same as Eq. 6.72, but divided by 2 because there is only one spin state for ^{4}He)

$$\rho(\epsilon) = \frac{(2M)^{\frac{3}{2}} L^3}{4\pi^2 \hbar^3} \epsilon^{\frac{1}{2}}. \tag{28.8}$$

Integrating over all energies gives N_{ex}

$$N_{ex} = \int_0^\infty \rho(\epsilon)\, n(\epsilon, T)\, \mathrm{d}\epsilon, \tag{28.9}$$

$$N_{ex} = \int_0^\infty \frac{(2M)^{\frac{3}{2}} L^3}{4\pi^2 \hbar^3} \epsilon^{\frac{1}{2}} \frac{1}{\mathrm{e}^{(\epsilon-\mu)/k_B T} - 1} \mathrm{d}\epsilon. \tag{28.10}$$

Using Eq. 28.7 to justify that $\epsilon - \mu \simeq \epsilon$

$$N_{ex} = \frac{(2M)^{\frac{3}{2}} V}{4\pi^2 \hbar^3} \left[\int_0^\infty \frac{\epsilon^{\frac{1}{2}}}{\mathrm{e}^{\epsilon/k_B T} - 1} \mathrm{d}\epsilon \right], \tag{28.11}$$

$$N_{ex} = \frac{(2M)^{\frac{3}{2}} V}{4\pi^2 \hbar^3} \left[(k_B T)^{\frac{3}{2}}\, 2.315 \right], \tag{28.12}$$

where the integral was evaluated numerically (cf. Eq. 21.52). Using Eq. 28.15

$$\frac{N_{ex}}{N} = 2.612 \frac{\Omega}{V_q}. \tag{28.13}$$

The BE condensation temperature is defined with the criterion $N_{ex} \simeq N$, so only a tiny fraction of atoms are in the ground state. Using an approach analogous to finding a critical temperature when the order parameter is small (cf. Eqs. 2.55 to 2.58), we set

$$1 = 2.612 \frac{\Omega}{V_q}, \tag{28.14}$$

giving the condition $\Omega/V_q = 0.3828$. Above this fraction, or below the temperature of Eq. 28.17, there is an increasing fraction of atoms in the ground state, becoming 1 at $T = 0$.

Bose–Einstein condensation occurs when the thermal de Broglie wavelengths of the atoms overlap significantly.

The quantum behavior of bosons responsible for Bose–Einstein (BE) condensation can be understood by considering the quantum volume V_q discussed in Section 12.4. Recall that the quantum volume is essentially the cube of the thermal de Broglie wavelength, λ, and has this form from Eqs. 12.22 and 12.24

$$V_q = \frac{h^3}{(2\pi\, M\, k_B T)^{3/2}}. \tag{28.15}$$

The amount of volume occupied by one ^{4}He atom in units of V_q is

$$\frac{\Omega}{V_q} = \frac{V}{N} \frac{(2\pi\, M\, k_B T)^{3/2}}{h^3}, \tag{28.16}$$

where the total volume V is $V = \Omega N$. The number of quantum volumes per atom, Ω/V_q, varies as $V T^{3/2}$, all other terms in Eq. 28.16 being constants for a given material. The wavefunctions for the atoms overlap more when they are compressed together (smaller V) or if they are cooled to lower temperature (larger λ).

The critical temperature for BE condensation occurs when $\Omega/V_q \simeq 1$, or more accurately $\Omega/V_q = 0.3828$ as shown in Box 28.2. Working out constants, the BE condensation temperature is

$$T_{BE} = \frac{115}{V_M^{2/3} M} \text{ [K]}, \tag{28.17}$$

where the units of molar volume V_M are cm^3/mol and M is the molecular weight. For ^{4}He with $M = 4$ and its known V_M, Eq. 28.17 gives $T_{BE} = 3.1$ K. This is comparable to the experimental observation of superfluidity at 2.17 K.

Some, but not all, properties of ^{4}He at low temperatures can be associated with Bose–Einstein condensation (BEC). A problem is that the helium atoms have chemical interactions, which are weak, but impede modeling them as a gas at low temperatures. A better atomic BEC was produced in 1995, when a specialized laser technique cooled a gas of Ru atoms to a temperature of 170 nK [434, 435]. What can be said about ^{4}He at low temperatures is that the atoms enter a collective quantum state, and this state has remarkable properties.

28.2 Superfluidity

28.2.1 Liquid and Solid Helium

Helium remains a liquid even at the lowest temperatures – it does not solidify unless it is under pressure. This peculiar behavior originates in part with the low mass of ^{4}He. We note, however, that the mass of H_2 is even lower, but hydrogen solidifies at 14 K under ambient pressure. The other special feature of He suppressing solidification is the weak interaction between He atoms.[1] The low mass of the ^{4}He atom gives a significant zero-point energy that repels the atoms. The idea is that the atoms are confined to boxes approximately the size of the atomic volume

$$\frac{4\pi}{3} r_a^3 = V_a, \tag{28.18}$$

where V_a is the inverse of their number density. Confinement to the distance r_a gives a zero-point momentum uncertainty Δp

$$\Delta p \, r_a \simeq \hbar. \tag{28.19}$$

[1] The attractive potential between H_2 molecules is not strong either, but is an order of magnitude larger than between He atoms.

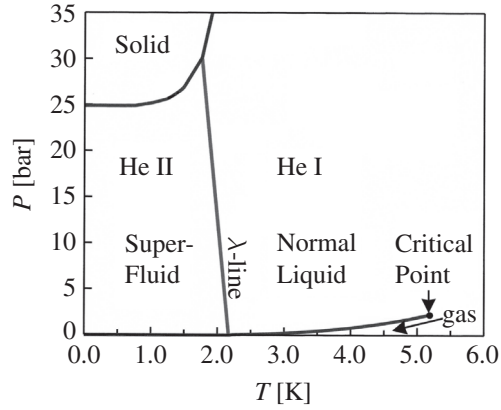

Figure 28.1 Low-temperature region of the P–T phase diagram of helium.

The zero-point energy, E_0, is

$$E_0 = \frac{(\Delta p)^2}{2M} \simeq \frac{\hbar^2}{M r_a^2}. \tag{28.20}$$

Because the interatomic potential between He atoms is weak, with a minimum at perhaps –2.5 meV, the strong dependence of E_0 on r_a^{-2} from Eq. 28.20 suppresses the close approach of He atoms. At atmospheric pressure the He atoms cannot become dense enough to form a solid. The potentials involved are quite small, however, so a pressure of 25 atmospheres (2.5 MPa) is sufficient to form solid He. Figure 28.1 is the phase diagram of helium, showing regions of solid, liquid, and gas (with a critical point). The near-vertical "λ-line" designates the superfluid transition.

28.2.2 Superfluid Phase Transition of ^{4}He

The third law of thermodynamics requires an equilibrium state with zero entropy at 0 K, so a liquid, with its many internal degrees of freedom, would seem an unlikely candidate to be an equilibrium phase at the lowest temperatures. What happens is that below 2.17 K, liquid ^{4}He begins to undergo a Bose–Einstein-like condensation of some fraction of its atoms. These N_0 atoms are all in the same quantum state. With no random thermal occupancies of other states, combinatoric arguments give zero entropy for the condensate (i.e., $k_B \ln 1 = 0$), unlike the N_{ex} atoms that are not condensed. It is useful to consider helium at temperatures below 2.17 K as a two-phase mixture of He I (normal) and He II (superfluid). The fraction of He II becomes 1 at 0 K. The heat capacity of helium across the superfluid transition is shown in Fig. 28.2. The phase transition is often called a "lambda transition" because the curve of $C_P(T)$ has a shape that bears some resemblance to the Greek letter λ. A λ-shape is a general characteristic of second-order phase transitions such as magnetic transitions, and even chemical order–disorder transitions if they are in equilibrium.

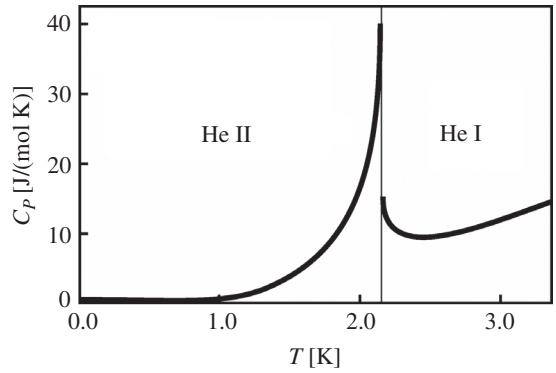

Figure 28.2 Heat capacity of helium through the superfluid transition at 1 bar pressure.

Along with zero entropy, He II has other peculiar properties. One is superfluidity, which means that He II has no viscosity. The superfluid phase has a spectacular ability to leak through small channels or cracks in an experimental apparatus. A related phenomenon occurs when a thin film of He II coats the walls of its container.[2] By a siphon action, the He II leaks out of the container by going over the walls to settle in locations of lower height.

Another peculiar property is the enormously high thermal conductivity of He II. Thermal transport is not by typical mechanisms of independent phonons. It appears to be better understood as a collective motion of the superfluid atoms of He II, maybe more like convection. Temperature is equalized rapidly in He II, and it does not bubble at hot spots, for example. Mixtures of He I and He II sustain waves of temperature which are analogous to but different from the density waves of sound in a liquid. These thermal waves are called "second sound."

The combination of superfluidity and zero entropy causes other strange properties of He II. With superleaks through which only He II passes quickly, liquid ^{4}He can be separated into regions richer in He II than normal He I. It is observed that the temperature of a region filled with He II is lowered, whereas the loss of He II causes a rise in temperature. From the heat capacity of the total liquid, these experiments can be used to show that the entropy of He II is zero, or close to it. Although there is a finite entropy difference between He I and He II, the phase change from He I to He II upon cooling begins with an infinitesimal amount of He II, and is a second-order transition.

There is a limit to the rate of superfluid flow, beyond which quantum behavior is lost. This is somewhat less than the velocity of sound. At low rates of flow, the thermal excitations in He II (named "rotons" for historical reasons, but they are essentially phonons) can leave the He II and deposit their energy into the He I. At higher rates of flow, however, these excitations build up in the He II and cause it to lose superfluidity.

[2] This requires helium to wet the surfaces of most materials, which is generally true because helium atoms are attracted to most materials more strongly than they are attracted to each other.

28.3 Condensate Wavefunction

A basic way to discuss what a superfluid phase is, and what it does, is to discuss its wavefunction. The wavefunction of a system of condensed bosons is macroscopic, and quantum behavior occurs on a large scale. For example, a supercurrent of electrons flowing without resistance down a long wire is a characteristic of a macroscopic wavefunction for Cooper pairs. Resistance, or a change in velocity of the electron current, would require a change in this macroscopic quantum state involving a transition to another wavefunction.

First recall how an electron wavefunction is used in quantum mechanics. A wavefunction for an electron about an atom reflects the probability of finding the electron at a location, but there is more to the wavefunction than the average density implied by this probability. First, the electron is not a fuzzy object with the shape of the wavefunction, but is a small particle that might be found at different locations. Second, it is the phase of the electron wavefunction that really imparts wave behavior. The phase allows constructive or destructive interference of the electron wavefunction with itself, and this interference changes as a local potential alters the electron energy and momentum, for example. The phase of the wavefunction ψ is lost when the electron probability density is evaluated as the real quantity $\psi^*\psi$, so the wavefunction is often of more interest for quantum mechanics than is the density. The phase, $\theta(\vec{r},t)$, can vary in space and in time, and appears in a phase factor of the wavefunction as $e^{i\theta(\vec{r},t)}$.

In macroscopic quantum phenomena, we are interested in variations of phase that occur over macroscopic dimensions. The simplest wavefunction that could be interesting is

$$\psi(\vec{r},t) = \psi_0(\vec{r},t)\, e^{i\theta(\vec{r},t)}, \tag{28.21}$$

where ψ_0 and θ are both real functions. The probability density of our macroscopic state (e.g., the density of a superfluid) is

$$\rho(\vec{r}) = \psi^*(\vec{r},t)\,\psi(\vec{r},t), \tag{28.22}$$

$$\rho(\vec{r}) = \psi_0(\vec{r},t)\, e^{-i\theta(\vec{r},t)}\ \psi_0(\vec{r},t)\, e^{i\theta(\vec{r},t)}, \tag{28.23}$$

$$\rho(\vec{r}) = \psi_0^2(\vec{r},t), \tag{28.24}$$

since ψ_0 is real. For a macroscopic state with Avogadro's number of particles, the probability density is expected to be essentially the same as the actual density of the particles (^{4}He atoms, for example), so for a mass density ρ_M

$$\psi_0(\vec{r},t) = \sqrt{\frac{\rho_M(\vec{r},t)}{M}}. \tag{28.25}$$

Evidently the ψ_0 by itself gives classical behavior. The quantum behavior with wavefunction interference comes with the complex exponential $e^{i\theta(\vec{r},t)}$.

If $\psi(\vec{r},t)$ is an appropriate wavefunction, it must obey the Schrödinger equation

$$i\hbar\frac{\partial\psi}{\partial t} = -\frac{\hbar^2}{2M}\nabla^2\psi + V\psi, \tag{28.26}$$

where for now it is assumed that V is a constant. To start, substitute the one-dimensional form of Eq. 28.21 into Eq. 28.26

$$\mathrm{i}\hbar\frac{\partial}{\partial t}\psi_0(x,t)\mathrm{e}^{\mathrm{i}\theta(x,t)} = \frac{\partial^2}{\partial x^2}\psi_0(x,t)\mathrm{e}^{\mathrm{i}\theta(x,t)} + V\,\psi_0(x,t)\mathrm{e}^{\mathrm{i}\theta(x,t)}. \tag{28.27}$$

These results are needed

$$\frac{\partial}{\partial x}\psi_0\mathrm{e}^{\mathrm{i}\theta} = \frac{\partial\psi_0}{\partial x}\mathrm{e}^{\mathrm{i}\theta} + \mathrm{i}\frac{\partial\theta}{\partial x}\psi_0\mathrm{e}^{\mathrm{i}\theta}, \tag{28.28}$$

$$\frac{\partial}{\partial x}\psi = \frac{\partial\psi_0}{\partial x}\mathrm{e}^{\mathrm{i}\theta} + \mathrm{i}\frac{\partial\theta}{\partial x}\psi, \tag{28.29}$$

which can be combined with the independent, orthogonal y- and z-derivatives to give the gradient

$$\vec{\nabla}\psi(\vec{r},t) = \left[\vec{\nabla}\psi_0\right]\mathrm{e}^{\mathrm{i}\theta(\vec{r},t)} + \mathrm{i}\left[\vec{\nabla}\theta(\vec{r},t)\right]\psi. \tag{28.30}$$

Recall the gradient is essential to the momentum operator, $\underline{p} = -\mathrm{i}\hbar\,\vec{\nabla}$. The momentum $\vec{p}$ as $\underline{p}\psi = \vec{p}\,\psi$ can be calculated using Eq. 28.30

$$\underline{p}\psi(\vec{r},t) = -\mathrm{i}\hbar\,\vec{\nabla}\psi(\vec{r},t), \tag{28.31}$$

$$\vec{p}\,\psi(\vec{r},t) = -\mathrm{i}\hbar\left[\vec{\nabla}\psi_0\right]\mathrm{e}^{\mathrm{i}\theta(\vec{r},t)} + \hbar\left[\vec{\nabla}\theta(\vec{r},t)\right]\psi, \tag{28.32}$$

$$\vec{p} = -\mathrm{i}\hbar\frac{\vec{\nabla}\psi_0}{\psi_0} + \hbar\,\vec{\nabla}\theta(\vec{r},t). \tag{28.33}$$

The first term of Eq. 28.33 depends on the properties of the real function ψ_0, and gives classical behavior for the mass density of Eq. 28.25. We therefore ignore this term,[3] and focus on the spatial variations of the phase that give intrinsic quantum behavior

$$\vec{p} \simeq \hbar\,\vec{\nabla}\theta(\vec{r},t)\ . \tag{28.34}$$

Equation 28.34 can be used to calculate a velocity $\vec{v}_\mathrm{q} = \vec{p}/M$

$$\vec{v}_\mathrm{q} = \frac{\hbar}{M}\,\vec{\nabla}\theta, \tag{28.35}$$

which is a velocity for our macroscopic quantum state. It may be the velocity of a superfluid, for example. Note that $\vec{v}_\mathrm{q}$ depends on the gradient of the phase of the macroscopic wavefunction, a novel result. Likewise, from Eq. 28.34 an energy can be calculated

$$E_\mathrm{q} = \frac{p^2}{2M} = \frac{1}{2}Mv_\mathrm{q}^2, \tag{28.36}$$

$$E_\mathrm{q} = \frac{\hbar^2}{2M}\left[\vec{\nabla}\theta\right]^2. \tag{28.37}$$

This contribution to the energy of the macroscopic quantum state depends on the squared gradient of its phase, not its amplitude. This is also a new result for us.

[3] If the macroscopic quantum state is indeed large spatially, the first term is expected to be small anyhow.

Returning to the Schrödinger equation, Eq. 28.27, we see that it has terms that are real and terms that are imaginary, and these two sets of terms must obey separate equalities. The real terms obtained from Eq. 28.27, and its equivalent forms in y and z, give

$$\hbar \frac{\partial \theta}{\partial t} = \frac{\hbar^2}{2M} \frac{\nabla^2 \psi_0}{\psi_0} - \frac{\hbar^2}{2M} \left[\vec{\nabla \theta}\right]^2 - V. \tag{28.38}$$

For the same reason that we neglected the gradient of ψ_0 for the momentum in Eq. 28.33 (classical, and small for large macroscopic quantum states), we neglect the term with $\nabla^2 \psi_0$ in Eq. 28.38. Using Eq. 28.37 and then Eq. 28.36

$$-\hbar \frac{\partial \theta}{\partial t} = E_{\mathrm{q}} + V, \tag{28.39}$$

$$-\hbar \frac{\partial \theta}{\partial t} = \frac{1}{2} M v_{\mathrm{q}}^2 + V. \tag{28.40}$$

The energy of our macroscopic quantum state depends on the time variation of its phase. As an aside, in the case where $v_{\mathrm{q}} = 0$

$$-\hbar \frac{\partial \theta}{\partial t} = +V, \tag{28.41}$$

a relation that proves useful when there is an interface between two regions of different potential, as in a Josephson junction between superconductors [436, 437].[4]

A couple of cautionary points are in order. Measuring v_{q} is equivalent to measuring the phase of the macroscopic wavefunction, and this is generally not possible. The density of the superfluid is measurable, however, and if the flux of density (equivalent to a probability current) is also measured, v_{q} can be deduced. Finally, we did not develop the second equation obtained from the imaginary terms obtained from Eq. 28.30 (see Problem 28.3b and [438, 439]). This second equation provides an analysis of fluid flow, and many properties of superfluidity and superconductivity are treated as the dynamics of nondissipative fluids.

28.4 Superconductivity: 1. Electron–Phonon Interaction

Electrical conductivity in metals is by conduction electrons in states near the Fermi surface, which are the electrons that give metals interesting responses. Some of these conduction electrons can also be responsible for superconductivity, a phenomenon of zero electrical resistance discovered by H. Kamerlingh Onnes in 1911, shortly after he had liquified helium [440]. Superconductivity has similarities to superfluidity, in that Bose–Einstein condensation is helpful for understanding both of them. The vexing problem for superconductivity, however, is that electrons are not bosons, and cannot by themselves condense into

[4] The ac and dc Josephson effects occur across an insulating junction that is thin enough to allow a tunneling current. In the absence of an applied voltage, a phase difference between the two superconducting regions causes a supercurrent through the junction. If a voltage is imposed across the junction, the phase difference will evolve as in Eq. 28.41.

a ground state. A remarkable achievement in 1957 was the theory of superconductivity by Bardeen, Cooper, and Schreiffer (BCS). It involves "Cooper pairs" of two electrons having opposite spins, coupled by an interaction with a phonon. This Cooper pair has zero spin, and behaves as a boson [441]. Cooper pairs, when stable at low temperatures, are capable of condensation and superconducting properties. Superconductivity is explained by the BCS theory as a superfluid of Cooper pairs [439, 442].

Another important property of the two electrons in a Cooper pair is that they have opposite k-vectors. This comes about because there are far more possibilities for such pairs of electrons to change their momenta if the pair has zero total momentum. Consider, for example, a spherical Fermi surface, and recall that only electrons near the Fermi surface are able to change their states by interaction with a phonon. To interact by exchange of a small phonon energy, these two electrons must be very near the Fermi surface in energy and wavevector $|k_\mathrm{F}|$, but they do not necessarily need opposite wavevectors to interact. With opposite wavevectors so $\vec{k}_{F1} + \vec{k}_{F2} = 0$, however, the scattering can be to two states $\vec{k}'_{F1}$ and $\vec{k}'_{F2}$ with any orientation on the Fermi surface, so long as the final states also have opposite momentum ($\vec{k}'_{F1} = -\vec{k}'_{F2}$). On the other hand, if $\vec{k}_{F1} + \vec{k}_{F2} \neq 0$, conservation of the total momentum leads to severe restrictions on the orientations of the final wavevectors. The two electrons in a Cooper pair are therefore in the states $|\vec{k}'_F \uparrow\rangle$ and $|-\vec{k}'_F \downarrow\rangle$.

It is important to relate the velocities of electrons near the Fermi surface and the frequencies of phonons. An electron moves quickly past an atom, setting it in motion with some probability. By the time the atom has reached its full displacement in a vibrational period, the electron has moved away by the distance ξ

$$\xi = \frac{v_\mathrm{F}}{\nu_\mathrm{D}}, \tag{28.42}$$

where v_F is the typical velocity of an electron at the Fermi surface, perhaps 10^8 cm/s, and ν_D is a typical phonon frequency such as a Debye frequency, perhaps 10^{13} s^{-1}. The result is $\xi = 1000$ Å. A second electron will see the largest effect from this phonon if it is separated from the first electron by the distance ξ. This is the typical size of a Cooper pair.[5] This is a big distance, and large numbers of Cooper pairs are intermingled within the volume of a superconductor. Across the large distance ξ, the Coulomb interaction between the paired electrons is screened by other electrons, so Coulomb repulsion is negligible. There is, however, an exchange interaction that favors opposite electron spins, and Cooper pairs contain electrons of opposite spin.

28.4.1 Electron–Phonon Interaction

The electron–phonon interaction (EPI) makes Cooper pairing possible. The full Hamiltonian of a crystal, H, is

$$H = H_\mathrm{n} + H_\mathrm{e} + H_\mathrm{ep}, \tag{28.43}$$

[5] This ξ is one measure of the "coherence length" of the superconductor, but a more proper calculation will obtain this length from the uncertainty relationship $\Delta x = \hbar/\Delta p$. The challenge is to get the Δp from the properties of the electrons near the Fermi surface.

where $H_{\rm n}$ is the contribution from the nuclei (i.e., phonons as in Eq. 26.8), $H_{\rm e}$ is the contribution from the electrons (including chemical bonding, electron–electron interactions, and thermal electronic excitations), and $H_{\rm ep}$ is the contribution from the EPI.

Very generally, the EPI involves both the coordinates of the electrons $\{\vec{r}^{\,\rm el}_\lambda\}$, and coordinates of the nuclei $\{\vec{r}^{\,\rm n}_j\}$

$$H_{\rm ep} = \sum_{\lambda,j} \hat{H}_{\rm ep}(\vec{r}^{\,\rm el}_\lambda, \vec{r}^{\,\rm n}_j). \tag{28.44}$$

More specifically, an EPI can be calculated to first order with contributions such as $I_{\lambda',j,\lambda}$

$$I_{\lambda',j,\lambda} = \left\langle \vec{k}_{\lambda'} \middle| \vec{e}_j(\vec{k}_j) \cdot \overrightarrow{\nabla_{\vec{r}^{\,\rm n}_j}} V(\vec{r}^{\,\rm el}_\lambda,\ \vec{r}^{\,\rm n}_j) \middle| \vec{k}_\lambda \right\rangle, \tag{28.45}$$

where λ and λ' denote the initial and final states of the electron, and j designates a nucleus. Central to Eq. 28.45 is how the electron potential energy changes with nuclear displacements, i.e., $\overrightarrow{\nabla_{\vec{r}^{\,\rm n}_j}} V(\vec{r}^{\,\rm el}_\lambda,\ \vec{r}^{\,\rm n}_j)$.

For a simple example, consider an electronic band formed from isotropic electrons, and a uniform dilation from changing the distances between nuclei

$$H^{\rm D}_{\rm ep} = -\sum_\lambda D\Delta(\vec{r}^{\,\rm el}_\lambda), \tag{28.46}$$

where $\Delta(\vec{r}^{\,\rm el}_\lambda)$ is the fractional change in volume at $\vec{r}^{\,\rm el}_\lambda$, and D is a "deformation potential." The electrons give the potential energy for pushing the nuclei closer together, so the electron coordinates $\vec{r}^{\,\rm el}_\lambda$ appear in the argument of Δ. For a large fractional compression, D is typically a few eV.[6] This simple approach is convenient because a $\Delta(\vec{r})$ is related to a displacement $\vec{u}(\vec{r})$ through its divergence, $\Delta(\vec{r}) = \vec{\nabla} \cdot \vec{u}$, so

$$H^{\rm D}_{\rm ep} = -D \sum_\lambda \vec{\nabla} \cdot \vec{u}(\vec{r}^{\,\rm el}_\lambda). \tag{28.47}$$

The displacement $\vec{u}(\vec{r})$ at the positions of the electrons can be composed of long-wavelength phonons as

$$\vec{u}(\vec{r}^{\,\rm el}_\lambda) = \sum_i \sqrt{\frac{\hbar}{2MN\omega_i}}\, {\rm e}^{-{\rm i}\vec{k}_i \cdot \vec{r}^{\,\rm el}_\lambda}. \tag{28.48}$$

Displacements $\vec{e}(\vec{k}_i)$ in a longitudinal phonon are along the wavevector $\vec{k}_i$

$$\vec{e}(\vec{k}_i) = \frac{\vec{k}_i}{k_i}. \tag{28.49}$$

Calculating the divergence of Eq. 28.47 with Eq. 28.48, and substituting $\omega_i = c_{\rm L}\, k_i$ ($c_{\rm L}$ is the longitudinal wave speed) gives[7]

$$I_{\lambda',i,\lambda} = -{\rm i}D \sqrt{\frac{\hbar}{2N\, mc_{\rm L}}}\, \sqrt{k_i} \left\langle \vec{k}_{\lambda'} \middle| {\rm e}^{-{\rm i}\vec{k}_i \cdot \vec{r}^{\,\rm el}_\lambda} \middle| \vec{k}_\lambda \right\rangle. \tag{28.50}$$

[6] Section 8.3.2 showed that electron energies are shifted by several eV under extreme compressions. In this section, however, we use D for much smaller elastic distortions and small energies.

[7] The prefactor of i would vanish if $\vec{u}$ were real in Eq. 28.48, giving a sine function in the integrand instead.

This EPI is from the phonon i, which includes a factor $\sqrt{k_i}$ that emphasizes large k. However, the potential is usually not a simple constant like D, but may contain a (screened) Coulomb potential, for which a summation over $\vec{r}_\lambda^{\,\mathrm{el}}$ will be a Fourier transformation giving a factor of $4\pi\, e^2/k^2$ for large k. The consequence is that both short- and long-wavelength phonons participate in the electron–phonon coupling. The details of an EPI calculation become intricate, requiring many more features of the electron and phonon dispersions than are accounted for with a simple deformation potential.

It is useful to separate H_{ep} into "adiabatic" and "nonadiabatic" parts. We have assumed that the nuclear motions are slow enough that the electron levels adapt continuously to the evolving structure, and the Born–Oppenheimer approximation is valid. This is an "adiabatic" behavior that does not allow the nuclear kinetic energy (i.e., $-\hbar^2/2M\,\nabla^2\psi(\vec{r}_{\mathrm{n}})$) to alter the electron states. Only the positions of the nuclei, $\vec{r}^{\,\mathrm{n}}$, alter the electron states through the potential energy $V(\vec{r}^{\,\mathrm{el}},\ \vec{r}^{\,\mathrm{n}})$. The adiabatic EPI depends on the nuclear displacements and electronic excitations caused by thermal energy (Section 26.5).

The "nonadiabatic" EPI does not require thermal activation, and the nonadiabatic EPI is the interaction responsible for superconductivity. For the electrons in a Cooper pair to move quasistatically without heating the crystal, there must be both creations and annihilations of the phonons that couple them as they scatter from one pair state $|\vec{k}\uparrow, -\vec{k}\downarrow\rangle$ to another $|\vec{k}'\uparrow, -\vec{k}'\downarrow\rangle$. The nonadiabatic EPI for superconductivity includes the product of two single-electron factors $I_{\lambda',i,\lambda}$ (Eq. 28.45) with an energy denominator.

28.4.2 Adiabatic or Nonadiabatic?

In both the adiabatic and nonadiabatic EPI the electrons are wavelike, but the nonadiabatic EPI also depends on the phase coherence of the nuclear wavefunction. For the adiabatic EPI, the energy levels of the electrons are determined by the instantaneous positions of the nuclei, which are considered as points in space. In both cases the electron wavefunction is altered by the nuclear displacements, and depends on $\overrightarrow{\nabla_{\vec{r}_j^{\,\mathrm{n}}}} V(\vec{r},\ \vec{r}^{\,\mathrm{n}})$, where $\vec{r}^{\,\mathrm{n}}$ is a nuclear coordinate, and we now use $\vec{r}$ for electron coordinates.

Consider one elementary interaction involving two electron states (one initially occupied and the second initially unoccupied) with wavevectors of $\vec{k}_1$ and $\vec{k}_2$, and one phonon with wavevector $\vec{q}$. Furthermore, assume the electron wavefunctions are of Bloch form with a spherically symmetric part localized at each atom. The energy that causes the electron transition from state 1 to 2 is

$$E_{\mathrm{ep}} = \iiint_{-\infty}^{+\infty} \psi^*_{\vec{k}_2}(r)\left(\mathrm{e}^{\mathrm{i}\vec{q}\cdot\vec{r}}\,\vec{e}_{\vec{q}}\cdot\overrightarrow{\nabla_{\vec{r}^{\,\mathrm{n}}}} V(r, r^{\mathrm{n}})\right)\psi_{\vec{k}_1}(r)\,\mathrm{d}^3\vec{r}. \tag{28.51}$$

When we use the Bloch form for the electron wavefunctions, $\psi_{\vec{k}}(\vec{r}) = \mathrm{e}^{\mathrm{i}\vec{k}\cdot\vec{r}}u(|\vec{r}-\vec{r}_j|)$, and include the phase $\mathrm{e}^{\mathrm{i}\vec{q}\cdot\vec{r}}$ of the phonon, the integral over all space vanishes unless $\vec{k}_1-\vec{k}_2+\vec{q} = \vec{g}$, as expected from the conservation of crystal momentum ($\vec{g}$ is a reciprocal lattice vector, possibly 0). The integral becomes a local one, dependent on the local function $u(\vec{r})$.

The gradient of V is unfamiliar, but we can recast it into a more familiar form if we assume that V depends only on the distance between the nucleus and the electron, i.e., $|\vec{r} - \vec{r}^{\,\mathrm{n}}|$, and the electron and nucleus are concentric. The gradient $\overrightarrow{\nabla}_{\vec{r}^{\,\mathrm{n}}}$ depends only on the magnitude of r^{n}, and the angular integrations of the isotropic integrand give 4π

$$E_{\mathrm{ep}} = 4\pi \cos\theta\ \delta(\vec{k}_1 - \vec{k}_2 + \vec{q}) \int_0^\infty u^*(|\vec{r} - \vec{r}_j|) \left(\frac{\partial}{\partial r^{\mathrm{n}}} V(r, r^{\mathrm{n}}) \right) u^*(|\vec{r} - \vec{r}_j|)\ \mathrm{d}r, \tag{28.52}$$

where $\cos\theta$ is the angle between the phonon polarization and the nuclear displacement. If V depends only on the distance between the nucleus and the electron

$$\frac{\partial}{\partial r^{\mathrm{n}}} V(r, r^{\mathrm{n}}) = -\frac{\partial}{\partial r} V(r, r^{\mathrm{n}}), \tag{28.53}$$

giving a core integral

$$\mathcal{I} = -\int_0^\infty u^* u \frac{\partial}{\partial r} V\ \mathrm{d}r, \tag{28.54}$$

which we integrate by parts to transfer the gradient from V to u

$$\mathcal{I} = -V u^* u \Big|_0^\infty + 2 \int_0^\infty V u \frac{\partial u}{\partial r}\ \mathrm{d}r, \tag{28.55}$$

assuming u is real, for simplicity. The first term on the RHS is zero at $r = \infty$, and except for s-electron wavefunctions, $u(r)$ is zero at $r = 0$. Finally

$$E_{\mathrm{ep}} = 8\pi \cos\theta\ \delta(\vec{k}_1 - \vec{k}_2 + \vec{q}) \int_0^\infty V u \frac{\partial u}{\partial r}\ \mathrm{d}r. \tag{28.56}$$

This recasting of Eq. 28.51 shows that the EPI requires a variation of the electron wavefunction across the interaction potential with the nucleus (e.g., a screened Coulomb field).

For the nonadiabatic EPI, the nuclear wavefunction needs to be coherent while there is a substantial variation in the electronic wavefunction (as in the integrand of Eq. 28.56). This coherence time must be at least $\tau_{\mathrm{coh}} = \hbar/E_{\mathrm{ep}}$, or the energy of the EPI would be ambiguous. Coherence requires that the nucleus does not move by more than its de Broglie wavelength, λ, during this time τ_{coh}. This $\lambda = \hbar/P$, where P is the nuclear momentum (typically P is set by temperature). It corresponds to a nuclear velocity $v = P/M$, where M is the nuclear mass, so the time to move across the de Broglie wavelength λ is τ'

$$\tau' = \frac{\lambda}{v} = \frac{\hbar M}{P^2}. \tag{28.57}$$

Coherence, and the nonadiabatic EPI require

$$\tau' > \tau_{\mathrm{coh}}, \tag{28.58}$$

$$\frac{1}{\tau'} < \frac{1}{\tau_{\mathrm{coh}}}, \tag{28.59}$$

$$\frac{P^2}{M} < E_{\mathrm{ep}}. \tag{28.60}$$

The LHS is essentially the nuclear kinetic energy. Typically the energy E_{ep} is a few meV, so the kinetic energy should be of order 10 K for coherence and a nonadiabatic EPI. The coherence required for the nonadiabatic EPI is lost with the thermal increase of nuclear velocity. The energy E_{ep} also needs to be larger than the energies of transitions that change the states of electrons, so the nonadiabatic EPI is not expected to be significant in insulators or most semiconductors with band gaps of order 1 eV or more. In short, the nonadiabatic EPI is expected mainly in metals at low temperatures. This is consistent with the characteristics of conventional superconductors.

The matrix element on the RHS of Eq. 28.45 (i.e., the integral of 28.51) is the same for both the nonadiabatic and the adiabatic EPI. Without coherence, however, the prefactor for the adiabatic EPI depends on the number of excitations of electrons and excitations of phonons, as described in Section 26.5 and illustrated in Fig. 26.6.

28.5 Superconductivity: 2. Phase Transition

28.5.1 Energy Gap and Critical Temperature

Cooper pairing of electrons is attractive, reducing the energy of the two electrons at the Fermi surface below their total energy of $2\epsilon_F$. The calculation of this favorable energy for pairing, called "the energy gap," is beyond the present scope, especially because the chemical potential of Cooper pairs changes as they condense into a ground state, somewhat similar to the superfluid problem discussed in Section 28.1. The gap in the energy spectrum, Δ, between these condensed electrons in the superconducting state and the normal electrons with energies at the Fermi level is often written as

$$\Delta = -2\hbar\omega_D \exp\left(-\frac{1}{V\rho(\epsilon_F)}\right). \tag{28.61}$$

The prefactor is an average of the phonon energy (a Debye energy), which sets the energy range of the interaction. The exponential includes an energy parameter V from a simple early model of the energy of Cooper pairing, which forms a dimensionless parameter when multiplied by the electron density of states at the Fermi level, $\rho(\epsilon_F)$.

For calculating thermodynamic quantities such as a critical temperature, it is more useful to know how the electron–phonon coupling depends on energy, rather than k-vector as in Eq. 28.45. This requires averaging over all electron states near the Fermi surface separated by $\vec{k}_i$ and differing in energy by a selected $\hbar\omega$. Small energies are involved in superconductivity, so $\hbar\omega$ is rather small, and the electron states are close enough to the Fermi surface that it is reasonable to use ground-state Fermi surface properties. The Éliashberg coupling function $\alpha^2 g(\omega)$, where $g(\omega)$ is the phonon DOS, accounts for all scattering between electron states on the Fermi surface. The function $\alpha^2 g(\omega)$ often looks similar to $g(\omega)$, although some parts of the spectrum are given different weights through the electron–phonon coupling factor, α^2.

An important moment is calculated by weighting the Éliashberg function with ω^{-1}, and can be shown to be [443]

$$2\int_0^{\omega_{\max}} \frac{\alpha^2 g(\omega)}{\omega} \mathrm{d}\omega = \frac{\rho(\epsilon_\mathrm{F})\langle I^2\rangle}{M\langle\omega^2\rangle} = \lambda\,, \tag{28.62}$$

where $\langle I^2\rangle$ is an average of I^*I of the integral in Eq. 28.45 over all electrons and all directions, $\langle\omega^2\rangle$ is a weighted second moment of the phonon DOS, and $\rho(\epsilon_\mathrm{F})$ is the electron DOS at the Fermi surface. The strength of the electron–phonon coupling is parameterized by λ, often called the "electron–phonon coupling parameter." In the BCS theory, the critical temperature T_c depends strongly on λ, which is essentially the same as $V\rho(\epsilon_\mathrm{F})$ in Eq. 28.61. A more complete treatment includes electron–electron interactions, sometimes with a parameter μ^*. McMillan adapted a result from BCS theory to more accurately account for experimental data [443, 444], obtaining this expression for the critical temperature of superconductivity

$$T_\mathrm{c} = \frac{\Theta_\mathrm{D}}{1.45}\ \exp\left[-\frac{1.04(1+\lambda)}{\lambda - \mu^*(1+0.62\lambda)}\right]. \tag{28.63}$$

For different elements λ varies from 0.3 to 1.3, being about 1.2 for V and 1.1 for Nb, which have T_c of 5.3 and 9.2 K, respectively, and 0.4 for Al, for which $T_\mathrm{c} = 1.1$ K. Here Θ_D is the Debye temperature, and μ^* represents a reduced Coulomb repulsion because the electron–phonon interaction is carried by the "slow" phonons. Typically $\mu^* \simeq 0.1$.

28.5.2 Thermodynamic Properties

At $T = 0$, some fraction of electrons are expected to be Cooper-paired as bosons, forming a liquid of zero entropy and zero heat capacity. With increasing temperature, energy is absorbed by this condensate, unpairing some of the electrons. There is a finite energy required to do this, called the "energy gap." A consequence is that the unpairing is thermally activated. Well below the superconducting critical temperature, T_c, we expect and find a heat capacity for the superconducting electrons

$$C_\mathrm{es} = \gamma A\, \mathrm{e}^{-bT_\mathrm{c}/T}, \tag{28.64}$$

where the activation energy, bT_c, is written so it scales explicitly with T_c. The constant b is approximately 1.5. The prefactor could be set arbitrarily, but it is assumed proportional to the heat capacity of the normal electrons, which is γT. The idea is that the electrons capable of participating in superconductivity are those near the Fermi surface, since they do not require much energy to change their state. These are the same electrons in a normal metal that absorb heat by thermal excitation to states above the Fermi energy.

A subtlety of the energy gap is that it varies with temperature. This is not surprising, in part because as more electrons enter the superconducting state, the electronic structure near the Fermi surface is altered. These changes are tricky to calculate, however. The gap is maximum at $T = 0$, but goes to zero at T_c. This leads to some confusion about whether the superconductivity transition is first order or higher order. The answer depends on the specific type of superconductivity. Simpler type I superconductivity as we have discussed

so far appears to be a second-order phase transition in the absence of an applied magnetic field. In the presence of a magnetic field, however, the superconducting phase expels the field, and has no change in its free energy. In contrast, the magnetic field permeates the normal phase, and its free energy has a different dependence on temperature. The entropy difference causes the superconducting transition to become first order in the presence of a magnetic field.

28.5.3 Ginzburg–Landau Theory and Type II Superconductivity

The correlation length ξ was discussed at the beginning of Section 28.4, but there is another length of importance in superconductivity, the distance of penetration of a magnetic field, λ'. A magnetic field destroys superconductivity because a net magnetic moment of the electrons breaks the Cooper pairs with opposite spins. With their perfect electrical conductivity, superconducting electrons are remarkably effective in screening magnetic fields, but there is a characteristic length, λ', over which they do so. It depends on the density of electrons, and is approximately 1000 Å for typical metals. This length has a different physical origin than the coherence length of the electrons, ξ.

The balance between these two length scales distinguishes type I superconductors (which do not contain any magnetic flux) from type II superconductors (which can admit magnetic flux in a peculiar way). The Ginzburg–Landau parameter, κ, is the ratio of these two lengths

$$\kappa = \frac{\lambda'}{\xi}. \tag{28.65}$$

- When κ is small, the material can effectively screen all magnetic fields, and type I behavior is observed.
- When κ is larger than $2^{-1/2}$, the spatial profile of the superconducting wavefunction (ψ in what follows) adapts to the varying magnetic field, causing a new microstructure of the normal and superconducting phases in a type II superconductor.

In type II superconductors the magnetic flux penetrates into the bulk material, reducing the total magnetic energy by reducing the peak field.[8] At the mesoscopic spatial scale, the superconducting matrix contains individual rods of normal metal that enclose magnetic flux. The way this works was figured out by Abrikosov in 1957 [445].

The interfacial energy between regions of normal and superconducting phases is an essential feature addressed by Ginzburg–Landau theory, reported in 1950 [446]. The interface is not abrupt, but has a diffuse character to it. The energy of the interface is handled in the same way as in phase field theory (Chapter 17). To obtain the domain wall energy in Ginzburg–Landau theory, the free energy change for a superconductor with a domain wall, ΔF, must be minimized

$$\Delta F = \frac{\hbar^2}{2m^*} \int_0^\infty \left[-\frac{1}{\xi'^2} |\psi|^2 + \frac{\beta}{2} |\psi|^4 + \left| \left(\frac{\nabla}{\mathrm{i}} - \frac{2\pi}{\Phi_0} \vec{A} \right) \psi \right|^2 \right] \mathrm{d}x, \tag{28.66}$$

[8] Because the magnetic energy scales as B^2, the magnetic flux prefers to spread out, much as the strain energy spreads out by the argument of Section 6.7.4.

where $\psi(\vec{r})$ is the pseudowavefunction of the superconducting phase (so that $|\psi(\vec{r})|^2$ is the local density of superconducting electrons), $\vec{A}$ is the vector potential of an external magnetic field, $\Phi_0 = hc/2e$ is the quantum of magnetic flux, m^* is the effective mass of a Cooper pair, β is a positive parameter to make the bulk part of the free energy have the form of Fig. 17.4, and ξ' is a coherence length for the theory.

Although a proper discussion of Eq. 28.66 is beyond the scope of this text, please compare the form of its integrand to that of Eq. 17.3. Notice the square gradient term $|\nabla\vec{\psi}(\vec{r})|^2$ in both equations. This makes a positive contribution to the free energy in problems of chemical unmixing, but with the factor –i, it can be either positive or negative for the interface between normal and superconducting phases. The case where it is positive corresponds to type I superconductivity, where the superconducting coherence length cannot accommodate the abrupt change in magnetic field. The case where it is negative allows for superconducting electrons to accommodate the variations in magnetic field, and the free energy is minimized by breaking the magnetic flux into small zones of minimum field, sometimes called vortex tubes. Each tube contains the quantum of flux $\Phi_0 = hc/2e$, pulling the superconducting electrons inwards by Lorentz forces. These electrons spiral around the tube. The interior of the tube is approximately the radius ξ, but supercurrents flow around it over the longer radius λ' to cancel the flux of $\Phi_0 = hc/2e$. These tubes of quantized flux are called Abrikosov vortices, or fluxons. The radial factor of the superconducting wavefunction, $R(r)$, is approximately

$$R(r) \sim \tanh\left(\frac{r}{\xi}\right), \tag{28.67}$$

which is roughly analogous to the width of an antiphase domain boundary in phase field theory, Eq. 17.35.

A "flux line lattice" of vortex tubes starts to form in a type II superconductor when it is exposed to an applied magnetic field that exceeds a "lower critical field." With increasing magnetic field, the vortex tubes pack more tightly together, often in a hexagonal array. These flux line lattices have been imaged by transmission electron microscopy, as shown in Fig. 28.3. The Lorentz microscopy technique is sensitive to the variations of magnetic fields in the sample, giving an effect integrated through the thin sample traversed by the electron beam.

At an "upper critical field," the flux line lattice becomes unstable. The tubes merge together, resulting in a permeating magnetic field that destroys the superconducting state. Fortunately, these upper critical fields can be quite high. Type II superconductors are the materials most useful today for making high-field magnets. Control of the flux line lattice by "pinning" the vortex tubes to impurities or other microstructural heterogeneities is a key strategy for increasing the upper critical field.

28.5.4 New High-Temperature Superconductors

An obvious figure of merit for superconductors is a high value of T_c, which was first reported in 1911 for solid Hg as approximately 4.16 K. By 1976 this had risen to 23.2 K for Nb_3Ge, and in 2001 superconductivity was found to be 40 K for MgB_2. These are

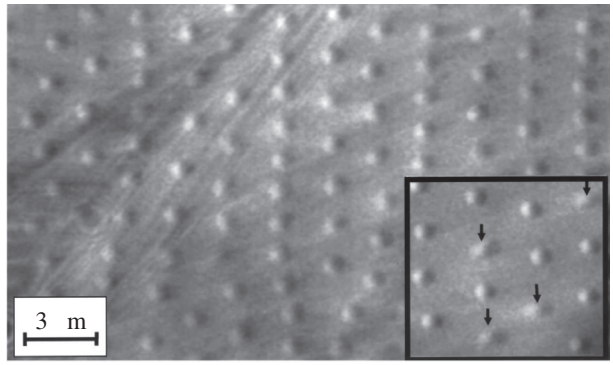

Figure 28.3 Lorentz micrographs of vortices in superconducting Bi-2212, imaged with a transmission electron microscope. When the sample is tilted, the vortex line images become elongated, as shown in the inset. Reproduced, with permission, from [447].

all "conventional" BCS superconductors, where electrons become bosons by interacting with phonons to form Cooper pairs. Conventional superconductors with the highest T_cs are metals having a high density of electrons at the Fermi surface and strong electron–phonon interactions.

A family of a new type of superconductors, often called "high-temperature superconductors," was discovered in 1986 [448], and is now represented by a family of "copper oxide superconductors." In related compounds, the record T_c has been reported to exceed 160 K for $HgBa_2(Ca,Cu)O_4$ under a pressure of 30 GPa. A second family of unexpected superconductors, based on iron pnictides such as iron arsenide, was discovered in 2008. These now have a T_c of over 55 K. In these materials the Fe atoms have magnetic moments, which is unexpected for Cooper pair formation. There is, in fact, a long experimental history showing how magnetism suppresses T_c in conventional superconductors.

Schematic T–c phase diagrams of these two new families of superconductors are shown in Fig. 28.4 [449]. The parent compounds, which are not superconducting, are antiferromagnetic. By adding electrons or holes to the electronic bands, the magnetism is suppressed, and the materials become superconducting with a maximum T_c at an optimal doping. Details of the phase boundaries and two-phase regions are not shown in these figures, in part because they are not yet sorted out. Systematically preparing chemically doped materials has been a challenge, and sample-to-sample variation has been an issue in this field of high-T_c superconductors.

Today it seems most likely that both the copper oxide and iron pnictide superconductors do not work by Cooper pairing of electrons through phonons, but understanding the pairing mechanism is a major topic of research. The $Y_1Ba_2Cu_3O_7$ (the "123 superconductor") is a layered compound with Cu–O planes that are stacked with some separation between each other. Superconductivity is believed two-dimensional within these Cu–O planes. At high temperatures, or at different stoichiometries, it is known that $Y_1Ba_2Cu_3O_7$ is an antiferromagnetic insulator with large exchange energies in the Cu–O planes. There has been extensive effort to understand the rich structures of electron charges and spins in

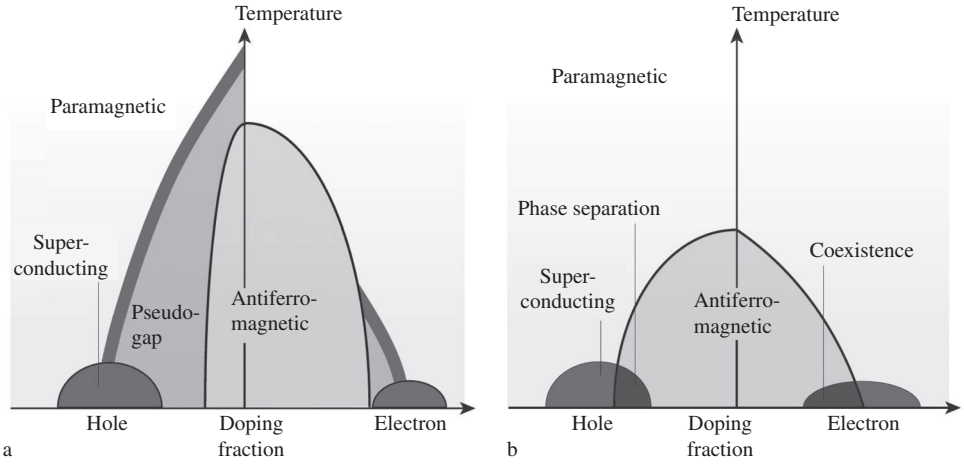

Figure 28.4 Approximate phase diagrams for high-T_c superconductors. (**a**) Copper-oxide-based superconductors. Chemical doping to add electrons or holes suppresses the magnetism of the nonsuperconducting "parent compound," and there is no coexistence of superconducting and antiferromagnetic phases. Within the dark gray regions is a somewhat strange metal with a "pseudogap" in its electronic density of states. (**b**) Phase diagram for the "122 family" of iron-based superconductors such as Fe_2As_2, for which chemical doping can be done by replacing some Fe with Ba or Co. This phase diagram shows the coexistence of antiferromagnetic and superconducting phases. Reprinted by permission from Macmillan Publishers Ltd: *Nature* [449] copyright 2010.

these materials, and to map out the energies and wavelengths of the spin excitations. There is, however, no consensus yet on how the electron pairing mechanism depends on these spin and charge structures.

Today one of the goals of research on iron pnictide superconductors is understanding the origin of the electron pairing mechanism, which might be simpler than that for the copper oxide superconductors. The iron arsenide systems show clear magnetic fluctuations which have temperature and compositional dependences that follow the superconducting transition. In regions of their T–c phase diagrams, some iron arsenides have a two-phase coexistence of domains of antiferromagnetic phase together with domains of superconducting phase, as labeled in Fig. 28.4b. There is intense interest in the relationships between the T_c for superconductivity and magnetism, chemical composition, and crystal structure. It seems likely that magnetic fluctuations are at the heart of the superconducting pairing in the iron pnictide superconductors, but in the year 2020 the details are unknown.

28.6 Correlated Electrons and the Hubbard Model

Coulomb interactions occur between electrons irrespective of spin. In addition to exchange interactions, Coulomb interactions between electrons affect the electron density and electron energies in ways beyond that of the single electron picture that we used to

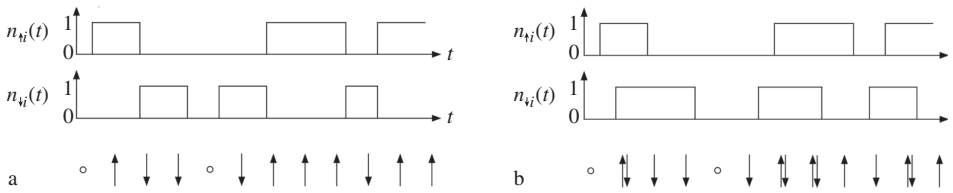

Figure 28.5 Occupancy of electron states on one atom site *i* versus time for correlated electrons in panel a and uncorrelated electrons in panel b. (**a**) Top: $n_{\uparrow i}(t)$, middle: $n_{\downarrow i}(t)$ if $U \gg 0$ and electrons are highly correlated, bottom: depiction of electrons at site *i* versus time. (**b**) Top: $n_{\uparrow i}(t)$, middle: $n_{\downarrow i}(t)$ if $U \sim 0$ and electrons are uncorrelated, bottom: depiction of electrons at site *i* versus time.

understand bonds and bands. Now we add a Coulomb energy penalty for placing two electrons at the same site (atom), encouraging the electrons to spread out over the different sites. This repulsive behavior tends to counteract the tendency to form bonds and bands. Coulomb effects serve to keep electrons away from each other, much as exchange does for electrons of like spin. One way to view the effect of electron correlations is as an enlargement of the "exchange hole" carried by each electron, but now there is a (different) region of electron avoidance for electrons of unlike spin, too.[9]

Consider two states for an electron at a site i, one with spin up and the other with spin down. The number, either 0 or 1, of electrons of spin ↑ at site i is $n_{\uparrow i}(t)$, and this number depends on time (similarly for $n_{\downarrow i}(t)$, the number of electrons of spin ↓ at site i). Define the energy penalty for placing a second electron on a site as U. With a large U, we expect a situation as shown in Fig. 28.5a, where electrons of unlike spin avoid each other on the atom site i. The correlated electron behavior is depicted in Fig. 28.5a by the complementary graphs of $n_{\uparrow i}(t)$ and $n_{\downarrow i}(t)$. For correlated electrons, with increasingly large U we expect

$$\left\langle n_{\uparrow i}(t)\, n_{\downarrow i}(t) \right\rangle \to 0, \tag{28.68}$$

where $\langle\ \rangle$ denotes a time average.

If the electron positions are uncorrelated, as may occur if $U = 0$ so the electrons of unlike spin do not interact at site i, we expect[10]

$$\left\langle n_{\uparrow i}(t)\, n_{\downarrow i}(t) \right\rangle = \left\langle n_{\uparrow i}(t) \right\rangle \left\langle n_{\downarrow i}(t) \right\rangle. \tag{28.69}$$

If $U = 0$ and the electrons are uncorrelated, the electrons hop between sites with no concern for another electron at a site. This "single-electron" behavior was implicitly assumed in our discussion of bonds and bands in Sections 6.2 and 6.3. In this case, all sites look like an average site. Now the addition of the on-site Coulomb repulsion, U, leads to new phenomena, including electronic phase transitions.

To make predictions, the strength of the on-site energy U needs to be compared to an energy that promotes free electron behavior. This is the band energy, ϵ_k, proportional to

[9] When these effects are included as a potential energy in a Hamiltonian for density functional theory, effects of both exchange and Coulomb correlations are typically summarized as a simplified term V_{xc}.

[10] This is much like the probability for finding neighboring atoms in a random solid solution, discussed in Section 7.2.

the number of electrons in the band, n_k. The "Hubbard Hamiltonian" [450, 451] combines these two electron tendencies as

$$H_H = -\sum_i \epsilon_k n_k + U \sum_i \left\langle n_{\uparrow i}(t) n_{\downarrow i}(t) \right\rangle. \tag{28.70}$$

The variables in Eq. 28.70 are mismatched, with nonlocal variables in the first term and local variables in the second. When electron correlations are strong, an electron gas model with nonlocal and noninteracting electrons is irrelevant, and a tight-binding model is a better starting point. The tight-binding model is based on the hopping of electrons between adjacent sites, and the band energy was presented in terms of the hopping integral $\langle a|\mathcal{H}|0\rangle$ in Eq. 6.59. This behavior is parameterized with the variable t (not related to time), which is proportional to the hopping integral $\langle a|\mathcal{H}|0\rangle$

$$H_H = -t \sum_i \left\langle n_i \right\rangle + U \sum_i \left\langle n_{\uparrow i}(t) n_{\downarrow i}(t) \right\rangle. \tag{28.71}$$

This is closer to the traditional form of the Hubbard Hamiltonian, which is written more precisely in second quantization formalism with creations and annihilations of electron state occupancies [451, 452]. The competition between the two terms in Eq. 28.71 is a competition between correlated and independent electron behavior, depicted in Figs. 28.5a and b, respectively.

As an example, the parameters of the Hubbard model can be used to plot a metal–insulator phase diagram in Fig. 28.6, where U/t is plotted as a function of electron density n. Insulator behavior is found when the electrons fill all states on all sites i, which occurs at a critical electron concentration, n_c. At n_c, a minimum ratio of energies for the on-site repulsion to the electron hopping, $(U/t)_c$, is required to suppress delocalized band behavior. A larger U/t corresponds to narrower bands (with poor electron hopping) and insulator behavior. Smaller U/t could correspond to better electron screening and metallic behavior.

"Doping" the electron concentration to add either electrons or holes allows for more empty states that can be filled by electron (or hole) hopping without changing the overall contribution from U. Metallic behavior is favored in doped materials.

Temperature also favors metallic behavior. For example, larger atom vibrations promote the hopping of small polarons (Section 9.2), which are local electrons plus local distortions

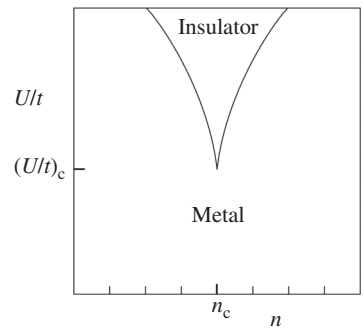

Figure 28.6 Metal–insulator phase diagram using the parameters of the Hubbard model, assuming a low temperature.

of the positions of neighboring cations. In polaron hopping, the local distortion must move with the electron. Thermal vibrations allow this to occur more frequently, increasing the electrical conductivity [102]–[104].

Because the tendencies for electron correlation can change with electron density and temperature, control of these parameters offers opportunities to control electronic properties such as conductivity, magnetism, and superconductivity. Electron correlations are fundamental to understanding the electronic properties of electronic oxides. Today correlated electron behavior is a major topic of research in condensed matter physics.

28.7 Quantum Critical Behavior

Quantum critical behavior has been studied intensely in the past decade or so [453–455]. All phase transitions discussed in this book so far have involved thermal fluctuations, where thermal activation generates excitations, defects, or states of higher energy in a low-temperature phase. In contrast, pure quantum phase transitions occur at $T = 0$, so thermal excitations are not involved. It is still useful to consider a competition between energy and entropy. Often the energy is associated with magnetic interactions, although pressure, electric fields, and effects of chemical doping can also be used to tune energetic preferences in the material, much as for conventional phase transitions. The entropy, however, is associated with entangled quantum fluctuations. These occur by tunneling between states, or, stated somewhat more accurately, by creating superpositions of wavefunctions in a basis set, such as a superposition of spin-up and spin-down states. Complex entanglements are not always analogous to conventional entropy, however.[11]

Today there are many known types of quantum phase transitions, perhaps as many as thermodynamic phase transitions. Quantum critical behavior encompasses phenomena from the subnuclear to the cosmological. Studying them and organizing this knowledge is a research topic today, but it uses many-body quantum mechanics that is beyond the scope of this text. Nevertheless, quantum phase transitions do occur in materials, and materials have proved important testbeds for studying them. Importantly, there are effects from quantum phase transitions that are still seen at finite temperatures, and these effects may appear in relatively common materials [456].

28.7.1 Quantum Ising Lattice at Low Fields

A convenient model for quantum phase transitions, as for phase transitions in general, is the one-dimentional Ising lattice, even though a phase transition does not occur at finite T in 1D. There are some good realizations of this system in materials with spins that can

[11] There is an analogy to the use of the entropy concept for defining the "complexity" of computer programs. Program complexity is sometimes evaluated, like entropy, as the logarithm of the number of possible internal paths inside the program. The path is deterministic, of course, or the program would not run. Nevertheless, highly interconnected programs are evaluated as having a high complexity.

select a direction parallel or antiparallel to a crystal axis, owing to spin–orbit coupling that is directed by the chemical environment of the atom. At low temperatures, only two spin states are possible at each site, $|\uparrow\rangle$ and $|\downarrow\rangle$. Assuming ferromagnetic alignment, there are two possible states at $T = 0$

$$|\Uparrow\rangle = \prod_j |\uparrow\rangle_j \quad \text{or} \quad |\Downarrow\rangle = \prod_j |\downarrow\rangle_j. \tag{28.72}$$

To induce a quantum phase transition in this system, we can apply a magnetic field, but we apply it sideways to push the spins into states like $|\rightarrow\rangle$. The applied magnetic field pushes the spin system out of the state $|\Uparrow\rangle$ and towards $|\Rightarrow\rangle$ by generating defects. In the basis of $|\uparrow\rangle$ and $|\downarrow\rangle$, the field creates defects of flipped spins. We analyze these in pairs, and make the superposition

$$|\rightarrow\rangle_j = \frac{|\uparrow\rangle_j + |\downarrow\rangle_j}{\sqrt{2}}, \tag{28.73}$$

which removes the preferred up or down direction of the ferromagnet.[12] Treating the pairs of spins as a new quasiparticle called a "spinon" is convenient when considering chains of spins

$$\uparrow\ \uparrow\ \uparrow\cdot\downarrow\ \downarrow\ \downarrow\cdot\uparrow\ \uparrow\ \uparrow\ \uparrow \tag{28.74}$$

$$\uparrow\ \uparrow\cdot\downarrow\ \downarrow\ \downarrow\ \downarrow\ \downarrow\cdot\uparrow\ \uparrow\ \uparrow \tag{28.75}$$

where the two kinks are highlighted with the ·. The two have moved outwards from line 28.74 to line 28.75. This rearrangement costs no energy if the system is truly one-dimensional with only first-neighbor interactions. A single kink cannot be annihilated – the chain will always contain an even number of them, assuming it has the same ferromagnetic alignment at both ends. This is a simple example of entanglement of two quasiparticles.

Detailed experimental studies have been possible with antiferromagnetic chains in 1D. Here is the creation and propagation of a pair of kink-like defects called "spinons," which starts by flipping one spin in an antiferromagnetic chain

$$\uparrow\ \downarrow\ \uparrow\ \downarrow\ \uparrow\ \downarrow\ \uparrow\ \downarrow\ \uparrow\ \downarrow \tag{28.76}$$

$$\uparrow\ \downarrow\ \uparrow\ \downarrow\cdot\downarrow\cdot\downarrow\ \uparrow\ \downarrow\ \uparrow\ \downarrow \tag{28.77}$$

$$\uparrow\ \downarrow\ \uparrow\cdot\uparrow\ \downarrow\ \uparrow\cdot\uparrow\ \downarrow\ \uparrow\ \downarrow \tag{28.78}$$

$$\uparrow\ \downarrow\cdot\downarrow\ \uparrow\ \downarrow\ \uparrow\ \downarrow\cdot\downarrow\ \uparrow\ \downarrow \tag{28.79}$$

The energy of spinon excitations depends on their numbers, and less on their spatial distribution. This differs from spin waves or magnons (Section 21.4), which have a discrete energy corresponding to each spatial wavelength. For a particular wavevector, spinon excitations are distributed continuously from zero energy to a maximum. This maximum has its largest value of $-\pi J_1$ at a wavevector of $k = \pi/a$, where a is the first neighbor

[12] It is not necessary to specify that the superposition is $|\leftarrow\rangle_j$ or $|\rightarrow\rangle_j$ because the direction of our applied field is to the right.

distance between spins. (Here we use J_1 from Eq. 21.1 for first neighbors only, and J_1 is negative for an antiferromagnet.) This gives another difference between a spinon and an antiferromagnetic magnon, for which the unit cell is $2a$ and the shortest wavelength is $4a$. A periodicity of $2\pi/4a = \pi/2a$ is expected to be the maximum energy of the magnon, and its energy decreases with larger k until the energy is a minimum again at $k = \pi/a$ (where the spinon continuum has its maximum). Differences in the energy dispersions of spinons and magnons have proved most helpful for identifying spinons in antiferromagnets.

28.7.2 Quantum Ising Lattice at High Fields

At a sufficiently high field, we expect a state with spin alignment along the field direction

$$|\Rightarrow\rangle = \prod_j |\rightarrow\rangle_j. \tag{28.80}$$

We rewrite the product function of Eq. 28.80 with Eq. 28.73

$$|\Rightarrow\rangle = \prod_j^N \frac{|\uparrow\rangle_j + |\downarrow\rangle_j}{\sqrt{2}}. \tag{28.81}$$

Expanding the product in Eq. 28.81 gives a sum of 2^N terms, each of equal weight. When the quantum paramagnet is resolved into up and down spin states, it has an equal number of both, just like the average for the conventional paramagnet. Unlike the conventional paramagnet, the spins are not fluctuating independently in time, and there is never an imbalance of up or down spins owing to fluctuations.

Like a conventional paramagnet, as the field is reduced there will be a critical point where the spins need to decide on the state $|\Uparrow\rangle$ or $|\Downarrow\rangle$. As the up/down symmetry is broken at the critical point, the spin structure has a large correlation length and is quite complicated. It is not fully understood. The 1D quantum spin chain has the Hamiltonian

$$\mathcal{H} = -\sum_j J s_i^z s_{i+1}^z + H s_i^x, \tag{28.82}$$

where the spins are along the z-direction and the magnetic field H is along the x-direction, and J and H are positive. It turns out that the phase transition occurs at the critical field $H_c = J/2$. A way to look at this phase transition is to start at low field, and recognize that the kinks as in Eq. 28.73 reduce the magnitude of the favorable exchange energy in Eq. 28.82. With less favorable cooperative alignment of the spins in the chain, at H_c the magnetic field can change the symmetry, and the ferromagnet becomes a paramagnet. Near H_c the spins are exploring various possible states, but they do not do so in an uncorrelated manner as in a conventional Curie transition. Theoretical work has obtained some critical exponents (as discussed in Section 27.1) for quantities near the quantum critical point, and as expected there is a divergence of the correlation length ξ that describes the size of entangled regions [454, 455].

28.7.3 Finite Temperature and Phase Diagram

An interesting aspect of quantum critical transitions is their influence on behavior at finite temperatures. For our magnetic chain, the quantum critical state is technically present only at one precise magnetic field H_c, but at lower or higher fields there are small regions that show quantum coherence. At finite temperatures these smaller regions become relevant to behavior involving spin relaxations or scattering processes, for example. The competition with incoherent thermal fluctuations depends on the relaxation time. The relaxation time for quantum fluctuations is independent of temperature. What is important for thermal relaxation is the time τ it takes for a spin wave to cross a region of quantum coherence, assumed to have the correlation length ξ_q

$$\tau = \frac{\xi_q}{v_{sw}}, \tag{28.83}$$

where v_{sw} is the velocity of a spin wave packet. The coherence length for quantum fluctuations that are comparable to the thermal energy is

$$\xi_q = \frac{\hbar v_{sw}}{k_B T}, \tag{28.84}$$

and this is smaller with increasing T, as expected. The characteristic time separating quantum from thermal behavior is

$$\tau = \frac{\hbar}{k_B T}, \tag{28.85}$$

which also decreases with T.

For quantum critical behavior, the coherence length and characteristic time are shorter as the applied field departs from H_c. At finite temperatures, Eqs. 28.84 and 28.85 give short-range and short-time effects of quantum coherence that are important over a wider range of magnetic fields than at $T = 0$. This behavior is often summarized in the phase diagram of Fig. 28.7. A thermal phase transition in a 1D system is allowed only at $T = 0$ (e.g., Problem 4.1), hence a thin strip of ferromagnetic phase is shown along the axis at $T = 0$. The pure quantum paramagnet exists at $H = \infty$, but spin flips in this

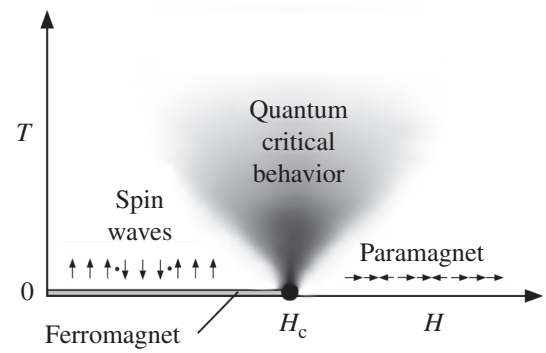

Figure 28.7 *T–H* phase diagram for one-dimensional quantum Ising ferromagnet.

structure occur at lower fields. The transition to an up-spin or a down-spin ferromagnet is at H_c, which includes entanglements over a diverging length scale. Shorter correlation lengths for quantum entanglements occur for H near H_c, and these are important at finite temperature for timescales given by Eq. 28.85, located in the region labeled "Quantum critical behavior."

Problems

28.1 Estimate the zero-point energy (per atom) of liquid ^{4}He when it has a typical density of 145 kG m^{-3}. How does this compare with the expected minimum in interatomic potential energy of 2.5 meV/atom?

28.2 Equation 28.8 was for a density of states in three dimensions. For one dimension, show that $N_{ex}(T)$ (as in Eq. 28.12) does not converge.

28.3 This problem works some details of the condensate wavefunction, its momentum, and its energy.

(a) Perform the straightforward manipulations to obtain the gradient in Eq. 28.30 from its components, as in Eq. 28.29.

(b) Starting with the one-dimensional form of the Schrödinger equation in Eq. 28.27, separate it into two equations for its real and imaginary terms.
The equation from the imaginary terms gives a continuity equation of the form $\partial\rho/\partial t = -\vec{\nabla}\cdot\vec{j}$ (cf. Eq. 3.25). Showing this deserves extra credit.

(c) Show how the three-dimensional form of Eq. 28.38 is obtained.

Further Reading

Part IV Advanced Topics

D.C. Wallace, *Statistical Physics of Crystals and Liquids* (Singapore: World Scientific, 2002).

J.M. Yeomans, *Statistical Physics of Phase Transitions* (Oxford: Clarendon Press, 2002).

Chapter 22

F. Ducastelle, *Order and Phase Stability in Alloys* (Amsterdam: North-Holland, 1991), Chapter 3.

Chapter 23

R. Kikuchi, "The path probability method," *Supplement of Progress of Theoretical Physics* **35**, 1 (1960).

Chapter 24

A.G. Khachaturyan, *Theory of Structural Transformations in Solids* (New York: Wiley-Interscience, 1983), Chapters 7, 8, 13.

Chapter 25

G.L. Squires, *Introduction to the Theory of Thermal Neutron Scattering* (Mineola, NY: Dover, 1978).

Chapter 26

D.C. Wallace, *Thermodynamics of Crystals* (Mineola, NY: Dover, 1998).

B. Fultz, "Vibrational Thermodynamics of Materials," *Progress in Materials Science* **55**, 247–352 (2010).

G. Grimvall, *The Electron–Phonon Interaction in Metals* (Amsterdam: North-Holland, 1981).

Chapter 27

D. Chandler, *Introduction to Modern Statistical Mechanics* (New York: Oxford University Press, 1987).

D.L. Goodstein, *States of Matter* (New York: Dover, 1985), Chapter 6.

J.M. Yeomans, *Statistical Physics of Phase Transitions* (Oxford: Clarendon Press, 2002).

Chapter 28

D.R. Tilley and J. Tilley, *Superfluidity and Superconductivity* (London: Institute of Physics Publishing, 1994).

M. Tinkham, *Introduction to Superconductivity* Second Edn. (Mineola, NY: Dover, 1996).

References

[372] M.J. Richards and J.W. Cahn, *Acta Metall.* **19**, 1263 (1971).
[373] S.M. Allen and J.W. Cahn, *Acta Metall.* **20**, 423 (1972).
[374] J. Kanamori, *Prog. Theor. Phys.* **35**, 16 (1966).
[375] M. Kaburagi and J. Kanamori, *Prog. Theor. Phys.* **54**, 30 (1975).
[376] G. Ceder, G.D. Garbulsky, D. Avis, and K. Fukuda, *Phys. Rev. B* **49**, 1 (1994).
[377] M. Sluiter, P. Turchi, Z. Fu, and D. de Fontaine, *Physica A* **148**, 61 (1988).
[378] L.B. Hong and B. Fultz, *Phys. Rev. B* **52**, 6230 (1995).
[379] N.G. Van Kampen, *Stochastic Processes in Physics and Chemistry*, Second Edn. (Elsevier, Amsterdam, 2004).
[380] B. Fultz, *Acta Metall.* **37**, 823 (1989). *Ibid.* **37**, 2841 (1989).
[381] B. Fultz, *J. Mater. Res.* **5**, 1419 (1990).
[382] K. Gschwend, H. Sato, and R. Kikuchi, *J. Chem. Phys.* **69**, 5006 (1978).
[383] K. Gschwend, H. Sato, R. Kikuchi, H. Iwasaki, and H. Maniwa, *J. Chem. Phys.* **71**, 2844 (1979).
[384] B. Fultz, *J. Less-Common Metals* **168**, 145 (1991).
[385] B. Fultz, *J. Mater. Res.* **7**, 946 (1992).
[386] Z.-Q. Gao and B. Fultz, *Philos. Mag.* **67**, 787 (1993).
[387] M. Becker and W. Schweika, *Scripta Mater.* **35**, 1259 (1996).
[388] L. Anthony and B. Fultz, *J. Mater. Res.* **9**, 348 (1994).
[389] B. Fultz, *Philos. Mag. B* **67**, 253 (1993).
[390] L.-Q. Chen and A.G. Khachaturyan, *Acta Met. Mater.* **39**, 2533 (1991).
[391] Y. Wang, L.-Q. Chen, and A.G. Khachaturyan, *Acta Met. Mater.* **41**, 279 (1993).
[392] Y. Wang and A.G. Khachaturyan, *Acta Mater.* **45**, 759 (1997).
[393] B. Sepiol and G. Vogl, *Phys. Rev. Lett.* **71**, 731 (1993).
[394] G. Vogl, O.G. Randl, W. Petry, *et al.*, *J. Phys. Condens. Matter.* **5**, 7215 (1993).
[395] D. Kmiec, B. Sepiol, M. Sladecek, *et al.*, *Phys. Rev. B* **75**, 054306 (2007).
[396] M. Kaisermayr, J. Combet, H. Ipser, *et al.*, *Phys. Rev. B* **63**, 054303 (2001).
[397] M. Leitner, B. Sepiol, L.M. Stadler, B. Pfau, and G. Vogl, *Nature Mater.* **8**, 717 (2009).
[398] S.W. Lovesey, *Theory of Neutron Scattering from Condensed Matter*, Volume 1 (Clarendon Press, Oxford, 1984).
[399] G.L. Squires, *Introduction to the Theory of Thermal Neutron Scattering* (Cambridge University Press, Cambridge, 1978), reprinted by Dover, Mineola, NY, 1996.
[400] L. Van Hove, *Phys. Rev.* **95**, 249 (1954).
[401] N.W. Ashcroft and N.D. Mermin, *Solid State Physics* (Holt, Rinehart and Winston, New York, 1976), Appendix L.

[402] C.W. Li, M.M. McKerns, and B. Fultz, *J. Amer. Ceramic Soc.* **94**, 125 (2011).
[403] G.A. Samara and P.S. Peercy, *Phys. Rev. B* **7**, 1131 (1973).
[404] P.D. Bogdanoff, B. Fultz, J.L. Robertson, and L. Crow, *Phys. Rev. B* **65**, 014303 (2002).
[405] M.E. Manley, R.J. McQueeney, B. Fultz, *et al.*, *Phys. Rev. B* **65**, 144111 (2002).
[406] D.S. Kim, H.L. Smith, J.L. Niedziela, C.W. Li, *et al.*, *Phys. Rev. B* **91**, 014307 (2015).
[407] D.S. Kim, O. Hellman, J. Herriman, *et al.*, *Proc. Natl. Acad. Sci.* **115**, 1992 (2018).
[408] O. Delaire, M.S. Lucas, J.A. Muñoz, M. Kresch, and B. Fultz, *Phys. Rev. Lett.* **101**, 105504 (2008).
[409] J.A. Muñoz, M.S. Lucas, O. Delaire, *et al.*, *Phys. Rev. Lett.* **107**, 115501 (2011).
[410] C.W. Li, M.M. McKerns, and B. Fultz, *Phys. Rev. B* **80**, 054304 (2009).
[411] T. Lan, X. Tang, and B. Fultz, *Phys. Rev. B* **85**, 094305 (2012).
[412] T. Lan, C.-W. Li, and B. Fultz, *Phys. Rev. B* **86**, 134302 (2012).
[413] T. Lan, C.-W. Li, J.L. Niedziela, *et al.*, *Phys. Rev. B* **89**, 054306 (2014).
[414] E.R. Cowley and R.A. Cowley, *Proc. Roy. Soc. London A* **287**, 259 (1965).
[415] C.W. Li, X. Tang, J.A. Muñoz, *et al.*, *Phys. Rev. Lett.* **107**, 195504 (2011).
[416] A.M. Zagoskin, *Quantum Theory of Many-Body Systems* (Springer, New York, 1998).
[417] A.A. Maradudin and A.E. Fein, *Phys. Rev.* **128**, 2589 (1962).
[418] R.C. Shukla and E.R. Cowley, *Phys. Rev. B* **3**, 4055 (1971). *Ibid.* **58**, 2596 (1998). *Ibid.* **62**, 3232 (2000).
[419] D.C. Wallace, *Thermodynamics of Crystals* (Dover, Mineola, NY, 1998).
[420] P.G. Klemens, in *Solid-State Physics*, Volume 7, F. Seitz and D. Turnbull, Eds. (Academic Press, New York, 1958), p. 1.
[421] X. Tang and B. Fultz, *Phys. Rev. B* **84**, 054303 (2011).
[422] J.M. Wills and W.A. Harrison, *Phys. Rev. B* **28**, 4363 (1983).
[423] J.A. Muñoz, M.S. Lucas, L. Mauger, *et al.*, *Phys. Rev. B* **87**, 014301 (2013).
[424] M.S. Lucas, J.A. Muñoz, O. Delaire, *et al.*, *Phys. Rev. B* **82**, 144306 (2010).
[425] O. Delaire, M. Kresch, J.A. Muñoz, *et al.*, *Phys. Rev. B* **77**, 214112 (2008).
[426] O. Delaire, K. Marty, M.B. Stone, *et al.*, *Proc. Natl. Acad. Sci. USA* **108**, 4725 (2011).
[427] I.M. Lifshitz, *Sov. Phys. JETP* **11**, 1130 (1960).
[428] F.C. Yang, J.A. Muñoz, O. Hellman, *et al.*, *Phys. Rev. Lett.* **117**, 076402 (2016).
[429] M.R. Collins and H.C. Teh, *Phys. Rev. Lett.* **30**, 781 (1973).
[430] M. Suzuki, M. Katori, and X. Hu, *J. Phys. Soc. Jpn.* **56**, 3092 (1987).
[431] D.L. Goodstein, *States of Matter* (Dover, New York, 1985), Chapter 6.
[432] H.J. Maris and L. Kadanoff, *Amer. J. Phys.* **46**, 652 (1978).
[433] D. Chandler, *Introduction to Modern Statistical Mechanics* (Oxford University Press, Oxford/New York, 1987), Chapter 5.
[434] M.H. Anderson, J.R. Ensher, M.R. Matthews, C.E. Wieman, and E.A. Cornell, *Science* **269**, 198 (1995).
[435] The Nobel Prize in Physics 2001, www.nobelprize.org/nobel_prizes/physics/laureates/.

[436] B.D. Josephson, *Phys. Lett.* **1**, 251 (1962).
[437] B.D. Josephson, *Adv. Phys.* **14**, 419 (1965).
[438] D.R. Tilley and J. Tilley, *Superfluidity and Superconductivity* (Institute of Physics Publishing, London, 1994).
[439] M. Tinkham, *Introduction to Superconductivity*, Second Edn. (Dover, Mineola, NY, 1996).
[440] H. Kamerlingh Onnes, *Leiden Comm.* **120b**, **122b**, **124c** (1911).
[441] L.N. Cooper, *Phys. Rev.* **104**, 1189 (1956).
[442] J. Bardeen, L.N. Cooper, and J.R. Schrieffer, *Phys. Rev.* **108**, 1175 (1957).
[443] W.L. McMillan, *Phys. Rev.* **167**, 331 (1968).
[444] P.B. Allen and R. Dynes, *Phys. Rev. B* **12**, 905 (1975).
[445] A.A. Abrikosov, *Zh. Eksperim. Teor. Fiz.* **32**, 1442 (1957).
[446] V.L. Ginzburg and L.D. Landau, *Zh. Eksperim. Teor. Fiz.* **20**, 1064 (1950).
[447] A. Tonomura, *J. Electron Microsc.* **52**, 11 (2003).
[448] G. Bednorz and K.A. Müller, *Z. Phys. B* **64**, 189 (1986).
[449] I.I. Mazin, *Nature* **464**, 183 (2010).
[450] J. Hubbard, *Proc. Roy. Soc. London A* **276**, 238 (1963). *Ibid* **281**, 401 (1964).
[451] U. Rössler, *Solid State Theory* (Springer, Berlin, 2004), Chapter 7.
[452] K. Yosida, *Theory of Magnetism* (Springer, Berlin, 1998).
[453] J.A. Hertz, *Phys. Rev. B* **14**, 1165 (1976).
[454] S. Sachdev, *Science* **288**, 5465 (2000).
[455] S. Sachdev and B. Keimer, *Phys. Today* **64**, 29 (2011).
[456] I.S. Lyubutin, V.V. Struzhkin, A.A. Mironovich, *et al.*, *Proc. Natl. Acad. Sci. USA* **110**, 7142 (2013).

Index